Combustion Characteristics of Alternative Liquid Fuels

Cheng Tung Chong

Hughes Hall

A dissertation submitted for the

Degree of Doctor of Philosophy

Aug 2011

Declaration

This dissertation is the result of my own work and includes nothing which is the outcome of work done in collaboration except where specifically indicated in the text. This thesis has not been submitted in whole or in part as consideration for any other degree or qualification at the University of Cambridge or any other University or similar institution. In compliance with regulation, this dissertation does not exceed 65,000 words, and contains 112 figures.

Cheng Tung Chong

Aug 2011

Acknowledgement

List of Publications

Journal papers

Cheng Tung Chong, Simone Hochgreb, Measurements of laminar flame speed of acetone/methane/air mixture, Combustion and Flame, vol. 158, pp. 490-500, 2011.

Cheng Tung Chong, Simone Hochgreb, Measurements of laminar flame speeds of liquid fuels: Jet-A1, diesel, palm methyl esters and blends using particle imaging velocimetry (PIV), Proceedings of the Combustion Institute, vol. 33, pp. 979-986, 2011.

Cheng Tung Chong, Simone Hochgreb, Spray characteristics of a plain-jet airblast atomizer (In preparation)

Cheng Tung Chong, Simone Hochgreb, Fundamental spray combustion characteristics of rapeseed methyl esters (RME) (In preparation)

Conference proceedings

Cheng Tung Chong, Simone Hochgreb, Spray combustion characteristics of palm biodiesel, 7th Mediterranean Combustion Symposium 2011, Chia Laguna, Cagliari, Sardinia, Italy, September 11-15, 2011 (Accepted for oral presentation)

Cheng Tung Chong, Ruigang Zhou, Simone Hochgreb, Emission measurements of premixed counter-rotating swirling flames, 8th Asia Pacific Combustion Symposium, Hyderabad, India, December 10-13, 2010.

Abstract

Combustion characteristics of alternative liquid fuels

Cheng Tung Chong

Envisaged application of biodiesel in gas turbine engines or furnaces requires extensive tests on the deflagration properties of biodiesel. The laminar flame speeds of Palm Methyl Esters (PME) and blends of PME with conventional fuels are determined using the jet-wall stagnation flame configuration. The same technique is also used to measure the laminar flame speed of diesel, Jet-A1, n-heptane, acetone, methane and methane/acetone. The spray atomization characteristics of a plain-jet airblast atomizer are investigated using a phase Doppler anemometry (PDA) under non-reacting conditions. The droplet size and velocity distribution of biodiesels are compared to conventional fuels. For spray combustion investigations, a generic gas turbine-type combustor is developed to compare the spray flame established from PME, rapeseed methyl esters (RME), diesel, Jet-A1 and biodiesel blends. The spray droplet characteristics in the flame and the flow field in the combustor are investigated. Chemiluminescence imaging of OH* and CH* are applied to capture the global flame structure and heat release region. Flame spectroscopy and long bandpass filtered imaging at > 550 nm are performed to evaluate the tendency of soot formation. In general, biodiesels exhibit flame shapes and spray droplet characteristics that are comparable to conventional fuels. In spite of the higher fuel specific consumption, the emission of NO_x is found to be lower for biodiesels compared to conventional fuels. The results show that biodiesels can potentially be used as alternative fuels for gas turbine operation.

Contents

7   Summary and Conclusion

List of Figures

CHAPTER 4

CHAPTER 5

CHAPTER 6

List of Tables

Chapter 1

Introduction

1.1 Background

Biofuels have been identified as a potential alternative to conventional petroleum-based fuels due to their renewability and reduced emissions. At present, many studies focus on the performance and emission of biofuels under internal combustion engine conditions, production process of biofuels and the effect of biofuels blends with conventional fuels. However, fundamental combustion properties and chemical kinetic descriptions of biofuels are still underinvestigated. Understanding of the fundamental combustion behaviour of biofuels is crucial for flame modelling to allow accurate prediction of performance and to identify the precursor of harmful pollutants.

In this dissertation, the combustion properties of biodiesel laminar flame speed is measured and compared to conventional petroleum-based fuels. The performance of biodiesels in gas turbine condition is investigated in a swirling spray flame established under gas turbine conditions. Spray combustion using biodiesels is of considerable interest especially in industrial gas turbines, micro gas turbines and furnaces. The combustor flow field, spray flame droplet characteristics, global flame shapes are investigated and the data is provided for use as validation targets for spray flame modelling. In this chapter, the motivation of this research is described, followed by the objectives and research scope.

1.2 Biofuels overview

The demand for petroleum-based fuels is on the rise due to industrialisation and the growing number of ground vehicles. The continuous usage of fossil fuels will eventually deplete the non-renewable world oil reserves. Another problem associated with over reliance of fossil fuels is the emissions of greenhouse gases (GHGs), which contributes to global climate change. Realisation of the need to reduce dependency on fossil fuels and GHGs emissions has prompted the search for renewable, efficient and non-polluting alternative fuels.

In recent years, biomass-derived fuels (biofuels) have gained much attention as potential alternatives to fossil fuels. Apart from the advantage of renewability, biofuels have shown to be sustainable and less harmful to the environment, especially those derived from 2nd generation biofuels where lingo-cellolusic are used as feedstock [1]. Biomass could be processed into solid, liquid or gaseous fuel depending on the feedstock and conversion process. Solid biomass fuel can be co-fired with coal in power plant for power generation [2]. Liquid or gaseous fuels derived from biomass can be used in various combustion applications such as vehicle engines, boiler, burner etc.

Conversion of biomass into biofuels can be performed through thermochemical or biochemical reactions as shown by the process chart in Fig. 1.1. Under the thermochemical gasification process, biomass is first gasified in the air- or oxygen-blown gasifiers to extract the product gases containing carbon monoxide (CO) and hydrogen (H_2). The mixture of these gases is known as synthetic gas (syngas) which can be used to power a combined cycle power plant. Syngas can be processed into liquid fuels via the Fisher-Tropsch (FT) process. Although FT process is a promising way to produce liquid biofuels of desired characteristics and composition, a high production cost becomes the economic barrier for large scale production.

Biomass pyrolysis is another thermochemical process used to produce liquid biofuels [3]. The principle of pyrolysis process is to thermally expose the organic materials in the absence of oxygen to generate hot fuel vapours before condensing them into bio-oil. Bio-oils have been reportedly used in diesel engines and gas

turbines [4], but their inferior physical properties such as high viscosity would require modification to the existing fuel delivery system.
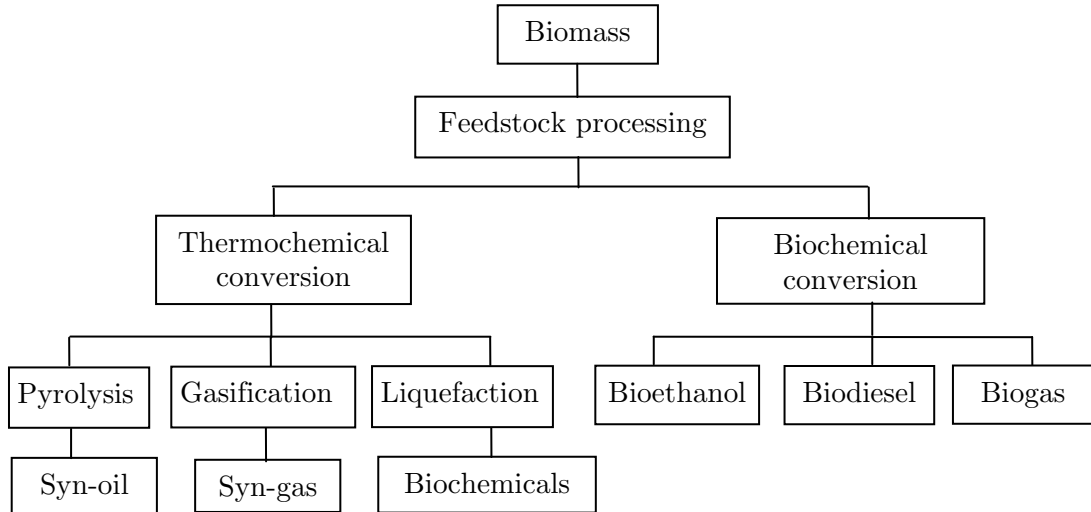
Figure 1.1: Biomass conversion processes (adapted from [5])

At present, global biofuels production consists of bioethanol and biodiesels that are produced through biochemical conversion process. Bioethanol can be produced from sugar or starch such as wheat, barley maize, sugar beet or potatoes. Crops that contain starch or cellulose need to undergo hydrolysis to convert the carbohydrates into sugar prior to microbial fermentation. Water is removed from the fermented fuels through distillation process to obtain bioethanol. Bioethanol contains characteristics close to light distillates such as naphtha and hence is generally used in blends with gasoline [6].

Biodiesel is another important fuel that is increasingly produced globally. The composition of biodiesel is typically a combination of long chain fatty acid methyl esters (FAME) derived from vegetable oils or animal fats through the transesterification process [7]. The transesterified fuels contain physical properties comparable to those of petroleum-based diesel fuels and are suitable to be used neat or in blends for diesel engines. The main feedstock for biodiesel production are oilseeds, palm oil, rapeseed, soybean and animal fats.

1.2.1 Global biofuels production

Biofuels can broadly be categorised into two groups. The first group is termed as the first generation biofuels which refers to biofuels derived from feedstock that are food crops. The second group is known as the second generation biofuels which refers to biofuels derived from lignocellulosic biomass such as agricultural by-product that are non-food crops. At present, global production of biofuels is concentrated on the first generation of biofuels due to high yield of oil. Although non-food crops are desirable for biofuel production, the relatively lower yield of cellulose still presents competition of arable land with food crops. There is also the potential of algae-derived fuels but the technology is still at its infancy stage. The world major producers of bioethanol and biodiesels in 2009 are listed in Table 1.1. Corn, wheat and sugarcane are the main feedstock for bioethanol production. The US is the largest producer of bioethanol in the world, accounting for 53.9% of the world total production in 2009, followed by Brazil which is the second largest producer with 34.2%. Although total bioethanol production by the EU countries (3.6 billion liters) is less 10% of those produced by the US, the EU produce 52.4% of the world biodiesels [8, 9]. Germany and France are the largest producers of biodiesel within the EU. Rapeseed is widely used as feedstock in the EU, whereas Brazil and the US utilise soybean for biodiesel production. The use of palm oil to produce biodiesel is less common and accounts for less than 10% of the world production. Palm biodiesel is primarily produced by countries such as Malaysia, Thailand and Colombo.

Table 1.1: Biofuels production in year 2009 [8, 9]

Bioethanol			Biodiesel		
Country	Major feedstock	(billion liters)	Country	Major feedstock	(billion liters)
US	Corn	41	France	Rapeseed	2.6
Brazil	Sugarcane	26	Germany	Rapeseed	2.6
China	Corn, sugarcane	2.1	US	Soybean	2.1
Canada	Wheat	1.1	Brazil	Soybean	1.6
France	Sugarbeet, wheat	0.9	Argentina	Soybean	1.4
Germany	Wheat	0.8	Spain	Oilseeds	0.6
Spain	Barley, Wheat	0.4	Thailand	Oil palm	0.6
Thailand	Sugarcane, cassava	0.4	UK	Rapeseed	0.5
Other countries		3.3	Other countries		5
World total		76	World total		17

Global bioethanol production has grown at the average rate of 18% per annum since year 2000 as shown in Fig. 1.2 [10]. The US and Brazil produced a total of 67 billion liters of bioethanol in 2009, accounting for 88% of the world total production. More than 360 million barrels of petroleum fuels were replaced by the consumption of ethanol in the US [9]. Since 2006, the US has overtaken Brazil to be the world leading bioethanol producer. Biodiesel accounts for 18.3% of the total biofuels produced in 2009. The interest in biodiesel began seriously in 2001. In between 2001 and 2009, the averaged annual production growth rate has been about 40%. The EU is the main producer of biodiesel, representing 50% of the total biodiesel output in 2009. Germany has been the main biodiesel producer in the EU but the production declined to around 2.6 billion litres in 2009. Biodiesel production is likely to increase due to the emerging producing countries like India, China, Indonesia and Malaysia.
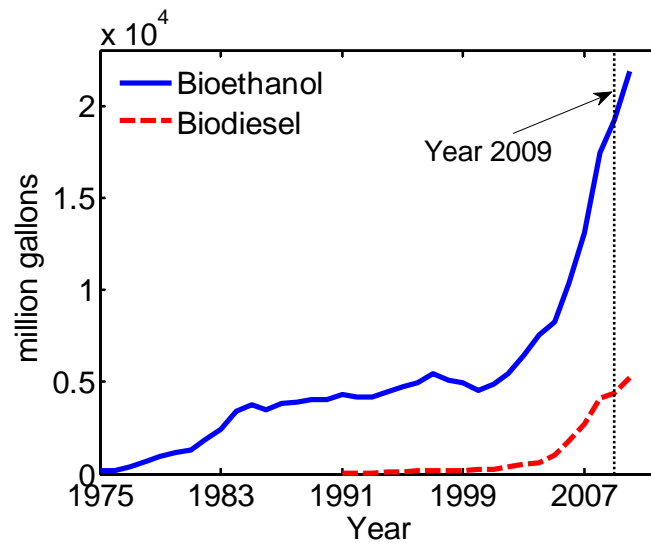
Figure 1.2: Global biofuel production capacity [10]

The growth of biofuel is attributed to governmental policies that favour their use. Table 1.2 lists the biofuel programs implemented worldwide. In Brazil, the government has mandated the blending of 20-25% ethanol with gasoline in government vehicles since the 1970s. The use of a flex-fuel car which operates using pure ethanol, blends or gasoline is encouraged and has been well-received by the public. In the US, farm tax incentive on corn and soy farming biofuels, and blending mandates facilitate the production of biofuels. In Germany, tax is exempt for biodiesel, making the biodiesel price artificially lower than conventional diesel [8].

It has been projected that the production of biofuels will continue to grow in the coming years. The emergence of alternative fuels highlights the need to characterise the combustion properties of these fuels to ensure that the safety, reliability and integrity of the combustion system is not compromised.

Table 1.2: Biofuels blending mandates [9]

Country	Mandate
Australia	E2 in New South Wales, increasing to E10 by 2011; E5 in Queensland by 2010
Argentina	B5 by 2010; E5 by 2010
Bolivia	B2.5 by 2007 and B20 by 2015; E10
Brazil	B5, E20-E25 currently
Canada	E5 by 2010 and B2 by 2010; E5 in Alberta; E7.5 in Saskatchewan; E8.5 in Manitoba; E5 in Ontario; Quebec 5% target by 2012 from advanced biofuels
China	E10 in 9 provinces
Colombia	B10 by 2010 and B20 by 2012; E8 by 2010
Dominican Republic	E15 and B2 by 2015
India	E5 by 2008 and E20 by 2018; E10 in 13 states
Italy	E3.5, B3.5
Jamaica	E10 by 2009
Malaysia	B5 by 2008
Mexico	E6.7 by 2010 in Guadalajara, by 2011 in Monterrey, by 2012 in Central Valley
Pakistan	B5 by 2015; B10 by 2025
Paraguay	E18-E24; B5
Peru	B5 by 2011; E7.8 by 2010
Philippines	B2 and E10 by 2011
Portugal	B7 by 2010
South Korea	B3 by 2012
Spain	B5.8 by 2010
Thailand	B3 by 2010, E10
United Kingdom	B3.25
United States	E10 in Iowa, Hawaii, Missouri, and Montana; E20 in Minnesota; B5 in New Mexico; E2 and B2 in Loiusiana and Washington State
Uruguay	B5 by 2012, less than E5 until 2015, greater than E5 after 2015

* E denotes the fuel ethanol, B denotes biodiesel, the number behind E/B is the percentage of biofuels by volume.

1.3 Objectives

The objective of this dissertation is to investigate the combustion properties and performance of biodiesels relative to conventional fuels such as diesel and aviation Jet-A1 fuels. The experimental result is expected to be useful for combustor design and biodiesel flame modelling. The following are the objectives of the research:

(a) To establish an experimental setup and technique capable of measuring laminar flame speed of gaseous and liquid fuels.

(b) To measure the laminar flame speed of methane/acetone/air.

(c) To measure the laminar flame speed of liquid fuels, i.e., acetone, n-heptane, diesel, Jet-A1 and PME at elevated temperatures.

(d) To characterize the atomization characteristic of a plain-jet airblast atomizer using practical fuels.

(e) To establish a gas turbine type combustor capable of preheating the main air and stabilizing a swirling spray flame. The burner flow field and droplets characteristics are characterized under reacting flow conditions.

 (f) To obtain the flame spectroscopy, OH* and CH* chemiluminescence and the long bandpass filtered images of flames established with different fuels.

(g) To compare the emission performance of different fuels using the swirl burner.

(h) To develop a systematic methodology for liquid fuel combustion characterization applicable to other alternative fuels.

1.4 Research scope

The main interest of this research is to evaluate the combustion properties of palm biodiesels quantitatively through experimental methods. The obtained combustion database can be used as validation targets for chemical kinetic mechanism, two-phase spray modelling or reacting flow modelling in a generic combustor. In general, the experimental work is divided into two parts. The first part focuses on the measurement of fundamental combustion properties, i.e., laminar flame speeds. The laminar flame speeds of gaseous and liquid fuels are measured using an established method from the literature. The second part investigates the spray combustion characteristics under a generic gas turbine type burner typical of those in the practical combustion systems. Several diagnostics methods including phase Doppler anemometry, particle imaging velocimetry, chemiluminescence imaging, and emission measurements are utilized to examine the combustion characteristics of biodiesel spray flames relative to those of baseline fuels.

1.5 Thesis organisation

This dissertation consists of seven chapters. Chapter 1 begins with the introduction to the research scope and the objectives of this research. Chapter 2 describes the technique and methodology established to measure laminar flame speed. The technique is first validated with the existing literature data before being applied to investigate the effect of acetone in methane/air mixture on laminar flame speed. The measurement of the acetone/air laminar flame speed is also performed.

Chapter 3 provides the measurements the laminar flame speed of liquid fuels using the established technique from Chapter 2. The laminar flame speed of n-heptane is measured at room and elevated temperature, partly for technique validation. Further on, the setup is utilised to measure the laminar flame speed of practical fuels such as diesel, Jet-A1, PME and blends of PME with conventional fuels.

Chapter 4 focuses on the spray and atomization characteristic of a plain-jet airblast atomizer under non-reacting and reacting conditions. This chapter reviews the mechanism and the previous spray work performed on a plain-jet airblast atomizer. The review is extended to include previous studies of swirling spray flame burner. Following the literature review, the non-reacting spray rig setup and the swirl burner design and configurations are described. The measurement techniques and operating conditions used to investigate the spray droplets, flow field in the swirl burner and emissions are also included.

Chapter 5 shows the results and discussion on the droplet characterisation of non-reacting and reacting spray. For the non-reacting spray, details of the spray including droplets distributions within the spray, droplet transport, effect of varying air-to-liquid ratio are investigated to understand the atomizer. The use of different fuels provides insights on the sensitivity of fuel physical properties on spray atomization process. The same measurement technique of phase Doppler anemometry (PDA) is applied to characterise the droplets in the reacting flow within a generic gas turbine burner,

Further characterisation of the swirl burner is reported in Chapter 6. The flow field in the burner is examined using the planar imaging velocimetry (PIV) technique under reacting and non-reacting conditions. The global flame structures of the swirling flame established through various fuels are investigated through optical measurements method, i.e., OH* and CH* chemiluminescence imaging, broadband filtering imaging and flame spectroscopy. Lastly, the emission performance of biodiesels and conventional fuels under gas turbine conditions are reported. A summary, conclusions and suggestions for future research is provided in Chapter 7.

1.6 References

[1]   R. E. H. Sims, W. Mabee, J. N. Saddler, and M. Taylor, "An overview of second generation biofuel technologies," *Bioresource Tech.,* vol. 101, pp. 1570-1580, 2010.

[2]   D. Sequera, A. K. Agrawal, S. K. Spear, and D. T. Daly, "Combustion performance of liquid biofuels in a swirl-stabilized burner," *J. Eng. Gas Turb. Power,* vol. 130, pp. 032810.1-032810.10, 2008.

[3]   B. Damstedt, J. M. Pederson, D. Hansen, T. Knighton, J. Jones, C. Christensen, L. Baxter, and D. Tree, "Biomass cofiring impacts on flame structure and emissions," *Proc. Combust. Inst.,* vol. 31, pp. 2813-2820, 2007.

[4]   V. Lupandin, R. Thamburaj, and A. Nikolayev, "Test resutls of the OGT2500 gas turbine engine running on alternative fuels: biooil, ethanol, biodiesel, and crude oil," *ASME paper no. GT2005-68488,* 2006.

[5]   A. Demirbas, "Progress and recent trends in biofuels," *Progr. Energy Combust. Sci.,* vol. 33, pp. 1-18, 2007.

[6]   M. Balat, H. Balat, and C. Öz, "Progress in bioethanol processing," *Prog. Energy Combust. Sci.,* vol. 34, pp. 551-573, 2008.

[7]   A. Demirbas, "Biodiesel production from vegetable oils via catalytic and non-catalytic supercritical methanol transesterification methods," *Prog. Energy Combust. Sci.,* vol. 31, pp. 466-487, 2005.

[8]   G. R. Timilsina and A. Shrestha, "How much hope should we have for biofuels?," *Energy,* vol. In Press, Corrected Proof, 2010.

[9]   REN21., "Renewables 2010 global status report," REN21 Secretariat, Paris 2010.

[10]   "Earth Policy Institute http://www.earth-policy.org/data_center/C26."

Chapter 2

Laminar flame speeds of acetone/methane/air mixtures

2.1 Introduction

Laminar flame burning velocity is defined as the propagation rate of the normal flame front relative to the unburnt mixture. It is an important property for a premixed flame as it embodies the fundamental information on diffusivity, reactivity, and exothermicity of the combustible hydrocarbon mixture [1]. Laminar flame speeds are also practical building blocks for understanding fuel behaviour in devices that operate via mixture deflagration. Values for laminar flame speeds can be used directly in turbulent combustion models, or indirectly as validation targets for chemical kinetic models. To date, there has been much progress in the field of laminar flame speed measurements owing to the advent of laser diagnostics, camera technology and optics. The hydrocarbon laminar flame speeds measured in the past range from simple gaseous fuels to multicomponent practical liquid fuels. In this chapter, the motivation for the measurement of laminar flame speed of acetone/methane/air mixture is discussed, followed by the review of flame speed measurement techniques. A technique is chosen to measure the laminar flame speed for the present experiment. The experimental results are compared to numerically calculated values using a base methane chemical kinetic mechanism (GRI-Mech 3.0) extended with acetone oxidation and pyrolysis reactions.

2.2 Deflagration properties of acetone/methane/air mixtures

Planar Laser Induced Fluorescence (PLIF) has been widely used to gain insight into the instantaneous, two-dimensional structure of mixing and combustion processes of fuel and oxidizer. Fluorescent tracers can either be added into the combustible mixture to mark the unburnt fuel in non-reacting region where the signal is usually weak, or can be found inherently in the reacting region (e.g., OH, NO and CH in combusting flow). The fuel tracer added to the combustible should not disturb the flow, and the fluorescent signal from the tracers must be proportional to their molecular concentration in order to represent the concentration of the targeted fuel represented in the PLIF images. Some of the fuel tracers that emit high fluorescent signals are acetone, formaldehyde, toluene, nitric oxide and 3-pentanone. Among these, acetone (CH_3COCH_3) has been extensively used as molecular tracer in acetone PLIF technique for flow visualization of non-reacting [2] and reacting flows [3-5] due to its photophysical characteristics.

Upon excitation by ultraviolet source between 225-320 nm, acetone molecules emit a strong fluorescence signal in the violet-blue-green range of 350-550 nm within the UV and visible spectrum [3]. The acetone fluorescing signal allows the visualisation of spatial and temporal dynamics within reacting flows which then permits the derivation of useful information including local mixture fraction and scalar dissipation rates. The fluorescence lifetime of acetone molecules is approximately 3 ns and the signals exhibit linear correlation with laser light intensity. The high fluorescence signal intensities enable the use of low seeding concentrations in the flow of interest. From a practical level, acetone is relatively inexpensive, non-toxic and has high vapour pressure, which enables convenient control of seeding concentrations in gaseous mixtures at room temperature [4].

The function of acetone as a fuel tracer is to mix homogeneously and mark the fuel until complete consumption occurs at the flame front. The extent of which acetone marks the fuel effectively is determined by its destruction rate relative to the target fuel. Due to the combustible nature of acetone, the seeding concentration must be low to ensure minimum perturbation on the mixture and flame, and yet sufficiently strong

imaging signal can still be obtained. Yip *et al.* [5] seeded 10 % acetone by volume into a methane/air mixture in a low speed jet flame experiment. They calculated that the seeding of 10 % acetone by volume into methane/air mixture increases the fuel stream's density and heat of combustion by 26 % and 10 % respectively but suggested that the effects were tolerable. Robin *et al.* [6] managed to reduce the acetone seeding quantity to 5 % by volume without sacrificing signal quality.

There has been little investigation on the effect of acetone seeding and the reactive characteristics of the mixture. As a result, the chemical behaviour of acetone as a tracer on the target fuel in hot oxidising environment remains unclear. Degardin *et al.* [7] computed that 5 % of acetone seeding has negligible effect on methane/air mixture laminar flame speed but no experimental validation was performed. Pichon *et al.* [8] reported no observable effect on the ignition delay measurement when 15 % by mole of the heptane is replaced by acetone in a stoichiometric heptane/air mixture. Understanding the role of the fuel tracer in a combustible mixture requires the understanding of acetone oxidation. This chapter examines the effect of acetone as a tracer in methane flames as well as a single reactant.

Acetone oxidation in the gas phase (< 1000 K) has been studied extensively [9-12]. Tsuboi *et al.* [13] conducted the study of thermal oxidation and decomposition of acetone diluted with argon behind the reflected shock wave by using UV absorption and IR emission diagnostics at a temperature range of 1240-1620 K. The measurements of ultraviolet absorption by CH_3COCH_3 and the infrared emission due to CO_2 were performed to obtain the concentration profiles. They proposed an oxidation scheme of $CH_3COCH_3 \rightarrow CH_3COCH_2 \rightarrow H_2C_2O \rightarrow H_2CO \rightarrow CO \rightarrow CO_2$. Sato and Hidaka [14] utilized the UV absorption and IR emission techniques and conducted a shock tube and modelling study of acetone pyrolysis and oxidation in the temperature range of 1050-1650 K and at pressures between 1.2 and 3.2 atm, and subsequently constructed a 51-species, 164-reaction mechanism. Chaos *et al.* [15] studied acetone oxidation in a flow reactor at 12.5 atm and 950 K, and developed an acetone chemical kinetic model consisting of 46 species and 248 reversible reactions. The most recently developed acetone mechanism is reported by Pichon *et al.*[8], comprising 419 reactions and 81 species based on the dimethyl ether mechanism.

Experimental data regarding the global flame response of acetone in flame-relevant conditions is relatively scarce in the literature for mechanism validation. There have been only two sets of laminar flame speed measurements: one measured by Pichon *et al.* using the spherical bomb method and another by Gibbs and Calcote [16] utilising the Bunsen burner method. The ignition delay of acetone was measured by Pichon *et al.* using a shock tube in the temperature range of 1340-1930 K at the pressure of ~ 1 atm. More detailed information at low pressure was provided by Li *et al.* [17], who conducted the species profiles measurements of low-pressure premixed acetone flames by utilising a flat flame established by a McKenna burner. The measurements were carried out using molecular-beam mass spectrometry, with tunable synchrotron radiation in the vacuum ultraviolet region used to selectively photoionise each species. These measurements of lean and the rich acetone flames were able to detect 26 and 38 combustion intermediates respectively.

The objective of the present experiment is to measure the laminar flame speed of acetone/methane/air and acetone/air. The commonly employed techniques for laminar flame speed measurement are reviewed in the following section, and a suitable method is chosen for the experiments.

2.3 Laminar flame speed measurement techniques

2.3.1 Bunsen burner method

In this method, the premixed reactants flow along a cylindrical tube in a uniform laminar flow to the flame, which is stabilized at the burner rim via heat loss, forming a cone-shaped flame. A mean flame speed across the flame area can be obtained by dividing the volumetric flow rate of the mixture by the luminous cone surface area [18], or by measuring the local velocity component of the flow normal to the flame surface, $U_o \sin\theta$ where U_o is the flow velocity and θ is the angle of the half cone angle. The disadvantages of the burner method include the non-adiabaticity of flame due to heat loss to burner rim which tends to decrease the flame speed. The tip of the flame is affected by stretch effects due to the high curvature number which may weaken or intensify the flame. Difficulty also arises in determining the flame surface

area which could lead to inaccurate results. The local normal velocity measurement method gives results to within 20 % accuracy for example, but this will be for a locally strained flame, due the non-normality of the streamlines to the flame.

2.3.2 Unsteady flame in a tube method

This method involves igniting the combustible mixture filled in a long cylindrical tube with an open end. The rate of the propagation of the flame into the unburned reactant along the tube is determined as the flame speed. If the flame appears to be hemispherical in the tube, the flame speed can be determined through the relation $S_L A_f = u_m \pi R^2$, where S_L is the flame speed, A_f is the cross-sectional area of the tube, u_m is the local hemisphere velocity and R is the radius of the hemisphere. However, this method contains some inherent weaknesses: (a) one is the buoyancy effect which distorts the flame front, resulting in the non-uniformity of the flame that deviates from the geometric area of the tube, (b) wall quenching also has a significant impact on the propagating speed, (c) a pressure wave is formed when the flame is propagating, causing the mixture ahead of the flame to gain velocity due to the change of density. These effects have to be accounted for in the determination of unstrained flame speed [19].

2.3.3 Soap bubble method

The gas mixture contained in a soap bubble is ignited at the centre by a spark to create a spherical flame that spreads radially through the mixture. The burned gases expand radially outwards, causing the soap film to expand. The flame velocity can be determined via the relation $S_L = V_f r_i^3 / r_f^3$, where V_f is the average spatial velocity of the flame front, r_i is the initial radius of the soap bubble, and r_f is the final radius of the sphere of burned gas [20]. The growth of the flame front along the radius is photographed at high speed to determine the flame propagation rate. This method assumes that the spherical flame spreads uniformly in radial direction under constant pressure. Some of the difficulties of this method include the uncertainty in the

temperature ratio of the burned and unburned gases, heat loss to the electrodes and deformation of flame cellular structure for fast flames [19, 20].

2.3.4 Flat flame method

A flat flame is stabilised via heat loss on a porous metal plate or a series of small tubes. The rate of heat loss is controlled by the mixture flow rate. The gaseous mixture is ignited at high flow rate and adjusted until the flame is flat. The diameter of the flame is measured and divided by the volume flow rate of unburned gas to determine the flame speed. However, this method is only applicable to mixtures having low burning velocities, on the order of 15 cm/s or less [21]. Botha and Spalding [22] extended the flat flame method to measure higher flame speed by using a water-cooled porous disk. The cooling effect induces heat loss from the flame and stabilises the flame closer to the disk. The tests are repeated at different cooling rates so that the values of flame speed S_L can be plotted against the cooling rates. To obtain the adiabatic flame speed S_L, extrapolation of the curve of S_L versus cooling rate back to zero cooling rate is performed. Some uncertainty is associated with this method including the unknown loss of radical species such as H to the porous plate. Van Maaren *et. al.* [23] utilized the flat flame method to measure the adiabatic flame speed of methane/air mixtures and good agreement was achieved when compared to the literature. The adiabatic flame speed is determined based on the measurement of the burner plate temperature profile. The uniform plate temperature profile indicates zero net heat loss of flame and hence the adiabatic flame speed is obtained. The adiabatic flat flame method was further extended to measure the laminar flame speed of ethane, propane, n-butane and isobutene by Bosschaart and De Goey [24].

2.3.5 Spherical bomb method

In this method, a quiescent combustible mixture situated in a constant volume environment is ignited by a spark, causing a variation of pressure due to adiabatic compression of the unburned gas as the flame propagates outwardly. By simultaneously

recording the pressure history and instantaneous flame radius, the flame speed can be determined through the following expression

$$S_L = \left(1 - \frac{R^3 - r^3}{3p\gamma_u r^2} \frac{dp}{dr}\right) \frac{dr}{dt} \qquad (2.1)$$

where S_L is the flame speed, R is the sphere radius, r is the instantaneous flame radius and γ_u is the specific heat ratio of the unburned gas [20]. For spherically expanding flames, the stretch created on the premixed flame-front is well defined. The outwardly propagating flame images can be used to determine the unstretched laminar flame speed by means of extrapolation to zero stretch. The associated Markstein length L_b with the unstrained flame speeds is useful in expressing the onset of flame instabilities and the stretch influence on flame quenching. From the plot of unstretched flame speed S_n against flame stretch rate K, the Markstein length of burned gas can be derived from the linear relation of $S_l - S_n = L_b K$, where S_l is the unstretched flame speed. The unstretched flame speed S_n can be determined at the intercept value of $K = 0$ [25, 26]. This method is the one of the few that can reach higher pressure, and it has been applied extensively for such measurements [27]. Some of the limitations of this method are the effect of buoyancy on flame, heat loss to electrodes due to intrusive ignition, stretch effects, and the development of intrinsic pulsating and cellular instabilities [1]. These weaknesses are also present in other methods, but those usually cannot be used at high pressure conditions.

2.3.6 Counterflow flame configuration

The counterflow flame configuration consists of two opposing jets with same air-fuel ratio and exit velocity is used to create two flat flames stabilized on stagnation planes. Determination of the unstrained laminar flame speed is performed by extrapolating the reference flame speed back to zero strain rates. The reference flame speed is defined as the local flame speed at the position before the flow accelerates through the flame whereas the corresponding strain rate is derived from the upstream axial velocity gradient [28]. The counterflow flame technique presents the advantage of assuring downstream adiabaticity due to the dual flame configuration. However,

difficulties can arise in determining the location of the stagnation point, as slight fluctuations or time variations in jet momentum cause the point to move in space during the experiment. Coupling of the acoustic properties of the two jets can also lead to oscillations and instabilities in the flame [29].

2.3.7 Jet-wall stagnation flame configuration

The jet-wall stagnation flame configuration consists of one burner and a stagnation plate downstream of the burner outlet. The impingement of premixed hydrocarbon/air on the wall creates a flat, one-dimensional flame that stabilizes through hydrodynamic strain when ignited. The velocity of the flow from the burner outlet decelerates upon approaching the flame front. The flow accelerates when passing through the flame due to the expanded gas volume before slowing down again when approaching the wall. The reference flame speed is identified as the location before the flow accelerates through the flame, while the velocity gradient upstream of the flame is referred as the strain rate. The unstrained laminar flame speed can be obtained by extrapolating the reference flame speed as a function of strain rate back to zero strain rates.

The difference between the counterflow flame configuration and the jet-wall setup lies primarily on the downstream adiabaticity of the established flame. The opposed flame method has the advantage of maintaining downstream flame adiabaticity, whilst the jet-wall configuration loses heat to the solid wall. The effect of heat loss to the wall on laminar flame speed has been addressed by Egolfopoulos *et al.* [30]: their experimental and numerical results suggest that the impinging wall has negligible effect on the laminar flame speed, even though the wall temperatures are set far below the flame adiabatic temperature. Mendes-Lopes [31] quantified the effect of heat loss to the water-cooled stagnation plate and reported minimum effect of the plate on laminar flame speed. The use of lower strain rates and larger nozzle separation distances can increase the accuracy of laminar flame speeds [28, 32]. However, although laminar flame speed is minimally affected, the presence of the wall alters the structures of the flame and significantly influences the flame extinction mechanism [30].

2.4 Previous results from the jet-wall stagnation technique

The jet-wall stagnation method has been used in the past for laminar flame speed measurements. Vagelopoulos and Egolfopoulos [33] measured the unstretched laminar flame speed of methane/air, ethane, propane/air using the jet-wall configuration without performing any extrapolation. The flame speed was directly determined when the planar flame undergoes transition from positive to negative stretch region, during which the flame undergoes a near-zero strain rate condition. The minimum velocity at this near-zero stretch state was regarded as true laminar flame speed. Mendes-Lopes and Daneshyar [34] utilised the jet-wall setup to measure the laminar flame speed of propane/air mixtures and the effect of strain rates on flame speeds.

Dong *et al.* [35] utilised the jet-wall setup to measure the laminar flame speeds of ethane/air mixture seeded with helium and with nitrogen. The result was compared to numerical simulation obtained from GRI-Mech 3.0. The ethane/air/helium laminar flame speed was over predicted but ethane/air/nitrogen dilution shows closer agreement. Natarajan *et al.* [18] measured the flame speed of $H_2/CO/CO_2$ mixture for a range of temperatures and compared the strained flame with simulation results obtained from GRI Mech 3.0 [36] and H_2/CO mechanism of Davis *et al.* [37]. The measurement showed the strained laminar flame speeds for lean mixture of 50:50 H2:CO at 700 K and $\phi = 0.6$ and 0.8 were underpredicted by both the mechanisms through OPPDIF predictions. However, good agreement between the data in [18] and simulation result was achieved for 5-20 % H_2/CO mixtures at elevated pressure of 5 atm, initial temperature of 300 K and $\phi = 0.6$. The flame speed database derived from the jet-wall setup is useful in improving the accuracy of the mechanisms.

Zhao [38] employed the jet-wall stagnation flame configuration coupled with particle imaging velocimetry (PIV) to measure the laminar flame speed of gaseous and liquid fuels. For gaseous fuels, propane/air and dimethyl ether/air mixtures were measured. A preheating method was used to vaporise liquid fuels of n-heptane/air and n-decane/air mixture to elevated temperatures prior to measurements. Measurements were also performed on the gasoline surrogate fuel consisting of n-heptane and iso-

octane mixture at 500 ℃. The laminar flame speed of the surrogate fuel was compared to actual gasoline and primary reference fuel (PFR) model [39].

From previous studies, the jet-wall stagnation flame configuration has been shown to be a suitable method for gaseous and liquid fuel laminar flame speed measurements. The relatively simple setup of a single burner and a plate can be extended to include the heating facility for flame speed measurements at elevated temperature. Hence, the jet-wall stagnation flame configuration has been chosen for the present experiments as a solid compromise between accuracy and ease of operation.

2.5 Flame stretch and differential diffusion effects

All flames are subjected to aerodynamic stretching, manifested through either flow non-uniformity, flame curvature or flame unsteadiness [1]. Flame stretch is defined as the fractional rate of change of a flame surface area [40], $K = 1/A.dA/dt$, which can be decomposed into contributions from aerodynamic strain, flame curvature and flame motion [41]. The stretch effect on laminar flame speed is dependent on the Lewis number of the mixture, Le $= \lambda/(\rho c_p D)$, which is defined as the ratio between heat diffusivity $\alpha = \lambda/\rho c_p$ and species diffusivities, D. For mixtures with Le = 1, the heat and mass transfer are in balance and the net effect on the flame speed is close to zero. For Le < 1, the flame speed tends to increase with strain rate due to the local flame acceleration. A flame front with a convex orientation to the reactants tends to accumulate heat in the products adjacent to the flame front and accentuates the convex curvature. Conversely, the thermal diffusivity through conduction is greater than molecular diffusion for Le > 1. This results in the decrease of flame speed with strain rates as the flame front that curves convex towards the reactants slows down due to thermal influence on the reactant mixture, causing the flame front to straighten itself and become stabilized.

In laminar flame speed measurements, the effect of flame stretch must be accounted for and systematically corrected to obtain unstretched flame speed values. The relation of the strain effect of the flame to the thermal-diffusivity of the mixture is manifested in the slope of the unstrained flame speed S_u against stretch rate K. Under the condition of one-dimensional stagnation flame, Kumar *et al.* [42] showed that the

flame response with stretch rate variation differs according to fuel mixture. For stoichiometric or rich mixtures of n-heptane and iso-octane where Lewis numbers are subunity Le < 1, the S_u increases with increasing K. In these cases, the flame speed increases locally if there is any kind of protrusions appearing on the flame front, thus decreases the local flame stability. Conversely, the Lewis numbers for the lean mixtures of n-heptane and iso-octane are greater than unity Le > 1. This results in the decrease of flame speed with the increase of flame stretch rate. Any protrusion on the flame front due to the increase of stretch will result in the suppression of local flame speed, hence the flame is stabilised.

2.6 Experiments

2.6.1 Burner system setup

Laminar flame speed measurements were carried out by utilising the jet-wall stagnation flame configuration coupled with particle imaging velocimetry (PIV) technique. The burner consisted of a converging nozzle with 22 mm exit diameter and was shrouded by a 3 mm wide annular nitrogen flow to prevent air entrainment from disturbing the flame. The burner flow impinged on a flat, water-cooled brass surface with a diameter of 100 mm, and the distance between burner outlet and plate over the nozzle diameter ratio (L/D) was varied over the range of 0.6 to 1.0 to stabilize the flame. The jet-wall stagnation setup is shown in Fig. 2.1.

An in-house fluidized bed seeder was employed for PIV velocity measurements. The geometry and mechanism of the solid particle seeder is described in Appendix A1. The seeder contained an internal swirler and was used in conjunction with a magnetic stirrer. The seeding particle used in the experiment was hydrophobic AEROSIL® Amorphous Silica R812 S with a size distribution in submicron range ($\sim$ 0.3-0.4 μm) and a density of 0.05 g/cm³. The compressed air flow was dried and filtered to remove any moisture before fluidizing the particles to prevent agglomeration. A bypass valve was installed upstream of the burner to vary the flow rate of the mixture at the nozzle outlet, so the stretch rates can be varied while maintaining the same mixture composition and seeding density.
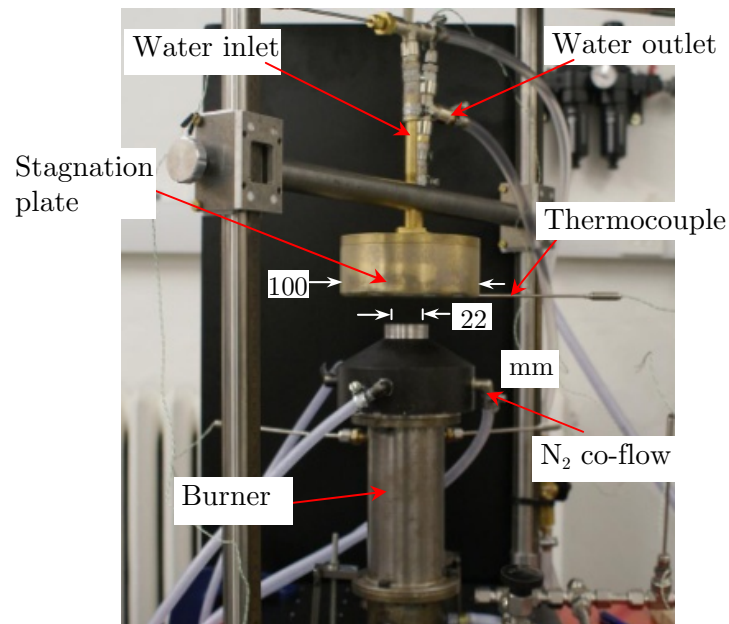
Figure 2.1: Jet-wall stagnation configuration for laminar flame speed measurement

2.6.2 Acetone/methane/air mixture preparation
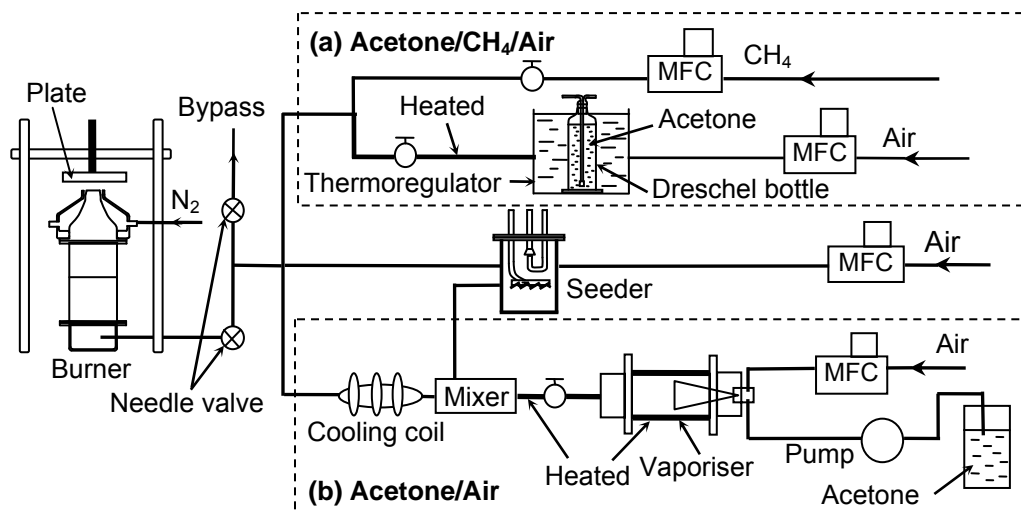
Figure 2.2: Flow delivery system for (a) acetone/methane/air and (b) acetone/air mixture.

In this experiment, the acetone seeding concentration in methane/air is defined as the percentage of acetone in total fuel by mole $\alpha = X_a/X_f$. The equivalence ratio of the mixture is calculated based on the total mixture of methane/acetone/air. Liquid acetone was vaporised into gaseous form before seeding into the methane/air mixture by utilising a bubbling system typical of those used in acetone PLIF setup in the flow delivery system, as shown in Fig. 2.2a. A 250 ml Dreschel bottle containing HPLC grade liquid acetone (99.8+% pure; Fisher Scientific) was immersed in the fixed temperature thermoregulator. The desired acetone vapour was then obtained by flowing air at a constant rate through the Dreschel bottle regulated by an Alicat® mass flow controller (MFC). The acetone vaporisation rate was calibrated using the long average weighting method with different flow rates at fixed bath temperatures. The temperature of the hot bath was monitored by an unsheathed fine gauge K-type thermocouple and the variation shown was ± 0.5 K. High temperature, chemical-resistant PTFE tube was used at the outlet of the Dreschel bottle for acetone vapour flow delivery and was heated with OMEGA® rope heater. The partial pressure of acetone was maintained below the saturation pressure at any point along the line to prevent condensation. Measurements with a fast FID showed that the acetone vaporisation rate becomes inconsistent at high gas bubbling rates due to the disequilibrium between the liquid and air chamber. Hence, only low flow rates of air (<1 l/min) were used as bubbling air for acetone seeding. The vapour-pressure line and the calibration of the acetone vapour mass flow rate is shown in Appendix A2. Methane (99.5% pure; BOC) and primary air flow rates were regulated by Alicat® and Bronkhorst® MFCs respectively, which deliver ± 1 % full scale accuracy.

2.6.3 Acetone/air mixture preparation

At high flow rates, the vaporization rate in the Dreschel bottle was excessive and led to unstable performance. For these cases, the acetone bubbler method was replaced with a vaporiser fitted with an atomizer for high levels of acetone. The liquid acetone was delivered to the vaporiser using a high precision microannular gear pump via the chemical resistant Tygon® tubing. No bubbles were observed along the fuel line, indicating a smooth and consistent delivery of fuel. The full scale accuracy of the pump

is $\pm$ 1 %. Part of the total air ($\sim$ 40 %) was diverted to vaporise the fuel while the rest ($\sim$ 60 %) was used to seed the flow. The air flow rates were separately regulated by two MFCs. The vaporiser was heated by an Omega® rope heater and insulated using high temperature resistant material. A K-type thermocouple was used to monitor the temperature and the heating was controlled using a phase-angled power temperature controller. The temperature within the vaporiser was maintained at $\sim$ 50 °C to ensure the partial pressure of acetone stays within the gaseous phase. The vaporised fuel was then mixed with the remaining seeded air in the mixing chamber before passing through the copper cooling coil upstream of the burner. The partial pressure of acetone was kept under saturation pressure along the line to avoid condensation. A K-type thermocouple was fitted at the burner body to monitor the mixture temperature. The schematic diagram of the system is shown in Fig. 2.2b.

2.6.4 PIV setup

The jet-wall stagnation velocity flow field was obtained using a planar PIV system. The mixture flow was uniformly seeded with submicron-size silica particles. A dual laser head, double pulsed Nd:YAG laser (Litron Lasers:NANO-L-200-15 PIV) was used to generate a light sheet with a thickness of $\sim$ 0.5-1.0 mm to illuminate the uniformly dispersed particles in the flow. The vertical plane of the light sheet was generated from the laser beam by using a cylindrical diverging lens. The laser energy used in this experiment was around 40 mJ/pulse at 532 nm with $\sim$ 4 ns pulse width. The light scattered from the seeding particles in the flow was recorded by a 12 bit, 2048 x 2048 pixels Imager Pro X 4M CCD camera with a pixel pitch of 7.4 x 7.4 μm at double frame mode of 4.5 Hz. The camera was fitted with a 60 mm/F2.8 Nikkor lens coupled with an optical band pass filter centered at 532 nm to minimize the effect of flame luminosity. The timing of the laser system and camera was synchronized by a LaVision® Programmable Timing Unit Version 9 (PTU 9). The commercial software Flowmaster from LaVision was used for image acquisition and the analysis of image pairs. The field of view was fixed at 35 x 35 mm with a magnification factor M equal to 0.43.

2.6.5 PIV accuracy and uncertainty

The timing between PIV pulses Δt ($\sim$ 150-200 µs) was chosen such that the particle movement in the reference flame speed region is within 1/4 of the interrogation window. The cross-correlation is performed using the adaptive multi pass with decreasing window feature, where the initial subregion of 64 x 64 is used before spatially window shifted to the final 32 x 32, with 50% subregion overlapped to optimize the spatial resolution of the velocity field. The seeding density is kept to around 6-10 pixels per subregion to obtain high quality PIV correlations. The peak-height validation method is applied where the ratio of highest peak to second highest peak in the correlation plane is kept at 1.2 for vector validation and to remove spurious vectors. The timing error for the laser is typically small ($\sim$ 4 ns) and does not contribute significantly to the error in velocity measurement. Another possible source of error for PIV is the particle lagging effect. Based on the Stokes number Stk $= \rho_p d^2 U_o / 18 \mu L_s$, where U_o is the characteristic fluid flow and L_s is the characteristic length scale, the calculated Stokes number for the particles in the flow is of the order of $10^{-5} << 1$, indicating the particle lagging effect is not significant. Peak locking effect due to the small signal of less than a single pixel is another possible source of error. The full scale PIV measurement error can be determined by the ratio of the nominal correlation peak value (0.1 pixel) [43] to the maximum displacement permitted, namely 1/4 of the final interrogation window [44]. Since the final interrogation area used in all the image processing is 32 x 32, the accuracy of the axial and radial velocity measurement is determined as $\pm$ 1.25 % full scale. The number of image pair taken for each condition was at least 250 - 500.

2.6.6 Laminar flame speed determination

The planar 2-D velocity vector field obtained using PIV is analyzed to determine the reference stretched flame speed and the imposed strain rate. An example of the 2-D velocity vector map and a flat flame image are shown in Fig. 2.3a and 2.3b respectively. From the burner outlet, the centreline axial velocity decreases towards the stagnation point, reaching a minimum velocity as it approaches the upstream boundary of the preheat zone, before accelerating through the flame due to thermal expansion. To determine the strain rate K, the centreline axial velocity profile from the velocity map is extracted, as shown in Fig. 2.3c. The minimum axial velocity upstream of the thermal mixing layer is identified as the reference burning velocity $S_{ref.}$ The velocity gradient immediately preceding the reference point is determined as the axial strain rate K. The flow pattern is reflected in the radial velocity profile at the reference position (Fig. 2.3d), where the linear radial velocity gradient can be more accurately be employed to determine the axial strain rate, as $K = 2a$ [42].

Based on the variation of the reference flame speed with K, the unstretched laminar flame speed can be determined by using the methodology of either linear or nonlinear extrapolation to zero stretch rate. The non-linear extrapolation method was introduced by Tien and Matalon [45] due to the non-linear relation between S_{ref} and K as $K \rightarrow 0$ based on the asymptotic analysis using potential flows. However, Vagelopoulos et $al.$ [28] showed that if the Karlovitz number Ka $= a_m K/(S_u^o)^2$, is lower than 0.1, where a_m is the thermal diffusivity of the unburnt mixture, laminar flame speeds obtained from the linear extrapolation under these conditions yield sufficiently accurate results. The typical range of strain rates of $\sim$ 100-250 s^{-1} derived from these experiments yield Ka<0.1, so the linear extrapolation is sufficient.
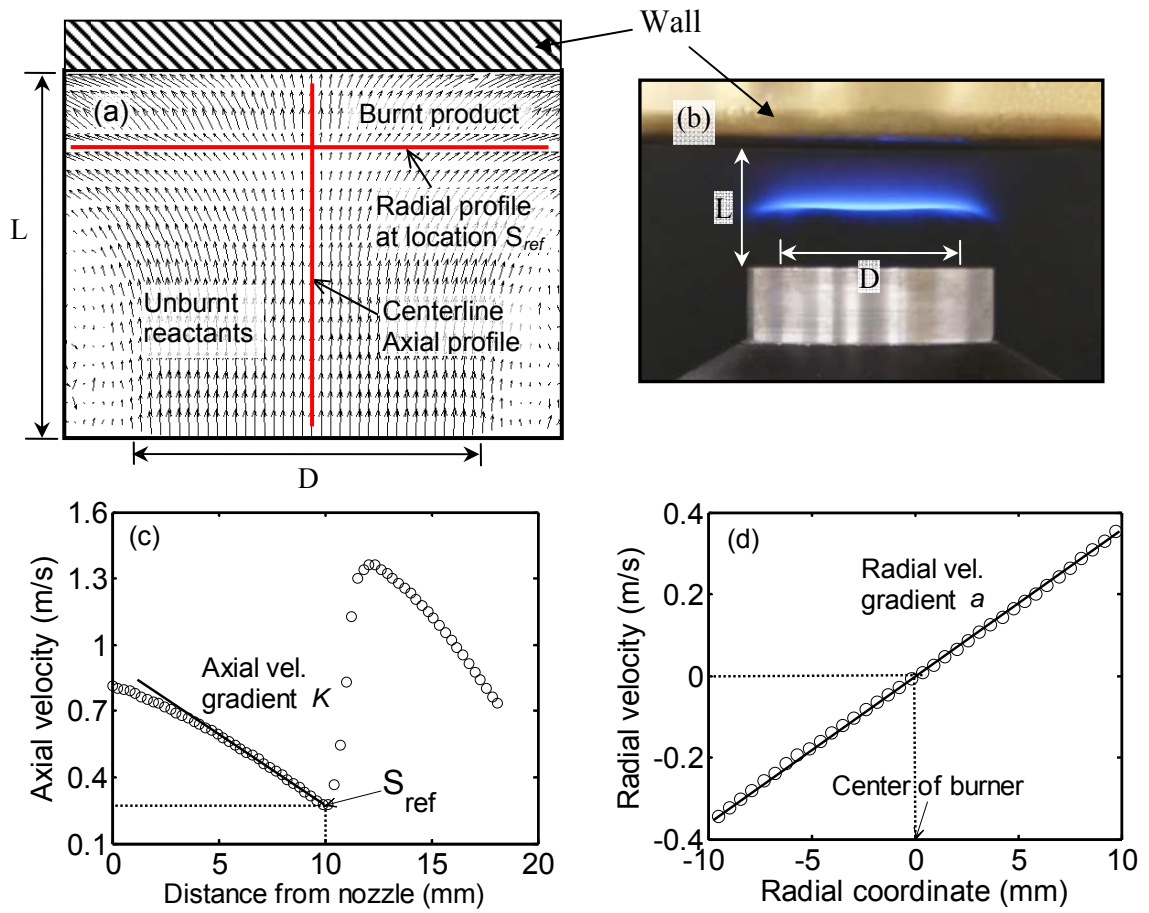
Figure 2.3: (a) Velocity vector map for an image pair (b) Image of a jet-wall stabilized flame (c) Axial velocity profile indicating the reference flame speed (d) Radial velocity profile used to derive the strain rate.
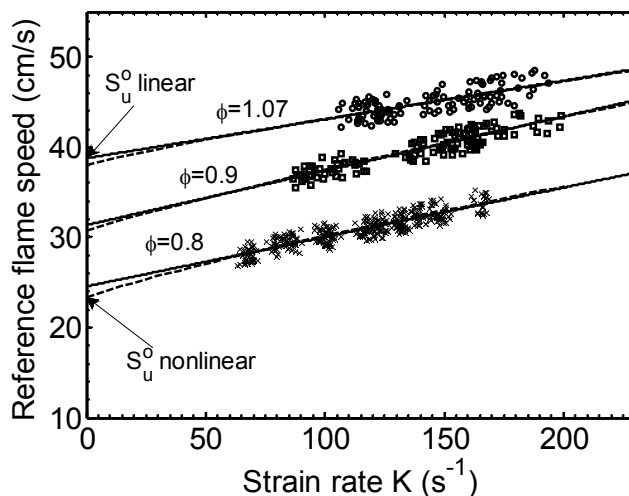
Figure 2.4: Example of (—) linear and (- - -) non-linear extrapolation to obtain the unstretched laminar flame speed for 9% acetone/methane/air mixture.

The extrapolations of unstretched flame speed have been performed using both the linear and non-linear method. The linear extrapolation yields slightly higher unstretched flame speeds by ~ 1-2 cm/s as demonstrated in Fig. 2.4, which is within the experimental uncertainty. Chao *et al.* [32] reported that the accuracy of linear extrapolation method can further be improved by increasing the nozzle-plate separation distance L or decreasing Ka. In this experiment, the use of a 22 mm diameter nozzle allows a relatively larger nozzle-plate distance as compared to the 14 mm diameter used in [42, 46]. The current jet-wall setup also provides a lower strain rate range than the opposed-jet configuration [30] and subsequently lower values of Ka, which favours the use of the linear method in deriving the unstretched laminar flame speed. Therefore, the subsequent flame speed results are reported based on the linear extrapolation method.

2.7 Numerical analysis

The laminar unstrained premixed flame speed calculations are performed using the RUN1DL code from COSILAB [47]. The GRI-Mech 3.0 mechanism [36] is used as the baseline, coupled with the acetone decomposition reactions. The GRI mechanism

consists of 325 elementary reactions with 53 species involved, and has been validated for methane and other gases over a wide range of pressure and temperature conditions. The sub mechanism of acetone is derived from the work by Sato and Hidaka [14] that describes the pyrolysis and oxidation phenomena. Some of the reactions rates are reviewed and updated in accordance to the latest reported values.

Table 2.1: Acetone sub-mechanism, units: cm mol s cal

Reactions	A	n	E	ref
$CH_3COCH_3 <=> CH_3CO+CH_3$	7.02E+21	-1.57	84684	[8]
$CH_3COCH_3+H <=> CH_3COCH_2+H_2$	9.80E+05	2.43	5162	[8]
CH3COCH3+O <=> CH3COCH2+OH	1.00E+13	0.00	5961	[48]
$CH_3COCH_3+OH <=> CH_3COCH_2+H_2O$	1.25E+05	2.48	445	[8]
$CH_3COCH_3+CH_3 <=> CH_3COCH_2+CH_4$	9.50E+03	2.50	8400	[14]
$CH_3COCH_2 <=> CH_2CO+CH_3$	1.00E+13	0.00	28000	[14]
$CH_3CO+M <=> CH_3+CO+M$	5.36E+27	-3.40	18900	[49]

The pyrolysis reaction of CH_3COCH_3 (+M) $\rightarrow$ CH_3CO+CH_3 (+M) is a unimolecular reaction. Ernst *et al.* [50] studied acetone pyrolysis in the temperature range of 1350-1650 K using a shock tube technique and proposed an initiation rate constant of $k = 2.7 \times 10^{16} \exp(-41115/T)$ s^{-1}. Sato and Hidaka determined the rate constant value of $k = 1.13 \times 10^{16} \exp(-41143/T)$ s^{-1} by using a shock tube at a higher temperature range of 1050-1650 K and at a total pressure between 1.2 and 3.2 atm. Pichon *et al.* reevaluated the pyrolysis reaction rate constant as $k = 7.018 \times 10^{21} T^{1.57} \exp(-42617/T)$ s^{-1} based on the chemical activation formulation of Quantum Rice-Ramsperger-Kassel theory and achieved good agreement with the reported data. Hence, this reaction rate constant is adopted in the current mechanism.

The general radical abstraction from acetone can be represented by the reaction $CH_3COCH_3+X \rightarrow CH_2COCH_3+XH$ where X represents a radical species. This step is important for chain-branching processes at high temperatures. The reaction rate constant for $CH_3COCH_3+H \rightarrow CH_3COCH_2+H_2$ has been determined by Ambidge *et al.* [51] at temperatures T < 1000K to be $k = 1.86 \times 10^{13} \exp(-3200/T)$ cm^{3}mol^{-1}s^{-1}. Sato and Hidaka reported $k = 2.30 \times 10^7 \exp(-5000/T)$ cm^{3}mol^{-1}s^{-1} and achieved good agreement with the value reported by Ambidge *et al.* at temperature below 440 K. Pichon *et al.* d

determined $k = 9.8 \times 10^5 T^{2.43} \exp(-2598/T)$, which fits the measured ignition delay data and agrees reasonably well with the value determined by Sato and Hidaka.
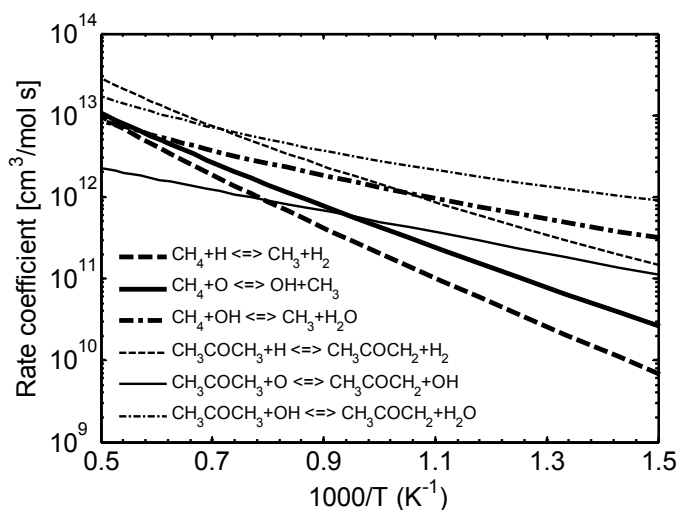
Figure 2.5: Reaction rate coefficients for radical attack on acetone and methane as a function of reciprocal temperature.

The rate constant of reaction $CH_3COCH_3+OH \rightarrow CH_3COCH_2+H_2O$ has been determined by Sato and Hidaka as $k = 2.00 \times 10^{13} \exp(-1511/T)$ $cm^3 mol^{-1} s^{-1}$ in the temperature range below 1000 K. Bott and Cohen [52] determined the value of k at 1200 K and reported $k = 5.3 \times 10^{12}$ $cm^3 mol^{-1} s^{-1}$. Pichon *et al.* determined $k = 1.25 \times 10^5 T^{2.48} \exp(-224/T)$ $cm^3 mol^{-1} s^{-1}$ based on the studies by Vasudevan *et al.* [53] and Yamada *et al.* [54] that cover the temperature range of 298-1300 K. Figure 2.5 shows the comparison of the reaction rate coefficients for the H atom abstraction by different radicals as a function of temperature. The acetone reaction rates are within the same order of magnitude as analogous reactions for methane in the high temperature region.

The sub-mechanism of acetone added to GRI-Mech 3.0 is shown in Table 2.1. The flame speed computation was performed with 0 %, 5 %, 9 % and 20 % of acetone by mole in the total fuel. Initially, the mechanism was developed to examine the effect of relatively low acetone seeding quantity (< 20% by mole) on methane/air mixture. Due to the interest in investigating the potential alternative acetone oxidation mechanism, the laminar flame speed of acetone/air mixture was computed using the

same mechanism and compared to experimental data. The key reactions involved in the chemistry level are discussed in section 2.9.2.

2.8 Results and discussion

2.8.1 Acetone/methane/air

The methane/air flame speed was measured at 298 K and 1 atm to validate the current experimental setup and technique. The variation in the mixture temperature was within $\pm$ 1 K. The result shows particularly good agreement when compared to the existing literature data and simulation [28] with the expected accuracy to within $\pm$ 1.5 cm/s as shown in Fig. 2.6. Throughout the experiment, some cases were selectively performed as control and good repeatability was obtained. Figure 2.7 shows the simulated and experimentally determined laminar flame speeds of methane/acetone/air mixtures at 298 K and 1 atm using PIV. The measurements were performed by seeding acetone at 5 %, 9 % and 20 % by mole of the total fuel into the methane/air mixture, and the equivalence ratio was determined based on the total mixture of acetone/methane/air. At stoichiometry, the differences among all cases of study are indistinct and are within 1.5 cm/s. The peak laminar flame speed of all cases are determined to be at $\phi \sim 1.08$, corresponding to the peak of methane/air flame. The result reveals that the acetone seeding has a more significant effect on rich mixtures, where 5 % of acetone seeding shows little difference compared to pure methane/air flame speed, but 9 % and 20 % of acetone seeding show an appreciable increase of flame speed about $\sim$ 3-6 cm/s.
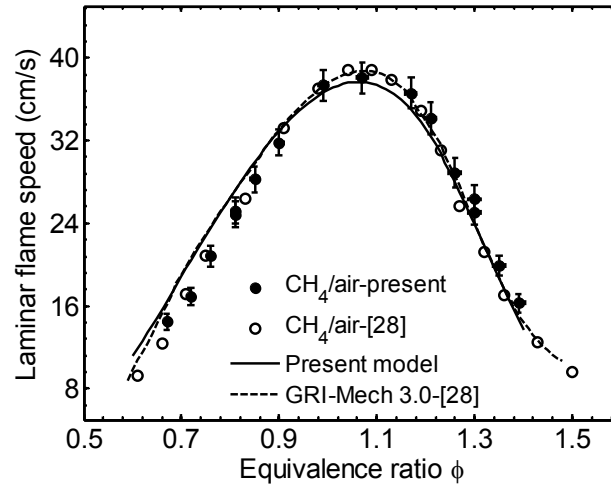
Figure 2.6: Laminar flame speed of methane/air mixture at 298 K and 1 atm (●) present, (○) Vagelopoulos et al. [28], (—) present model, (- - -) GRI-Mech 3.0 [28].
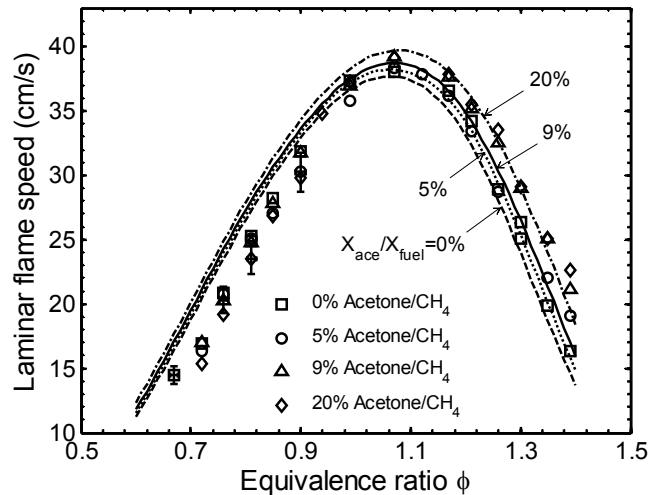
Figure 2.7: Laminar flame speed for (□) 0 %, (○) 5 %, (Δ) 9 % and (◊) 20 % of acetone in methane/air mixture at 298 K and 1 atm. Lines are simulation results for (----) 0 %, (....) 5 %, (—) 9 % and (-.-.) 20 % acetone/methane/air mixture using present model.

On the lean side, the data for all seeded cases are underpredicted by the model. Closer examination reveals the trend of slight reduction of flame speeds as the amount of acetone seeding increases. Figure 2.8 shows the absolute flame speed differences of the seeded cases relative to the baseline case of pure methane/air. The seeded case of 20 % shows ∼ 2 cm/s lower than the baseline case between the $\phi = 0.7$-0.9 as opposed to

the simulation that shows an increase of ~ 1.5 cm/s. The 9 % seeded case also shows ~ 2 cm/s lower at $\phi = 0.9$-1.0. The trend on the rich region concurs with the model, where the increase of acetone shows an increase of flame speed. Overall, the model slightly over predicts the lean side but captures the 0 %, 5 % and 20 % cases well on the stoichiometric and rich side. For the 9 % case, the model slightly under predicts the rich side. The peak flame speed is correctly captured by the model and the simulation is regarded to be in good agreement with the data.
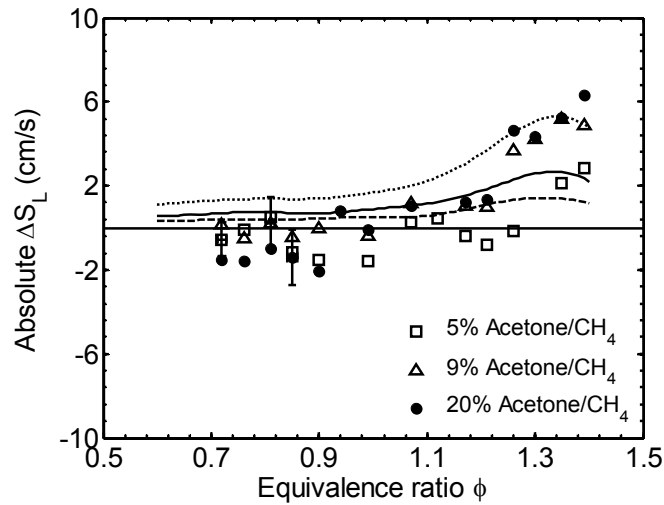
Figure 2.8: Absolute laminar flame speed differences of acetone/CH_4/air mixtures relative to pure methane/air. Simulation is denoted by (----) 5 %, (—) 10 % and (...) 20 % acetone/CH_4/air mixtures.

2.8.2 Acetone/air

Pure acetone flame speed measurements were carried out at 298 K and 1 atm between $\phi = 0.8$-1.4 and the results are shown in Fig. 2.9. The maximum flame speed was measured to be 42.5 cm/s at ~ 1.2, and the flame speed curve is seen to shift slightly towards the rich side. Compared to the experimental data, the simulation results slightly overpredict the stoichiometric region and under predict the fuel-rich region. The calculated maximum acetone flame speed is 42.4 cm/s at $\phi \sim 1.12$, which is very close to the measurement. The good agreement between the data and simulation is perhaps surprising, given the simplicity of the model regarding acetone reactions, and

34

the fact that no chemical kinetic constants were adjusted. However, this can be explained by the fact that acetone is readily converted into byproducts which are present in the methane submechanisms. The simulation predicts the measured acetone flame speeds with the expected accuracy to within ± 5 % on the lean and rich side.
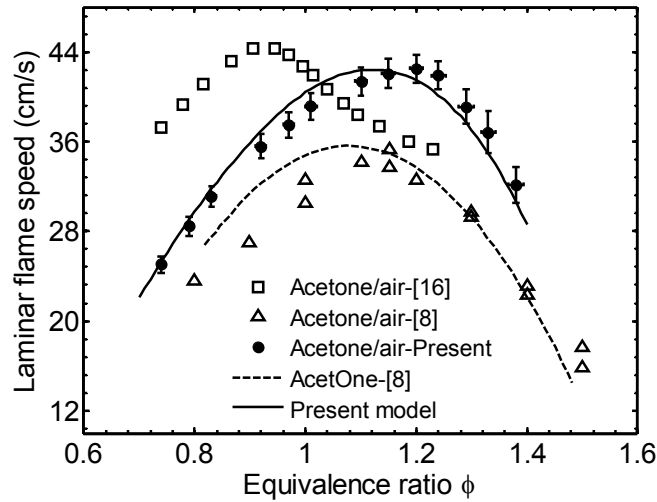
Figure 2.9: Laminar flame speed of acetone/air at 298 K and 1 atm, (●) present, (□) Gibbs and Calcote [16] , (Δ) Pichon *et al.* [8], (—) present model, (----) AcetOne [8].

The result is compared against the existing two sets of acetone flame speed data. Gibbs and Calcote [16] reported a maximum value of 44.4 cm/s at $\phi = 0.93$. Their measurement was carried out using the Bunsen burner angle method without accounting for the effect of stretch. The flame speed was derived based on the averaging method by assuming a constant speed across the total flame area. The burner method is known to be useful for rough estimations and has a large uncertainty due to influence of stretch. The second set of acetone flame speed data was performed using the spherical bomb method by Pichon *et al.* Their initial result [55] reported an initial measurements of maximum flame speed of 35.6 cm/s at $\phi = 1.25$ but did not agree well with the simulation. The discrepancy was attributed to the absorption and condensation problem in the bomb method. Subsequently, their improved measurements showed a more agreeable data with the maximum flame speed of 35.4 cm/s at $\phi = 1.15$ [8]. Their whole flame speed curve is located below the methane flame speed

curve, indicating slower laminar flame speed propagation than the methane/air mixture across the whole range of equivalence ratio.
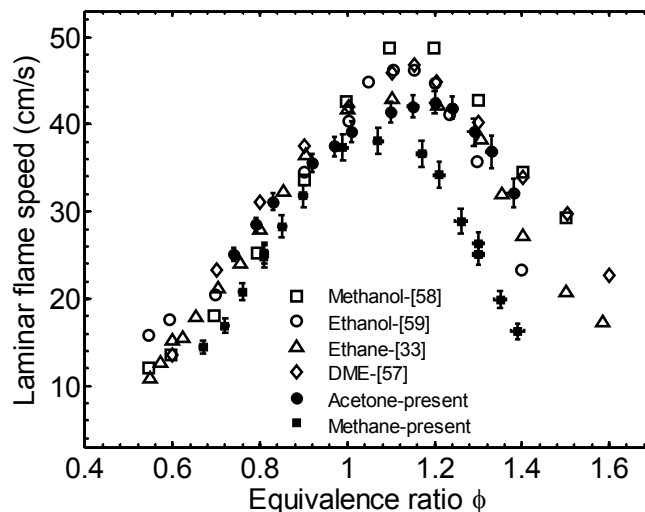
Figure 2.10: Comparison of laminar flame speed of acetone/air with the mixtures of air/ methane, ethane, DME, methanol and ethanol at 298 K and 1 atm.

The simulation performed by Pichon *et al.* shows the acetone flame speed curve is located below the methane/air flame speed curve. They used a mechanism based on the dimethyl ether mechanism comprising 419 reactions and 81 species coupled with the acetone submechanism adopted from the methylketone oxidation mechanism developed by Decottignies *et al.* [56]. In their study, Pichon *et al.* updated some of the most important combustion reaction rates, including $H+O_2 \rightarrow O+OH$ and $CO+OH \rightarrow CO_2+H$ and revalidated the mechanism with ignition delay time and flame speed data for hydrogen and methane oxidation. To improve the agreement of simulation with experimental data, they updated the rate constants of reactions $CH_3+H+M \rightarrow CH_4+M$, $CH_2+O_2 \rightarrow CO_2+2H$, $CH_2CO+OH \rightarrow CH_2OH+CO$, $HCCO+OH \rightarrow HCO+HCO$ and $HCCO+O_2 \rightarrow CO+CO+OH$. For the acetone mechanism, three acetone initiation reaction rate constants, namely $CH_3COCH_3+M \rightarrow CH_3CO+CH_3+M$, $CH_3COCH_3+OH \rightarrow CH_3COCH_2+H_2O$ and $CH_3COCH_3+H \rightarrow CH_3COCH_2+H_2$ were updated. The modified GRI-Mech 3.0 mechanism in the present work used three updated reactions rates in the acetone submechanism based on the values suggested by Pichon *et al.* as described in section 3.0 while all other reactions remain unchanged. The effect of the

three updated rates shows less than 3 % and 5 % increase of flame speed on the lean and rich side respectively when compared to the flame speed simulation using the original unmodified rates by Sato and Hidaka [14]. The changes are not significant and hence the updated rate constants are used.

Table 2.2: Comparison of fuel properties

Fuel (Molecular Formula)	LHV* (MJ/kg)	HOC+ (MJ/kg mixture)	T_{ad}++ (K)	S_{Lmax} (cm/s)
Methane (CH_4)	50.0	3.27	2084	37.3
Ethane (C_2H_6)	47.5	3.31	2190	42.9
Acetone (CH_3COCH_3)	29.6	3.33	2208	42.5
Methanol (CH_3OH)	20.1	3.16	2159	48.7
Ethanol (C_2H_5OH)	28.9	3.41	2169	42.2
DME (CH_3OCH_3)	28.9	3.41	2244	46.8

* Lower heating value

+ Heat of combustion at ϕ=1.2

++ Adiabatic flame temperature at ϕ=1.2

Figure 2.10 compares the experimentally determined acetone/air laminar flame speed data with methane/air (present data), ethane/air [33] mixtures, and other singly oxygenated species-DME/air [57], methanol/air [58] and ethanol/air [59]. In general, acetone flames propagate faster than methane but slower than DME, methanol and ethanol. The acetone flame speed curve exhibits a shift towards the fuel-rich region similar to the behaviour of ethane, methanol, ethanol and DME where the maximum flame speed peaks at $\phi \sim$ 1.15-1.2. Comparison of the fuel combustion properties in Table 2.2 shows that oxygenated hydrocarbons have higher T_{ad} at ϕ = 1.2 and peak laminar flame speed than methane, concurring with the trend shown in the measurements. Figure 2.11 compares the normalized volumetric heat release rate of acetone/air flame with methane/air and 10% acetone/methane/air flame at ϕ = 1.0. The higher heat release rate of acetone indicates that although the final temperature is similar in all cases, the peak heat release rate is higher for acetone, possibly due to the immediate pathway to the formation of –C=O containing species and final oxidation. It is noted again that the equivalence ratio of all mixtures is calculated based on the total mixture of fuel (methane and acetone seeding) and air.
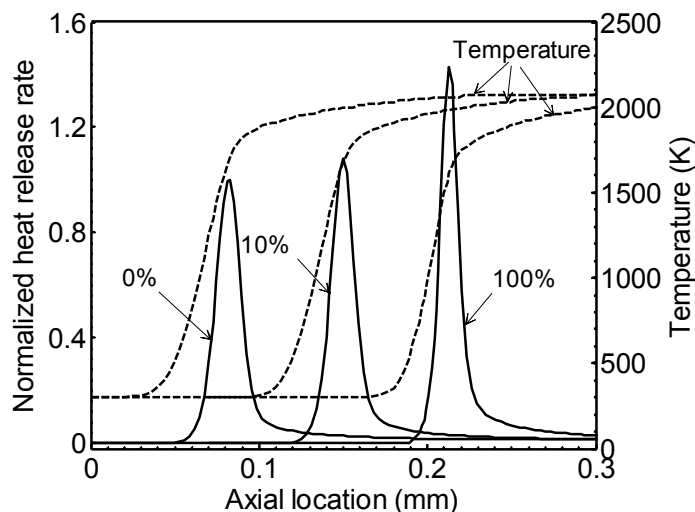
Figure 2.11: Normalized heat release rate (—) and temperature profile (---) of 0 %, 10 % acetone/methane/air and 100 % acetone/air mixture at $\phi = 1.0$.

The disagreement of the acetone/air flame speeds results with Pichon *et al.* could be due to the differences in experimental approach. The bomb method is a widely used method that permits the measurement at high pressure conditions, giving valuable data for chemistry mechanism validation. However, its shortcomings include the requirement of extreme care in mixture preparation, liquid fuel absorption and condensation problems and correction for flame stretch at small flame diameters. Pichon *et al.* utilised the Schlieren set-up for flame visualisation and reported no wrinkling on the flame. On the other hand, the jet-wall stagnation flame configuration, which is a variation of the more commonly adopted opposed-jet counterflow method, presents the potential problem of non-adiabaticity due to upstream and downstream heat loss. Zhao *et al.* utilised this method to measure the laminar flame speed of DME [46], n-decane [60] and gasoline surrogate fuel [39]. Unlike the spherical bomb method, the absorption problem is non-existent as long as the liquid fuel vaporisation is constant. The condensation problem can easily be avoided by ensuring the partial pressure of acetone is below the saturation pressure along the line. To ensure the fidelity of the data, the current technique is validated with methane/air mixture and good agreement and reproducibility is achieved.

The biggest difference between the jet stagnation configuration and the counterflow flame technique is the adiabaticity downstream of the flame. The counterflow method ensures there is no heat loss downstream of the flame, but for the jet stagnation method, flame quenching on the plate surface limits the stabilization of the flame at a higher strain rate. Egolfopoulos *et al.* [30] examined the effect of downstream heat loss on laminar flame speed and reported that the plate temperature has negligible effect on the laminar flame speed as long as the flame is several flame thicknesses away. However, the strain field and extinction strain rate achievable are significantly reduced.

2.9 Analysis of chemical mechanism

2.9.1 Acetone/methane/air

Given the accurate reproduction of the laminar flame speeds of mixtures of acetone and methane, it is useful to consider the detailed calculated species profiles within the flame. Figure 2.12 shows the normalized mole fractions of acetone relative to methane and the corresponding temperature profiles at fixed acetone seeding of 10 % by mole under lean, stoichiometric and rich conditions. In all cases, acetone decomposition has a longer induction time, but reacts faster than methane once the reaction starts. The 50 % mole fraction decomposition rate for the normalized concentrations coincides for both reactants, indicating the suitability of acetone to act as a tracer. The relatively small discrepancy between acetone and methane disappearance under all conditions indicates that acetone is a good reactive marker for methane in general.
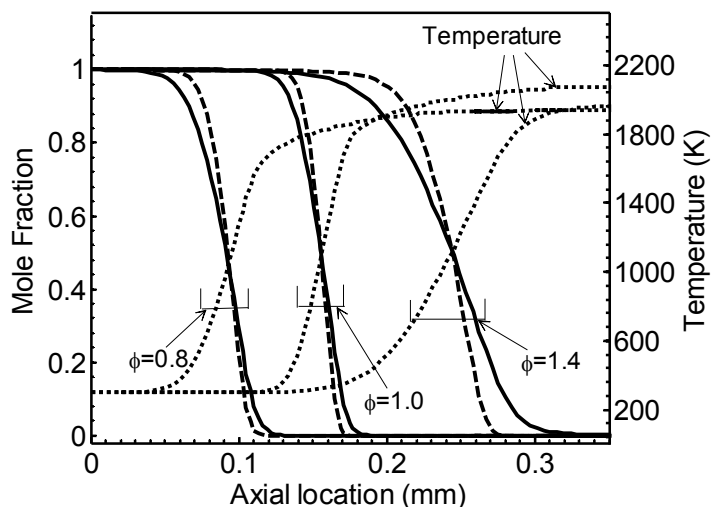
Figure 2.12: Normalized (——) CH_4 , (----)acetone and (...) temperature profiles for $\phi = 0.8$, 1.0 and 1.4.

The influence of acetone seeding at low concentration on radical production can be evaluated by comparing numerical simulations of mixtures with and without acetone. Figure 2.13a shows the comparison of species and temperature profiles of methane/air and 10% acetone/methane/air mixture at the lean mixture of $\phi = 0.8$. The seeding of acetone slightly increases the radical concentrations of OH, H and CO, indicating higher reactivity from the addition of acetone. This is supported by the study conducted by Decognitties et al. [56] where the seeding of 1-3 % methylethylketone also shows an increase of C_2 and C_3 intermediate hydrocarbon species, and subsequently enhances the production of CH_3 radical. Similarly, the acetone seeding also contributes to the radical CH_3 pool, which is essential for CO and CH_2O formation. Sensitivity analysis of acetone/methane/air in Section 6.0 shows that the dominant reactions are the same as those of a pure methane/air flame, albeit at a slightly different magnitude. For the rich acetone/methane/air mixture, the production of radicals (H, OH CO and CO_2) is significantly influenced by acetone seeding as shown in Fig. 2.13b. The flame is shifted towards the fresh gases while the flame thickness increases due to the presence of acetone in the mixture. The reactions involved in the rich mixture are significantly different from those in the lean mixture.
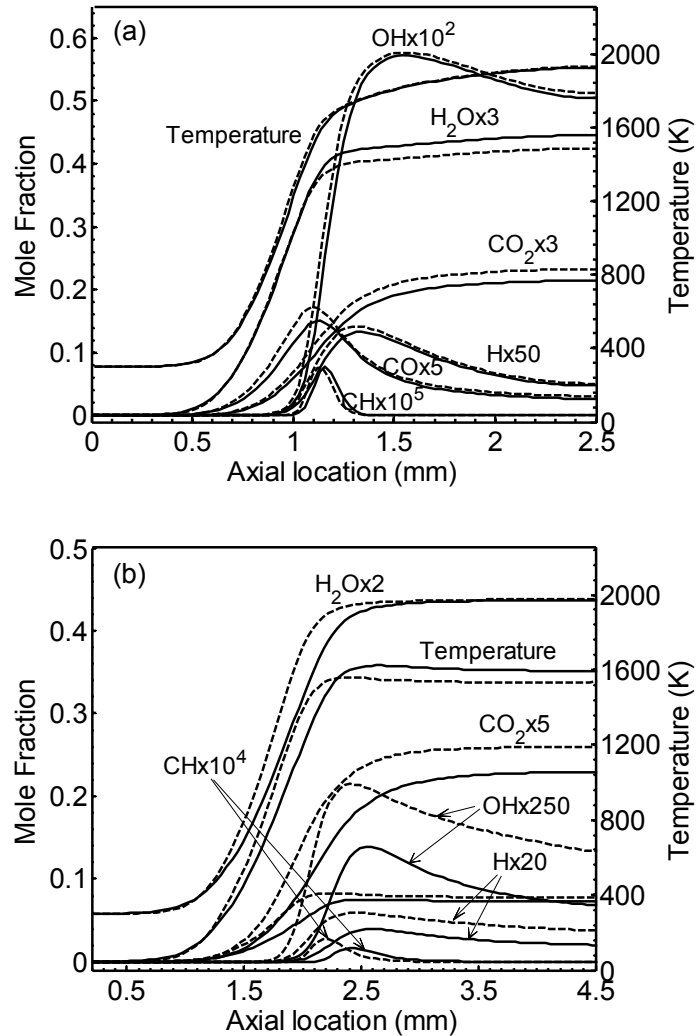
Figure 2.13: Radical species profiles of 0 % (—) and 10 % (---) of acetone addition into methane/air mixture at (a) $\phi = 0.8$ (b) $\phi = 1.4$.

2.9.2 Acetone/air

The modified chemical mechanism described above was used to calculate the acetone unstretched flame speed to explore the potential as an alternative mechanism. Figure 2.14 summarizes the main reaction pathways of the acetone oxidation at stoichiometric condition. The thermal decomposition of acetone leads to the direct formation of radical acetonyl (CH_3COCH_2), acetyl (CH_3CO), methyl (CH_3) and a

relatively small fraction of CH_4. More than 60 % of acetone decomposes into CH_3COCH_2 due to the H radical abstraction reactions $CH_3COCH_3+H \rightarrow CH_3COCH_2+H_2$ and $CH_3COCH_3+OH \rightarrow CH_3COCH_2+H_2O$. Acetonyl radical then decomposes to form ketene (67 %) and methyl (33 %) radical formation via the reaction $CH_3COCH_2 \rightarrow CH_2CO+CH_3$. Subsequently, the ethynyloxy radical HCCO is produced from the H abstraction of ketene reactions, namely $H+CH_2CO \rightarrow HCCO+H_2$ and $OH+CH_2CO \rightarrow HCCO+H_2O$. The ethynyloxy radical then contributes ~ 26 % to the formation of CO. This is a key pathway for acetone oxidation, which can be identified as $CH_3COCH_3 \rightarrow CH_3COCH_2 \rightarrow CH_2CO \rightarrow HCCO \rightarrow CO \rightarrow CO_2$. The decomposition of CH_2CO also produces significant CH_3 radical and CO (~ 17 % each) apart from HCCO (~ 63 %) which leads to the alternative oxidation paths. It is interesting to note that reaction $CH_3COCH_2 \rightarrow CH_2CO+CH_3$ contributes ~ 30 % to the formation of CH_3 radicals, thus establishing another important link between the acetone oxidation and C1 oxidation pathway. For the acetone pyrolysis pathway, the production of methyl and acetyl are formed via the reaction $CH_3COCH_3 \rightarrow CH_3CO+CH_3$. The acetyl radicals can further be decomposed to form methyl and carbon monoxide through the reaction $CH_3CO+M \rightarrow CH_3+CO+M$. Hence, the decomposition pathway of acetone is identified as $CH_3COCH_3 \rightarrow CH_3CO \rightarrow CH_3 \rightarrow CO$.
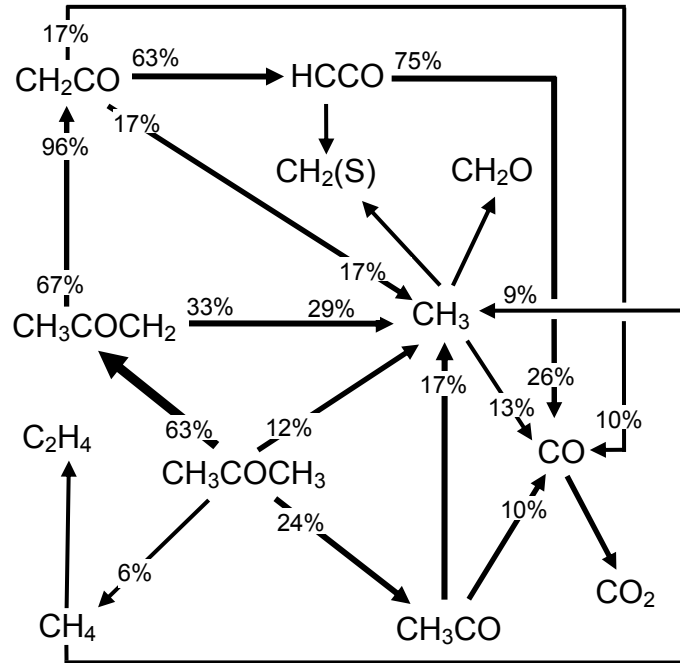
Figure 2.14: Schematic representation of acetone oxidation in the stoichiometric acetone/air flame. The percentages at the base of arrows represent the global consumption process; while the percentages at the point of arrows correspond to the contribution to the global formation process.

2.10 Sensitivity analysis
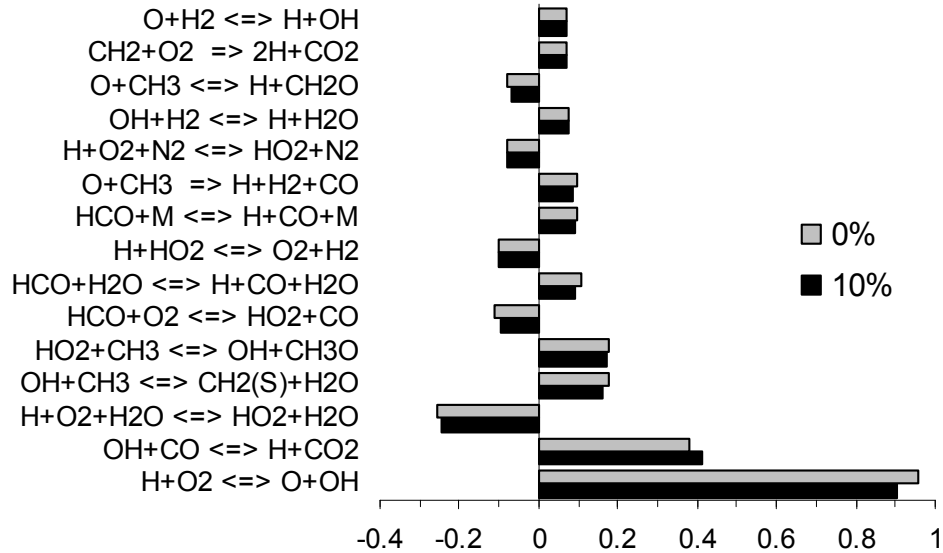
Figure 2.15: Sensitivity study of 0 % and 10 % of acetone/methane/air flame speed at 298 K and 1 atm for $\phi = 0.8$.

To understand the influence of individual reaction rates on flame propagation, sensitivity analysis was performed using the modified GRI-Mech 3.0. Figure 2.15 depicts the comparison of sensitivity coefficients for the laminar flame speed of 10 % acetone/methane/air with pure methane/air mixture at $\phi = 0.8$. The relatively small amount of acetone seeding does not affect the dominant reactions which determine flame speed. The reactions that the flame speed is most sensitive are the same as those of a pure methane/air mixture, which are dominated by the main chain branching reaction, $H+O_2 \rightarrow O+OH$, CO oxidation, $OH+CO \rightarrow H+CO_2$, methyl oxidation, $OH+CH_3 \rightarrow CH_2(S)+H_2O$ and HO_2 radical formation, $H+O_2+H_2O \rightarrow HO_2+H_2O$. The seeding of acetone into methane/air at lean conditions causes a slight decrease in the sensitivity of the $H+O_2 \rightarrow O+OH$ reaction but the CO oxidation reaction $OH+CO \rightarrow H+CO_2$ increases slightly compared to the pure methane/air flame. The increase in seeding concentration of acetone to 10 % and 20 % by mole into the methane/air mixture only increases the flame speed by 3 % and 5 % respectively. None of the

acetone pyrolysis and H abstraction reactions plays a major role in the flame speed in any of the stoichiometries.
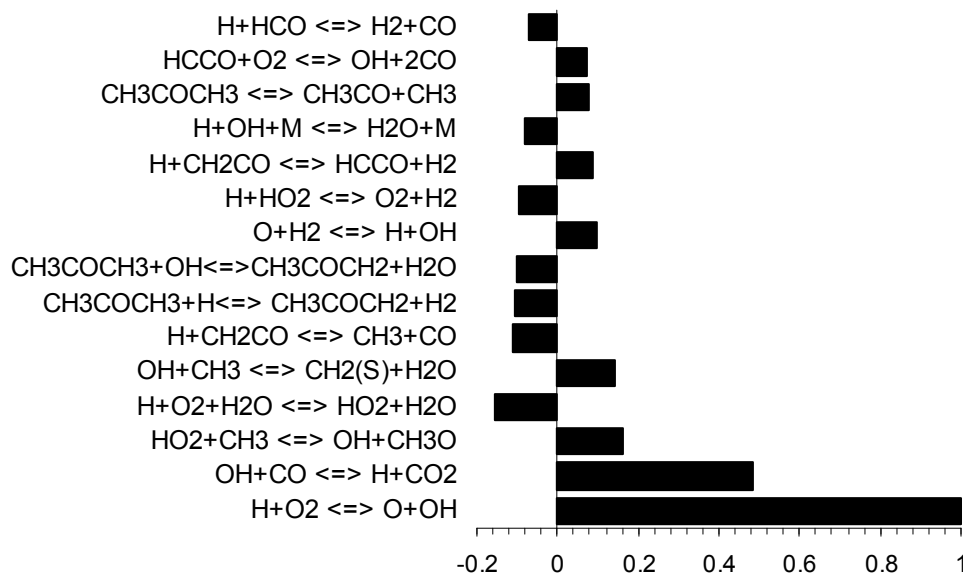
Figure 2.16: Sensitivity study of acetone/air flame speed at 298K and 1 atm for $\phi = 1.0$.

The sensitivity study of acetone/air flame at stoichiometric using the same modified GRI-Mech 3.0 is shown in Fig. 2.16. The most dominant reactions relative to flame speed are shown to be the main branching reaction, $H+O_2 \rightarrow O+OH$, CO oxidation, $OH+CO \rightarrow H+CO_2$, methyl oxidation, $HO_2+CH_3 \rightarrow OH+CH_3O$ and HO_2 radical formation, $H+O_2+H_2O \rightarrow HO_2+H_2O$. There are two acetone H abstraction reactions that are important to the laminar flame speed, namely $CH_3COCH_3+H \rightarrow$ CH3COCH2+H_2 and $CH_3COCH_3+OH \rightarrow CH_3COCH_2+H_2O$. These reactions are mainly responsible for the production of acetonyl radicals (CH_3COCH_2), a process driven by the H atom removal from acetone in the induction zone due to lower thermal stability of large fuel molecules. Comparison to the sensitivity analysis conducted by Pichon *et al.* shows disagreement even for the main reactions. Their most important reactions are $H+O_2 \rightarrow O+OH$, followed by the formyl decomposition, $HCO+M \rightarrow H+CO+M$, and curiously, H_2O decomposition, $H_2O+M \rightarrow H+OH+M$ and CH_4 formation, $CH_3+ H+M$

$\rightarrow$ CH$_4$+M. Importantly, none of their acetone reactions appear to matter for the laminar flame speed. Hence, it is not surprising that the laminar flame speed simulations are rather different due to the differences in elementary reactions.

2.11 Burner stabilized flame species profiles

The current model is further investigated using the acetone species profile measurements obtained by Li *et al.* [17]. Their measurements were carried out on a flat laminar premixed acetone flame stabilized by a 6.0 cm diameter McKenna burner. The temperature profiles were measured using a Pt/Pt-13% Rh thermocouple. To simulate the species profile as a function of height above the burner surface, the burner stabilized option in COSILAB is used and the same conditions and temperature profiles as reported by Li *et al.* were used as input. Simulation results using the given experiment temperature profile show a much narrower reaction zone between 0-2 mm. A similar problem was encountered by Pichon *et al.* when using the reported temperature profile. Significantly, the final species concentrations are far from the expected equilibrium values for the given stoichiometry and temperature. Thus even if the mechanisms should be inaccurate, the difference in final concentrations must lie in uncertainties in the stated stoichiometry or in the final measured temperature. The product species profiles show little sensitivity when a temperature profile 100 K lower than the given profile was used. Hence, a more drastic change to the temperature profile is needed to bring simulation into agreement to the actual measurement. Pichon *et al.* suggested an artificial temperature profile based on the equation $T(z) = T_i + [(T_f - T_i)\exp(-\alpha/z)]$, where T_i is the initial flame temperature, T_f is the final gas temperature, z is the height from burner outlet and α is a constant. The proposed values by Pichon *et al.* were $T_i = 400K$, $T_f = 1900$ K and $\alpha = 2.3$ and these parameters are used in this simulation.
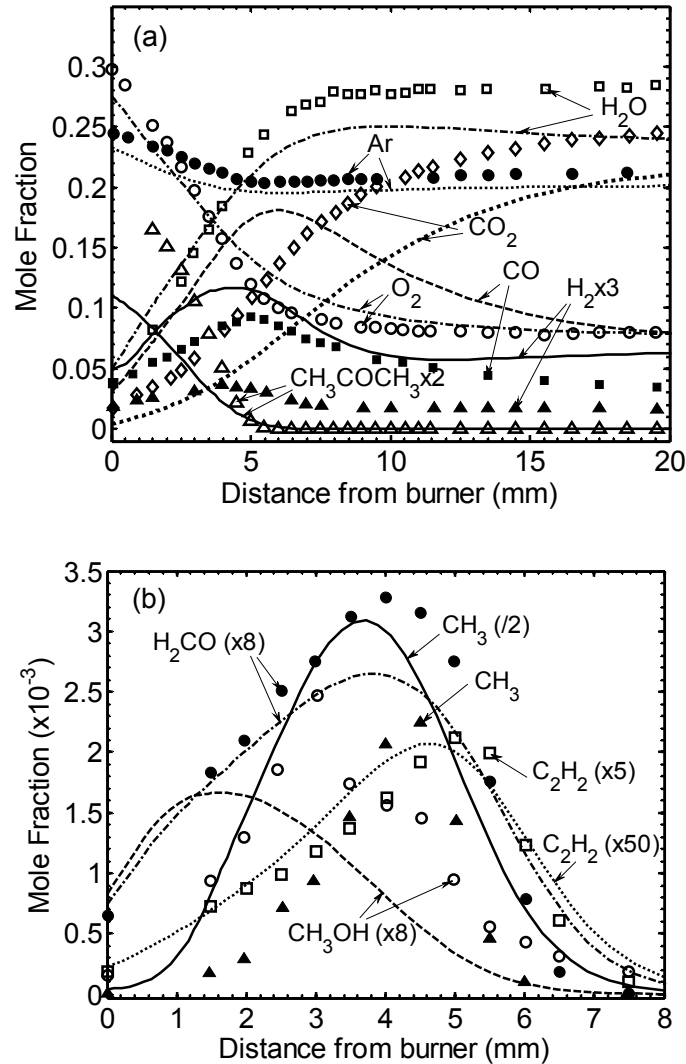
Figure 2.17: Comparison of (a) major and (b) minor species mole fractions as a function of height above the burner for lean ($\phi = 0.76$) acetone flame. Symbols are derived from [17] and lines are the results of present numerical simulation.

Figure 2.17a shows the mole fraction profiles of reactants and major products comparison between the simulated profiles using the current modified GRI-Mech 3.0 with the experimental profile measurements on lean ($\phi = 0.76$) premixed acetone flame. Li *et al.* identified the region between 0-5 mm where the fuel burnt out as the reaction zone and the region beyond 5 mm as post flame zone. Overall, the simulated result does not show a particularly good agreement with the measured data where the final major

products do not converge to the same concentration. The simulation under predicts the final concentrations of H_2O and CO_2 by 21 % and 17 %, but overpredicts the production of H_2 and CO by 3 and 2.6 times more respectively when compared to the measured data. Only the O_2 profile appears to be close to actual measurement. Figure 2.17b compares the mole fraction profiles of C1 species and C2 hydrocarbon with simulation results. The artificial temperature profile brings the species profiles closer to the actual measurement. The radicals of CH_2O and CH_3OH are of the same order of magnitude with the measurement. The radical CH_3 is overpredicted by a factor of two while the radical C_2H_2 is underpredicted by a factor of 10.

The comparison of the major products of rich acetone flame species profiles between simulation and measurements is shown in Fig. 2.18a. Following the lean case, the same artificial temperature profile is used as the initial profile. Due to the rich mixture of acetone/air ($\phi = 1.83$), the reaction zone from the measurement is shown to be between 0-11 mm before the oxygen is completely consumed. The simulation shows the complete consumption of acetone and oxygen occurs at 7 and 15 mm respectively. The acetone and oxygen consumption profiles are not predicted well in the preheat zone. On the product formation, the CO and H_2 are over predicted by 7 % and 18 % while the H_2O and CO_2 are under predicted by 14 % and 50 % respectively. Similar to the lean case, the mole fraction profiles of C1 species and C2 hydrocarbons are also compared in Fig. 2.18b. The CH_2O, CH_3 and C_2H_4 radicals are overpredicted by a factor of 20, 5 and 2 respectively while C_2H_2 radical is of the same order of magnitude as the measurement. From the burner flame stabilised species profile comparison, it is shown that the current modified GRI-Mech 3.0 could at least describe the formation of major products globally even though there are only a few reactions added to the established GRI-Mech 3.0. However, the minor species comparison indicates that there is still a large discrepancy between the data and the model. Although it is assumed that the reactions of smaller molecules broken down from the larger molecule would follow the described chemistry in GRI-Mech 3.0, an improved chemistry description for the transition of the larger radicals broken down from acetone to smaller ones is needed to better describe the minor species.
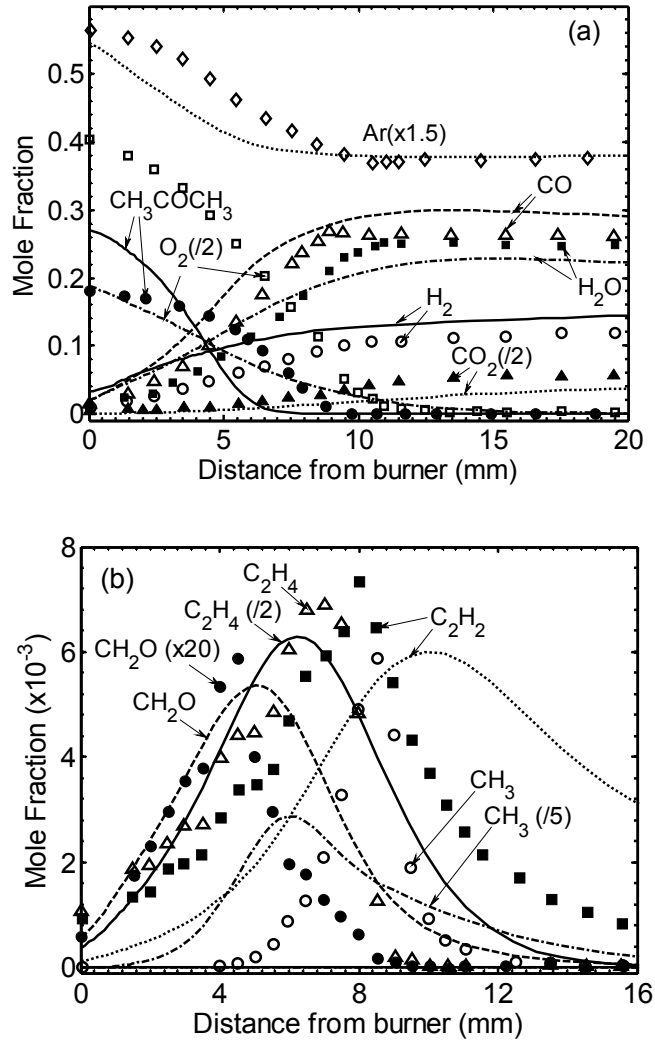
Figure 2.18: Comparison of (a) major and (b) minor species mole fractions for rich ($\phi = 1.83$) acetone flame. Symbols are derived from [17] and lines are the results of present numerical simulation.

2.12 Conclusion

The effects of the addition of acetone to methane/air mixture have been investigated by measuring the laminar flame speed of acetone/methane/air mixtures using the jet stagnation flame technique coupled with PIV at 298 K and 1 atm over a range of equivalence ratios. The effect of 0-20 % addition of acetone to lean methane/air mixtures is small with differences of less than 2 cm/s relative to the neat methane flame speed. The rich region shows a more significant influence of acetone on the laminar flame speed with 3-6 cm/s of flame speed increase. Simulations of flame speed for the mixtures were performed using the GRI-Mech 3.0 chemical mechanism coupled with an acetone submechanism, and the computed results show good agreement with the experimental data in general. The small effect of acetone on the methane flames shows that acetone is an adequate marker for the methane fuel in a reacting flow, as it does not significantly affect the methane reaction, and the 50 % mole fraction decomposition rate coincides with that of methane.

The acetone/air flame speed was measured using the same method and found to differ with literature, but broadly in agreement with other oxygenated fuels. The measurements show that the propagation of acetone/air flame is faster than the methane/air flame across the whole range of equivalence ratio. By using the same mechanism, the computed result shows the same trend and is in good agreement with the measurements. Hence, the methane-based mechanism coupled with acetone sub mechanism can potentially be used to describe acetone flames. However, simulations offered poor comparisons with results from a low pressure, burner-stabilized flame in a lean and rich flame, but the underlying reasons remain unexplained.

2.13 References

[1] C. K. Law, *Combustion physics*. New Jersey: Princeton University, 2006.

[2] R. A. Bryant, J. M. Donbar, and J. F. Driscoll, "Acetone laser induced fluorescence for low pressure/low temperature flow visualization," *Exp. Fluids*, vol. 28, pp. 471-476, (2000).

[3] A. Lozano, B. Yip, and R. K. Hanson, "Acetone: a tracer for concentration measurements in gaseous flows by planar laser-induced fluorescence," *Exp. Fluids*, vol. 13, pp. 369-376, (1992).

[4] M. C. Thurber, F. Grisch, B. J. Kirby, M. Votsmeier, and R. K. Hanson, "Measurements and modeling of acetone laser-induced fluorescence with implications for temperature-imaging diagnostics," *Appl. Opt.*, vol. 37, pp. 4963-4978, (1998).

[5] B. Yip, M. F. Miller, A. Lozano, and R. K. Hanson, "A combined OH/acetone planar laser-induced fluorescence imaging technique for visualizing combusting flows " *Exp. Fluids* vol. 17, pp. 330-336, (1994).

[6] V. Robin, A. Mura, M. Champion, O. Degardin, B. Renou, and M. Boukhalfa, "Experimental and numerical analysis of stratified turbulent V-shaped flames," *Combust. Flame*, vol. 153, pp. 288-315, (2008).

[7] O. Dégardin, B. Renou, and A. M. Boukhalfa, "Simultaneous measurement of temperature and fuel mole fraction using acetone planar induced fluorescence and Rayleigh scattering in stratified flames " *Exp. Fluids*, vol. 40, pp. 452-463, (2005).

[8] S. Pichon, G. Black, N. Chaumeix, M. Yahyaoui, J. M. Simmie, H. J. Curran, and R. Donohue, "The combustion chemistry of a fuel tracer: Measured flame speeds and ignition delays and a detailed chemical kinetic model for the oxidation of acetone," *Combust. Flame*, vol. 156, pp. 494-504, (2009).

[9] D. E. Hoare and T.-M. Li, "The combustion of simple ketones I-- Mechanism at low temperatures," *Combust. Flame*, vol. 12, pp. 136-144, (1968).

[10] D. E. Hoare and T.-M. Li, "The combustion of simple ketones II--Mechanism at high temperatures," *Combust. Flame*, vol. 12, pp. 145-154, (1968).

[11] J. A. Barnard and T. W. Honeyman, "The gaseous oxidation of acetone. I. The high-temperature reaction," *Proc. R. Soc. London. Ser. A*, vol. 279, pp. 236-247, (1964).

[12] J. A. Barnard and T. W. Honeyman, "The gaseous oxidation of acetone. II. The low-temperature reaction," *Proc. R. Soc. London. Ser. A*, vol. 279, pp. 248-259, (1964).

[13] T. Tsuboi, K. Ishii, and S. Tamura, "Thermal oxidation of acetone behind reflected shock wave," *17th Int. Colloq. Dynm, Explo. Reac. Sys. (Heidelberg, Germany)*, (1999).

[14] K. Sato and Y. Hidaka, "Shock-tube and modeling study of acetone pyrolysis and oxidation," *Combust. Flame*, vol. 122, pp. 291-311, (2000).

[15] M. Chaos, Z. Zhao, A. Kazakov, and F. L. Dryer, "An experimental and kinetic study of acetone oxidation in a flow reactor," in *31st Int. Symp. on Combust., Heidelberg, work-in-progress poster*, 2006.

[16] G. J. Gibbs and H. F. Calcote, "Effect of molecular structure on burning velocity," *J. Chem. Eng. Data*, vol. 4, pp. 226-237, (1959).

[17] Y. Li, L. Wei, Z. Tian, B. Yang, J. Wang, T. Zhang, and F. Qi, "A comprehensive experimental study of low-pressure premixed C3-oxygenated hydrocarbon flames with tunable synchrotron photoionization," *Combust. Flame*, vol. 152, pp. 336-359, (2008).

[18] J. Natarajan, T. Lieuwen, and J. Seitzman, "Laminar flame speeds of H2/CO mixtures: Effect of CO2 dilution, preheat temperature, and pressure," *Combust. Flame*, vol. 151, pp. 104-119, (2007).

[19] I. Glassman, *Combustion*, 3rd ed. ed. San Diego, California, USA: Academic Press, 1996.

[20] K. K. Kuo, *Principles of combustion*, 2nd ed.: John Wiley & Sons, 2005.

[21] J. Powling, "A new burner method for the determination of low burning velocities and limits of inflammability," *Fuel*, vol. 28, pp. 25, (1954).

[22] J. P. Botha and D. B. Spalding, "The laminar flame speed of propane/air mixtures with heat extraction from the flame," *Proc. Royal Soc. London. A, Math. Phy. Sci.*, vol. 225, pp. 71-96, (1954).

[23] A. Van Maaren, D. S. Thung, and L. R. H. De Goey, "Measurement of flame temperature and adiabatic burning velocity of methane/air mixtures " *Combust. Sci. Technol.*, vol. 96, pp. 327-344, (1994).

[24] K. J. Bosschaart and L. P. H. De Goey, "The laminar burning velocity of flames propagating in mixtures of hydrocarbons and air measured with the heat flux method," *Combust. Flame*, vol. 136, pp. 261-269, (2004).

[25] S. Y. Liao, D. M. Jiang, Z. H. Huang, K. Zeng, and Q. Cheng, "Determination of the laminar burning velocities for mixtures of ethanol and air at elevated temperatures," *Appl. Thermal Eng.*, vol. 27, pp. 374-380, (2007).

[26] X. Gu, Z. Huang, Q. Li, and C. Tang, "Measurements of laminar burning velocities and Markstein lengths of n-butanol-air premixed mixtures at elevated temperatures and pressures," *Energy Fuels*, vol. 23, pp. 4900-4907, (2009).

[27] M. L. D. Bradley, Kexin Liu, S. Verhelst, and R. Woolley, "Laminar burning velocities of lean hydrogen-air mixtures at pressures up to 1.0 MPa," *Combust. Flame*, vol. 149, pp. 162-172, (2006).

[28] C. M. Vagelopoulos, F. N. Egolfopoulos, and C. K. Law, "Further considerations on the determination of laminar flame speeds with the counterflow twin-flame technique," *Proc. Combust. Inst.*, vol. 25, pp. 1341-1347, (1994).

[29] J. M. Bergthorson, *Experiments and modeling of impinging jets and premixed hydrocarbon stagnation flames*. PhD: California Institute of Technology, 2005.

[30] F. N. Egolfopoulos, H. Zhang, and Z. Zhang, "Wall effects on the propagation and extinction of steady, strained, laminar premixed flames," *Combust. Flame*, vol. 109, pp. 237-252, (1997).

[31] J. M. C. Mendes-Lopes, *Influence of strain fields on flame propagation*. PhD: University of Cambridge, 1984.

[32] B. H. Chao, F. N. Egolfopoulos, and C. K. Law, "Structure and propagation of premixed flame in nozzle-generated counterflow," *Combust. Flame*, vol. 109, pp. 620-638, (1997).

[33] C. M. Vagelopoulos and F. N. Egolfopoulos, "Direct experimental determination of laminar flame speeds," *Proc. Combust. Inst.*, vol. 27, pp. 513-519, (1998).

[34] J. M. C. Mendes-Lopes and H. Daneshyar, "Influence of strain fields on flame propagation," *Combust. Flame*, vol. 60, pp. 29-48, (1985).

[35]   Y. Dong, C. M. Vagelopoulos, G. R. Spedding, and F. N. Egolfopoulos, "Measurement of laminar flame speeds through digital particle image velocimetry: Mixtures of methane and ethane with hydrogen, oxygen, nitrogen, and helium," *Proc. Combust. Inst.*, vol. 29, pp. 1419-1426, (2002).

[36]   G. P. Smith, D. M. Golden, M. Frenklach, N. W. Moriarty, Z, B. Eiteneer, M. Goldenberg, T. Bowman, R. K. Hanson, S. Song, W. C. Gardiner, V. V. Lissianski, and Z. Qin, "GRI-Mech 3.0 Available from www.me.berkeley.edu/gri_mech/."

[37]   S. G. Davis, A. V. Joshi, H. Wang, and F. Egolfopoulos, "An optimized kinetic model of H2/CO combustion," *Proc. Combust. Inst.*, vol. 30, pp. 1283-1292, (2005).

[38]   Z. Zhao, *Experimental and numerical studies of burning velocities and kinetic modeling for practical and surrogate fuels.* PhD: University of Princeton, 2005.

[39]   Z. Zhao, J. P. Conley, A. Kazakov, and F. L. Dryer, "Burning velocities of real gasoline fuel at 353 K and 500 K," *SAE Int.* , vol. 112, pp. 2624-2629, (2003).

[40]   B. Karlovitz, D. W. Denniston, and D. H. Knapschaefer, "Studies on turbulent flames," *Proc. Combust. Inst.*, vol. 4, pp. 613-620, (1952).

[41]   M. Matalon and B. J. Matkowsky, "Flames in fluids: Their interaction and stability," *Combust. Sci. Technol.*, vol. 34, pp. 295 - 316, (1983).

[42]   K. Kumar, J. Freeh, C. Sung, and Y. Huang, "Laminar flame speeds of preheated iso-Octane/O2/N2 and n-Heptane/O2/N2 mixtures " *J. Prop. Power*, vol. 23, pp. 428-436, (2007).

[43]   J. Westerweel, "Fundamentals of digital particle image velocimetry," *Meas. Sci. Technol.*, vol. 8, pp. 1379-1392, (1997).

[44]   M. P. Wernet, "A flow field investigation in the diffuser of a high-speed centrifugal compressor using digital particle imaging velocimetry " *Meas. Sci. Technol.*, vol. 11, pp. 1007-1022, (2000).

[45]   J. H. Tien and M. Matalon, "On the burning velocity of stretched flames," *Combust. Flame*, vol. 84, pp. 238-248, (1991).

[46]   Z. Zhao, A. Kazakov, and F. L. Dryer, "Measurements of dimethyl ether/air mixture burning velocities by using particle image velocimetry," *Combust. Flame*, vol. 139, pp. 52-60, (2004).

[47]   "Rotexo-Softpredict-Cosilab, GmbH and Co. KG Bad Zwischenahn (Germany) Version 2.1.0, 2008. Available from www.SoftPredict.com."

[48]   J. T. Herron, "Evaluated chemical kinetic data for the reactions of atomic oxygen O(P) with saturated organic compounds in the gas phase," *J. Phys. Chem. Ref. Data*, vol. 17, pp. 967-1026, (1988).

[49]   W. Tsang and R. F. Hampson, "Chemical kinetic data base for combustion chemistry. Part I. Methane and related compounds," *J. Phys. Chem. Ref. Data*, vol. 15, pp. 1087-1279, (1986).

[50]   Ernst. J., K. Spindler, and H. G. Wagner, "Untersuchungen zum thermischen Zerfall von Acetaldehyd und Aceton," *Ber. Bunsenges Phys. Chem.*, vol. 80, pp. 645, (1976).

[51]   P. F. Ambidge, J. N. Bradley, and D. A. Whytock, "Kinetic study of the reactions of hydrogen and oxygen atoms with acetone," *J. Chem. Soc., Faraday Trans. 1*, vol. 72, pp. 1870-1876, (1976).

[52] J. F. Bott and N. Cohen, "A shock tube study of the reactions of the hydroxyl radical with several combustion species," *Int. J. Chem. Kinetics*, vol. 23, pp. 1075-1094, (1991).

[53] V. Vasudevan, D. F. Davidson, and R. K. Hanson, "High-temperature measurements of the reactions of OH with toluene and acetone," *J. Phys. Chem. A*, vol. 109, pp. 3352-3359, (2005).

[54] T. Yamada, P. H. Taylor, A. Goumri, and P. Marshall, "The reaction of OH with acetone and acetone-d[sub 6] from 298 to 832 K: Rate coefficients and mechanism," *J. Chem. Phys.*, vol. 119, pp. 10600-10606, (2003).

[55] G. Black, S. Pichon, H. Curran, J. Simmie, and R. Donohue, "An experimental and modelling study of the combustion of acetone," *Proc. 3rd European Combust. Meeting (Crete, Greece)*, (2007).

[56] V. Decottignies, L. Gasnot, and J. F. Pauwels, "A comprehensive chemical mechanism for the oxidation of methylethylketone in flame conditions," *Combust. Flame*, vol. 130, pp. 225-240, (2002).

[57] Y. L. Wang, A. T. Holley, C. Ji, F. N. Egolfopoulos, T. T. Tsotsis, and H. J. Curran, "Propagation and extinction of premixed dimethyl-ether/air flames," *Proc. Combust. Inst.*, vol. 32, pp. 1035-1042, (2009).

[58] F. N. Egolfopoulos, D. X. Du, and C. K. Law, "A comprehensive study of methanol kinetics in freely-propagating and burner-stabilized flames, flow and static reactors and shock tubes.," *Combust. Sci. Technol.*, vol. 83, pp. 33-75, (1992).

[59] F. N. Egolfopoulos, D. X. Du, and C. K. Law, "A study on ethanol oxidation kinetics in laminar premixed flames, flow reactors, and shock tube," *Proc. Combust. Inst.* , vol. 24, pp. 833-841, (1992).

[60] Z. Zhao, J. Li, A. Kazakov, F. L. Dryer, and S. P. Zeppieri, "Burning velocities and a high-temperature skeletal kinetic model for n-Decane," *Combust. Sci. Technol.*, vol. 177, pp. 89-106, (2005).

Chapter 3

Laminar flame speeds of practical liquid fuel/air mixtures

3.1 Introduction

Practical liquid hydrocarbons are the main energy sources for ground and air transportation systems. The composition of practical fuels is complex, and often consists of a wide range of hydrocarbons including n-parrafin, iso-paraffin and aromatics that makes the elucidation of each component's chemistry in the fuels very difficult. A useful approach in developing chemical-kinetic mechanism for complex fuels is to use surrogate mixtures of pure hydrocarbons to replicate the physical and chemical characteristics of a practical fuel. The surrogate blend simplifies the complex practical fuels but maintains the essential characteristics of the targeted fuel. The fidelity of the surrogate model depends directly not only on the accuracy of the pure component models, but also the ability to reproduce the global flame characteristics of practical fuels. Hence, combustion properties such as laminar flame speed data of pure hydrocarbons and practical fuels can be very useful as target validation. In this chapter, the laminar flame speed work of surrogate components and practical fuels are reviewed, followed by the fuel properties and report on the liquid fuel flame speed measurements. The measured flame speeds of practical fuels can be used as direct input for turbulent combustion models, or to predict the laminar and turbulent premixed flame behaviour in general.

3.2 Laminar flame speed of heavy hydrocarbons

Single component hydrocarbons have been widely used to represent practical fuels. Large alkanes such as n-decane and n-dodecane are commonly used as surrogates for diesel and jet fuel to represent the bulk straight-chain paraffin components, whereas n-heptane and iso-octane have been adopted as primary reference fuels (PRF) to represent gasoline. Zhao *et al.* [1] utilised the jet-wall stagnation method to measure the laminar flame speed of actual gasoline and PRF blend and compared these with a numerical model at an elevated temperature of 500 ℃. For biodiesel, surrogate fuels such as n-decane, n-hexadecane and long chain methyl esters have been proposed as part of the chemical kinetic model [2, 3]. To ensure the fidelity of the constructed mechanism, the surrogate components need to be individually validated with a global oxidation response such as the laminar flame speed, extinction stretch rate or autoignition delay time.

Measurements of the laminar flame speeds of n-heptane have been performed by several groups. Davis and Law [4] and Huang *et al.*[5] measured its laminar flame speed at 298 K using the counterflow flame configuration over a range of equivalence ratios. Zhao [6] measured the n-heptane flame speed at room temperature using the jet-wall technique. Kwon *et al.* [7] reported the n-heptane flame speed data using the spherical bomb method at the mixture temperature of 298 K between equivalence ratios of 0.8 and 1.6. Although laminar flame speeds of n-heptane at room temperature have been measured, data at elevated temperatures are lacking. Kumar *et al.* [8] measured the laminar flame speeds of n-heptane with the unburned mixture temperature that spans between 298-470 K using the counterflow flame configuration.

Laminar flame speed data for larger n-alkanes such as n-decane and n-dodecane remain scarce. This is partly due to the difficulty in preparing the fuel/air mixture in the gaseous phase, especially for liquids with a high boiling point and low vapour pressure. Liquid fuel needs to be atomized, vaporised, mixed with air and subsequently maintained at a temperature above the saturation point to avoid condensation prior to combustion. Zhao *et al.* [9] reported the laminar flame speed of an n-decane flame at 500 K and atmospheric pressure over a range of equivalence ratios. Kumar and Sung [10] measured the laminar flame speed and extinction limits of n-decane/air and n-

dodecane mixtures over a range of equivalence ratios at elevated temperatures. Skjøth-Rasmussen *et al.* [11] conducted the laminar flame speed measurement of n-decane at 473 K using Bunsen flames but were not corrected for local stretch.

There is surprisingly little information on the laminar flame speeds of common liquid fuels such as jet fuel and diesel. This is due in part to the difficulty in representing practical fuels containing hundreds of components and significant compositional variability by surrogate fuels for the purpose of chemical kinetic modelling. For jet fuels, there have been some studies on the ignition delay and species profile measurements in jet-stirred reactors, but very few on laminar flame speed measurements [12, 13]. Eberius [14] measured the laminar flame speed of Jet-A1 fuel using the Bunsen burner method. Parsinejad *et al.* [15] utilised a cylindrical vessel and a spherical chamber to measure the flame speed and structure of JP-10 jet fuel while Kumar *et al.* [16] investigated the laminar flame speed and extinction stretch rates of Jet A and synthetic jet fuel (S-8) using the counterflow flame method. Although there are significant differences in the composition of these fuels, laminar flame speeds do not vary much.

Diesel oxidation chemical mechanisms have been mainly developed for autoignition applications in compression ignition engines. Large n-alkanes are typically used as surrogate components due to the bulk composition in diesel, but much modelling effort is still needed especially for cycloalkanes and aromatics to better describe the fuel characteristics [17]. At present, there is a lack of data describing the deflagrative oxidation of diesel. No measurement of diesel laminar flame speeds has ever been performed, although such data is useful for mechanism validation and can be used in gas turbine or furnace combustion modelling.

Fatty methyl ester based biodiesels have gained wide attention in the transportation sector and industry. The development of biodiesel chemical mechanisms is still at an early stage. Methyl butanoate ($C_5H_{10}O_2$), decanoate ($C_{11}H_{22}O_2$) and dodecanoate ($C_{13}H_{26}O_2$) have been studied as potential surrogates [18]. Herbinet *et al.* [3] developed a detailed chemical kinetic mechanism using methyl decanoate. The mechanism was able to describe the species reactions of rapeseed oil methyl ester experiments in a jet stirred reactor [19]. Seshadri *et al.* [20] performed experiments on

the extinction and ignition of methyl decanoate and the result agreed well with the skeletal mechanism of methyl decanoate.

Whereas biodiesels are likely to be used primarily in compression ignition engines, further envisaged applications such as gas turbines and furnaces require measurement of deflagrative properties. Yet to date there have been no measurements of real biodiesel laminar flame speeds. The effect of blending biodiesel with conventional fuels is also of interest in view of the growing trend of such practice in the industry. In this chapter, the physiochemical properties of the practical liquid fuels used throughout the dissertation is examined. The measurement of laminar flame speeds on n-heptane is performed using the jet-wall stagnation flame system developed in Chapter 2. Subsequently, the flame speeds of Jet A-1, diesel, palm methyl esters (PME) and blends are performed for both practical application and as a database for mechanism development.

3.3 Practical liquid fuels

3.3.1 Conventional fuels

Jet-A1 fuel is a complex hydrocarbon mixture consisting of approximately 50-65 % paraffins, 10-20 % aromatics and 20-30 % naphtenes [21] which is typically used in the aviation industry. Although the heating value of Jet-A1 fuel is similar to that of diesel, the power density per mass for Jet-A1 is higher due to its lower density. In this experiment, the standard Jet-A1 fuel is sourced from Conoco Limited, UK. Another practical fuel used in these experiments is the commercial grade diesel fuel commonly used in ground transport. Diesel fuel typically consists of 25-50 % of paraffins, 20-40 % of cycloparrafins and 15-40 % of aromatics [17]. Requirement for sulphur content is within 50 ppm level and below for use in developed countries. The present ultra low sulphur grade diesel fuel is obtained from a commercial Shell petrol station in the UK.

3.3.2 Biodiesels

Biodiesel is an alternative fuel that consists of a mixture mono-alkyl esters of long chain fatty acids derived from vegetable oils or animal fats through the process of transesterification. The reaction from the transesterification process is shown in Fig. 3.1, where the triglyceride from vegetable oil or animal fat reacts with alcohol such as methanol or ethanol to produce the end products of glycerol and methyl esters. The triglyceride molecule consists of long fatty acid chains (with radicals R_1, R_2 and R_3), which are esters of glycerol, an alcohol with a hydroxyl group on each of its three carbon atoms.
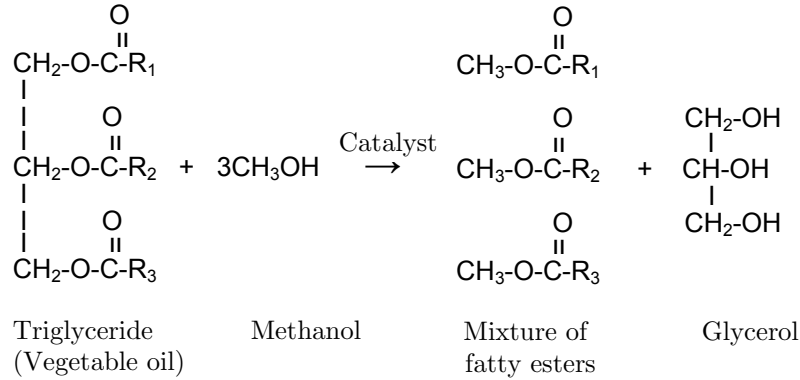
Figure 3.1: Transesterification reaction to produce methyl esters [22]

Vegetable oils are mixtures of triglycerides from various fatty acids. The main composition of triglycerides depends on the supplied feedstock. Table 3.1 shows the composition of the fatty acid profile of several feedstocks. The second column designates the number of carbon atoms: double bonds in the molecule. For example, oleic acid contains 18 carbons with one double bond in the molecule. The presence of a double bond indicates that the molecule is unsaturated. It is noted that rapeseed biodiesel consists of ~ 87 % unsaturated methyl esters while palm biodiesel contains only about 55 %. The difference in the methyl ester composition results in the variation of fuel physical properties. Palm biodiesel for instance, has a relatively higher pour point value of 15 ºC compared to rapeseed biodiesel of -10 ºC.

Table 3.1 Percentage of fatty acids composition of different vegetable oils [23]

Fatty acids	(no. of carbon: double bond)	Composition (%)			
		Rapeseed	Soybean	Jatropha	Palm
Lauric	(C12:0)	-	0.1	-	0.2
Myristic	(C14:0)	1.0	0.1	0.1	0.8
Palmitic	(C16:0)	3.5	10.2	15.6	39.5
Stearic	(C18:0)	0.9	3.7	10.5	5.1
Oleic	(C18:1)	64.1	22.8	42.1	43.1
Linoleic	(C18:2)	22.5	53.7	30.9	10.4
Linolenic	(C18:3)	8.0	8.6	0.2	0.1
Others		-	0.8	0.6	0.8

Table 3.2: Chemical structure of common fatty acids and their methyl esters [2]

Fatty acid	Structure	Methyl Ester	Structure
Palmitic ($C_{16}H_{32}O_2$)		Palmitate ($C_{17}H_{34}O_2$)	
Stearic ($C_{18}H_{36}O_2$)		Stearate ($C_{19}H_{36}O_2$)	
Oleic ($C_{18}H_{34}O_2$)		Oleate ($C_{19}H_{34}O_2$)	
Linoleic ($C_{18}H_{32}O_2$)		Linoleate ($C_{19}H_{32}O_2$)	
Linolenic ($C_{18}H_{30}O_2$)		Linolenate ($C_{19}H_{30}O_2$)	
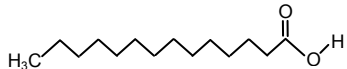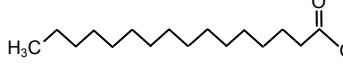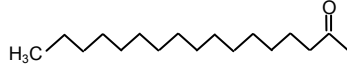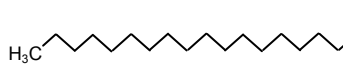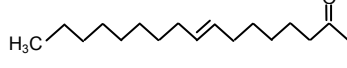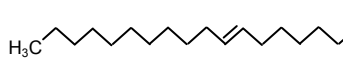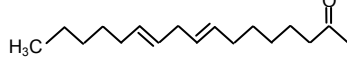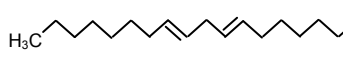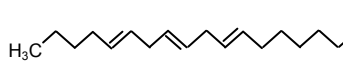
The chemical structures of the common fatty acids and their corresponding methyl esters obtained from the transesterification process are listed in Table 3.2. All methyl esters have a long alkyl chain attached to a methyl ester group. The differences are the length of the alkyl chain and the number of double bonds in the chain. Methyl oleate, methyl linoleate and methyl linolenate contain 1, 2 and 3 double bonds respectively while methyl palmitate and methyl stearate have no double. Longer alkyl chain results in a higher molecular weight.

3.3.3 Comparison of fuel properties

Gas chromatography (GC) is used to separate the hydrocarbon components in the fuels without chemical decomposition. The tests were carried out using a 30 meter DB5 type column (Supelco SLM-5ms) to qualitatively examine the fuel composition. The result for diesel, Jet-A1, palm methyl esters (PME) and rapeseed methyl esters (RME) is shown in Fig. 3.2 a-d respectively.
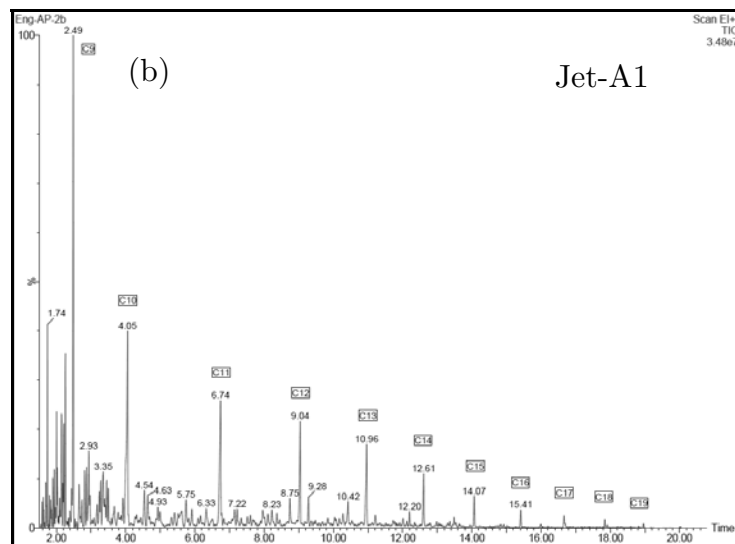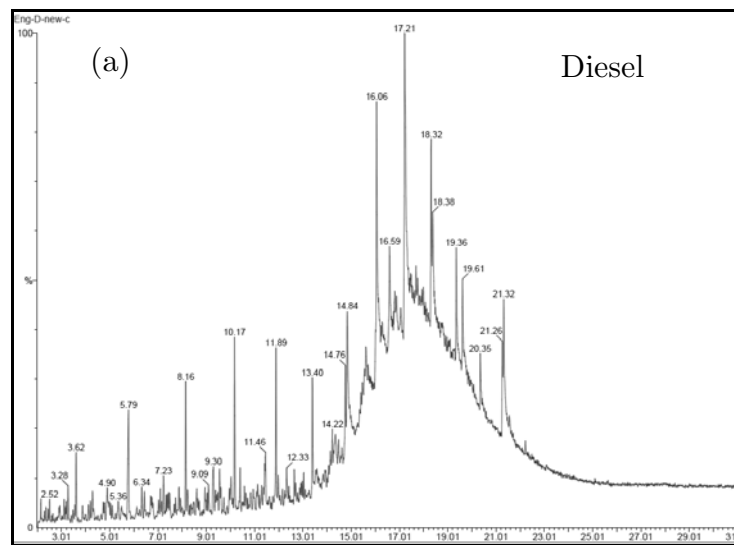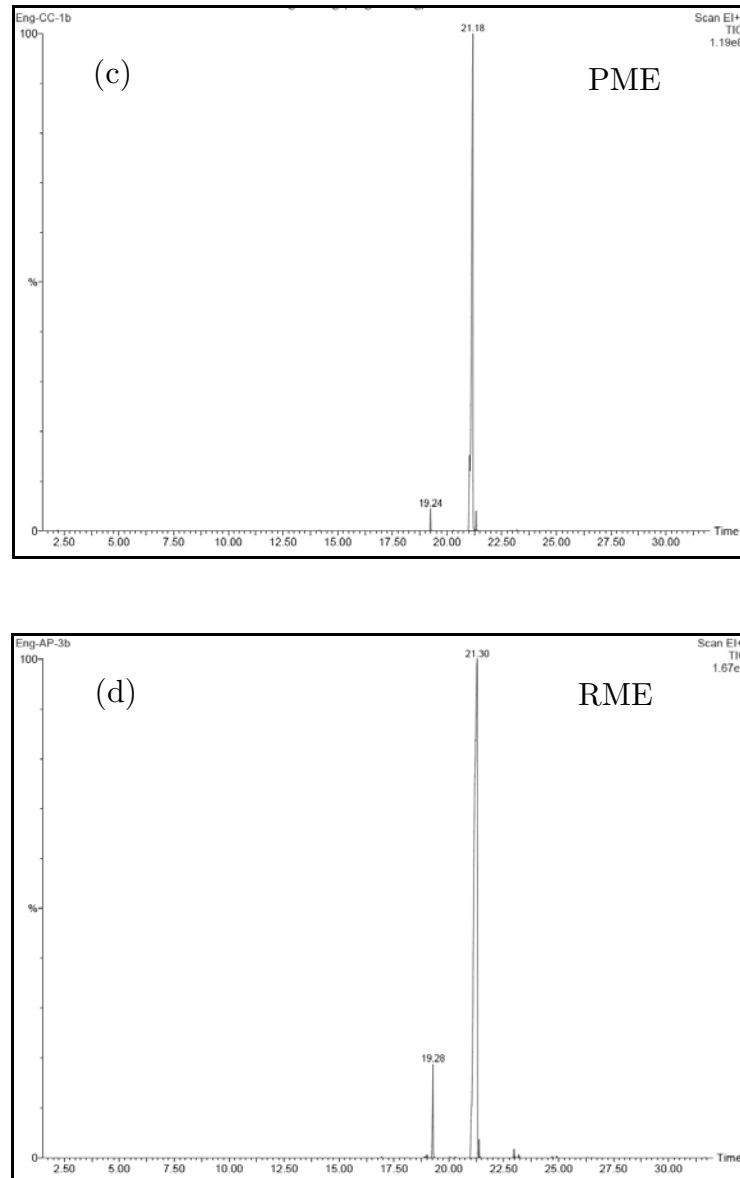
Figure 3.2: Gas chromatograph result for (a) diesel, (b) Jet-A1, (c) PME and (d) RME

The complex Jet-A1 and diesel fuels show a wide spectrum of hydrocarbons. Jet-A1 fuel shows the highest peak at around C-9 while the heavier diesel fuel indicates the peak around C-16. PME and RME exhibit rather similar trends, with one dominant peak and several satellite peaks around. This shows the relatively simple composition of biodiesels compared to diesel and Jet-A1 fuels. The chemical composition of biodiesels

is very different from conventional fuels. Biodiesels are oxygenated compounds of long chain fatty methyl esters while conventional fuels contain aromatics with no oxygen atom. Jet-A1 and diesel fuel contain higher H/C ratio than biodiesels. On the fuel physical properties, biodiesels are denser due to the higher molecular weights, with the approximated molecular weights of 296 g/mol for PME and RME. Diesel and Jet-A1 fuel are estimated as 226 g/mol and 153 g/mol based on the molecular formula of $C_{16}H_{34}$ and $C_{11}H_{21}$ respectively. Biodiesel contains higher boiling point components compared to baseline fuels, indicating the characteristic of low volatility. The viscosity of biodiesel is also slightly higher than baseline fuels.

Table 3.3: Properties of Diesel, Jet-A1, PME and RME

Properties	Jet-A1	Diesel	PME	RME
Approx. formula	$C_{11}H_{21}$	$C_{16}H_{34}$	$C_{19}H_{36}O_2$	$C_{19}H_{36}O_2$
H/C ratio*	1.98	1.9	1.89	1.89
C/O ratio*	-	-	9.83	10.06
Boiling range (^{o}C)	166-266	190-360	>215	>200
Spec. grav. 15°C	0.81	0.85	0.88	0.88
Pour point (^{o}C) [24]	-	-20	-18	-10
Flash point (^{o}C)[25]	38	60-72	174	170
Viscosity 40°C (cSt)[25]	-	2.6	4.5	4.83
Surface tension (mN/m) [26-28]	25.5[a]	28.0[a]	28.34[b]	29.24[b]
LHV (kJ/kg) [24]	43150	43090	36770	36800
Cetane number [23, 25]	-	52	62.6	51

* Laboratory analysis, value characterised at [a]25 ^{o}C and [b]40 ^{o}C

Biodiesels contain lower heating values than diesel and Jet-A1 fuels by ~ 17 % by mass. The lower power density results in higher specific fuel consumption compared to baseline fuels in combustion systems. PME and RME biodiesels have cetane numbers comparable to diesel fuel, indicating the similarity of the ignition characteristic. Comparison of the fuel properties between diesel, Jet-A1, PME and RME is presented in Table 3.3.

3.3.4 Properties of biodiesel blends

At present, biodiesel is mainly used in blends with commercial diesel for transportation sector. Most biodiesel blends produced for ground transportation contain at most 5 % biodiesel blend by volume as shown in Table 1.2. However, the trend suggests the blending limit is on the rise, as reflected by the blending standard of ASTM D7467 that specifies the properties of 6-20 % biodiesel blend with diesel by volume (Appendix B2). Blends of biodiesels with Jet-A1 fuel have yet to receive much attention, although there has been some interest in using Jet-A1/biodiesel blends in aviation gas turbine engines in recent years [29]. In view of the practical interest, the combustion properties of biodiesel blends with conventional fuels are investigated in this   dissertation.

The biodiesel blends used in the experiments are prepared by mixing the two parent fuels volumetrically. Biodiesel is miscible with diesel and Jet-A1 fuels as no sign of emulsions or layer separation was observed. The physical properties of the blends including the density, lower heating, and molecular weight values are estimated based on Kay's mixing rules $\phi = \Sigma x_i \phi_i$, where ϕ is the property of the blend and ϕ_i is the respective property of the ith component. By using the volume fraction instead of the molar fraction, the binary mixture takes the form of an arithmetic volume average $\phi_B = V_{F1}.\phi_{F1} + V_{F2}.\phi_{F2}$. The properties of the diesel, Jet-A1, PME and blends are shown in Table 3.4.

Table 3.4: Properties of Diesel, Jet-A1, PME and blends

Properties	Jet-A1	Diesel	PME	D50[+]	B50[+]
Approx. mol. weight	154	226	296	261	225
H/C ratio*	1.98	1.9	1.89	1.90	1.94
C/O ratio*	-	-	9.83	18.84	16.73
Boiling range ºC	166-266	190-360	>215	>200	>200
Spec. grav. 15ºC	0.81	0.85	0.88	0.87	0.85
Surface tension (nN/m)	25.5[a]	28.0[a]	28.34[b]	-	-
Viscosity 40ºC (cSt)	-	2.6	4.5	2.6-4	2.6-4
LHV (kJ/kg)	43150	43090	36770	39930	39960

* Lab analysis, value characterised at [a]25ºC and [b]40ºC
[+] D50 = 50% PME/diesel, B50 = 50% PME/Jet-A1

3.4 Experiments

3.4.1 Burner system setup

The jet-wall stagnation flame configuration coupled with particle imaging velocimetry (PIV) technique is used to measure the laminar flame speed. Description of the burner and flow delivery system for liquid fuel measurement has been presented in section 2.6.1, Chapter 2. In the present practical liquid fuel flame speed investigation, a converging nozzle of 14 mm exit diameter is used instead of the 22 mm in the methane/acetone/air flame speed experiment in Chapter 2. The ratio of the distance between the burner outlet and the water-cooled brass plate over the diameter of the burner nozzle (L/D) is fixed at 1.0. The burner and the lines are heated to ensure the partial pressure of the premixed fuel is maintained below the saturation pressure along the line to avoid condensation. The final temperature of the mixture is measured 2 mm from the burner outlet and the uncertainty is ± 4 K.

3.4.2 Liquid fuels tested

The biodiesel used in the current laminar flame speed measurement is the winter grade palm methyl ester (PME) supplied by Carotino Sdn. Bhd. Malaysia. The PME conforms to the European Union's EN14214 standard and the composition is approximated as 43.1% methyl oleate, 39.5% methyl palmitate, 10.4% methyl linoleate and 5% methyl stearate [23]. The kerosene Jet-A1 fuel is supplied by Conoco Limited, UK while the ultra low sulphur grade diesel fuel is obtained from a commercial Shell petrol station. Table 3.3 shows the properties of a typical Jet-A1 fuel, diesel and PME. Blending of PME with diesel and Jet-A1 fuel is performed at 10%, 20% and 50% volumetrically. No sign of emulsions or layer separation were found in the blends of PME with Jet-A1 and diesel fuel.

3.4.3 Preparation of fuel/air mixture

The liquid fuel is delivered to a stainless steel vaporiser using a high precision microannular gear pump with full scale accuracy of $\pm 1\%$ via the chemical-resistant Tygon® tubing. The liquid fuel enters the vaporiser through a modified atomizer externally mixed with preheated air for fuel atomization. About 40% of the bulk air is used for fuel vaporisation while the remaining is used for flow seeding. The atomizing air is maintained at a temperature lower than the boiling point of the fuel (~ 150 °C) to prevent prevaporisation in the fuel line that will result in flame oscillation. The vaporiser is heated by an Omega® rope heater (500 W) and is insulated using high temperature resistant material.

The internal temperature of the vaporiser is monitored by a K-type thermocouple coupled with a temperature controller. Figure 3.3 shows the schematic diagram of the vaporiser. The mixture temperature in the vaporiser is maintained at high enough temperature (~ 285 °C) for fuel vaporisation but lower than the autoignition temperature for safety reasons. The partial pressure of the heaviest hydrocarbon is checked to ensure the vapour is maintained in the gas phase at 470 K along the line including the bypass.
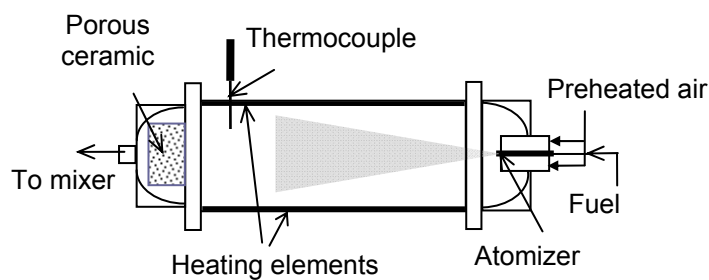
Figure 3.3: Schematic diagram of vaporiser
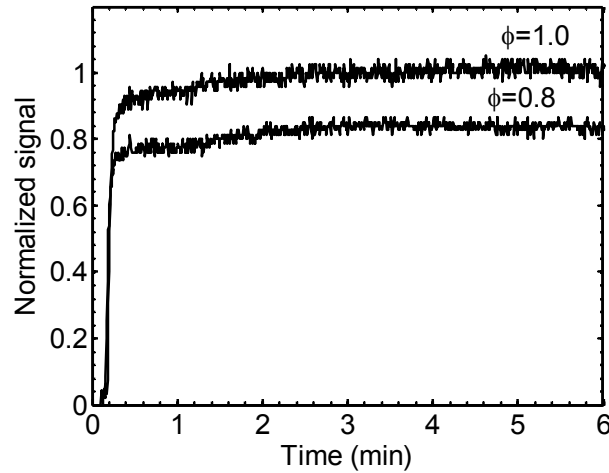
Figure 3.4: FID measurement of the consistency of Jet-A1 vaporisation

The normalized signal of a fast flame ionisation detector (FID) hydrocarbon sensor (Cambustion; HFR 500) for the vaporisation of Jet-A1 fuel obtained from the burner outlet is shown in Fig. 3.4. The vaporisation is steady after an initial phase (~ 2 min) and the flame is observed to stabilize without oscillation. The system is purged with compressed air after every measurement to ensure that no residual hydrocarbon and seeding particles are left accumulating in the line. The uncertainty of the mixture equivalence ratio is estimated to be ± 1 %, while the measured flame speeds are estimated to be within ± 4-5 %, as indicated in the error bars in the flame speed plots. The experimental setup of the burner system and PIV is shown in Fig. 3.5.

3.4.4 Determination of laminar flame speed

Particle imaging velocimetry technique is applied to the jet-wall stagnation flame method to derive the velocity flow field. The specification of the PIV and uncertainty has been described in section 2.6.4 and 2.6.5 in Chapter 2. From the derived velocity vector map, the centreline axial profiles are extracted to derive the value of reference flame speed and reference flame speed. The methodology of deriving the unstrained flame speed from the velocity field is explained in section 2.6.6, Chapter 2.
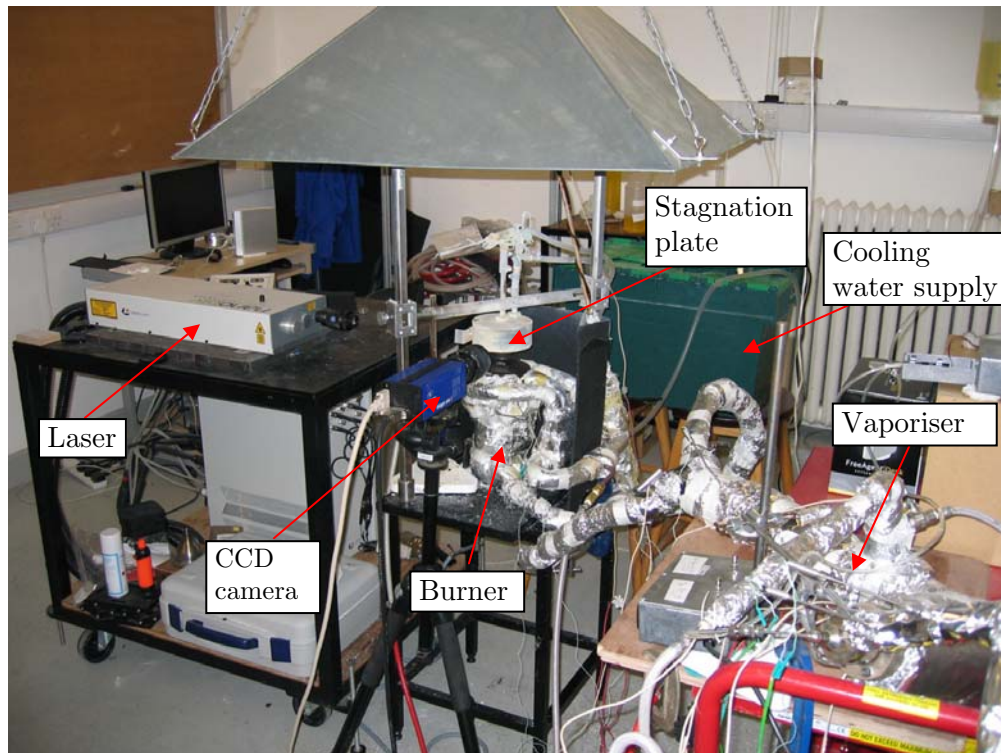
Figure 3.5: Setup for liquid fuel laminar flame speed measurements

3.5 Results and discussion

3.5.1 n-Heptane

Validation of the setup was performed by measuring the laminar flame speeds of n-heptane/air at T = 298 K, 400 K and 470 K and atmospheric pressure over a range of equivalence ratios. Figure 3.6 compares the laminar flame speed of n-heptane/air at $T = 298$ K with other literature data. Overall, the measurements at $T = 298$ K are very close to those reported by Huang *et al.* [5] and Davis and Law [35]. However, when compared to the measurements by Kumar *et al.* [8], the results show a more pronounced deviation in the region between $\phi = 0.9$ and 1.3. The peak flame speed of Kumar *et al.* is 43.9 cm/s at $\phi \sim 1.1$, about 6 cm/s higher than the current measurement. Simulation results for n-heptane/air extracted from Kumar *et al.* are shown here for comparison. The model developed by Davis and Law shows good agreement with the present data, although the stoichiometric and rich regions are slightly under predicted by 2 cm/s and 5 cm/s respectively.
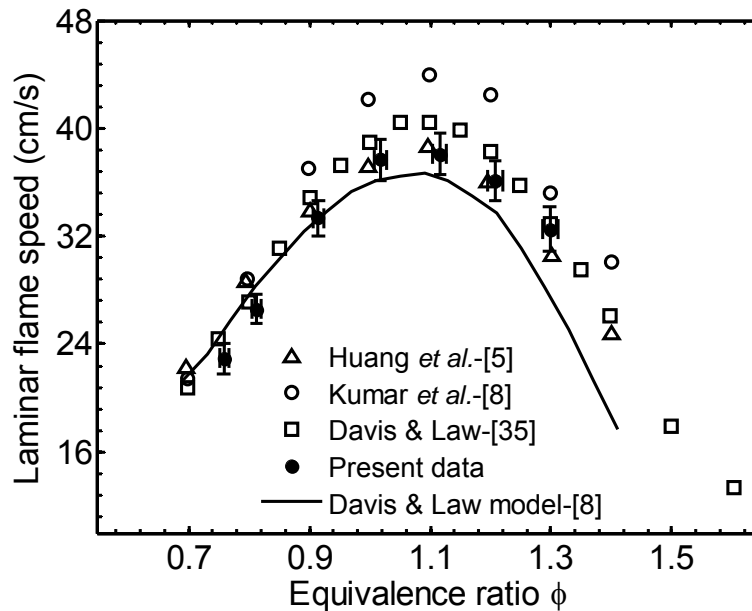
Figure 3.6: Laminar flame speed of n-heptane/air mixture as a function of equivalence ratio at T = 298 K at 1 atm.
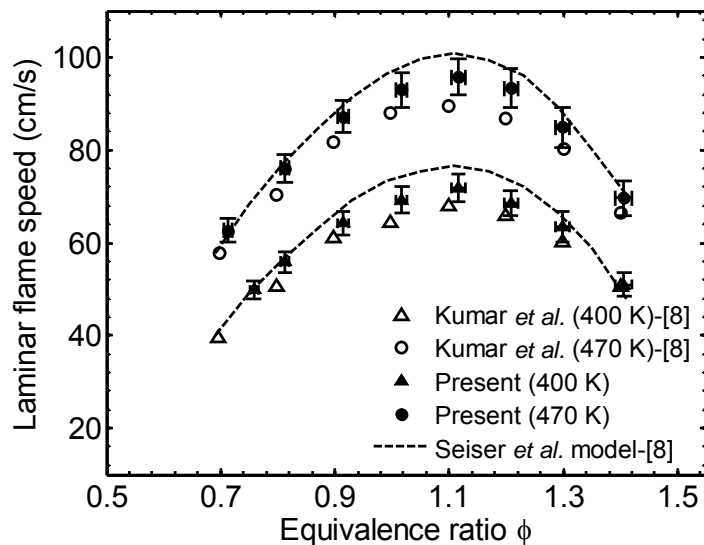
Figure 3.7: Laminar flame speed of n-heptane/air mixture as a function of equivalence ratio at T = 400 K and T = 470 K at 1 atm.

The n-heptane/air flame speed at elevated temperatures of $T = 400$ K and 470 K are compared to the measurements by Kumar *et al.* as shown in Fig. 3.7. The temperature variation at the burner exit is about $\pm$ 4 K. At $T = 400$ K, the present data shows the peak flame speed is 3.9 cm/s higher than the reported value by Kumar *et al.* and the comparison is within the accuracy of $\pm$ 5.7 %. The measured flame speed curve at $T = 470$ K, however, locates slightly above the reported data. The lean and rich regions are found to be 5 cm/s higher while the peak flame speed is 6.3 cm/s higher. The discrepancy could be attributed to the differences and uncertainties in experimental setup. Compared to the simulation by Kumar *et al.* that utilised the model developed by Seiser *et al.* [36], both sets of data are well predicted at the lean and rich regions but the stoichiometric region is overpredicted by 5.0 cm/s and 5.5 cm/s for $T = 400$ K and 470 K respectively. It is noted that the present data is compared against those obtained using the counterflow flame configuration. The results suggest that the current simpler jet-wall configuration can reproduce the results of opposed jet flames with good agreement, even at elevated temperatures.

3.5.2 Jet-A1

The measurements of laminar flame speeds of Jet-A1/air mixture were carried out at $T = 470$ K at 1 atm between $\phi = 0.75$-1.5. Figure 3.8 shows the comparison of the current result to the measurement of Jet-A1/air and synthetic jet fuel (S-8)/air obtained by Kumar *et al.* [16]. The present Jet-A1 flame speed result is comparable to S-8/air to within the uncertainty limit of $\pm$ 4.5 %. Jet-A1 fuel, which contains a large fraction of straight chain n-paraffins (50-65% by volume), exhibits similar characteristics as S-8 fuel which comprises almost entirely of straight-chain n-paraffins. The comparison to Jet A/air by Kumar *et al.* shows close agreement on the lean side but slightly higher on the stoichiometric and rich regions by 5 cm/s and 8 cm/s respectively. The discrepancy could be due to the variation in the composition of the jet fuel, especially aromatic compounds.

The current results are compared to the computational results presented by Kumar *et al.* using the Aachen kerosene surrogate mechanism developed by Honnet *et al.* [37], which assumes a surrogate composition of 80% n-decane and 20% trimethyl-benzene by weight. The model underpredicts the lean and stoichiometric region but is in good agreement on the rich side. The high n-paraffin content of the Jet-A1 fuel is possibly the main reason that enables good agreement with the model. Considering the relatively similar fuel properties between Jet-A1, Jet A and S-8, the current measurement reproduces the flame speed data to within the uncertainty limit and further validates the current technique for the measurement of complex fuels.
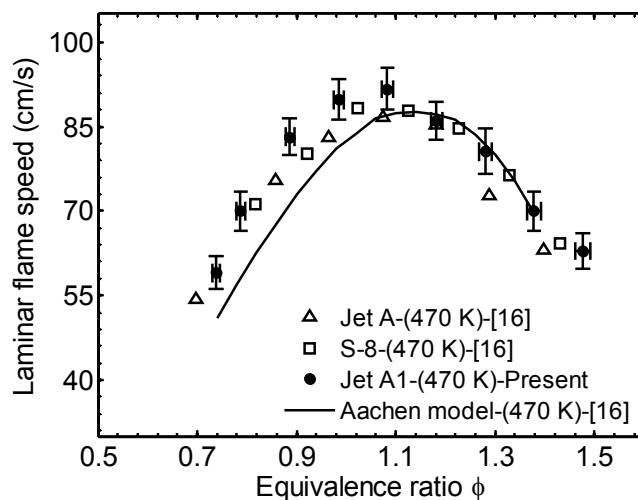
Figure 3.8: Comparison of laminar flame speed of Jet-A1/air mixture with jet fuels at T = 470 K and 1 atm.

Most of the complex fuel models use long n-alkane chain as part of the mechanism development. As such, the laminar flame speed of the complex fuel of Jet-A1 is compared to the straight-chain alkanes of n-decane and n-dodecane as presented in Fig. 3.9. Results by Zhao et $al.$ [9] were obtained at $T = 500$ K, and are slightly higher than the current values as expected. Comparison with the data by Kumar and Sung [10] shows that laminar flame speeds of n-decane are similar to those of Jet-A1 fuel at all stoichiometries, but the n-dodecane flame speed is slightly lower at regions between $\phi = 0.9$ and $\phi = 1.1$ This indicates that either straight chain hydrocarbon could be used as potential surrogate in developing the mechanism to describe Jet-A1 fuel. This is further demonstrated by the computational simulation performed by Kumar and Sung that used the n-decane mechanism developed by Zhao et $al.,$ which shows good agreement in the prediction of laminar flame speed.
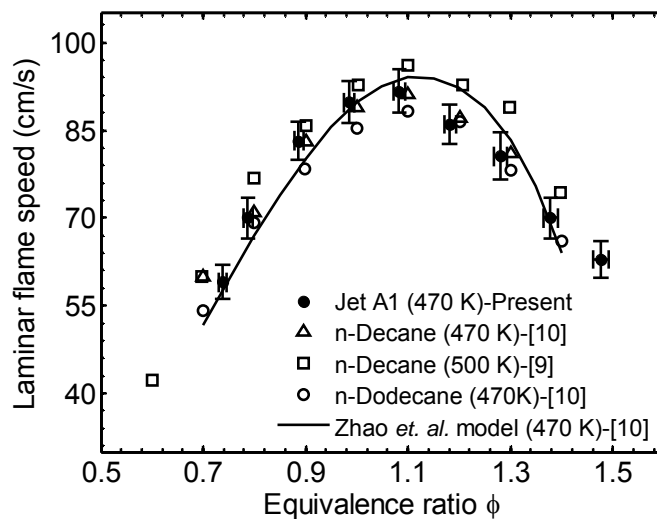
Figure 3.9: Comparison of laminar flame speed of Jet-A1/air mixture with (a) jet fuels and (b) n-alkanes at T = 470 K and 1 atm.

3.5.3 Diesel and palm biodiesel

Laminar flame speed data of diesel/air and palm methyl ester (PME)/air measured at elevated temperature of 470 K and 1 atm over a range of stoichiometries are presented in Fig. 3.10. Comparison to the highest n-alkane flame speed data available, n-decane and n-dodecane [10], shows that diesel/air flame speed is noticeably lower on the lean side but higher on the rich side. The diesel/air flame speed peaks around $\phi = 1.1$ with the maximum flame speed of 86.7 cm/s. The comparison shows that the diesel flame speed is close to n-dodecane at regions near stoichiometric, but the lean and rich sides are 7 cm/s lower and 8 cm/s higher respectively. A similar trend is also observed in the simulation performed by Kumar and Sung [10] using the n-decane mechanism developed by Zhao *et al.*. This is due to the influence of high aromatic content (15-40 %) in diesel fuel, which is known to exhibit lower flame speed than the n-paraffin and slightly higher reactivity on the fuel-rich region [4, 38]. However, the high aromatic content in diesel fuel is insufficient to explain the higher reactivity on the rich side, as aromatic is also present in Jet-A1 fuel. The unexpected results of diesel flame speed on the rich region is worthy of further investigations where fuel

decomposition may be more complex. Even so, it is safe to say that the diesel flame speed is somewhat lower than typical n-alkanes, which make up the bulk of the composition.
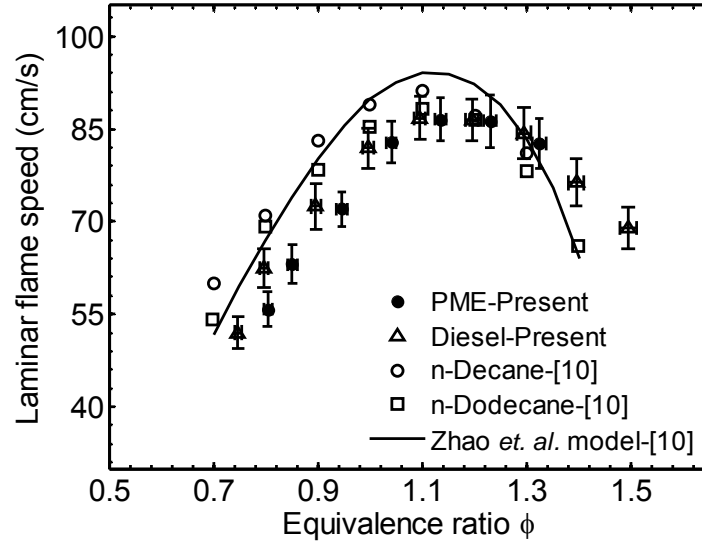
Figure 3.10: Comparison of laminar flame speed of Diesel/air and PME/air with single component n-alkane/air mixtures at T = 470 K and 1 atm.

For PME, the laminar flame speeds are slightly lower on the lean side but rather similar on the stoichiometric and rich region compared to diesel. The maximum flame speed of PME occurs at $\phi \sim 1.14$ with the value of 86.5 cm/s. The shift of the laminar flame speeds to a richer equivalence ratio is typical of oxygenated fuels, and is related to the existence of C=O bonds already in the fuel [4]. The lower reactivity of the PME on the lean side can be associated with the oxygen content and lower heating value of PME compared to diesel as shown in the fuel properties in Table 3.3. However, the adiabatic flame temperature and the lower heating value per total mixture mass of PME/air is close to that of diesel/air, which explains the rather similar flame speed curves between PME/air and diesel/air. Both fuel mixtures have adiabatic flame temperatures lower than n-decane ($T_f = 2623$ K) and n-dodecane ($T_f = 2622$ K), concurring with the experimentally measured lower flame speeds. The similarity between diesel and biodiesel is also shown in the jet stirred reactor test conducted by

Hakka *et al.* [2] where the oxidation of surrogates for diesel (n-decane/n-hexadecane) and biodiesel (n-decane/methyl palmitate) exhibit very similar oxygenated and hydrocarbon species profiles.

3.5.4 Blend of PME with Jet-A1
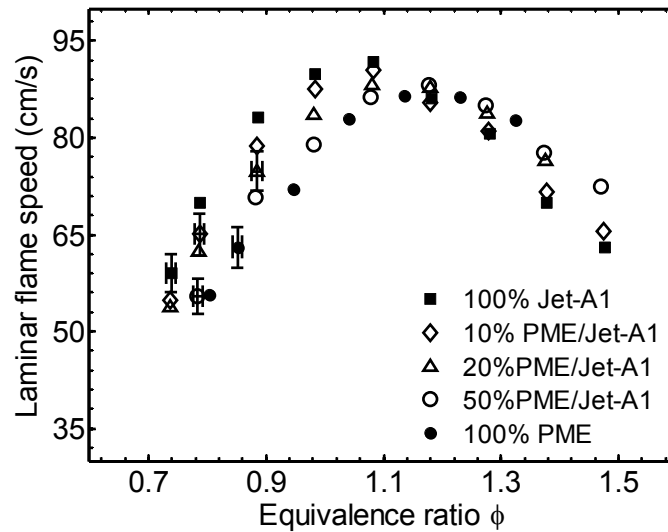
Figure 3.11: Comparison of laminar flame speed of Jet-A1/air, Jet-A1/PME/air and PME/air mixtures at T = 470K and 1 atm.

Figure 3.11 shows the laminar flame speed of the blends of PME with Jet-A1 fuel at fractions of 10 %, 20 % and 50 % by volume at $T = 470$ K and 1 atm between $\phi = 0.7\text{-}1.5$. The blends containing 10 % PME exhibit almost the same flame speed curve as Jet-A1, indicating the base fuel is still dominant. The effect becomes more pronounced when PME blending increases to 20 % by volume. The peak flame speed of 20 % PME blend is 88.3 cm/s at $\phi \sim 1.08$, about 3.5 cm/s lower than the peak of Jet-A1. The 50 % PME blend flame speed shows slightly faster flame propagation on the lean side (3.3 cm/s) but rather similar values at stoichiometric and fuel-rich region compared to pure PME/air. Overall, as the percentage of PME increases, the laminar flame speed curve shifts to the richer side, with the peak flame speed moving from $\phi \sim 1.08$ to ~ 1.2 as the PME blend percentage increases due to the influence of oxygen

addition from PME. The increased carbon and oxygen elements from blending PME contributes to the oxidation enhancement on the rich side, a trend which is also observable in oxygenated fuels where the rich region exhibits higher reactivity compared to pure n-alkanes [39, 40]. Jet-A1 fuel contains a high percentage of aromatics (~ 20 %) and higher energy content per total reacting mixture mass, while PME contains oxygen in the long methyl ester chain with no aromatic ring and lower energy content per mixture mass as indicated in Table 3.3. The adiabatic flame temperature of Jet-A1 fuel is slightly higher than PME, which is also reflected in the higher laminar flame speed.

3.5.5 Blend of PME with diesel

Figure 3.12 presents the laminar flame speed measurements of 10 %, 20 % and 50 % PME blends with diesel/air by volume at $T = 470$ K at 1 atm between $\phi = 0.7$-1.5. There is remarkably little difference between the laminar flame speeds considering the differences in composition, particularly with regard to the neat PME and diesel. Interestingly, the blends do not show linear results between the two curves, with the blends showing slightly higher laminar flame speeds than either neat fuel in the rich range. Once again, the laminar flame speeds of the blends are shifted to the rich side as the percentage of PME blend increases. 10 % PME blend shows slightly lower flame speed compared to diesel/air. The peak flame speed of 10 % PME/diesel blend is 85.2 cm/s at $\phi \sim 1.2$ while for pure diesel/air mixture is 86.7 cm/s at $\phi \sim 1.1$, with a slight shift of equivalence ratio to the fuel-rich side. For 20 % PME blend, the lean side shows 4.0 cm/s lower while the rich side is 5.2 cm/s higher than pure diesel/air mixture.
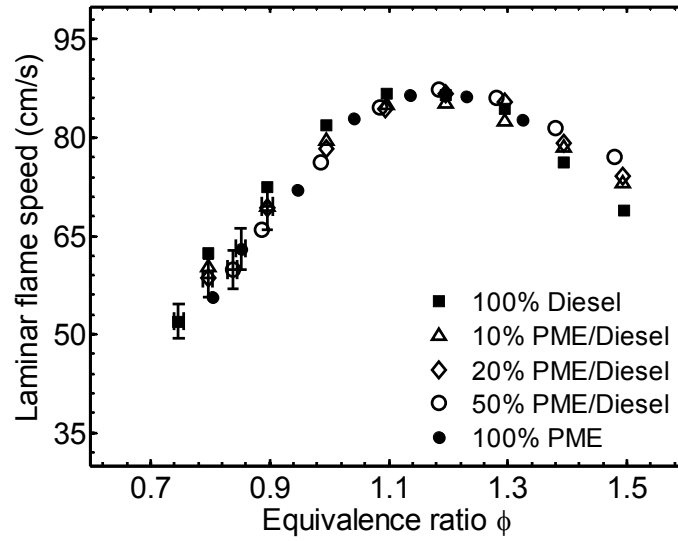
Figure 3.12: Comparison of laminar flame speed of Diesel/air, Diesel/PME/air and PME/air mixtures at 470 K and 1 atm.

In contrast with Jet-A1, the differences between the laminar speeds of the blends and the neat fuels are not obvious. The 50 % PME/diesel blend shows indistinguishable flame speeds compared to pure PME/air mixture, indicating the reactivity of both types of fuels are almost the same. The peak flame speed for 50 % PME blend is 87.3 cm/s at $\phi \sim 1.18$ compared to the peak of PME/air of 86.5 cm/s at $\phi \sim 1.14$. When compared to pure diesel/air, the lean side data of 50 % PME blend is 6.7 cm/s lower and the rich region is 8.2 cm/s higher. The increased reactivity on the rich side of the blends could be attributed to the influence of saturated methyl esters (~ 45 % in PME) which is known to increase the flame temperature [41], apart from the increased elements of carbon and oxygen attained from the blending. Overall, the blending of diesel and pure biodiesel does not have significant effect on the flame speed curves because of the rather similar properties between the two fuels, suggesting that biodiesel can be used as blends in practical appliances burning in deflagration mode.

3.6 Conclusion

Laminar flame speeds of Jet-A1/air, diesel/air, PME/air and the blends of PME with Jet-A1 and diesel at 10 %, 20 % and 50 % by volume have been measured using the stagnation flame configuration and PIV technique at 1 atm, 470 K over a range of equivalence ratios. The peak Jet-A1/air flame speed was measured to be 91.7 cm/s at $\phi \sim 1.08$. Comparison to n-decane and n-dodecane shows that large n-alkanes can be used as surrogates for Jet-A1 fuel due to their similar reactivity. For diesel/air mixtures, the laminar flame speeds are lower compared to n-decane and n-dodecane data on the lean side but higher on the rich side.

Blends of PME with hydrocarbons shift the peak flame temperature slightly to the fuel-rich side, with a corresponding decrease of flame speed in the lean side and an increase on the rich side. The lower flame temperatures of the PME blends are somewhat offset by the higher reactivity of the oxygen containing mixtures. The Jet-A1 blends are more affected by the fraction of PME added than the diesel blends. The discrepancy in flame speed shown in the blends of PME with Jet-A1 and diesel is attributed to the oxygen content and lower heat of combustion of PME, which leads to shifted peak temperatures and reactivity of the fuels. Further investigations using surrogate compounds are needed to explain in detail the specific reactions responsible for the changes.

3.7 References

[1]   Z. Zhao, J. P. Conley, A. Kazakov, and F. L. Dryer, "Burning velocities of real gasoline fuel at 353 K and 500 K," *SAE Int. ,* vol. 112, pp. 2624-2629, (2003).

[2]   M. H. Hakka, P.-A. Glaude, O. Herbinet, and F. Battin-Leclerc, "Experimental study of the oxidation of large surrogates for diesel and biodiesel fuels," *Combust. Flame,* vol. 156, pp. 2129-2144, (2009).

[3]   O. Herbinet, W. J. Pitz, and C. K. Westbrook, "Detailed chemical kinetic oxidation mechanism for a biodiesel surrogate," *Combust. Flame,* vol. 154, pp. 507-528, (2008).

[4]   S. G. Davis and C. K. Law, "Determination of and fuel structure effects on laminar flame speeds of C1 to C8 hydrocarbons," *Combust. Sci. and Tech.,* vol. 140, pp. 427 - 449, (1998).

[5]   Y. Huang, C. J. Sung, and J. A. Eng, "Laminar flame speeds of primary reference fuels and reformer gas mixtures," *Combust. Flame,* vol. 139, pp. 239-251, (2004).

[6]   Z. Zhao, *Experimental and numerical studies of burning velocities and kinetic modeling for practical and surrogate fuels.* PhD: University of Princeton, 2005.

[7]   O. C. Kwon, M. I. Hassan, and G. M. Faeth, "Flame/stretch interactions of premixed fuel-vapor/O2/N2 flames," *J. Prop. Power,* vol. 16, pp. 513-522, (2000).

[8]   K. Kumar, J. Freeh, C. Sung, and Y. Huang, "Laminar flame speeds of preheated iso-octane/O2/N2 and n-heptane/O2/N2 mixtures " *J. Prop. Power,* vol. 23, pp. 428-436, (2007).

[9]   Z. Zhao, J. Li, A. Kazakov, F. L. Dryer, and S. P. Zeppieri, "Burning Velocities And A High-Temperature Skeletal Kinetic Model For N-Decane," *Combust. Sci. Technol.,* vol. 177, pp. 89-106, (2005).

[10]   K. Kumar and C.-J. Sung, "Laminar flame speeds and extinction limits of preheated n-decane/O2/N2 and n-dodecane/O2/N2 mixtures," *Combust Flame,* vol. 151, pp. 209-224, (2007).

[11]   M. S. Skjoth-Rasmussen, M. Braun-Unkhoff, C. Naumann, and P. Frank, "Experimental and numerical study of n-decane chemistry," in *Proceedings of the European Combustion Meeting,* Orleans, France, 2003.

[12]   M. Colket, T. Edwards, S. Williams, N. P. Cernansky, D. L. Miller, F. N. Egolfopoulos, P. Lindstedt, K. Seshadri, F. L. Dryer, C. K. Law, D. Friend, D. B. Lenhert, H. Pitsch, A. F. Sarofim, M. Smooke, and W. Tsang, "Development of an experimental database and kinetic models for surrogate jet fuels " in *AIAA 2008-972* 46th AIAA Aerospace Sciences Meeting and Exhibit, Reno, Nevada, 2008.

[13]   P. Dagaut and M. Cathonnet, "The ignition, oxidation, and combustion of kerosene: A review of experimental and kinetic modeling," *Prog. Energy and Combust. Sci.,* vol. 32, pp. 48-92, (2006).

[14]   H. Eberius, P. Frank, Kick. T, Naumann. C, Steil. U, and C. Wahl, "EU project computational fluid dynamics for combustion no. GRDI-1999-10325," *Final report for subtask 1.2.3. (D 1.7),* (2001).

[15] F. Parsinejad, C. Arcari, and H. Metghalchi, "Flame structure and burning speed of JP-10 air mixtures," *Combust. Sci. and Tech.*, vol. 178, pp. 975-1000, (2006).

[16] K. Kumar, C.-J. Sung, and X. Hui, "Laminar flame speeds and extinction limits of conventional and alternative jet fuels " in *AIAA 2009-991* 47th AIAA Aerospace Sciences Meeting, 2009.

[17] J. T. Farrell, N. P. Cernansky, F. L. Dryer, D. G. Friend, C. A. Hergart, C. K. Law, R. M. McDavid, C. J. Mueller, A. K. Patel, and H. Pitsch, "Development of an experimental database and kinetic models for surrogate diesel fuels," *SAE Paper 2007-01-0201*,, vol. 2007 SAE World Congress, pp. 16-19 April 2007, (2007).

[18] A. J. Marchese, T. L. Vaughn, M. Hammill, and M. Harris, "Ignition delay of bio-ester fuel droplets," *SAE Technical Paper Series*,, vol. 2006-01-3302, (2006).

[19] P. Dagaut and S. Gaïl, "Chemical kinetic study of the effect of a biofuel additive on jet-A1 combustion," *J. Phys. Chem.*, vol. 111, pp. 3992-4000, (2007).

[20] K. Seshadri, T. Lu, O. Herbinet, S. Humer, U. Niemann, W. J. Pitz, R. Seiser, and C. K. Law, "Experimental and kinetic modeling study of extinction and ignition of methyl decanoate in laminar non-premixed flows," *Proc. of the Combust. Inst.*, vol. 32, pp. 1067-1074, (2009).

[21] P. Dagaut, A. El Bakali, and A. Ristori, "The combustion of kerosene: Experimental results and kinetic modelling using 1- to 3-component surrogate model fuels," *Fuel*, vol. 85, pp. 944-956, (2006).

[22] J. Van Gerpen, B. Shanks, R. Pruszko, D. Clements, and G. Knothe, "Biodiesel production technology," *NREL/SR-510-36244*, (2004).

[23] A. Gopinath, S. Puhan, and G. Nagarajan, "Relating the cetane number of biodiesel fuels to their fatty acid composition: a critical study," *Proc. of the Inst. of Mech. Eng., Part D: J. Automobile Eng.*, vol. 223, pp. 565-583, (2009).

[24] N. Hashimoto, Y. Ozawa, N. Mori, I. Yuri, and T. Hisamatsu, "Fundamental combustion characteristics of palm methyl ester (PME) as alternative fuel for gas turbines," *Fuel*, vol. 87, pp. 3373-3378, (2008).

[25] M. S. Graboski and R. L. McCormick, "Combustion of fat and vegetable oil derived fuels in diesel engines," *Progress in Energy and Combustion Science*, vol. 24, pp. 125-164, (1998).

[26] I. Sönmez and Y. Cebeci, "Investigation of relationship between critical surface tension of wetting and oil agglomeration recovery of barite," *Colloids and Surfaces A: Physicochemical and Engineering Aspects*, vol. 234, pp. 27-33, (2004).

[27] J. Kamrak, B. Kongsombut, G. Grehan, S. Saengkaew, K.-S. Kim, and T. Charinpanitkul, "Mechanistic study on spraying of blended biodiesel using phase Doppler anemometry," *Biomass and Bioenergy*, vol. 33, pp. 1452-1457, (2009).

[28] C. Allen, K. Watts, and R. Ackman, "Predicting the surface tension of biodiesel fuels from their fatty acid composition," *Journal of the American Oil Chemists' Society*, vol. 76, pp. 317-323, (1999).

[29] S. Blakey, L. Rye, and C. W. Wilson, "Aviation gas turbine alternative fuels: A review," *Proc. Combust. Inst.*, vol. 33, pp. 2863-2885, (2011).

[30] F. N. Egolfopoulos, H. Zhang, and Z. Zhang, "Wall effects on the propagation and extinction of steady, strained, laminar premixed flames," *Combust. Flame*, vol. 109, pp. 237-252, (1997).

[31] J. Westerweel, "Fundamentals of digital particle image velocimetry," *Meas. Sci. and Tech.*, vol. 8, pp. 1379-1392, (1997).

[32] M. P. Wernet, "Development of digital particle imaging velocimetry for use in turbomachinery," *Exp. in Fluids*, vol. 28, pp. 97-115, (2000).

[33] J. H. Tien and M. Matalon, "On the burning velocity of stretched flames," *Combust. Flame*, vol. 84, pp. 238-248, (1991).

[34] C. M. Vagelopoulos, F. N. Egolfopoulos, and C. K. Law, "Further considerations on the determination of laminar flame speeds with the counterflow twin-flame technique," *Proc. Combust. Inst.*, vol. 25, pp. 1341-1347, (1994).

[35] S. G. Davis and C. K. Law, "Laminar flame speeds and oxidation kinetics of iso-octane-air and n-heptane-air flames," *Proc. of the Combust. Inst.*, vol. 27, pp. 521-527, (1998).

[36] H. Seiser, H. Pitsch, K. Seshadri, W. J. Pitz, and H. J. Curran, "Extinction and autoignition of n-heptane in counterflow configuration," *Proc. of the Combust. Inst.*, vol. 28, pp. 2029-2037, (2000).

[37] S. Honnet, K. Seshadri, U. Niemann, and N. Peters, "A surrogate fuel for kerosene," *Proc. of the Combust. Inst.*, vol. 32, pp. 485-492, (2009).

[38] S. G. Davis, H. Wang, K. Breinsky, and C. K. Law, "Laminar flame speeds and oxidation kinetics of benene-air and toluene-air flames," *Proc. of the Combust. Inst.*, vol. 26, pp. 1025-1033, (1996).

[39] Y. L. Wang, A. T. Holley, C. Ji, F. N. Egolfopoulos, T. T. Tsotsis, and H. J. Curran, "Propagation and extinction of premixed dimethyl-ether/air flames," *Proc. Combust. Inst.*, vol. 32, pp. 1035-1042, (2009).

[40] F. N. Egolfopoulos, D. X. Du, and C. K. Law, "A comprehensive study of methanol kinetics in freely-propagating and burner-stabilized flames, flow and static reactors and shock tubes.," *Combust. Sci. Technol.*, vol. 83, pp. 33-75, (1992).

[41] S. K. Jha, S. Fernando, and S. D. F. To, "Flame temperature analysis of biodiesel blends and components," *Fuel*, vol. 87, pp. 1982-1988, (2008).

Chapter 4

Sprays in non-reacting and reacting flows

4.1 Non-reacting spray

4.1.1 Introduction

Atomization and spraying are liquid-gas two phase flows applied in a broad range of applications including paint coating, spray drying, evaporative cooling, medical devices, chemical industry, agriculture and combustion. In combustion chambers, the atomization process converts bulk liquid fuels into fine droplets with a high surface to mass ratio. The generated fine droplets facilitate high evaporation rates prior to combustion. The quality of the spray and the interaction between the droplets and air has direct relevance to combustion efficiency and emissions performance. Poor fuel atomization results in the formation of large droplets that vaporise at a prolonged time scale. This encourages local droplets burning in diffusion mode that enhances soot and NO_x formation [1]. Development of advanced low emission gas turbine combustors requires knowledge of the spray droplet size and distribution, as this information elucidates the residence and evaporation time scale of the droplets. This chapter reviews the theories behind atomization, previous work conducted on plain-jet airblast atomizer, swirling spray work under reacting conditions, followed by the description of the experimental setup and diagnostics used in the investigations of non-reacting spray and reacting spray characteristics with different fuels under atmospheric conditions.

4.1.2 Mechanism of plain jet atomization

The simplest atomization process can be achieved by discharging liquid fuel into a quiescent environment through a fine orifice under pressure. The jet breakup phenomenon that occurs via a fine liquid orifice can be described using linear stability theory. At low jet velocities ($Re \sim 10^2$), the surrounding gas induces an instability that leads to the formation of capillary waves on the jet. The uniformity of a liquid jet depends on the balance between the surface tension and inertia of the liquid. The dominant effect of surface tension prevents the instability from growing and droplets being formed. However, when the amplitude of the capillary waves continues to grow, a transition stage of jet breaking-up occurs when the Rayleigh instability mode is manifested. The liquid jet breaks-up when the wavelength grows larger than the jet diameter leading to droplets that are nearly twice the diameter of the jet column.

The increase of Re to between (10^2) and (10^5) leads to the first wind-induced regime. Under this regime, the jet breakup distance from the orifice outlet is shortened and the droplets formed are of the same order as the jet diameter. This is due to the oscillations caused by the frictional and pressure forces between the jet surface and the surrounding gas, thus making the liquid jet become wavy. The second wind-induced regime occurs when there is a further increase in Reynolds number to beyond the order of 10^5. In this regime, the wind stress at the gas and liquid interface strips off the droplets, and atomization occurs due to the short wavelength shear instability. The breakup of jet begins almost at the jet exit with droplets size distribution ranging from small to the size of jet diameter.

Reitz and Bracco [2] reported that liquid turbulence, jet velocity profile rearrangement effects, cavitation phenomena, and liquid supply pressure oscillation alone are insufficient to account for atomization. Instead, a combination of the aerodynamic interaction with the different mechanisms can describe the atomization regime. Classification of the jet breakup regime has been developed by Faeth [3]. The regime map elucidates the various stages of atomization through an orifice in the space of Ohnesorge number Oh vs Weber number We_g as shown in Fig. 4.1. Ohnesorge number indicates the effect of liquid viscosity in resisting atomization. This non-dimensional number is defined as the ratio of the viscous to surface tension force of the

liquid, $Oh = \mu_L/(\rho_L\sigma_L d_o)^{-1/2}$, where μ_L and σ_L refer to the viscosity and surface tension of the liquid respectively, while d_o refers to the air exit diameter of a plain-jet fuel atomizer.

Weber number We is defined as $We = \rho_A U_R^2 d_o/\sigma$, where ρ_A and U_R represent the air density and the relative velocity between the atomizing gas and liquid streams respectively. This dimensionless number indicates the ratio of the dynamic pressure force $(\rho_A U_R^2/2)$ to the surface tension force of the liquid (σ/d_o). A high Weber number indicates the likelihood of a liquid jet to disintegrate into droplets.
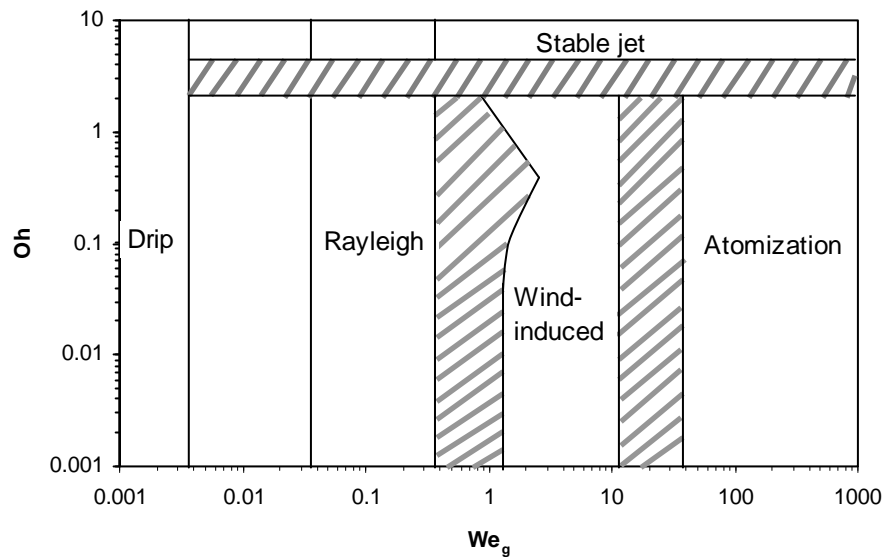
Figure 4.1: The breakup regime of a plain jet through an orifice developed by Faeth [3].

The concept of plain-jet atomization has been developed into the pressure-swirl atomizer, which is widely applied in gas turbine, oil furnaces and direct-injection spark engines. The general mechanism of this type of atomizer involves the usage of high pressure in the atomizer to accelerate the liquid into a central swirl chamber. The liquid is pushed against the wall through swirling effect that leads to the formation of a hollow air core. The centrifugal force applied to the liquid forces the liquid passing through the orifice as a thinned sheet. The unstable thin sheets then break into ligaments and finally into fine droplets. The spray characteristics of the pressure swirl nozzle have been reviewed and documented extensively [4].

4.1.3 Mechanism of plain-jet airblast atomization

Plain jet airblast atomization occurs when a liquid jet is atomized by a coaxial-flowing, atomizing gas stream. The high velocity stream of co-flowing air provides high intensity shear force to disintegrate the liquid jet. The nature of jet disintegration depends primarily on the relative velocity momentum between the air and liquid streams, U_R. If the relative velocities of the fuel and air streams are relatively low, the liquid breaks up via the classical wave instability mechanism. The wave instabilities induced by the generation of capillary and surface waves are imposed on the liquid jet, rendering droplet break up similar to liquid through a plain-jet orifice. If the relative velocity between the atomizing air and liquid jet fuel is high, the liquid jet breaks up immediately upon leaving the fuel orifice. This atomization mechanism is also known as "prompt" atomization [5].
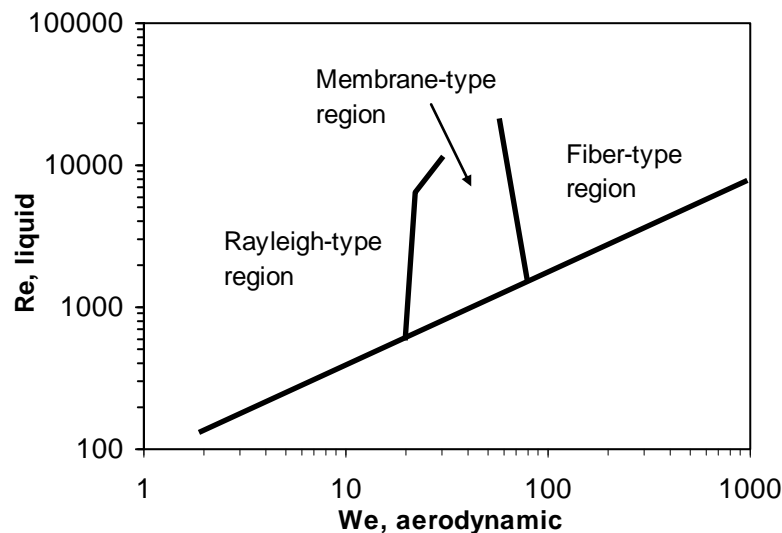
Figure 4.2: Breakup regime of liquid jet in a coaxial gas stream developed by Farago and Chigier [6]

The jet breakup phenomenon in airblast atomizers have been studied by several groups, and the wave mechanism is the commonly accepted model [7, 8]. Fast imaging techniques are typically used to observe the spray breakup process and the detailed

structure to complement the wave models as a form of validation. The descriptions of the airblast jet breakup process have been proposed by Farago and Chigier [6] in the space of Re_L vs We_g as shown in Fig. 4.2. The identified regimes are Rayleigh, membrane-type, fiber-type and superpulsating breakup process.

Rayleigh breakup induced by the wave-instability mode produces droplet sizes of the order of the jet diameter. When the jet is stretched into a thin sheet, the membranous sheet breaks up due to the Kelvin-Helmholtz instability that occurs at the interface of two co-flowing fluids of different densities and velocities. This type of atomization is known to occur at the membrane-type region where the diameter of the droplets produced is smaller than the liquid jet diameter. For fiber-type jet disintegration, atomization begins with the unstable growth of short-wavelength. Thin, thread-like fibers is formed and peeled off from the liquid-jet interface before breaking up via the nonaxisymmetric Rayleigh mechanism. The droplets produced are much smaller than the membrane-like ligaments. This breakup mechanism of jets is analogous to second wind-induced and atomization regimes of the plain jet breakup in quiescent air.

The fiber-type disintegration mode can also be classified under the "prompt atomization", given the relative air-fuel velocity that is high enough to achieve the airblast Weber numbers that produces immediate breakup upon injection. The superpulsating regime is induced when the atomizing air flow rate is extremely high. The moving air stream imparts momentum onto the surface of the liquid jet, forming large-scale eddy structures and curling the liquid sheet. The distorted sheet forms an undulating motion, which finally burst into ligaments and drops of various sizes.

Lasheras and Hopfinger [9] presented a breakup regime, as shown in Fig. 4.3, in the parameter space of liquid Reynolds number $Re_,$ aerodynamic Weber number We and the parameter of momentum flux ratio M. Fine atomization with uniform small droplets can be achieved beyond the upper boundary of the membrane breakup. The fiber-type disintegration occurs when the relative air-fuel velocity is high enough to produce immediate breakup upon injection. This regime can be achieved beyond the membrane regime where We is of the order of (10^3).
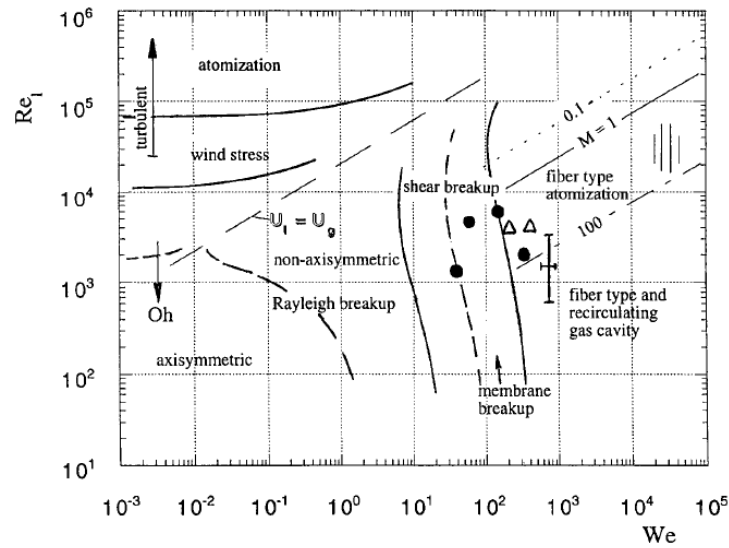
Figure 4.3: Breakup regime of liquid jet in a coaxial gas stream developed by Lasheras and Hopfinger [9].

4.1.4 Parametric studies of airblast atomizer

Airblast atomizers present advantages over pressure atomizers, including lower operating liquid pressure to produce a finer spray, enhanced air-fuel mixing, higher combustion efficiency and higher turndown ratio [10]. The working principle of a twin-fluid atomizer involves the use of an external airstream to shear the liquid jet into ligaments and form droplets. The effects of geometry and liquid properties on the spray qualities of airblast atomizer have been reviewed and documented by Lefebvre [10]. The main factors affecting airblast prompt atomization are the relative liquid-air velocity U_R, the ratio of atomizing air to liquid mass flow rates (ALR), and the liquid surface tension. At high atomizing air velocity, the atomization process occurs rapidly, rendering the liquid viscosity and air density to have minimum effect on the mean droplet size. The air-to-liquid ratio (ALR) can affect the atomization regimes drastically. At ALRs more than 3, good atomization can be obtained with fine droplets. An increase of the ALR beyond this value does not increase the degree of atomization significantly.

Nukiyama and Tanasawa [11] investigated the performance of a plain-jet airblast-type atomizer and derived an empirical equation for the droplet Sauter mean diameter (SMD). They concluded that the liquid jet orifice diameter has no effect on mean drop size. Lorenzetto and Lefebvre [12] showed that the plain-jet airblast atomizer produces a mean drop size that is inversely proportional to the relative velocity between the air and the liquid for low viscosity liquids. It was also reported that the liquid orifice size has little influence on the mean drop size for low viscosity liquids but roughly in proportion to $d_0^{0.5}$ for liquid with high viscosity.

In a similar study conducted by Rizk and Lefebvre [13], the result shows that an increase in air pressure, air velocity, and air/liquid ratio tend to lower the mean drop size, but the SMD is shown to depend on the square root of the fuel-orifice diameter. This dependence on fuel-orifice is supported by Liu *et al.* [14], in which a large jet orifice diameter is reported to have more pronounced effect on SMD values than small jet orifice. A non-monotonic trend was observed where the droplet SMD shows a decrease followed by an increase as the jet diameter increases. The inconclusiveness of the effect of fuel-orifice diameter on SMD could be attributed to the angle at which the air impinges on the liquid fuel. In the injector used by Liu *et al.* [14], the liquid jet and atomizing air are injected parallel into the open air with no impinging angle imposed by the atomizing air. Lorenzetto and Lefebvre [12] used a nozzle where the liquid fuel is impinged or blasted at an extreme angle by the air stream prior to nozzle exit. This results in the "prompt" atomization, which shows less dependence on the fuel jet diameter. Beck *et al.* [15] reported that the geometry of the injector affects the dependence of SMD on the initial liquid sheet thickness. Table 4.1 lists some of the plain-jet atomization investigations conducted previously.

There is a lack of spray data derived from practical fuels. Spray characterisation of practical fuels such as biodiesels would be useful in view of the different physical liquid fuel properties compared to conventional fuels. Spray data from twin-fluid atomizer using biodiesel [16] is scarce and not as comprehensive as its counterpart-pressure atomizer [17, 18]. In this study, the spray droplet characteristics of biodiesels are investigated using a plain-jet airblast atomizer and the results are compared to conventional fuels.

Table 4.1: Comparison of plain-jet airblast atomizer experiments

Atomizer schematic/ Author	Experimental	Findings and results
  Nukiyama and Tanasawa [11]	• Co-flowing air impinges on liquid jet at 90° near exit. • Droplets are measured from spray deposited on oil-coated slides. ALR is varied and different liquid properties are tested.	• SMD correlation derived, no effect of liquid jet orifice diameter on D_{32}. • $SMD = 0.585 \left(\dfrac{\sigma}{\rho_L U_R^2} \right)^{0.5} + 53 \left(\dfrac{\mu_L^2}{\sigma \rho_L} \right)^{0.225} \left(\dfrac{Q_L}{Q_A} \right)^{1.5}$
  Lorenzetto and Lefebvre [12]	• Coaxial flowing air impinges on liquid. • Droplet size are measured by light-scattering technique. Parameters investigated including liquid properties, air velocity, fuel outlet diameter and ALR.	• SMD correlation derived. Good atomization for ALR>3. Fuel orifice size has minimum effect on D_{32} for low viscosity fluids. • $SMD = 0.95 \left[\dfrac{(\sigma_L W_L)^{0.33}}{\rho_L^{0.37} \rho_A^{0.3} U_R} \right] \left(1 + \dfrac{W_L}{W_A} \right)^{1.70} + 0.13 \left(\dfrac{\mu_L^2 D_o}{\sigma_L \rho_L} \right)^{0.5} \left(1 + \dfrac{W_L}{W_A} \right)^{1.7}$
  Rizk and Lefebvre [13]	• Co-axial air impinges on the liquid fuel. • Droplet size measured by light-scattering technique. Parameters varied including liquid (kerosene, water), ALR, air pressure, atomizer hole diameter.	• SMD shows a power dependence of 0.5 to liquid orifice diameter. • $\dfrac{D_{32}}{d_o} = 0.48 \left(\dfrac{\sigma}{\rho_A U_R^2 d_o} \right)^{0.4} \left(1 + \dfrac{1}{ALR} \right)^{0.4} + 0.15 \left(\dfrac{\mu_L^2}{\sigma \rho_L d_o} \right)^{0.5} \left(1 + \dfrac{1}{ALR} \right)$
  Eroglu and Chigier [5]	• Co-axial flow of air and liquid. • SMD and velocity measurements using PDPA, compared with spray images. Water is used, air flow rate is varied.	• Bimodal drop size distribution (peaks at center and at spray boundary). Minimum mean droplet velocities at the center and maximum near spray boundary.
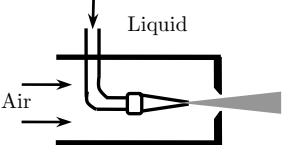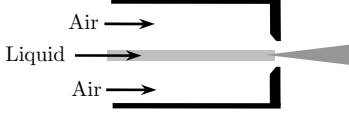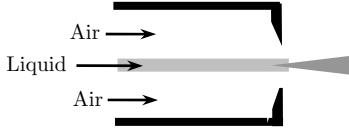
4.2 Reacting spray

4.2.1 Introduction

Combustion of liquid fuel sprays power a variety of systems including gas turbines, compression-ignition engines, furnaces, boilers and other equipment. To mitigate harmful emissions generated from combustion, understanding of the controlling parameters and mechanism involved in the fuel oxidation process is important. For combustion systems utilising liquid fuels, the spray atomization process is one of the key areas for investigation, as the quality of droplets generated has direct relevance to emissions. For instance, incomplete vaporisation of droplets promotes the formation of NO_x and unburned hydrocarbons. Characterisation of spray droplets in spray combustion is necessary to elucidate the spatial distribution of fuel droplets within the combustor and the correlation with emissions. Another important consideration for spray combustion is the interaction of the droplets with the air flow, as the turbulence intensity of the air can affect droplet evaporation, air/fuel mixing, flame shape and flame stability. Due to the complexity of spray combustion, detailed investigation often requires the decoupling of gas and liquid phase. The surrounding air flow needs to be characterised as well as the characteristics of the droplets within the spray flame. In this section, a review on the previous spray combustion literature is presented.

4.2.2 Spray combustion literature

The understanding of the phenomena involved in liquid fuel spray combustion is crucial for designing a more fuel efficient and low emission devices. There are several important parameters involved in spray combustion including fuel composition, droplet size, gas composition and temperature, the relative velocity between the droplets and the air and the combustor pressure [19]. When a spray flame is established, the complex interaction of air, fuel and chemistry results in the simultaneous heat, mass and momentum transfer in addition to chemical reactions. To obtain insight into the combustion phenomena in a spray flame such as heat release rates, flame stabilization

mechanism or the formation of combustion emissions, a detailed investigation of the droplet trajectories and the statistical description of droplet size and distribution is necessary from the practical and computational point of view.

There have been many studies on spray combustion in the past. Syred and Beer [20], Faeth [21], Liley [22] and Smoot and Hill [23] have reviewed extensively the physical models and the chemical processes involved in spray and droplet combustion. Chigier and McCreath [19] highlighted the necessity to acquire the information about droplet size, velocity distribution and their interrelations to connect the single droplet combustion with spray combustion. In spray combustion experiments, several techniques have been utilised to quantitatively measure the droplet characteristics. Double flash photography technique was used to obtain data on droplet size and velocity in reacting spray by McCreath and Chigier [24]. Beretta *et al.* [25] employed the ensemble light scattering technique to determine droplet size and number concentration in fuel sprays and spray flame. The advent of laser diagnostics has greatly advanced the study of spray combustion. Phase/Doppler interferometry has been widely utilised to spatially measure the droplet size and velocity distribution within the spray in burning and non-burning condition [26, 27]. Most of the spray combustion experiments are conducted using either the pressure swirl or twin-fluid atomizer, and the established spray flames could be either in an open or confined environment.

4.2.3 Spray droplet evaporation and mixing

In a spray combustion system, the liquid fuel spray is often accompanied by the swirling air stream. The swirling air vaporises the fuel droplets, forms the recirculation zone and enhances the mixing of fuel and air for combustion. The effect of imparting swirling air on spray evaporation rates has been studied [28-30]. Rao and Lefebvre [31] reported the most significant factors that influence spray evaporation rate are air temperature and mean droplet size. Chin *et al.* [32] studied the transient effect of spray evaporation that occurs during the heat-up period. Other factors can also affect droplet vaporisation rate, including air velocity, fuel injection pressure, axial distance from the injector and change in atomizer flow number [31].

Owen *et al.* [33] showed that the variation of inlet swirling air can change the interaction between the spray and the air stream and subsequently affect the fuel evaporation and fuel-air mixing rates. Komiyama *et al.* [28] compared the droplet evaporation and fuel-air mixing characteristics between pressure and air-assist atomizers. It was reported that the evaporation time is lesser than the mixing time for an air-assist atomizer, thus the jet length scale and kinetic energy govern the mixing process instead of the evaporation process. For pressure atomizer, the fuel-air mixing is controlled by both the kinetic energy of the jet fuel and the evaporation characteristics of the fuel droplets.

The atomizing air for twin-fluid atomizer has significant effect on the spray droplet size, transport and evaporation rate. Yule *et al.* [30] mapped out the droplets distribution of twin-fluid atomized kerosene spray. The result indicates that large droplets exhibit different trajectories compared to the smaller droplets, which are prone to preferential vaporisation. This is also observed by McDonell and Samuelsen [34] where the presence of swirling atomizing air greatly enhances the vaporization rate in twin-fluid atomizer. Sornek *et al.* [35] further reported that the atomizing air, air temperature and mean droplet size are significant factors in influencing spray evaporation, but the spray evaporation could also have influence on the self-excited combustion instability. Aftel *et al.* [36] demonstrated that flames established with Ar and CO_2 show higher luminosity. They suggested that the presence of O_2 in the atomizing gas can significantly enhance droplet evaporations and combustion.

4.2.4 Droplet transport within a spray flame

The mixing process of fuel droplets and air is critical to understanding the dynamics of a spray flame. Information regarding the air and fuel mixing can be derived from the detailed description of the droplets size and distribution, droplet trajectories and the relative velocity of the droplets to the gas flow. Chigier *et al.* [37] described the transport of droplets in a flame established from a hollow cone pressure jet spray combustion in the wake of a bluff body. The study shows the small droplets in the range between 0-50 μm are influenced by the trajectory route and turbulent fluctuations. Fine droplets have smaller inertia-to-drag ratio and larger surface-to-

volume ratio compared to larger droplets. Hence, the ignition delay time is small and the droplets are rapidly evaporated and consumed. The swirling air affects the droplet/air velocity field and the spatial distribution of the droplet size and number density. Larger droplets are transported downstream relatively unperturbed by the surrounding air stream while smaller droplets are entrained by the recirculating flow. In addition, it was observed that the instabilities during jet breakup appear to result in droplet clustering further downstream [27].

Ghaffarpour and Chehroudi [38] investigated the swirling spray flame established from a pressure-swirl atomizer. It was reported that most of the fuel vapour forms a cloud that diffuses towards the high temperature zone near the outer boundary of the flame. They inferred that most droplets do not burn individually, but rather as a vapour cloud that burns as a diffusion flame in a turbulent flow. From the PDA spatial measurements, the effect of the flame on the spray structure includes the increase of mean drop velocity and SMD values, and reduction of droplet velocity fluctuations compared to swirl spray without flame. The spray cloud is found to widen as a result of combustion, but the flame extinguishes if the swirl flow rate is increased beyond a certain limit.

The effect of fuel properties on the spray structure was examined by Presser *et al.* [39] using the phase/Doppler interferometry technique. They established the swirl flame with a pressure swirl atomizer in open air. Fuels with higher viscosity are reported to generate larger droplets. The droplet distribution shows both positive and negative velocities near the center of the spray, where the mean velocity is low. Broader droplet size distribution is observed near the nozzle exit compared to locations at downstream. The time-resolved instantaneous droplet size, velocity and arrival statistics have also shown to be informative. Hodges *et al.* [40] discovered an unsteady statistical behaviour due to a droplet clustering effect within the shear layer formed near the inner spray boundary, and at locations near the fuel nozzle. The droplet clustering effect is found to occur for droplets with the size range of 0-20 μm in diameter.

The droplet transport of spray flame generated from twin-fluid atomizer is also widely studied. The high relative velocity of atomizing air accelerates the droplets along the axial axis and promotes droplet vaporisation. Onuma and Ogasawara [41] reported

that the vapour cloud formed from droplet vaporisation burns as a diffusion flame, similar to a pressure swirl flame [38]. They further showed that the heavy oil spray flame exhibit the turbulent diffusion flame structure based on the similarity in NO concentration profiles [42]. The flame boundaries are located outside the spray boundaries where the mixture of vapour and air mixture are confined and reaction occurs [19, 26].

Mao *et al.* [43] reported that the controlling mechanism for the spray flame structure is dependent upon the droplet-gas interaction and the transport processes that occur within the spray core. They observed that the large drops in the outer spray edges are not influenced by the flame, but the internal spray flame structure is drastically varied as shown by the changes of magnitude and shape of the droplet distributions compared to a non-reacting flow. As the droplets are transported by the high momentum of air, the presence of flame further accelerates the droplets [44]. Chigier and McCreath [19] explained that this phenomenon could be due to the reduction in the drag coefficient of burning droplets, or the reduction in the relative velocity between the gas and droplets in a hot environment where the gas volume expands and temperature increases. Within the recirculation zone, the larger droplets undergo deceleration. The longer residence time of the large droplets increases the mass transfer to the vapour phase.

In the airblast kerosene spray flame experiment conducted by Styles and Chigier [45], the droplet diameter was found to decrease in the initial region of the spray due to secondary atomization, but larger droplets are registered further downstream due to the effect of preferential vaporisation of small droplets. Edwards and Rudoff [26] mapped out the mean structure of a spray flame established using an airblast atomizer. The centre recirculation zone is separated by the internal flame zone. The gaseous diffusion flame zone is marked at the location of the close to the air/fuel mixing boundary.

4.2.5 Stabilization of swirling flames

Chigier and McCreath [19] stated that the requirements for swirl flame stabilization include a mixture ratio that is within the flammability limits, sufficient

velocities to match the burning velocities and the sufficient supply of heat to a sustain reaction in the primary reaction zone. In a swirling flame, small droplets are transported along the axis by entraining the spray via the reverse flow induced by the recirculation air. The hot combustion products entrained from downstream to the inner core of the spray provide the enthalpy required for droplet vaporisation and combustion. As the vapour mass increases, reaction is initiated within the spray region, a diffusion flame is established along the air/fuel mixing boundary outside of the spray [26].

Despite the central toroidal recirculation zone, a corner recirculation zone also exists within the combustor. Both recirculation zones can assist in the flame stabilization by entraining the smaller droplets and hot combustion species from the downstream region of the flame to the flame root. The corner recirculation zone has the lower mean temperature due to the cooling wall effect and lower mean fuel fraction. The centre toroidal recirculation zone is caused by the radial pressure gradient induced by the swirl. Apart from transporting hot reactive combustion species from the downstream region, the centre recirculation zone provides an aerodynamic blockage and reduces the gas velocities necessary to stabilize a flame [46].

The intensity of the swirl can influence the stability of the flame significantly. Tangirala *et al.* [47] found that a recirculation zone will not form for a swirl number between 0 and 0.6. For swirl number $S > 0.6$, a toroidal recirculation zone is formed which increases flame stability as the chemically hot combustion products can be transported back to the flame root. The recirculation flow also creates a region of zero axial velocity where the flame speed and flow speed are properly matched. Further increase of swirl number from 1.0 to 4.0 reduces the turbulence level and flame stability. Excessive swirl could also force the flame to move to positions near the combustor wall, resulting in local hot spots.

4.3 Flame chemiluminescence and spectroscopy

4.3.1 Introduction

In combustion, chemiluminescence refers to radiation from excited molecules produced by chemical reactions within a flame. The intensity of radical chemilumines-

cence can be related to specific chemical reactions. For example, CH* is radiated prior to advancing to the C_2 reaction chain. OH* is produced through oxidation of CH before the final steps in the CH_x oxidation chain [48]. For this reason, quantitative measurements of the global flame behaviour can be inferred by correlating the chemiluminescence signals to the chemical processes of the flames to derive meaningful information such as heat release rate and equivalence ratio. With the advent of laser, optics and camera technology, chemiluminescence diagnostics are able to provide quantitative measurements of these species radiation at high resolution. In this section, the literature of flame chemiluminescence applications is reviewed, as the technique will be utilised to examine the flame reaction zones of the swirl flame.

4.3.2 Chemiluminescence diagnostic

The chemiluminescence characteristics from excited radicals such as OH*, CH* and CO_2* are shown to be good indicator for heat release rate [49]. Delabroy *et al.* [50] imaged the temporal evolution of vortical structures within a flame using CH* chemiluminescence as a marker. Ikeda *et al.* [51] studied the reaction zone and flame front structures of premixed turbulent propane flame by measuring the chemiluminescence of OH*, CH* and C_2*. It has been established that the intensity of the chemiluminescence emission from the flame reaction zone increases linearly with the fuel flow rate at a fixed equivalence ratio. This characteristic serves as the basis to correlate chemiluminescence intensity to local and overall heat release rates [52-54].

Flame chemiluminescence has been widely applied in the study of combustion instabilities to characterize the temporal fluctuation of global or local heat release distribution. The OH* chemiluminescence measurement was used to derive the heat release rate from a pulse combustor [55, 56]. Padmanabhan *et al.* [57] optimized the combustor performance with respect to volumetric heat release and pressure fluctuations of a premixed flame using CH* and C_2 emission detection as an adaptive optimal control strategy. Lawn [58] determined the instantaneous heat release of a local swirl flame region by correlating the OH* chemiluminescence signal with the fluctuating pressure that operates under a low acoustic self-excitation mode. Lieuwen and Neumeier [59] showed that the response of CH* chemiluminescence is non-linearly

related to the pressure oscillation imposed on the premixed flame in a combustor. The unstable operating condition was further investigated by Venkataraman *et al.* [60] via CH* chemiluminescence images to study the flame heat-release structure. The obtained images reveal the flame-vortex interaction and its influence on instabilities. It has also been shown through CH* imaging that combustion instability can significantly alter the flame structure and flame extinction under certain conditions [61].

Some of the parameters that could affect the radical chemiluminescence as an indicator of heat release rate have been investigated. Higgins *et al.* [62] reported that the strain rates between 200 s^{-1} and 700 s^{-1} has no influence on CH* chemiluminescence in a premixed counter-flow flame configuration. This suggests that the effect of strain may not be the sole factor that influences chemiluminescence intensity. The effect of turbulence on chemiluminescence intensity has also been studied [63, 64]. Lee and Santavicca [64] varied the inlet velocity of a lean premixed flame and found that the influence of turbulence on CO_2^* intensity is not pronounced. They also showed that the effect of equivalence ratio variation, such as those in the partially premixed flame, has relatively small influence on the chemiluminescence intensity. Najm *et al.* [48] reported that OH*, CH*, CH and C_2^* are not reliable indicators for local flame extinction especially in regions with huge unsteady flame curvature. Instead, HCO was proposed as a better alternative in correlating with flame heat release rate with the unsteady curvature and strain rate [65].

There have been attempts in correlating chemiluminescence intensity with the equivalence ratio of hydrocarbon/air mixtures. Dandy and Vosen [66] reported that OH* chemiluminescence intensity exhibits an exponential dependence on equivalence ratio in the range of $0.65 < \phi < 0.9$. Kojima *et al.* [67] reported a strong correlation between the peak intensity ratios of OH*/CH*, C_2^*/CH* and C_2^*/OH* with the equivalence ratio between 0.9 and 1.5 for premixed flames. The monotonic relation of OH*/CH* with equivalence ratio and the independence of OH*/CH* intensity to strain rate has been shown in [49]. The intensity ratios of C_2/OH* and C_2^*/CH*, however, are reported to exhibit a non-monotonic relation to the equivalence ratio and subject to the influence of strain rate. Docquier *et al.* [68] utilised the intensity ratios of OH*/CH* and CO_2^*/CH* as part of control system to monitor equivalence ratio and control the fuel mass flow rate.

Muruganandam *et al.* [69] performed a study of the chemiluminescence emissions of swirling flames in a generic combustor. The result shows the ratio of peak intensities of CH^*/OH^* increases monotonically with equivalence ratio between 0.6 and 1.2 for natural gas flames. For liquid swirl flames, an n-heptane flame shows that C_2^*/OH^* is a more sensitive measure of ϕ compared to CH^*/OH^*, and the determination of axial variation in ϕ for the partially premixed flow fields agrees with the expected trend. They also concluded that OH^* signal was found to be a good indicator of heat release rate for lean mixtures compared to CH^* or C_2^*. The chemiluminescence characteristics of CH^* and CO_2^* have been used to develop optical-based sensor for fuel/air mixture ratio monitoring in a combustor. It has been observed that the fuel-air mixedness and inlet temperature variations over 50 K have little effect on the overall flame chemiluminescence intensity [70]. Arias *et al.* [71] utilised the emission ratio of C_2^*/CH^* obtained from spectral analysis to determine the thermal combustion efficiency and CO emissions.

The effect of pressure on chemiluminescence has also been studied. Ikeda *et al.* [72] reported that the intensity ratio of OH^*/CH^* shows negligible dependence on pressure. They concluded that OH^*/CH^* ratio estimated from spectral analysis can be a good marker for equivalence ratio even for a high pressure flame. Muruganandam *et al.* [69] however, reported that pressure affects the CH^* and OH^* signals emitting from the flames. Higgins *et al.* [62] found that CH^* exhibits a power law dependence with equivalence ratio and pressure in a study involving the pressure range of 0.5 to 2.5 MPa and the equivalence ratio range between $\phi = 0.66$ and 0.86.

4.4 Emissions

4.4.1 Introduction

Alternative fuels should ideally produce lower NO_x, SO_x, CO, CO_2 and particulate matter than conventional petroleum fuels. Biofuels are among the alternative fuels that present the potential of emission reductions. At present, biofuels are mainly used in ground vehicles. Bioethanol is widely used as blends with gasoline in spark ignition engines while biodiesel is blended with diesel for use in compression

ignition engines. There is considerable interest in applying biodiesel in combustion systems such as industrial gas turbines, micro gas turbines and furnaces. In this section, a review on the emissions from gas turbines using biodiesel and the formation of pollutants is presented.

4.4.2 Review on biodiesel emissions

Biodiesels are increasingly being used in ground transportation system. For this reason, most emission studies of biodiesel is focused on the internal combustion reciprocating engines such as compression ignition (CI) engine [73] or highly homogeneous compression ignition (HCCI) engine [74]. However, reports on the biodiesel emissions of NO_x and CO from existing engines have been inconsistent. Some studies have shown that biodiesel reduces the emissions CO, UHC, PM emissions but increases NO_x [75-77], while others have reported the decrease of NO_x [78-80]. Such discrepancy in the literature could be attributed to the variation of parameters such as the engine models, injection timing or the quality of the biodiesel. Nevertheless, these results reveal the potential of biodiesel and provide the necessary insights to implement emission mitigating measures.

As mentioned previously, the use of biodiesel is not restricted only to diesel engines. There is growing interest in using biodiesel in gas turbine type engines for power generation. However, information related to biodiesel utilization in gas turbine engines remains relatively scarce. The emission results of biodiesel derived from internal combustion engines are not inferable to gas turbines due to the distinct difference in flame structure, i.e., compression type engine operates with an intermittent non-premixed reaction under extreme high pressure, whereas gas turbine combustor produces an overall lean, partially-premixed reaction with longer residence time for the droplet vaporisation process [81].

One of the advantages of the gas turbine is the greater flexibility in fuel choice with lesser fuel chemistry constraints. For example, the cetane number of a fuel is an important parameter for internal combustion engines but not for gas turbines. In recent years, several field tests have demonstrated the feasibility of using alternative fuels such as bio-oil, ethanol, biodiesel and blends in gas turbine engines [82-84]. In a field

test that utilised a 40 MW, E class gas turbine, the NO_x emission of rapeseed methyl esters was reported to be lower compared to diesel fuel [84]. The observed lower NO_x emission is due to the lower adiabatic flame temperature of biodiesel compared to diesel fuel, as explained by Glaude *et al.* [85] through a detailed calculation of the enthalpy and free energy of the mixtures. Higher adiabatic flame temperatures such as the case using diesel fuel, encourages the production of higher NO_x through the mechanism of "thermal NO_x". However, Ellis *et al.* [86] examined the emissions of soy, palm biodiesel and 20 % biodiesel blend with diesel volumetrically in a semi-closed cycle gas turbine. The result showed almost similar emissions of NO and CO for all the fuels tested.

There have also been some biodiesel emission studies in a micro gas turbine combustor. Krishna [87] examined the emissions of soy biodiesel and blends of soy biodiesel with diesel fuel in a 30 kW microturbine (Capstone C30). The result showed that all the biodiesel blends including the neat soy biodiesel exhibited the reduction of CO and NO emissions compared to diesel fuel without any loss of thermal efficiency. However, this result contradicts the more recent experiments that utilised the same 30 kW microturbine (Capstone C30) [81], where soy biodiesel was used and the NO emission was shown to be higher compared to diesel fuel. Variation of the air-liquid mass ratio (ALR) parameter shows significant influence on the emissions performance. NO emissions for biodiesel were found to decrease with an increasing ALR. The experiment showed that optimized NO and CO emissions can be achieved with the modification of the operating conditions or injector.

Nascimento *et al.* [88] investigated the thermal and emission performance of castor biodiesel and biodiesel blends with diesel in a 30 kW diesel microturbine engine. The thermal performance showed that the use of pure biodiesel fuel resulted in a higher fuel specific consumption compared to diesel due to the lower heating value. The emission result showed an increase of CO and a decrease of NO emissions compared to diesel fuel. Comparison of the emissions performance of biodiesel and Jet-A1 fuel was performed by Habib *et al.* [89] in a 30 kW gas turbine engine. The fuels tested were biodiesel derived from soy, canola, rapeseed, animal-based and blends of biodiesel with Jet A fuel. The results indicated that although the turbine inlet and engine exhaust gas temperature did not show significant changes with the fuel type, the CO and NO

emission concentration decreased when biodiesels were used. Pure biodiesel was also found to show higher thermal efficiencies than Jet A and biodiesel blends.

Ramotowski *et al.* [90] investigated the emissions performance of palm and soy biodiesel using a gas turbine engine hardware (Solar Turbines Centaur 50 fuel nozzle). The combustor inlet air was preheated to 625 K and the pressure of the combustor was maintained at atmospheric conditions. The NO and CO emissions level of the biodiesels was lower than from diesel fuel. The higher NO emissions of diesel is due to the presence of fuel-bound nitrogen. Biodiesel contains no fuel-bound nitrogen and hence the NO emission level of biodiesel is similar to natural gas and Fisher-Tropsch fuel (S-8) [90].

Sequera *et al.* [91] utilised a generic gas turbine type combustor to establish a swirling spray flame for the investigations of biodiesel emissions. The fuels tested were diesel, soy methyl ester, soy ethyl ester and bio-oil pyrolised from hardwood. The results demonstrated that lower emissions of NO_x and CO were obtained for the biodiesel-blended fuels at the operating conditions when all the fuel flow rates are kept constant. An increase of atomizing air through the atomizer resulted in the reduction of emissions. A similar trend was also observed in the experiments conducted by Panchasara *et al.* [92] using the same setup. They reported that an increase of 67 % in the atomizing air flow rate could reduce the emissions of CO and NO by a factor of 5 and 10 respectively. The reduction of the NO emissions is associated with the lower flame temperature as a result of the increase of atomizing air.

Hashimoto *et al.* [93] investigated the emissions of palm biodiesel relative to diesel in a gas turbine type burner at atmospheric pressure. The atomizer used in the burner was a pressure-swirl type. It was reported that NO emissions for palm biodiesel were consistently lower compared to diesel fuel when plotted as a function of excess air ratio, droplet SMD, atomizing air pressure and viscosity. The measured CO and unburned hydrocarbons were within the range of 2 ppm.

From the review, most studies show that biodiesel produces lower NO and CO emissions when operating under the gas turbine conditions. The presence of oxygen in biofuel molecules contributes to locally leaner combustion, increased fuel consumption and thermal efficiency as observed in some experiments. The following section describes the mechanism of pollutant formation.

4.4.3 Formation of pollutants

4.4.3.1 Mechanism of NO_x formation

Oxides of nitrogen can result in the formation of smog and acid rain that are detrimental to the environment and human health. Since combustion is the primary source for NO_x formation, a detailed understanding of the mechanism of NO_x formation can assist in developing strategies to reduce pollutants in combustion systems. Generally, NO_x appears in the form of nitric oxide (NO) and nitrogen dioxide (NO_2) but the former dominates during the combustion process. Several routes have been identified through which NO is produced, namely thermal NO, prompt NO, fuel NO, and the nitrous oxide route.

Thermal NO mechanism

Formation of NO_x through the thermal NO mechanism becomes predominant at temperatures around or above 1800 K, which is typically the temperature range that occurs in most gas turbine combustor under lean and stoichiometric conditions. Thermal NO is also known as the Zel'dovich mechanism [94] which consists of three main reactions:

$$O + N_2 <=> NO + N \tag{4.1}$$

$$N + O_2 <=> NO + O \tag{4.2}$$

$$N + OH <=> NO + H \tag{4.3}$$
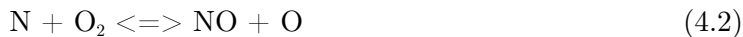
The first reaction is a rate-limiting step due to the low reaction rate constant. In this reaction, a high activation energy is required to break the strong triple bond in the N_2 molecule. The formation rate of NO can be calculated through the reaction steps using the steady state assumption for the N-atom concentration, and a partial equilibrium assumption for the oxygen molecule concentration. Equation 4.3 is known as the extended Zel'dovich mechanism developed by Lavoie [95]. The result indicates that thermal NO formation is strongly dependent on the combustion temperature. Oxygen concentration influences the formation of NO but to a lesser degree [96].

The formation of thermal NO is predominant at the equivalence ratio of $\phi = 0.8\text{-}1.0$. Lower thermal NO emissions can be achieved at fuel-lean ($\phi < \sim 0.6$) and fuel-rich ($\phi > \sim 1.7$) regions. The lean-premixed-prevaporised (LPP) gas turbine combustor employs lean mixture combustion for thermal NO control.

Prompt NO mechanism

The prompt NO mechanism is typically referred as the Fenimore mechanism [97]. The route to prompt NO formation involves a rapid reaction of hydrocarbon radicals such as CH, CH_2, C_2 or C_2H with nitrogen that leads to the formation of hydrogen cyanic acid (HCN) and a nitrogen atom. The principle reactions for prompt NO formation are

$$N_2 + CH <=> HCN + N \tag{4.4}$$

$$C_2 + N_2 <=> 2\ CN \tag{4.5}$$

The single nitrogen atom associated with the production of HCN in reaction 4.4 participates in the NO formation via reactions 4.1 and 4.3 from the Zel'dovich thermal NO mechanism to form NO. The activation energy required for reaction 4.4 is much lower than the formation of thermal NO. The CN from the reaction 4.5 could produce NO through reaction with oxygen. Bachmeier *et al.* [98] measured the prompt O as a function of equivalence ratio for a range of hydrocarbon. The result indicates that maximum prompt NO is attained at the fuel-rich region until $\phi = 1.4$.

NO from fuel-bound nitrogen

The presence of nitrogen in fossil fuels can lead to significant production of nitrogen oxides during combustion. The production of fuel NO is dependent on the combustion conditions and the level of nitrogen in the fuel. When nitrogen-containing fuel is present, high fuel NO is obtained for lean and stoichiometric mixture. The fuel NO production depends weakly on the local temperature as the reactions involved requires low activation energy.

Prior to the formation of fuel NO, the nitrogen compounds in the fuel undergo thermal decomposition before entering the combustion stage. The precursors to fuel NO formation are typically the smaller, nitrogen-containing molecules or radicals such as

HN_3, NH_2, NH, HCN and CN. The oxidation of these nitrogen-bound molecules to NO is rapid and comparable to the time scale of energy-release reaction. Fuels that contain aromatic rings could contribute to the level of fuel NO [99] in the combustion process.

Nitrous oxide mechanism

N_2O is an important species formed in fuel-lean flame. The formation of N_2O is through the reaction of third body M recombination with O and N_2, such as

$$N_2 + O + M <=> N_2O + M \qquad\qquad (4.6)$$

The N_2O produced may subsequently react with O atoms to form NO

$$N_2O + O <=> NO + NO \qquad\qquad (4.7)$$

Under fuel-lean condition, the formation of NO via N_2O is dominant at temperatures around 1500 K. The low temperature deters the formation of Thermal NO while the Prompt NO cannot be produced due to the lack of radicals (such as CH) necessary for reaction initiation [100]. Under fuel-rich conditions, the principal N_2O formation reaction involves NO and nitrogen-containing radicals such as

$$NH + NO <=> N_2O + H \qquad\qquad (4.8)$$

$$NCO + NO <=> N_2O + CO \qquad\qquad (4.9)$$

The N_2O produced from reaction 4.8 and 4.9 under fuel-rich conditions will rapidly react with H atoms to form N_2 via

$$N_2O + H <=> N_2 + OH \qquad\qquad (4.10)$$

4.4.3.2 Mechanism of CO formation

Carbon monoxide (CO) is a colourless, odourless gas that is poisonous. The principle intermediate reaction for the production of CO is mainly through the high temperature oxidation of methyl radical

$$CH_3 + O_2 <=> HCO + H_2O \qquad\qquad (4.11)$$

The HCO produced from reaction 4.11 contributes to the formation of CO via

$$HCO + OH <=> CO + H_2O \qquad\qquad (4.12)$$

$$HCO + M <=> H + CO + M \qquad\qquad (4.13)$$

CO is predominantly formed under stoichiometric or fuel-rich conditions. In a gas turbine combustor, the CO production is inversely related to the formation of NO. In the stoichiometric region where NO emission is high, CO emission is found to be lowest. On the contrary, at fuel-lean or fuel rich regions where NO is low, the CO emission is shown to increase.

4.5 Experiments

4.5.1 Non-reacting spray setup
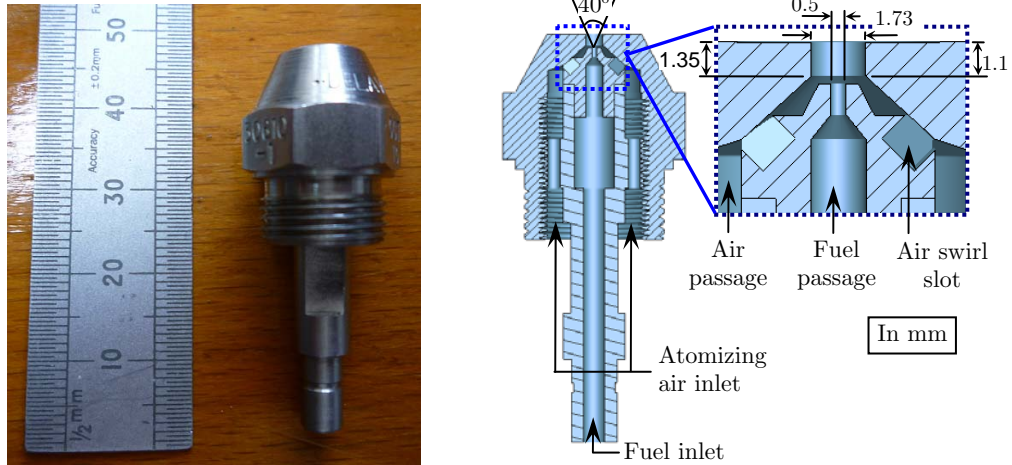
Figure 4.4: Schematic of the plain-jet airblast atomizer

A commercial atomizer (Delavan: SN type-30610-1) manufactured by Delavan Spray Technologies is employed for the present study. The schematic of the atomizer internal geometry is shown in Fig. 4.4. The liquid and gas phases are supplied independently to achieve controllable inlet conditions for both phases. Liquid fuel is injected through the central tube and the atomization is achieved via the impingement of high-velocity air from the surrounding annular tube on the liquid jet. The atomizing air is directed through tangential slots at the angle of 30° to increase the impinging force on the liquid. The fuel orifice d_o is 0.5 mm while the coaxial air orifice d_a is 1.73 mm. The nominal spray cone angle specified in the data sheet is 40° at the supplied air pressure of 0.2-1.0 bar. The fuel flow rate is accurately metered using a Bronkhorst$^\circledR$ Coriolis mass flow controller (M13 mini CORI-FLOW$^\circledR$) which delivers a pulsation free liquid flow rate with ± 0.4 % accuracy. The atomizing air is supplied by using a Bronkhorst$^\circledR$ thermal mass flow controller, which delivers an accuracy of ± 1 %. The atomizer is housed in an adaptor and fixed to a vertical stand. All components of the experimental setup are mounted to an optical table. The flow delivery system of the test rig is shown in Fig. 4.5. The atomizer outlet is facing downward so the spray droplets generated can be collected in a container. The injection of atomizing air

through the air orifice incurs a pressure drop that is linearly related to the air mass flow rate, as presented in Appendix C1.
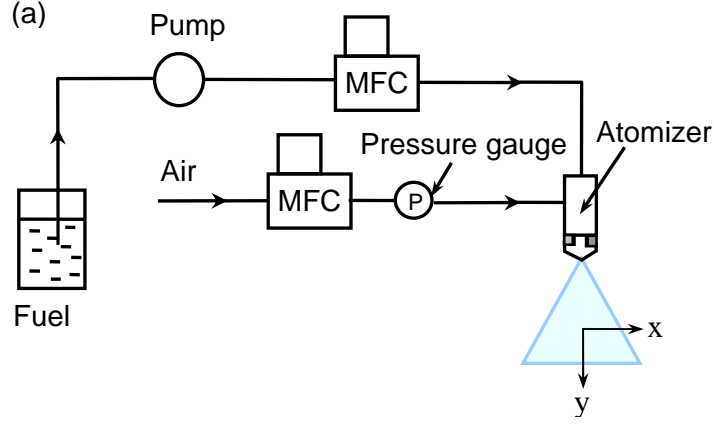
Figure 4.5: Schematic of the spray setup for PDA measurements

4.5.2 Swirl burner and flow delivery system

The swirl burner in this experiment consists of a circular quartz tube forming the combustor wall and a swirler at the burner outlet. The axial swirler consists of eight straight vanes fixed at an angle of 45° which generates strong swirl intensity. The swirl number, S_N is calculated as 0.78 based on the equation

$$ S_N = \frac{2}{3} \left[\frac{1 - (D_h/D_s)^3}{1 - (D_h/D_s)^2} \right] \tan \theta \qquad (4.14) $$

where D_h and D_s represent the swirler hub diameter and the swirler diameter respectively, and θ is the angle of the swirl blade from the centreline [101]. A plain-jet airblast atomizer (Delavan: SN type-30610-1) is placed concentrically with the swirler. Description of the geometry of the atomizer is shown in section 4.5.1. The swirl vanes and airblast nozzle are flush mounted to the burner face as shown in Fig. 4.6b. The swirler is held by a central tube designed for delivering atomizing air and liquid to the atomizer. The liquid spray generated from the atomizer is enveloped by the swirling air coaxially. A schematic of the single swirl flame burner configuration is presented in Fig. 4.6a. A circular quartz tube with the internal diameter of 100 mm and 180 mm in

length is placed concentrically with the burner to form a generic gas turbine dump combustor.

The primary swirling air flow is heated with two in-line air heaters (750 W/heater) arranged in series. The burner plenum and body are additionally heated with 3 Omega® rope heaters (500 W/heater) and insulated with high temperature heat-resisting materials to the reduce heat loss. A 1.5 mm thermocouple is placed 10 mm under the swirler to measure the temperature of the preheated air near the burner outlet. The heating facilities allow the main air to be heated to a temperature of 350 °C. The signal from the thermocouple provides feedback to the temperature controller of the heaters. The uncertainty in the temperature measurement of the preheated air at the burner outlet is within ± 5 K. The whole burner including the swirler is constructed from stainless steel. The plain-jet airblast atomizer is housed in a custom-made adaptor that allows independent control of atomizing air and fuel flow. The fuel flow rate is accurately metered and supplied by the Bronkhorst® Coriolis mass flow controllers (M13 mini CORI-FLOW®) which delivers a full scale accuracy of ± 0.4 %. The main air and the atomizing air lines are regulated separately by two Bronkorst® thermal mass flow controllers (MFC) which deliver the full scale accuracy of ± 1 %. The schematic of the burner and flow delivery system is shown in Fig. 4.7.
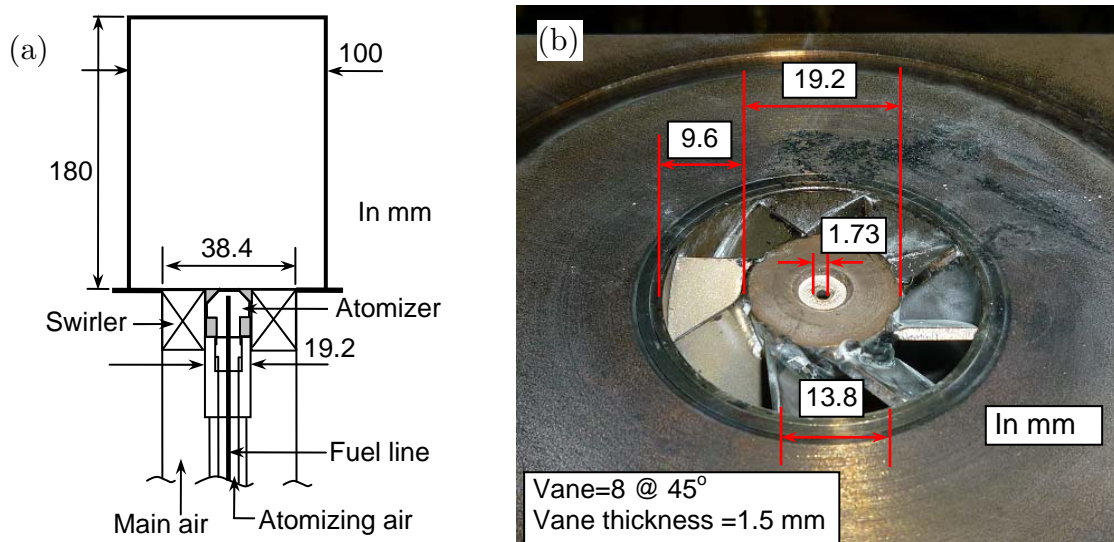
Figure 4.6: (a) Schematic of the swirl burner and (b) the geometric description of swirler.
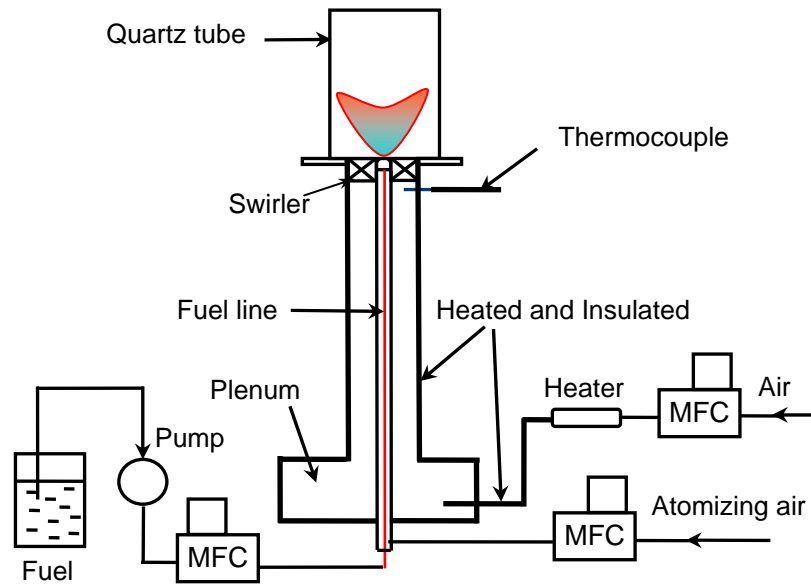
Figure 4.7: Schematic of the single swirl burner and flow delivery system
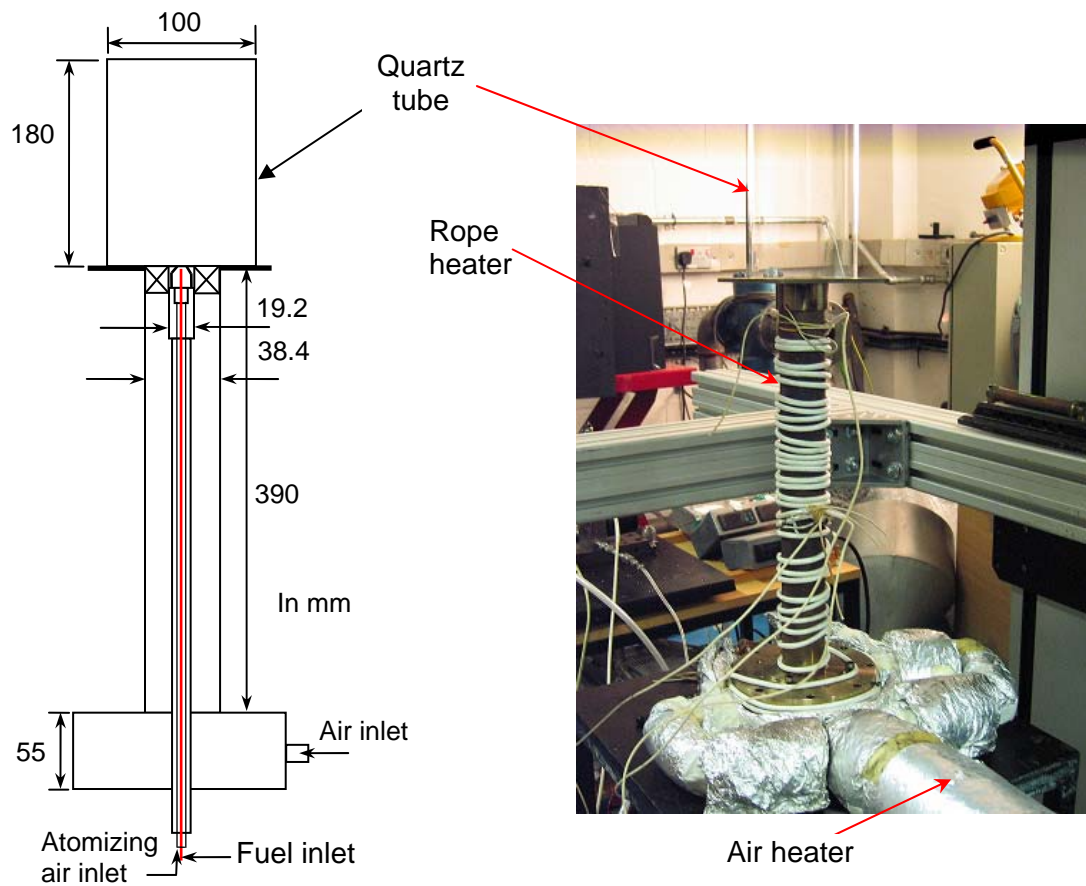
Figure 4.8: (a) Schematic and the (b) actual setup of the swirl burner

4.6 Measurement techniques
4.6.1 Phase Doppler anemometry (PDA)

The droplet size and velocity have been measured by a one-component phase-Doppler anemometer. The droplet size is determined based on the measured phase shift difference between two Doppler bursts, whereas the droplet velocity is obtained from the Doppler burst frequency [102, 103]. The PDA system (Dantec 112 mm Fiber PDA) consists of an Ar-ion laser (Coherent: Innova 70C), a transmitter and receiver probe, Bragg cell and a processor with BSA software for signal processing. The generated laser beam wavelength is 514.5 nm at the power of 0.8 W. The laser beam produced is split into two almost identical beams before being transmitted to form a measurement volume at the focal length of the lens of 500 mm. The Bragg cell imposes a Doppler frequency shift of 40 MHz on one beam for velocity directional recognition to avoid ambiguity.

The receiving optics that houses the detectors is positioned at 56 and 57 degrees off axis in the forward scattering mode for the non-reacting and reacting spray experiments respectively. The presence of three detectors in the receiving optics eliminates the ambiguity of the droplet size associated with spatial phase shifts of over 360°. The scattered light is collected by a receiving lens with a focal length of 310 mm. The transmitting and receiving optics are mounted onto a traverse system equipped with stepper motors that allows the spatial translation in three directions with the accuracy of ± 0.1 mm. The setting of the beam transmitter and receiving optics for the PDA system is shown in Table 4.2. The photomultiplier voltage was adjusted to obtain maximum sensitivity without saturation to obtain optimum measurement conditions for both large and small droplets. Spherical validation rate for the droplets size measurements are set to 10 %. The statistical uncertainty is estimated to be ± 2 % for the droplets velocity and diameters, which is attributable to possible optical misalignment or errors in the photomultiplier voltage settings. Validation rates determined by the PDA software for droplet velocity and size during the measurements were at least 90 %.

Table 4.2: PDA operational parameters

Transmitting optics	
Wavelength	514.5 nm
Power	0.8 W
Beam spacing	45 mm
Beam width	2.2 mm
Focal Length	500 mm
Number of fringes	26
Width of measurement volume	0.149 mm
Length of measurement volume	3.312 mm
Receiving Optics	
Focal length	310 mm
Scattering angle (non-reacting)	57º
Scattering angle (reacting)	56º

Operating conditions for non-reacting spray

The non-reacting spray experiment is divided into two parts; the first is to investigate the effect of varying the atomizing air/liquid mass flow ratio (ALR) on the spray, while the second part compares the spray atomization of different fuels. The effect of ALR is investigated using diesel as the liquid fuel. The air and liquid fuels are supplied at room temperature of 293 K. The variation of air/fuel mass ratio is set at between 1 and 6, which corresponds to the atomizing air velocity of 55-300 m/s. Table 4.3 shows the nozzle exit parameters. The Weber number We, which defines the inertia over the surface tension of the liquid fuel, increases as the relative velocity between air and liquid jet is increased.

Comparison of the effect of fuel properties on atomizing characteristics is performed using diesel, Jet-A1, palm methyl esters (PME) and rapeseed methyl esters (RME). Biodiesels are known to be denser, contain higher viscosity and surface tension than conventional fuels of Jet-A1 and diesel. The air/liquid mass ratio is fixed at 2, in which the fuel mass flow rate is maintained constant at 0.14 g/s and the atomizing air is fixed at 0.28 g/s. The effect of blending biodiesels with conventional fuels at 50% by volume is also investigated. The physical properties of the fuels and blends are listed in Table 3.3 and 3.4 in Chapter 3. The PDA measurement of drop sizes and velocities have been performed at the axial locations of y = 30, 50 and 80 mm downstream of the

atomizer tip (y = 0 mm), as illustrated in Fig. 4.9a. In each axial plane, measurements were carried out along the radial direction. Each spatial measurement was performed by acquiring a maximum number of 50,000 samples or within 80 seconds at the spatial spacing of 1 mm.

Table 4.3: Nozzle exit flow parameters

Gas phase	Air
Air supply pressure (P_a)	0.1-2.6 bar
Air exit velocity (V_a)	55-300 m/s
Air mass flow rate ($\dot{m}_a$)	0.14-0.84 g/s
Air Reynolds number (Re_a)	6201-34099
Liquid phase	Diesel
Liquid fuel mass flow rate ($\dot{m}_f$)	0.14 g/s
Liquid exit velocity (V_f)	0.83 m/s
Liquid Reynolds number (Re_f)	128
Air/liquid ratio (ALR)	1-6
Weber number (We)	62-1907

Operating conditions for reacting spray

The main bulk swirling air flow is preheated to a temperature of 350 °C while the liquid fuel and atomizing air are delivered to the atomizer at room temperature. The interaction of the swirling air flow with the liquid spray forms a globally lean mixture. To compare the combustion characteristics of the fuels, the flames are established at the same power output condition. The air and fuel mass flow rates are metered accordingly based on the fuels energy content to obtain the burner power output at 6 kW while maintaining the global equivalence ratio of $\phi = 0.47$. The atomizing air-to-fuel mass flow rate ratio (ALR) is set constant at 2.0 for all test cases. The operating conditions are shown in Table 4.4 for the respective fuels. Measurements were taken at axial positions of y = 10, 15 and 20 mm downstream of the burner outlet as indicated in Fig. 4.9b. Locations close to the spray outlet were not measured as the dense spray region may cause the PDA measurements to be unreliable. A minimum of 2000 data points were taken for each spatial point along the radial profiles. The general PDA setup relative to the swirl burner is shown in Fig. 4.10

112

Table 4.4: Operating conditions under the same power output

Fuel	φ	AFR	Air (g/s)	Atomizing air (g/s)	Fuel (g/s)	Power (kW)
Diesel	0.47	31.80	4.15	0.28	0.14	6.0
Jet-A1	0.47	31.42	4.09	0.28	0.14	6.0
PME	0.47	26.75	4.04	0.32	0.16	6.0
RME	0.47	26.75	4.04	0.32	0.16	6.0
*B50/RB50	0.47	28.35	3.96	0.30	0.15	6.0
*D50/RD50	0.47	28.38	3.96	0.30	0.15	6.0

*B50=50% PME/50% Jet-A1; RB50=50% RME/50% Jet-A1;
  D50=50% PME/50% Diesel ; RD50=50% RME/50% diesel
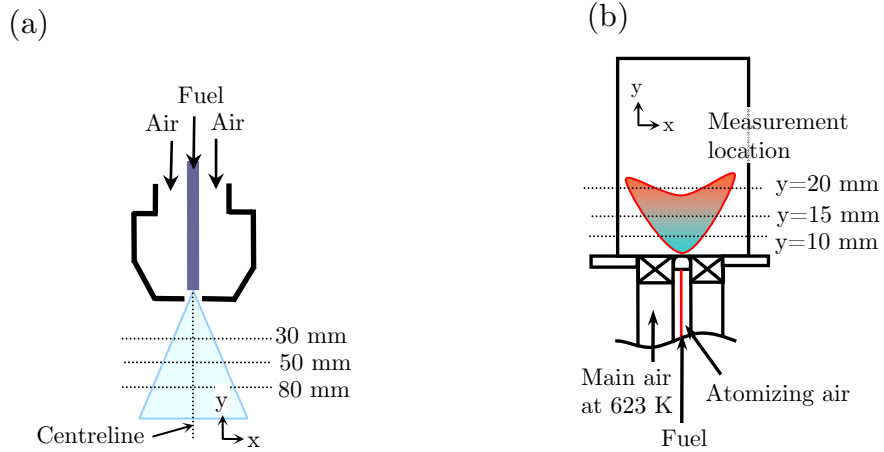
Figure 4.9: Locations where the PDA measurements were taken for the (a) non-reacting spray and (b) reacting spray in a swirl burner
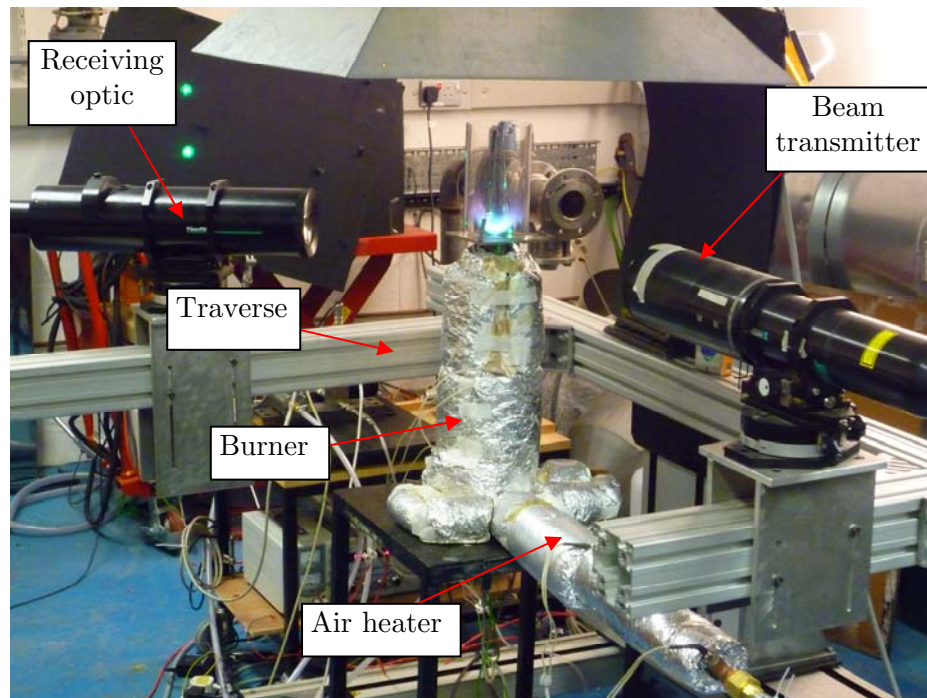
Figure 4.10: Setup for PDA measurements

4.6.2 Particle imaging velocity (PIV)

For PIV measurements, the total bulk flow of air is split into two lines, of which about 90 % is passed through the air heater, while the remaining 10 % is used for PIV seeding. The seeding air line is controlled using an Alicat® MFC which delivers a full scale accuracy of ± 1 %. PIV seeding is performed by using oil droplets and solid particles as flow tracking particles for non-reacting and reacting flow respectively. The submicron olive oil droplets are generated using a nebuliser whereas the solid particles are seeded into the main flow using an in-house fluidized bed seeder. The solid particle used in reacting flame is hydrophobic AEROSIL Amorphous Silica R812 S with a size distribution in submicron range (~ 0.3-0.4 μm) and a density of 0.05 g/cm³.

A 2D PIV system (La Vision) is utilised to characterise the flow field within the combustor under reacting and non-reacting flows. The laser energy used in this experiment is 20-30 mJ at 532 nm with ~4 ns pulse width for flows. The timing between the pulses (~ 80-150 μs) is chosen to allow sufficient particle movements over one quarter of the interrogation windows. Description of the PIV setup is shown in section 2.6.4 and 2.6.5, Chapter 2.

Operating conditions for PIV

The flow fields at the burner outlet are investigated under non-reacting and reacting conditions. For non-reacting flows, the flow fields are measured with and without enclosure. The effect of flow rate variation and temperature on the burner flow field are examined at open air condition without a spray. For the swirling spray flow, the main air flow temperature is maintained at T = 20 ºC and 350 ºC. The reacting flow field in the combustor is investigated for spray flame established from diesel, Jet-A1, RME and PME. The operating conditions for the non-reacting flow are shown in Table 4.5. The reacting flow operating flow field is shown in Table 4.4, excluding the blends.

Table 4.5: Operating flow rate for non-reacting flow

Flow at burner outlet	Condition	Main air (g/s)	Atomizing air (g/s)	Fuel (g/s)
Air flow	Unconfined	4.36	-	-
Air flow + Spray	Unconfined	4.36	0.28	0.14
Air flow	Confined	4.36	-	-
Air flow + Spray	Confined	4.36	0.28	0.14

4.6.3 Chemiluminescence imaging

Chemiluminescence imaging of OH* and CH* is performed on the swirling spray flames using an intensified CCD camera (La Vision®). A UV lens is used with a bandpass filter centred at 308 ± 10 nm and 430 ± 10 nm for OH* and CH* imaging respectively. The gain of the intensifier for OH* and CH* chemiluminescence is set to 85 % and 80 % respectively, and the gate delay time is set to 80 µs. To image the sooty region of the flames, a 60 mm/F5.6 Nikkor lens fitted with a long bandpass filter (Thorlab; FEL0500) with the cutoff wavelength of > 550 nm is used with the CCD camera. The intensified CCD camera is focused on the side of the swirl burner as shown in Fig. 4.11. A spectrometer (USB2000+; Ocean Optics) is used to derive the spectrally resolved flame spectrum. The time-averaged spectra are obtained with an integration time of 1s and the signal-to-noise ratio of > 10.
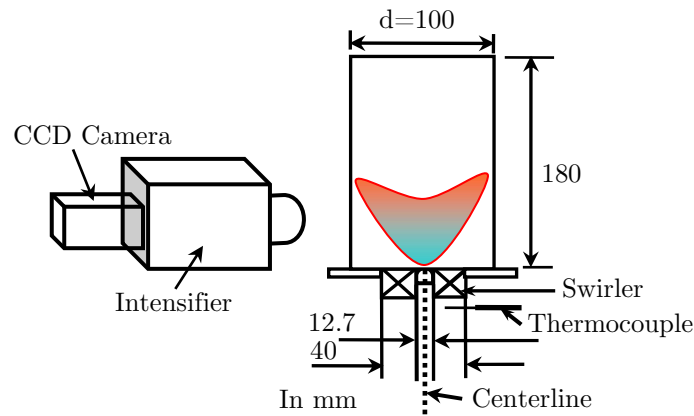
Figure 4.11: Schematic of the flame imaging experiment

Operating conditions for chemiluminescence imaging

The chemiluminescence imaging is performed under the condition of same fuel mass flow rate and same burner power output. The operating flow rates for the same power output condition is shown in Table 4.4, while the fuel and flow rates for the same fuel mass flow rate condition is shown in Table 4.6.

Table 4.6: Operating conditions

Same fuel mass flow rate						
Fuel	ϕ	AFR	Air (g/s)	Atomizing air (g/s)	Fuel (g/s)	Power (kW)
Diesel	0.47	31.8	4.14	0.28	0.14	6.0
Jet-A1	0.47	31.4	4.08	0.28	0.14	6.0
PME	0.47	26.8	3.44	0.28	0.14	5.1
RME	0.47	26.8	3.44	0.28	0.14	5.1
D50*	0.47	28.4	3.66	0.28	0.14	5.5

* D50 represents 50 % PME/50 % diesel

4.6.4 Emissions measurement

The sampling probe is placed 10 mm inwards from the combustor outlet to sample across the burner exit at locations as indicated in Fig. 4.12. The inlet diameter of the sampling tube is 4 mm and the sampling gas volume is around 6 L/min. By placing the sampling probe on a stepper motor-controlled traverse, the emission measurements can be performed and repeated at the defined locations. The sampling line is heated to the temperature of 180 ℃ and insulated to prevent condensation of post-combustion products. For each spatial location, the probe samples for two minutes to allow the readings to settle under steady state condition. Prior to measurements, the gas analyzer is calibrated with calibration gases.
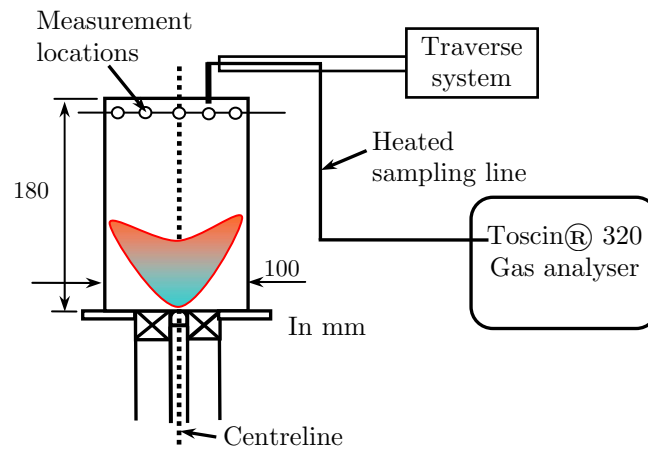
Figure 4.12: Schematic of the setup for emissions measurement

The post-combustion emissions of CO, CO_2, NO, NO_2 and O_2 were measured using a Tocsin 320® gas analyzer at the combustor outlet. The detection of CO, NO, NO_2 and O_2 is based on the electrochemical principle, where the gas diffused into the sensor reacts with the electrodes selectively depending on the targeted gas. The current generated from the electrodes is proportional to the concentration of gas. The CO_2 is measured via an infra red sensing technique. The infrared energy in the sampling chamber will be absorbed by targeted gas and the response is related to the concentration of the gas.

Operating conditions for emissions measurements

Emission measurements were performed on spray flames established from diesel, Jet-A1, PME, RME and blends under continuous, steady state conditions. The main swirling air was preheated to 350 ℃ prior to mixing with the liquid fuel spray. The flames were established at lean conditions under the same power output (Table 4.4). The emissions were also measured as a function of the burner power output and atomizing air-to-fuel mass ratio (ALR).

4.7 Conclusion

The previous studies on the atomization characteristics of the airblast atomizer are reviewed in this chapter. To extend the spray investigation in reacting flow conditions, the review on the swirling spray combustion is conducted, followed by the description of the experimental setup for the non-reacting and reacting spray experiments. The reacting spray flame is investigated using a generic gas turbine combustor. Several diagnostic techniques are applied to investigate the characteristics of droplets, flow field, reaction zone and emissions in the combustor. The operating conditions for each of the measurement techniques are presented.

4.8 References

[1]   X. Jiang, G. A. Siamas, K. Jagus, and T. G. Karayiannis, "Physical modelling and advanced simulations of gas-liquid two-phase jet flows in atomization and sprays," *Prog. Energy Combust. Sci.*, vol. 36, pp. 131-167, (2010).

[2]   R. D. Reitz and F. V. Bracco, "Mechanism of atomization of a liquid jet," *Physics of Fluids*, vol. 25, pp. 1730-1742, (1982).

[3]   G. M. Faeth, "Structure and atomization properties of dense turbulent sprays," *Symp. (Int.) Combust.*, vol. 23, pp. 1345-1352, (1991).

[4]   A. H. Lefebvre, *Atomization and sprays*: Taylor & Francis, 1989.

[5]   H. Eroglu and N. Chigier, "Initial drop size and velocity distributions for airblast coaxial atomizers," *J. Fluids Eng.*, vol. 113, pp. 453-459, (1991).

[6]   Z. Farago and N. Chigier, "Morphological classification of disintegration of round liquid jets in a coaxial air stream," *Atomization and Sprays*, vol. 2, pp. 137-153, (1992).

[7]   C. M. Varga, J. C. Lasheras, and E. J. Hopfinger, "Initial breakup of a small-diameter liquid jet by a high-speed gas stream," *J. Fluid Mech.*, vol. 497, pp. 405-434, (2003).

[8]   C. Engelbert, Y. Hardalupas, and J. H. Whitelaw, "Breakup phenomena in coaxial airblast atomizer," *Proc. R. Soc. London A*, vol. 451, pp. 189-229, (1995).

[9]   J. C. Lasheras and E. J. Hopfinger, "Liquid jet instability and atomization in a coaxial gas stream," *Ann. Rev. Fluid Mech.*, vol. 32, pp. 275-308, (2000).

[10]   A. H. Lefebvre, "Airblast atomization," *Prog. Energy Combust. Sci.*, vol. 6, pp. 233-261, (1980).

[11]   S. Nukiyama and Y. Tanasawa, "Experiments on the atomization of liquid in an airstream," *Trans.Soc, Mech. Engrs. Japan*, vol. 5, pp. 68-75, (1939).

[12]   G. E. Lorenzetto and A. H. Lefebvre, "Measurements of drop size on a plain jet airblast atomization," *AIAA J.*, vol. 15, pp. 1006-1010, (1977).

[13] N. K. Rizk and A. H. Lefebvre, "Spray characteristics of plain-jet airblast atomization," *J. Eng. Gas Turb. Power*, vol. 106, pp. 634-638, (1984).

[14] H. Liu, W. Li, X. Gong, X. Cao, J. Xu, X. Chen, Y. Wang, G. Yu, F. Wang, and Z. Yu, "Effect of liquid jet diameter on performance of coaxial two-fluid airblast atomizers," *Chem. Eng. Proc.*, vol. 45, pp. 240-245, (2006).

[15] J. E. Beck, A. H. Lefebvre, and T. R. Koblish, "Airblast atomization at conditions of low air velocity," *J. Prop. Power*, vol. 7, pp. 207-212, (1991).

[16] J. Kamrak, B. Kongsombut, G. Grehan, S. Saengkaew, K.-S. Kim, and T. Charinpanitkul, "Mechanistic study on spraying of blended biodiesel using phase Doppler anemometry," *Biomass and Bioenergy*, vol. 33, pp. 1452-1457, (2009).

[17] S. H. Park, H. J. Kim, H. K. Suh, and C. S. Lee, "Experimental and numerical analysis of spray-atomization characteristics of biodiesel fuel in various fuel and ambient temperatures conditions," *Intl. J. Heat Fluid Flow*, vol. 30, pp. 960-970, (2009).

[18] H. J. Kim, S. H. Park, and C. S. Lee, "A study on the macroscopic spray behaviour and atomization chatacteristics of biodeisel and dimethyl ester sprays under increased ambient pressure," *Fuel Proc. Technol.*, vol. 91, pp. 354-363, (2010).

[19] N. A. Chigier and C. G. McCreath, "Combustion of droplets in sprays," *Acta Astronautica*, vol. 1, pp. 687-710, (1974).

[20] N. Syred and J. M. Beér, "Combustion in swirling flows: A review," *Combust. Flame*, vol. 23, pp. 143-201, (1974).

[21] G. M. Faeth, "Evaporation and combustion of sprays," *Prog. Energy Combust. Sci.*, vol. 9, pp. 1-76, (1983).

[22] D. G. Lilley, "swirl flows in combustion: A review," *AIAA J.*, vol. 15, pp. 1063-1078, (1977).

[23] L. D. Smoot and S. C. Hill, "Critical requirements in combustion research," *Prog. Energy Combust. Sci.*, vol. 9, pp. 77-103, (1983).

[24] C. G. McCreath and N. A. Chigier, "Liquid-spray burning in the wake of a stabilizer disc," *Symp. (Intl.) Combust.*, vol. 14, pp. 1355-1363, (1973).

[25] F. Beretta, A. Cavaliere, and A. D'Alessio, "Ensemble laser light scattering diagnostics for the study of fuel sprays in isothermal and burning conditions," *Symp. (Intl.) Combust.*, vol. 20, pp. 1249-1258, (1985).

[26] C. F. Edwards and R. C. Rudoff, "Structure of a swirl-stabilized spray flame by imaging, laser doppler velocimetry, and phase doppler anemometry," *Symp. (Intl.) Combust.*, vol. 23, pp. 1353-1359, (1991).

[27] C. Presser, A. K. Gupta, and H. G. Semerjian, "Aerodynamic characteristics of swirling spray flames: Pressure-jet atomizer," *Combust. Flame*, vol. 92, pp. 25-30, IN1-IN2, 31-44, (1993).

[28] K. Komiyama, R. C. Flagan, and J. B. Heywood, "The influence of droplet evaporation on fuel-air mixing rate in a burner," *Symp. (Intl.) Combust.*, vol. 16, pp. 549-560, (1977).

[29] Y. E. Banhawy and J. H. Whitelaw, "Experimental study of the interaction between a fuel spray and surrounding combustion air," *Combust. Flame*, vol. 42, pp. 253-275, (1981).

[30] A. J. Yule, C. Ah Seng, P. G. Felton, A. Ungut, and N. A. Chigier, "A study of vaporizing fuel sprays by laser techniques," *Combust. Flame*, vol. 44, pp. 71-84, (1982).

[31] K. V. L. Rao and A. H. Lefebvre, "Evaporation characteristics of kerosine sprays injected into a flowing air stream," *Combust. Flame*, vol. 26, pp. 303-309, (1976).

[32] J. S. Chin, R. Durret, and A. H. Lefebvre, "The Interdependene of Spray Characteristics and Evaporation History of fuel sprays," *J. Eng. Gas Turb. Power*, vol. 106, pp. 639-644, (1984).

[33] F. K. Owen, L. J. Spadaccini, J. B. Kennedy, and C. T. Bowman, "Effects of inlet air swirl and fuel volatility on the structure of confined spray flames," *Symp. (Intl.) Combust.*, vol. 17, pp. 467-473, (1979).

[34] V. G. McDonell and G. S. Samuelsen, "Effect of fuel injection mode on fuel vapor in reacting and non-reacting methanol sprays," *Symp. (Intl.) Combust.*, vol. 24, pp. 1557-1564, (1992).

[35] R. J. Sornek, R. Dobashi, and T. Hirano, "Effects of turbulence on dispersion and vaporization of droplets in spray combustion," *Proc. Combust. Inst.*, vol. 28, pp. 1055-1062, (2000).

[36] R. Aftel, A. K. Gupta, C. Cook, and C. Presser, "Gas property effects on droplet atomiation and combustion in an air-assist atomier," *Symp. (Intl.) Combust.*, vol. 26, pp. 1645-1651, (1996).

[37] N. A. Chigier, C. G. McCreath, and R. W. Makepeace, "Dynamics of droplets in burning and isothermal kerosene sprays," *Combust. Flame*, vol. 23, pp. 11-16, (1974).

[38] M. Ghaffarpour and B. Chehroudi, "Experiments on Spray Combustion in a Gas Turbine Model Combustor," *Combust. Sci. Technol.*, vol. 92, pp. 173 - 200, (1993).

[39] C. Presser, A. K. Gupta, C. T. Avedisian, and H. G. Semerjian, "Fuel property effects on the structure of spray flames," *Symp. (Intl.) Combust.*, vol. 23, pp. 1361-1367, (1991).

[40] J. T. Hodges, C. Presser, A. K. Gupta, and C. T. Avedisian, "Analysis of droplet arrival statistics in a pressure-atomized spray flame," *Symp. (Intl.) Combust.*, vol. 25, pp. 353-361, (1994).

[41] Y. Onuma and M. Ogasawara, "Studies on the structure of a spray combustion flame," *Symp. (Intl.) Combust.*, vol. 15, pp. 453-465, (1975).

[42] Y. Onuma, M. Ogasawara, and T. Inoue, "Further experiments on the structure of a spray combustion flame," *Symposium (International) on Combustion*, vol. 16, pp. 561-567, (1977).

[43] C.-P. Mao, G. Wang, and N. Chigier, "An experimental study of air-assist atomizer spray flames," *Symp. (Intl.) Combust.*, vol. 21, pp. 665-673, (1988).

[44] V. G. McDonell and S. Samuelsen, "Gas and dropl behaviour in reacting and non-reacting air-blast atomizer sprays," *J. Prop. Power*, vol. 7, pp. 684-691, (1991).

[45] A. C. Styles and N. A. Chigier, "Combustion of air blast atomized spray flames," *Symp. (Intl.) Combust.*, vol. 16, pp. 619-630, (1977).

[46] R. Hadef and B. Lenze, "Measurements of droplets characteristics in a swirl-stabilized spray flame," *Exp. Ther. Fluid Sci.*, vol. 30, pp. 117-130, (2005).

[47]   V. Tangirala, R. H. Chen, and J. F. Driscoll, "Effect of heat release and swirl on the recirculatioin within swirl-stabilized flames," *Combust. Sci. Technol.*, vol. 51, pp. 75-95, (1987).

[48]   H. N. Najm, P. H. Paul, C. J. Mueller, and P. S. Wyckoff, "On the adequacy of certain experimental observables as measurements of flame burning rate," *Combust. Flame*, vol. 113, pp. 312-332, (1998).

[49]   Y. Hardalupas and M. Orain, "Local measurements of the time-dependent heat release rate and equivalence ratio using chemiluminescent emission from a flame," *Combust. Flame*, vol. 139, pp. 188-207, (2004).

[50]   O. Delabroy, E. Haile, F. Lacas, S. Candel, A. Pollard, A. Sobiesiak, and H. A. Becker, "Passive and active control of NOx in industrial burners," *Exp. Therm. Fluid Sci.*, vol. 16, pp. 64-75, (1998).

[51]   Y. Ikeda, J. Kojima, T. Nakajima, F. Akamatsu, and M. Katsuki, "Measurement of the local flamefront structure of turbulent premixed flames by local chemiluminescence," *Proc. Combust. Inst.*, vol. 28, pp. 343-350, (2000).

[52]   R. B. Price, I. R. Hurle, and T. M. Sugden, "Optical studies of the generation of noise in turbulent flames," *Symp. (Intl.) Combust.*, vol. 12, pp. 1093-1102, (1969).

[53]   J. Diederichsen and R. D. Gould, "Combustion instability: Radiation from premixed flames of variable burning velocity," *Combust. Flame*, vol. 9, pp. 25-31, (1965).

[54]   B. Higgins, M. Q. McQuay, F. Lacas, J. C. Rolon, N. Darabiha, and S. Candel, "Systematic measurements of OH chemiluminescence for fuel-lean, high-pressure, premixed, laminar flames," *Fuel*, vol. 80, pp. 67-74, (2001).

[55]   J. O. Keller and K. Saito, "Measurements of the combusting flow in a pulse combustor," *Combust. Sci. Technol.*, vol. 53, pp. 137 - 163, (1987).

[56]   H. Buechner, C. Hirsch, and W. Leuckel, "Experimental investigations on the dynamics of pulsated premixed axial jet flames," *Combust. Sci. Technol.*, vol. 94, pp. 219 - 228, (1993).

[57]   K. T. Padmanabhan, C. T. Bowman, and J. D. Powell, "An adaptive optimal combustion control strategy," *Combust. Flame*, vol. 100, pp. 101-110, (1995).

[58]   C. J. Lawn, "Distributions of instantaneous heat release by the cross-correlation of chemiluminescent emissions," *Combust. Flame*, vol. 123, pp. 227-240, (2000).

[59]   T. Lieuwen and Y. Neumeier, "Nonlinear pressure-heat release transfer function measurements in a premixed combustor," *Proc. Combust. Inst.*, vol. 29, pp. 99-105, (2002).

[60]   K. K. Venkataraman, L. H. Preston, D. W. Simons, B. J. Lee, J. G. Lee, and D. A. Santavicca, "Mechanism of combustion instability in a lean premixed dump combustor," *J. Prop. Power*, vol. 15, pp. 909-918, (1999).

[61]   J. C. Broda, S. Seo, R. J. Santoro, G. Shirhattikar, and V. Yang, "An experimental study of combustion dynamics of a premixed swirl injector," *Symp. (Intl.) Combust.*, vol. 27, pp. 1849-1856, (1998).

[62]   B. Higgins, M. Q. McQuay, F. Lacas, and S. Candel, "An experimental study on the effect of pressure and strain rate on CH chemiluminescence of premixed fuel-lean methane/air flames," *Fuel*, vol. 80, pp. 1583-1591, (2001).

[63]   I. R. Hurle, R. B. Price, T. M. Sugden, F.R.S., and A. Thomas, "Sound emission from open turbulent premixed flames," *Proc. Royal Soc. A*, vol. 303, pp. 409-427, (1968).

[64] J. G. Lee and D. A. Santavicca, "Experimental diagnostics for the study of combustion instabilies in lean premixed combustor," *J. Prop. Power*, vol. 19, pp. 735-750, (2003).

[65] H. N. Najm, O. M. Knio, P. H. Paul, and P. S. Wyckoff, "A study of flame observables in premixed methane-air flames," *Combust. Sci. Technol.*, vol. 140, pp. 369 - 403, (1998).

[66] D. S. Dandy and S. R. Vosen, "Numerical and Experimental Studies of Hydroxyl Radical Chemiluminescence in Methane-Air Flames," *Combust. Sci. Technol.*, vol. 82, pp. 131 - 150, (1992).

[67] J. Kojima, Y. Ikeda, and T. Nakajima, "Spatially resolved measurement of OH*, CH*, and C2* chemiluminescence in the reaction zone of laminar methane/air premixed flames," *Proc. Combust. Inst.*, vol. 28, pp. 1757-1764, (2000).

[68] N. Docquier, F. Lacas, and S. Candel, "Closed-loop equivalence ratio control of premixed combustors using spectrally resolved chemiluminescence measurements," *Proc. Combust. Inst.*, vol. 29, pp. 139-145, (2002).

[69] T. M. Muruganandam, B. H. Kim, M. R. Morrell, V. Nori, M. Patel, B. W. Romig, and J. M. Seitzman, "Optical equivalence ratio sensors for gas turbine combustors," *Proc. Combust. Inst.*, vol. 30, pp. 1601-1609, (2005).

[70] R. V. Bandaru, S. Miller, J. G. Lee, and D. A. Santavicca, "Sensors for measuring primary zone equivalence ratio in gas turbine combustors," in *Advanced sensors and monitors for process industries and the environment*, Boston, MA, USA, 1999.

[71] L. Arias, S. Torres, D. Sbarbaro, and P. Ngendakumana, "On the spectral bands measurements for combustion monitoring," *Combust. Flame*, vol. In Press, Corrected Proof, (2011).

[72] Y. Ikeda, J. Kojima, and H. Hashimoto, "Local chemiluminescence spectra measurements in a high-pressure laminar methane/air premixed flame," *Proc. Combust. Inst.*, vol. 29, pp. 1495-1501, (2002).

[73] M. Arai, T. Saito, and T. Furuhata, "Effect of biodiesel fuel on direct injection diesel engine performance," *J. Prop. Power*, vol. 24, pp. 603-608, (2008).

[74] A. Weall and N. Collings, "Highly homogenous compression ignition in a direct injection diesel engine fuelled with diesel and biodiesel," *J. Fuels Lubricants*, vol. 116, pp. 646-660, (2007).

[75] M. N. Nabi, M. S. Akhter, and M. M. Zaglul Shahadat, "Improvement of engine emissions with conventional diesel fuel and diesel-biodiesel blends," *Bioresource Technol.*, vol. 97, pp. 372-378, (2006).

[76] M. Canakci, "Combustion characteristics of a turbocharged DI compression ignition engine fueled with petroleum diesel fuels and biodiesel," *Bioresource Technol.*, vol. 98, pp. 1167-1175, (2007).

[77] D. AltIparmak, A. Keskin, A. Koca, and M. Gürü, "Alternative fuel properties of tall oil fatty acid methyl ester-diesel fuel blends," *Bioresource Technol.*, vol. 98, pp. 241-246, (2007).

[78] D. H. Qi, L. M. Geng, H. Chen, Y. Z. Bian, J. Liu, and X. C. Ren, "Combustion and performance evaluation of a diesel engine fueled with biodiesel produced from soybean crude oil," *Renew. Energy*, vol. 34, pp. 2706-2713, (2009).

[79]   H. Aydin and C. IlkIllç, "Effect of ethanol blending with biodiesel on engine performance and exhaust emissions in a CI engine," *Appl. Thermal Eng.*, vol. 30, pp. 1199-1204, (2010).

[80]   B. Kegl, "Influence of biodiesel on engine combustion and emission characteristics," *Appl. Energy*, vol. 88, pp. 1803-1812, (2011).

[81]   C. D. Bolszo and V. G. McDonell, "Emissions optimization of a biodiesel fired gas turbine," *Proc. Combust. Inst.*, vol. 32, pp. 2949-2956, (2009).

[82]   V. Lupandin, R. Thamburaj, and A. Nikolayev, "Test results of the OGT2500 gas turbine engine running on alternative fuels: biooil, ethanl, biodiesel, and crude oil," in *ASME Turbo Expo 2005:Power for land, sea, and air*, Reno, Nevada, USA, 2005, pp. Paper No. GT2005-68488 pp. 421-426.

[83]   H. D. Chiang, I. Chiang, and H. Li, "Performance testing of microturbine generator system fuel by biodiesel," in *ASME Turbo Expo 2007: Power for land, sea, and air*, Motreal, Canada, 2007, pp. Paper no. GT2007-28075 pp. 459-466.

[84]   M. Molière, E. Panarotto, M. Aboujaib, J. M. Bisseaud, A. Campbell, J. Citeno, P. Maire, and L. Ducrest, "Gas turbine in alternative fuel applications: biodiesel field test," in *ASME Turbo Expo 2007: Power for land, sea, and air*, Montreal, Canada, 2007, pp. Paper no. GT2007-27212 pp. 397-406.

[85]   P.-A. Glaude, R. Fournet, R. Bounaceur, and M. Molière, "Adiabatic flame temperature from biofuels and fossil fuels and derived effect on NOx emissions," *Fuel Proc. Technol.*, vol. 91, pp. 229-235, (2010).

[86]   W. Ellis, W. Lear, B. Singh, A. Srinivasan, J. Crittenden, and S. Sherif, "Flameless combustion of biofuels in a semi-closed cycle gas turbine," in *46th AIAA Aerospace Sciences Meeting and Exhibition*, Reno, Nevada, 2008.

[87]   C. R. Krishna, "Performance of the capstone C30 microturbine on biodiesel blends," Brookhaven National Laboratory (2007).

[88]   M. A. R. Nascimento, E. S. Lora, P. S. P. Corrêa, R. V. Andrade, M. A. Rendon, O. J. Venturini, and G. A. S. Ramirez, "Biodiesel fuel in diesel micro-turbine engines: Modelling and experimental evaluation," *Energy*, vol. 33, pp. 233-240, (2008).

[89]   Z. Habib, R. Parthasarathy, and S. Gollahalli, "Performance and emission characteristics of biofuel in a small-scale gas turbine engine," *Appl. Energy*, vol. 87, pp. 1701-1709, (2010).

[90]   M. J. Ramotowski, R. J. Roby, L. D. Eskin, and M. S. Klassen, "Fuel flexibility for dry low emission gas turbines-cleanly burning biofuels, coal liquids and petroleum fuels," in *PowerGen International 2007* New Orleans, LA, 2007.

[91]   D. Sequera, A. K. Agrawal, S. K. Spear, and D. T. Daly, "Combustion performance of liquid biofuels in a swirl-stabilized burner," *J. Eng. Gas Turb. Power*, vol. 130, pp. 032810.1-032810.10, (2008).

[92]   H. V. Panchasara, B. M. Simmons, A. K. Agrawal, S. K. Spear, and D. T. Daly, "Combustion performance of biodiesel and diesel-vegetable oil blends in a simulated gas turbine burner," *J. Eng. Gas Turb. Power*, vol. 131, pp. 031503.1-031503.11, (2009).

[93]   N. Hashimoto, Y. Ozawa, N. Mori, I. Yuri, and T. Hisamatsu, "Fundamental combustion characteristics of palm methyl ester (PME) as alternative fuel for gas turbines," *Fuel*, vol. 87, pp. 3373-3378, (2008).

[94]   J. B. Zel'dovich, "Oxidation of nitrogen in combustion and explosion," *Comptes Rendus (Doklady) de l'Academiedes Sciences de l'URSS*, vol. 51, pp. 217-220, (1946).

[95]   G. A. Lavoie, "Spectroscopic measurements of nitric oxide in spark ignition engines," *Combust. Flame*, vol. 15, pp. 97-108, (1970).

[96]   I. Glassman, *Combustion*, 3rd ed.: Academic press, 1996.

[97]   C. P. Fenimore, "Formation of nitric oxide in premixed hydrocarbon flames," *Symp. (Intl.) Combust.*, vol. 13, pp. 373-380, (1971).

[98]   F. Bachmaier, K. H. Eberius, and T. Just, "The formation of nitric oxide and the detection of HCN in premixed hydrocarbon-air flames at 1 atmosphere," *Combust. Sci. Technol.*, vol. 7, pp. 77 - 84, (1973).

[99]   A. Levy, "Unresolved problems in SOx, NOx, soot control in combustion," *Symp. (Intl.) Combust.*, vol. 19, pp. 1223-1242, (1982).

[100]   K. K. Kuo, *Principles of combustion*, 2nd ed.: John Wiley & Sons, Inc., 2005.

[101]   J. M. Beer and N. A. Chigier, "Combustion aerodynamics," *Appl. Sci. Publ. Lond.*, (1972).

[102]   F. Durst and M. Zare, "Laser Doppler measurements in two-phase flows," in *Proceedings LDA-Symposium Copenhagen*, Copenhagen, Denmark, 1975, pp. 403-429.

[103]   W. D. Bachalo and M. J. Houser, "Phase/Doppler spray analyzer for simultaneous measurements of drop size and velocity distributions," *Opt. Eng.*, vol. 23, pp. 583-590, (1984).

Chapter 5

PDA results and discussion

In this chapter, the PDA results for the non-reacting spray are first presented, followed by the spray flame droplet characteristics in an enclosed swirl burner. The non-reacting spray experiment is performed to investigate the atomization characteristics of a plain-jet airblast atomizer. For the reacting spray experiment, the developed swirl burner employs the same atomizer for fuel atomization. The experimental setup, operating conditions for the PDA droplet characterisation are shown in chapter 4.

5.1 Non-reacting spray results

5.1.1 Effect of air/fuel mass ratio

5.1.1.1 Droplet size distribution

The variation of atomizing air/fuel mass ratio (ALR) is an effective control parameter to achieve low emissions in gas turbine combustor [1]. Here, the effect of ALR on droplet size distribution is examined. Sauter mean diameter (SMD) is defined as $SMD = \sum N_i D_i^3 / \sum N_i D_i^2$, where N_i and D_i are the number of drops and middle diameter of size range i respectively. SMD represents the diameter of the drop whose ratio of volume to surface area is the same as that of the entire spray. This notation is

of most relevant to spray combustion, as the mass transfer of fuel from liquid droplets is of interest, and will be adopted in this dissertation.
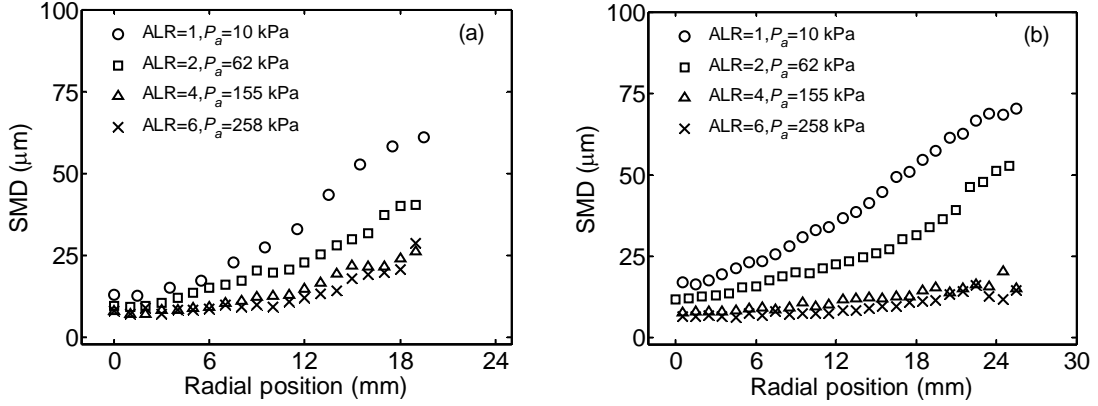
Figure 5.1: Droplet SMD profiles at the axial distance of (a) 30 mm and (b) 50 mm from atomizer tip.

The radial distributions of droplet SMD profiles on one side of the centreline (x = 0 mm) at downstream locations of y = 30 and 50 mm are shown in Fig. 5.1. The other half plane was measured and the symmetry of the spray structure was confirmed. Overall, the SMD values decreases with the increase of ALR. This is due to the increased relative velocity of air and liquid at high ALRs that assists in prompt atomization. The inverse relation of the droplet SMD with ALR concurs with the findings by previous investigators [2, 3]. Here, the radial variation of SMD shows that the difference in droplet SMD between different ALR is more pronounced near the spray boundary. This is due to the lower relative velocity at the spray periphery region that is insufficient to breakup the droplets. The increase of ALR reduces the SMD significantly, but a threshold exists where droplet SMD reduction is not obvious for high ALR. In particular, the increase of ALR from 4 to 6 shows insignificant reduction of SMD despite a 66 % increase in air supply pressure. The restricted reduction of SMD values at high ALR is due to the balance between the shear force due to relative flow velocity and the resistance for disintegration imposed by the liquid fuel.

The radial distributions of droplet SMD show lower values at the spray centre but gradually increase towards the spray boundary. Disintegration of the liquid jet into

droplets occurs rigorously at radii x = 0-6 mm for ALR = 1 and 2, but the lower relative velocity at radii x > 6 mm results in larger droplets. High ALRs of 4 and 6 provide sufficiently high relative velocity to disintegrate the droplets even at a downstream location of 50 mm, as observed in the relatively flat radial profile of SMD. The present result of the SMD profile shows a significantly different distribution compared to the result presented by Kamrak *et al.* [4]. In their twin-fluid atomizer investigation, it was reported that the droplet SMD profile (50 mm downstream) shows higher values at the centreline than those at the spray periphery, slightly different to the present result. The author explained that the higher concentration of droplets at the central area results in droplet collisions and hence the higher SMD values. This is possible considering the supplied air pressure (400 kPa) is higher than the current experiment (258 kPa at ALR = 6). Another factor that could result in the difference in SMD profiles is the internal geometry of the nozzle, which was not reported by Kamrak *et al.* [4]. It is noted that the impinging angle of the atomizing air on the liquid jet, the relative position of the fuel orifice to the air orifice, and the ratio of air/fuel orifice diameters could significantly affect the droplet distributions.

In another twin-fluid atomizer study conducted by Eroglu and Chigier [5], the radial distribution of SMD shows high SMD values at the centreline and towards the spray boundary. It was visualized using a fast camera that the liquid jet formed a ladle-shaped ligament at the atomizer outlet. The branching and subsequent break-up of the ligaments led to the breakup of droplets with the lowest SMD concentrating at the radial position between the spray centreline and spray periphery. The nozzle that they employed shows the fuel orifice is flush mounted with the air orifice outlet, resulting in no impinging angle by the atomizing air on the liquid jet. For the present atomizer, the fuel orifice outlet is placed slightly inward than the air outlet to enable the impingement of air on the liquid jet at an extreme angle, thus resulting in "prompt" atomization that falls under the fibre-type jet disintegration regime as shown in Fig. 4.3, Chapter 4.

5.1.1.2 Droplet mean velocity and RMS velocity distribution

The radial distributions of droplet axial mean axial velocity as a function of air supply pressure at the atomizer downstream positions of y = 30 and 50 mm are presented in Fig. 5.2a and 5.2b respectively. In general, the droplet mean velocities increase correspondingly to the increase of the ALR. The droplets exhibit their highest velocity at the centreline but slowly decrease towards the spray boundary. The profile shape obtained is similar to those shown by Kamrak *et al.* [4]. The slight increase of the velocity at the spray boundary (radii of x = 18 mm) could be due to the influence of air entrainment. As the axial distance from the atomizer outlet increases, the droplet momentum decreases, resulting in the reduction of mean velocity. The high droplet velocity at the centreline of the spray corresponds to the lowest SMD values, indicating the effect of a high relative velocity that results in smaller droplets. As the velocity approaches zero near the spray boundary, the droplet size increases. The high inertia of larger droplets imposes a drag force on the droplets that lower the relative velocity, whilst smaller droplets travel with high velocity with relatively low drag. Apart from lowering the droplet size by increasing the air supply pressure, the penetration length of the droplets is also increased.
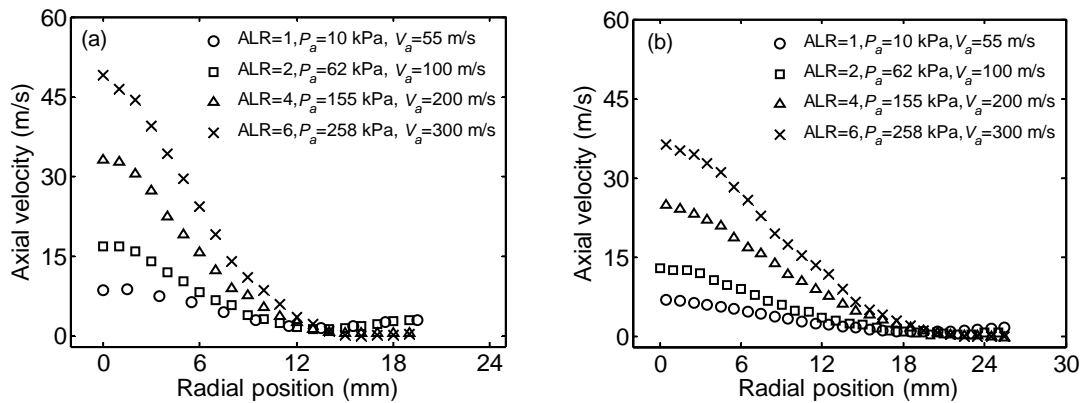
Figure 5.2: Droplet mean axial velocity profiles at the axial distance of (a) 30 mm and (b) 50 mm from the atomizer tip as a function of ALR.

The radial distributions of the droplet mean rms velocity at the downstream location of y = 50 mm is shown in Fig. 5.3a. In general, the rms values are highest for

smaller droplets at the centreline region for ALR = 2, 4 and 6 and slowly decrease towards the spray boundary. The small droplets at the spray centreline respond to the air velocity fluctuations more closely. For ALR = 1, the droplet rms is lower at the centreline but increases at the spray boundary, in particular beyond radii x = 18 mm. The increase of droplet velocity rms corresponds to the increase of atomizing air velocity or ALR. By dividing the drop velocity rms with respect to the axial velocity, the profiles show a characteristic shape which is independent of the air supply pressure as indicated in Fig. 5.3b. The profiles at the spray centreline region show low droplet velocity fluctuations but gradually increase towards the spray boundary. At radii x=18 mm and beyond, the irregularity of the droplet size and lower velocity imposes larger droplet fluctuations.
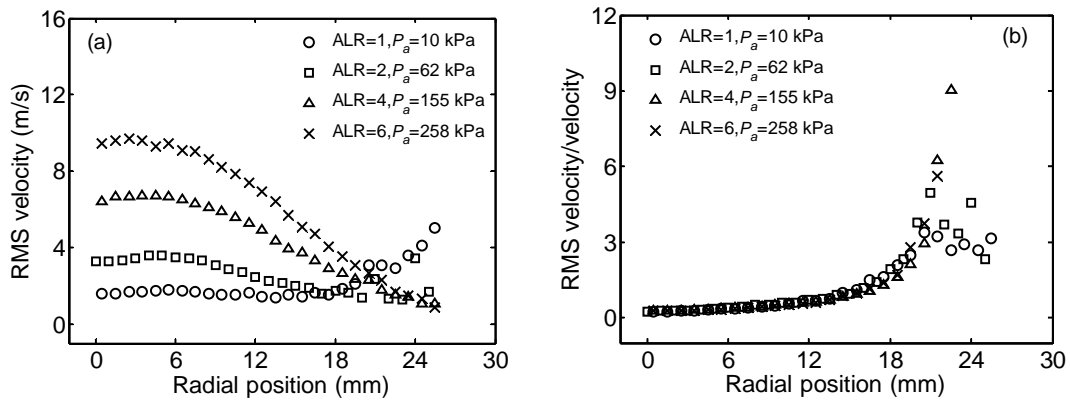
Figure 5.3: Droplet (a) rms axial velocity profiles and (b) rms velocity/velocity at the axial distance of 50 mm from the atomizer tip.

5.1.1.3 Droplet distribution and size-velocity correlations
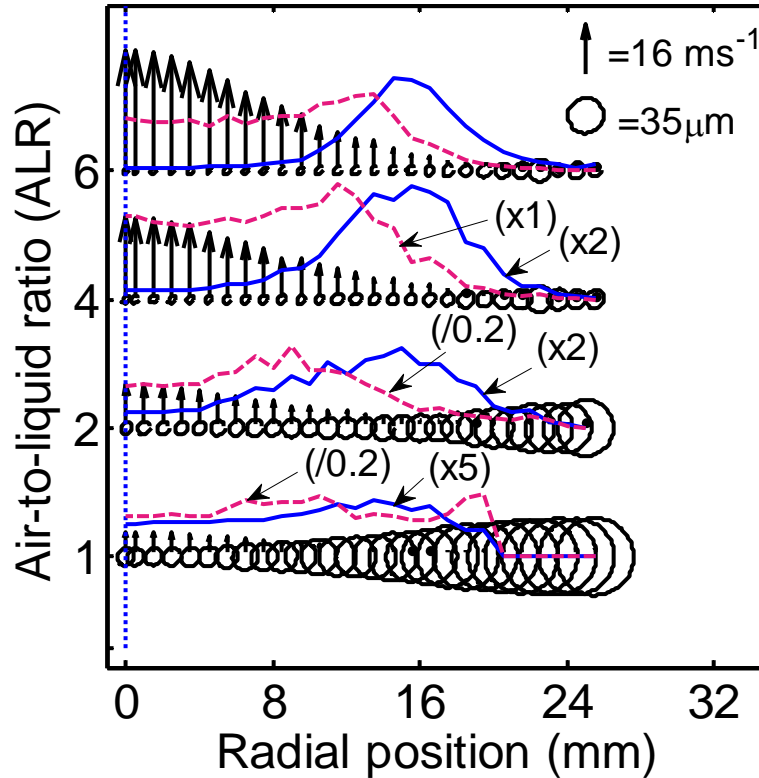
Figure 5.4: Radial distribution of droplet velocity ($\uparrow$), SMD (o), concentrations (—) [#/cm^3/s] and volumetric flux (---) [cm^3/cm^2/s] for different ALR at the axial location of 50 mm downstream of atomizer outlet. The droplet concentration and volumetric flux values are normalized to the peak value at ALR = 6.

Comparison of the radial distributions of the droplet size and velocity at different ALRs is shown in Fig. 5.4. The small droplets at the centreline region attain high velocity while the larger droplets at the spray boundary show low droplet velocity. The low droplet SMD values at higher ALRs are reflected in the smaller size of droplets compared to lower ALR. The radial profiles of the droplets concentration and volume flux are superimposed on the droplet distributions. The droplet number density and volume flux profiles are normalized to the respective maximum magnitude at ALR = 6. In general, the droplet number density profiles shows a peak biased towards the spray boundary compared to the profiles of droplet volume flux. The droplet distribution characteristics at the axial location y = 50 mm is similar to the profiles at y = 30 mm,

and hence only the profiles of y = 50 mm is shown here. From Fig. 5.4, the maximum droplet concentration locates at region x = 14-15 mm, as compared to the peak volume flux at radial locations x = 9-12 mm. The difference in spatial positions between the two profile peaks is due to the weighting effect of larger droplets. Larger droplets carry significantly higher mass than the smaller droplets. Despite the higher droplet density near the spray boundary, the peak flux is skewed away from the droplet density peaks as a result of the interaction between the droplet velocity and size. Smaller droplets with lower drag force are prone to accumulate at larger radii.

Although the liquid mass flow rates for each ALR cases are fixed constant at 0.14 g/s, the magnitudes of the droplet density and volume flux are different. The rigorous disintegration of the liquid jet at high ALR results in higher number of droplets than the lower ALR cases. The difference in droplet concentration between ALR = 1 and 6 is by a factor of approximately 5. However, the droplet volume flux shows a reverse trend in which the ALR = 1 shows higher magnitude than ALR = 6 by a factor of 5. Variation in the magnitude of volume flux is due to the difference in droplet size. At high ALR, the small droplets produced are prone to vaporisation due to the larger exposed surface area and the increased convective mass transfer of fuel to the quiescent environment.

Figure 5.5 shows the probability density function (PDF) of drop velocity and size at different ALRs at the radial position of x = 9 mm and y = 50 mm downstream of the atomizer outlet. The radii x = 9 mm corresponds to the region where the maximum volume flux is located, as shown in Fig. 5.4. At ALR = 1, the relatively lower velocity results in the skewed distribution of droplet diameter that is biased towards larger values. As the relative velocity between the gas and liquid phase increases as a result of higher ALR, the droplet diameter histogram shows a reduced presence of larger droplets. The droplet mean velocity typically shows a normal distribution for all conditions. The increase of ALR results in the increase of velocity magnitude and the wider spread of the mean velocity distribution.
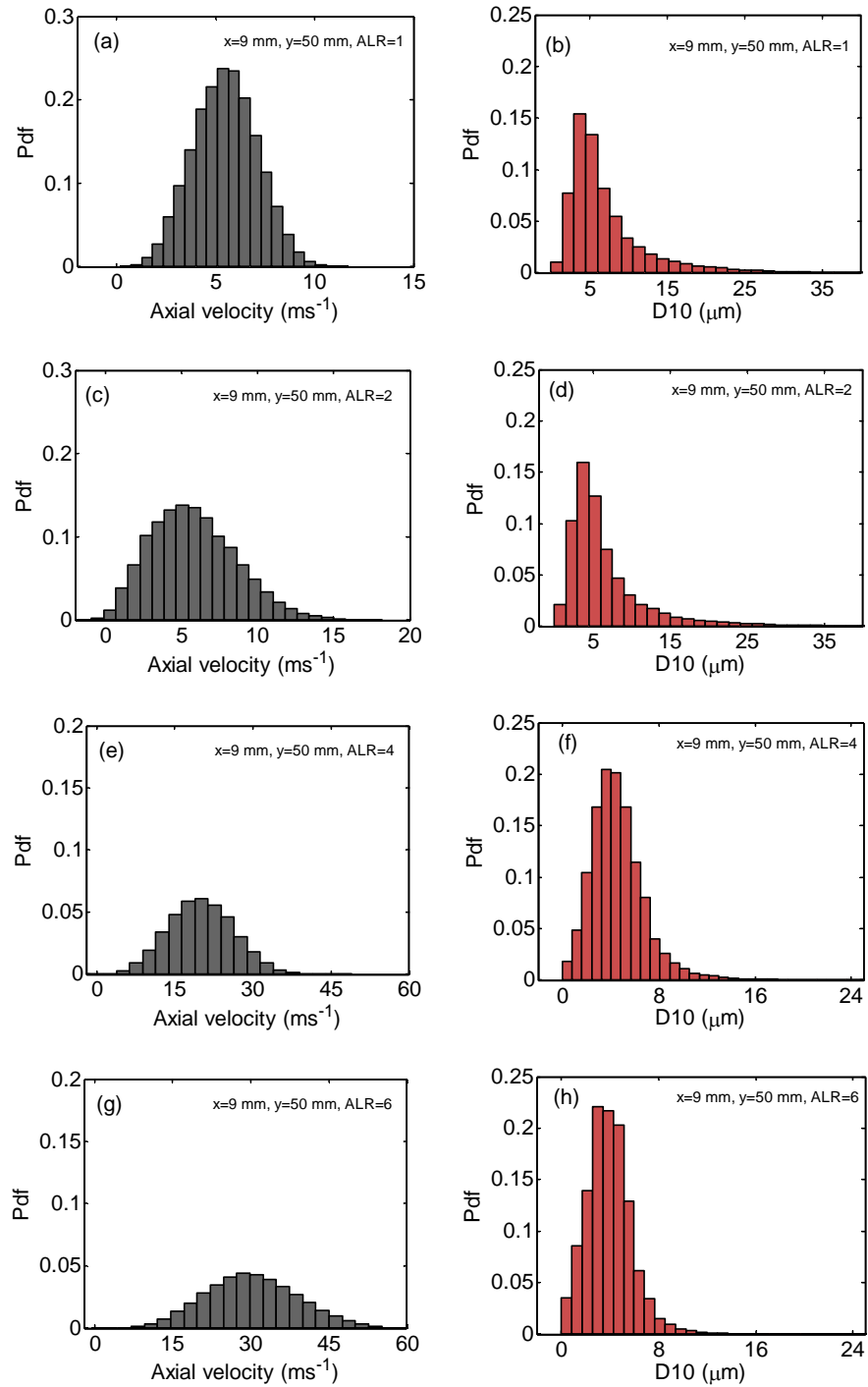
Figure 5.5: Probability density functions of droplet mean axial velocity (a,c,e,g) and diameter (b,d,f,h) at the radial position of 9 mm and downstream axial position of 50 mm for different ALR.

5.1.1.4 Spray centreline profiles

The spray centreline axial distribution of droplet velocity and SMD profiles using diesel fuel at different ALRs are shown in Fig. 5.6a and 5.6b respectively. The disintegrated droplets at the tip of atomizer attain high velocity, which decreases as the downstream axial distance increases due to the imposed drag force and loss of momentum. The initial droplet velocity depends on the supplied air pressure, which determines the relative velocity between the gas and liquid phases. At high ALR = 6, the droplets attain the velocity of 59 m/s compared to 19 m/s at the axial position of 20 mm. The velocity difference between the two conditions is by a factor of ~ 3 while the pressure drop difference is by a factor of ~ 4. The droplet size shows the inverse relation to ALR, where the high ALR = 6 shows the lowest droplet SMD values. At ALR = 2, the droplet SMD value increases from 10 μm to 15 μm between the downstream axial positions of 35 mm and 110 mm. The noticeable increase of droplet size with increasing downstream axial distance could be due to the entrainment of larger droplets from the spray boundary to the inner spray zone. The swirling atomizing air induces a radial pressure difference between the spray inner core and outer zone, and thus the entrained radial velocity transports the larger droplets inwards. Another possibility is the effect of droplet coalescence due to collisions between droplets or spatial dispersion of droplets in the spray [4, 6]. At ALR = 6, the distribution of droplets along the axial centreline is rather uniform. The increase of ALR results in higher relative velocity difference between liquid jet and atomizing air and hence provides the momentum and shearing force necessary for jet breakup into fine droplets. The high axial flow and the relatively weaker inward radial flow at high ALR provides insufficient force to entrain the droplets, and hence the increase of droplet size with the increasing axial distance is insignificant.
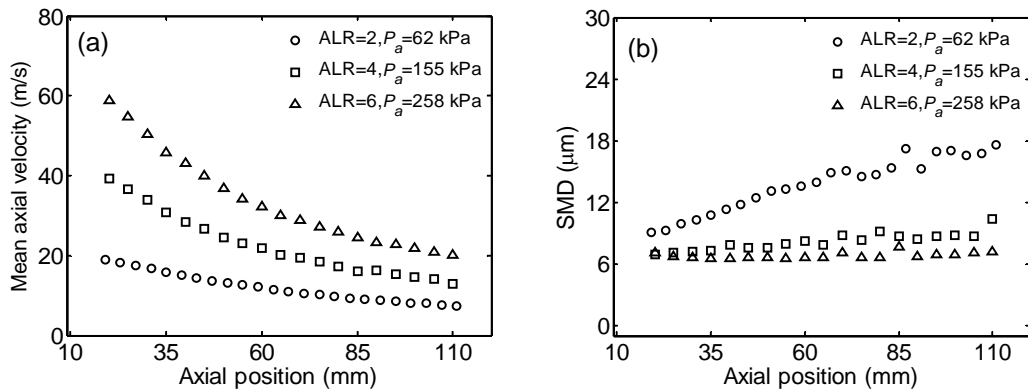
Figure 5.6: The spray centreline distribution of droplet (a) mean axial velocity profiles and (b) SMD at different ALR.

5.1.1.5 Droplet SMD correlations
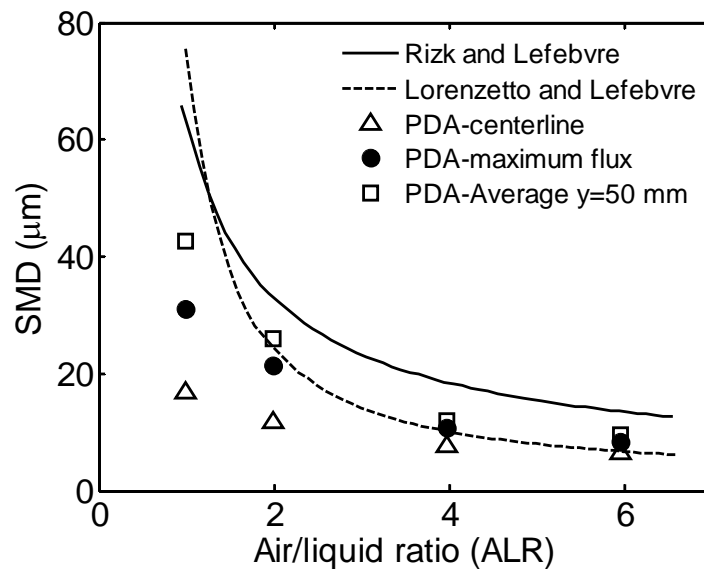
Figure 5.7: Comparison of the PDA-derived SMD measurements against the empirically-correlated values for diesel fuel.

The PDA-derived data for the profile of 50 mm downstream of spray outlet are compared to the empirical values derived from correlations developed by Lorenzetto and Lefebvre [2] and Rizk and Lefebvre [3]. The PDA data are presented in three forms; (i) the centreline droplet SMD value, (ii) the droplet SMD value at the location of

maximum flux and (iii) the averaged droplet SMD of the radial profile. The equation developed by Lorenzetto and Lefebvre is

$$D_{32} = 0.95 \left[\frac{\left(\sigma_L W_L\right)^{0.33}}{\rho_L^{0.37} \rho_A^{0.3} U_R} \right] \left(1 + \frac{1}{ALR}\right)^{1.70} + 0.13 \left(\frac{\mu_L^2 d_o}{\sigma_L \rho_L}\right)^{0.5} \left(1 + \frac{1}{ALR}\right)^{1.7} \qquad (4.1)$$

where D_{32} is Sauter mean diameter, σ is surface tension, μ is dynamic viscosity, W is the mass flow rate, ρ is the density, U_R is the relative velocity, d_o is the liquid orifice diameter whilst the subscript A and L represent air and liquid respectively. The SMD correlation was derived from low viscosity liquids and the SMD is independent of the initial jet diameter, d_o. Rizk and Lefebvre [3] developed an equation for SMD using a light scattering technique. The SMD correlation is expressed as

$$\frac{D_{32}}{d_o} = 0.48 \left(\frac{\sigma}{\rho_A U_R^2 d_o}\right)^{0.4} \left(1 + \frac{1}{ALR}\right)^{0.4} + 0.15 \left(\frac{\mu_L^2}{\sigma \rho_L d_o}\right)^{0.5} \left(1 + \frac{1}{ALR}\right) \qquad (4.2)$$

where ALR represents the atomizing air-to-liquid ratio. Comparison of the PDA-measured droplet SMD values with the empirical values is shown in Fig. 5.7. In general, the global trend shows that droplet size decreases with increasing ALR. The PDA-derived droplet SMD values at the centreline of the profile demonstrate the power dependence of -0.55 on ALR, ($D_{32} \propto ALR^{-0.55}$), while the droplet SMD at the location of the maximum volume flux shows the power dependence of -0.78 on ALR ($D_{32} \propto ALR^{-0.78}$). The SMD values at the location of maximum volume flux shows good agreement when compared to the droplet SMD values derived from the equation by Lorenzetto and Lefebvre [2], except for ALR = 1 which shows the lower PDA-derived droplet SMD by a factor of 2.4. The droplet SMD values obtained by averaging the radial profile of droplet SMD at location y = 50 mm shows a negative power dependence of -0.85 to ALR ($D_{32} \propto ALR^{-0.85}$). The SMD values are in good agreement with the empirical values predicted from the correlation by Lorenzetto and Lefebvre for ALR = 2 and above, but the droplet SMD is overpredicted at ALR = 1 by a factor of 2. Comparison to the correlated values of Rizk and Lefebvre [3] shows a systematic lower droplet SMD values across the whole ALR range.

It is noted that the empirical correlations developed using atomizers that are not completely geometrically similar to the present atomizer. Differences in atomizer

configuration such as the angle at which the atomizing air impinges on the liquid jet could have significant influence on the spray atomization. Besides, the empirical correlations were derived from light scattering technique that does not elucidate the information of droplet distribution spatially. Instead, the ensemble droplets in the spray structure including the larger droplets at far downstream were averaged. The current PDA method measures the droplets velocity and size distribution at each spatial location within the spray. Despite the difference in measurement method, the empirical correlation and PDA-derived data are able to show the droplet SMD trend in relation to ALR. The advantage of PDA measurement method is that detailed information such as the spatial and pdf distribution of the spray droplets can be obtained.
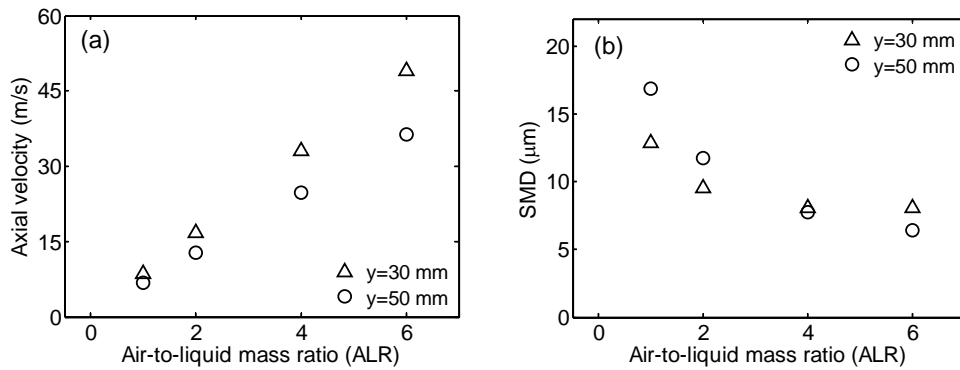
Figure 5.8: The diesel fuel droplets (a) axial velocity and (b) SMD values as a function of ALR at the centreline of 30 and 50 mm downstream of the atomizer outlet.

The measured droplet mean axial velocity at the spray centreline (x = 0 mm) and downstream axial locations (y = 30 and 50 mm) from the nozzle tip as a function of ALR is shown in Fig. 5.8a. The droplet velocity at the spray centreline shows a linear relation to ALR for both axial positions. The increase of ALR results in higher relative velocity, which translates into higher droplet momentum from the nozzle outlet. The droplet velocity decreases from position y = 30 mm to downstream y = 50 mm due to the loss of momentum, and deceleration of droplets is highest for ALR = 6. The corresponding droplet SMD values are shown in Fig. 5.8b. Droplet SMD values exhibit negative power dependence to ALR. At ALR = 1 and 2, the droplet SMD values at axial location y = 30 mm is lower than those at y = 50 mm downstream, For ALR = 6,

the droplets at y=50 mm is smaller than those at y = 30 mm downstream, which suggests secondary droplet breakup due to the sufficiently high shear force imposed on the gas and liquid. Similar droplet SMD values at the centreline of y=30 and 50 mm is observed for ALR = 4.

The droplet SMD values as a function of Weber number at the radial position where the maximum volume flux and droplets concentration locations are shown in Fig. 5.9a and 5.9b respectively. In general, the trend shown in both cases is rather similar. At $We^{1/2} < 50$ which corresponds to ALR < 3, the droplet SMD values show an increase of ~ 2-3 µm as the droplets travel downstream from the axial location of y = 30 mm to 50 mm. For $We^{1/2} > 50$, the reverse is observed where the droplet SMD values at downstream location 50 mm is lower than those at 30mm. According to the airblast atomizer breakup regimes proposed by Lasheras and Hopfinger [7] as shown in Fig. 4.3, Chapter 4, the current atomizer exhibits fiber-type breakup due to the high Weber number of $We^{1/2} > 25$. At ALR=1, atomization occurs at the membrane-type regime which explains the formation of large droplets as shown in Fig. 5.1.
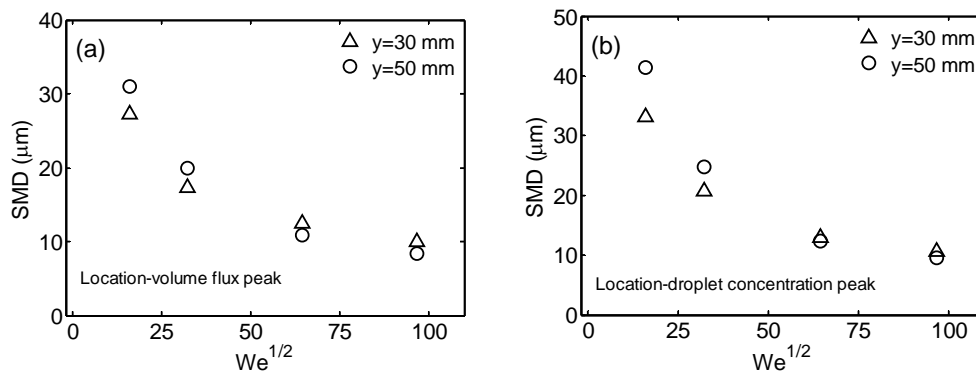
Figure 5.9: The SMD values of diesel fuel droplets at the position of (a) maximum volume flux (b) maximum droplet concentration as a function of Weber number.

5.1.2 Effect of fuel type

5.1.2.1 Droplet size distribution
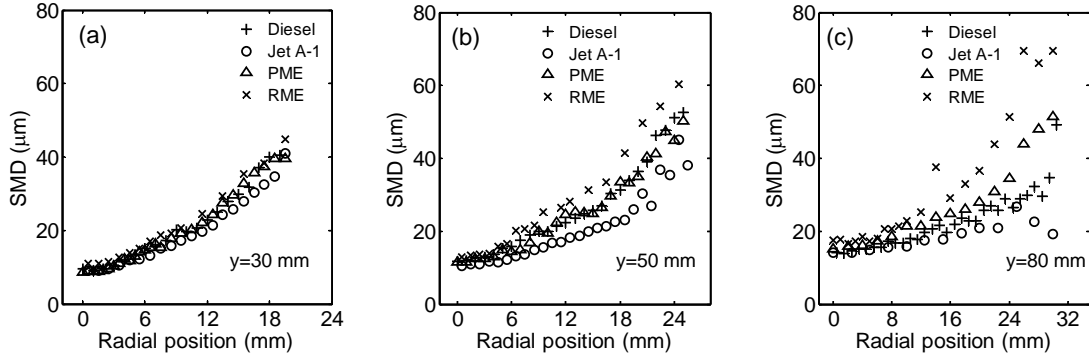
Figure 5.10: The radial distribution of droplet SMD profiles at downstream axial positions of (a) 30 (b) 50 and (c) 80 mm from the atomizer outlet under the condition of same fuel mass flow rate of 0.14 g/s and ALR = 2.

Biodiesel spray atomization is of interest in view of increasing usage in existing combustion systems especially in compression ignition engines. The envisaged application of biodiesel in gas turbines and furnaces is the reason for the present airblast atomizer study using biodiesel. Here, the atomization characteristics of biodiesel in an airblast atomizer are compared to conventional fuels of diesel and Jet-A1. Comparison of the droplet characteristics are performed under the same atomizing air-to-liquid fuel mass ratio of 2, in which the fuel mass flow rate is maintained constant at 0.14 g/s. The half-plane radial distribution of droplet mean SMD values at downstream locations of 30, 50 and 80 mm from the nozzle tip is shown in Fig. 5.10. Two biodiesels are tested in this experiment, namely palm methyl esters (PME) and rapeseed methyl esters (RME).

The radial distribution of droplet SMD show the lowest values at the spray centreline region but the SMD values gradually increase towards the spray boundary. Such distribution of droplets could be in due to the effect of swirl in the atomizer. It has been reported by Préaux *et al.* [8] that the addition of swirl to the atomizing air reduces the mean drop size at the centre of the spray but has no effect on the drop size at the spray boundary. The population of small drops at the centreline has significant implication on combustion, as evaporation rate is enhanced to enable a more complete

and efficient combustion. The swirl also allows the increase of lateral spreading of the spray and hence the larger spray cone angle. The presence of swirl in the current atomizer also explains the difference in droplet radial distribution compared to other result obtained from atomizer without swirl [5].

At 30 mm downstream from the nozzle tip, the droplet SMD profiles of the fuels considered are rather similar. Jet-A1 fuel shows a slightly noticeable lower SMD value compared to the other heavier fuels. The discrepancy of the droplet SMD become more pronounced at further downstream axial positions. At y = 50 mm from nozzle tip, RME shows distinctively higher SMD values especially near the spray boundary whereas Jet-A1 remains consistently low. At the radial position x = 20 mm of axial location y = 50 mm, the droplet SMD of Jet-A1 droplets is 20 % lower compared to PME and diesel, and 43 % lower compared to RME droplets. The low Jet-A1 SMD indicates the higher tendency of Jet-A1 to breakup and atomize compared to other heavier fuels. This is because Jet-A1 fuel has lower viscosity and surface tension values compared to other heavier fuels. Besides, vaporisation of Jet-A1 droplets occurs more easily due to the higher surface area and the increased convective mass transfer. Diesel and PME exhibit relatively similar SMD values at y = 30 and 50 mm downstream but the difference becomes more pronounced at y = 80 mm. PME shows higher SMD values than diesel due to the higher viscosity and surface tension. The radial distribution of the droplet SMD profile shows a slight increase of ~ 2 µm at the spray centreline region for all fuels. The slight increase of droplet size at the spray centreline region could be due to the entrainment of droplets from the spray boundary as a result of the radial pressure difference induced by the swirling atomizing air flow. Another possibility is the effect of coalescence as a result of high collision rates between droplets.

5.1.2.2 Droplet mean velocity and RMS velocity distribution
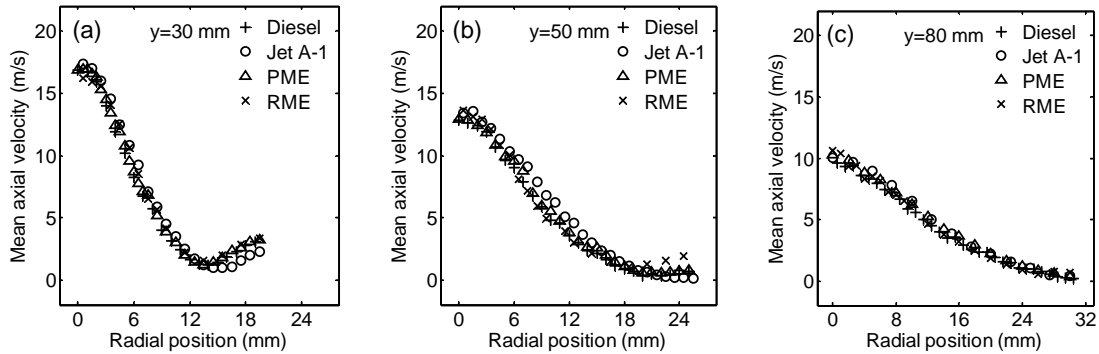
Figure 5.11: The radial distribution of droplet mean velocity profiles at downstream axial positions of (a) 30 (b) 50 and (c) 80 mm from the atomizer outlet under the condition of same fuel mass flow rate of 0.14 g/s and ALR = 2.

The radial distributions of the droplet mean axial velocity at the downstream axial positions of y = 30, 50 and 80 mm from atomizer outlet are shown in Fig. 5.11. Overall, the plain-jet airblast atomizer shows the characteristic droplet velocity distribution with the highest value at the spray centreline (x = 0 mm) region. The droplet velocity decreases with the increasing radial position towards the spray boundary. Droplets attain the highest momentum near the nozzle outlet but slowly decay as the droplets travel downstream and results in a lower velocity. Comparison of the velocity profiles shows that the four fuels considered exhibit indistinguishable profiles, indicating the independent influence on the fuel physical properties. Instead, the droplet velocity is mainly governed by the momentum of the atomizing air. At ALR = 2, the atomizing air velocity is ~ 100 m/s whilst the liquid jet velocity is ~ 0.8 m/s. The relatively higher velocity of the gas phase shows the dominating influence of air over the liquid. The kinetic energy from the air is used to shear the liquid jet into droplets. At position y = 30 mm downstream of the atomizer outlet, centreline droplet velocity peaks at ~ 17 m/s. The profile shows a narrow curve as the spray is still in a developing phase. Further downstream the spray, the droplets decelerate as the spray spreads wider. The peak velocities at the downstream axial position of y = 50 mm and 80 mm are ~ 13 m/s and ~ 10 m/s respectively.
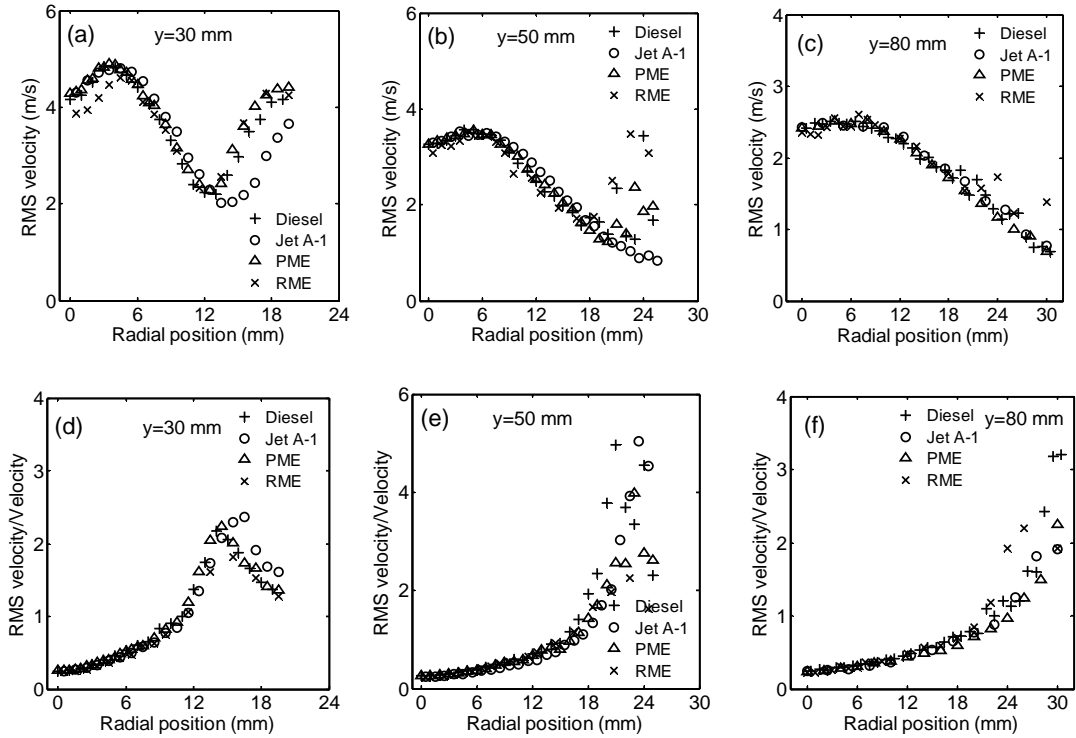
Figure 5.12: The radial distribution of rms velocity profiles (a,b,c) and ratio of rms to velocity (d,e,f) at downstream axial positions of y = 30, 50 and 80 mm from the atomizer outlet under the condition of same fuel mass flow rate of 0.14 g/s and ALR = 2.

The corresponding radial distributions of droplet rms velocity at different downstream axial locations are shown in Fig. 5.12a-c. In general, the droplet velocity rms profiles are almost similar for all the fuels tested. The profiles show a peak at a distance from the centreline where the velocity gradient is highest. For the downstream axial location y = 30 mm, the rms velocity is found to increase near the spray boundary as the droplet velocity increase between the radii x = 13 mm and 18 mm. The profiles at y = 50 and 80 mm show a decreasing trend after the peak near the centreline. However, this does not mean that the droplet velocity fluctuation is low. By dividing the velocity rms with the respective spatial velocity as presented in Fig. 5.12d-f, the ratio shows high fluctuation near the spray boundary due to the presence of a wide range of droplets with different size. Large droplets tend to lag in the flow due to the drag force imposed compared to small droplets. The common trend shown in all axial locations is that the fluctuation is lower at the spray centreline region but slowly

increases towards the spray periphery. The plots show higher degree of scatter when the ratio of velocity rms/velocity is more than 1, where the variability of droplet velocity indicates the presence of the unstable shear layer as the inner jet entrains outer stagnant air.

5.1.2.3 Droplet concentration and volume flux
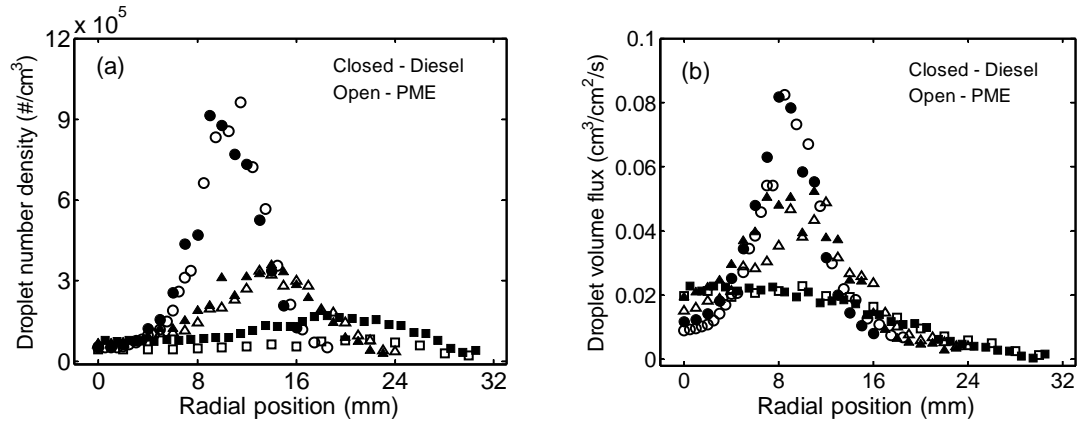
Figure 5.13: Profiles of droplet (a) number density and (b) volume flux for diesel and PME at the axial location of y = (o) 30, (Δ) 50 and (□) 80 mm downstream the atomizer outlet under the same fuel mass flow rate condition of 0.14 g/s and ALR = 2.

The spatial distributions of the droplet number density for diesel and PME at the downstream axial locations of 30, 50 and 80 mm from the nozzle outlet are shown in Fig. 5.13a. The figure shows the peak concentration of droplets located at a radial distance from the centreline for the axial positions of y = 30 and 50 mm. The profile at y = 80 mm downstream shows a relatively even distribution of droplets. In general, diesel exhibits similar droplet concentration distribution as PME under the same fuel mass flow rate condition. At radii x = 10 mm and y = 30 mm downstream, the peak droplet density value for both fuels is ~ $9x10^5$ droplets/cm^3. The spreading of the spray at further downstream location shifts the peak radially. At y = 50 mm downstream, the maximum number of droplets are concentrated at the radial position of 15 mm from centreline with the peak value of ~ $4x10^5$ droplets/cm^3. The concentration of the droplets at the radial position away from the spray centreline highlights the diffusion of the droplet cloud, even though the spray generated originates from a solid cone. At the

downstream axial location of y = 80mm, the droplet number density value becomes lower than $2x10^5$ droplets/cm^3 with the peak locating at the radii of 18 mm. At this distance, the spray is reasonably uniform, with evenly distributed droplet concentrations.

The corresponding volume flux profiles are shown in Fig. 5.13 b. The profiles at axial position 30 and 50 mm downstream show a distinct peak at a distance from centreline, while the profile at y = 80 mm from nozzle outlet exhibits a uniform distribution of droplets at the centerline. The peak locations of the volume flux are different compared to the droplets concentration profiles. For instance, the droplet number density peaks at the radial position of between x = 9 and 11 mm at downstream y = 30 mm, whereas the volume flux peak is located at the radial position between 8 and 9 mm. The difference in the peak locations between the volume flux and droplet concentration profiles is due to the interaction of atomizing air with droplets and the weighting effect of droplets. Larger droplets carry significantly higher volume flux compared to smaller droplets. The skewed normal distribution of droplet size at each spatial location determines the volume flux distribution. The peak volume flux values at y = 30 and 50 mm downstream of nozzle are 0.08 and 0.05 cm^3/cm^2/s respectively. For y = 80 mm downstream, the droplet volume flux is distributed at the centreline region despite the lower concentration of droplets.

5.1.2.4 Spray centreline profiles
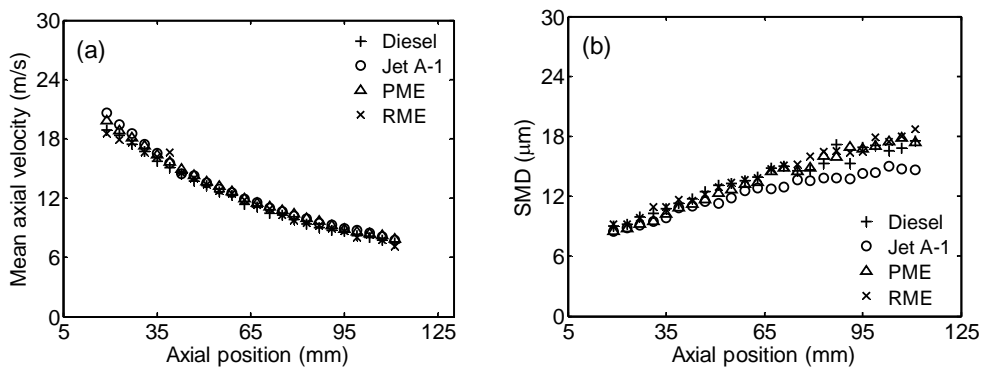
Figure 5.14: Droplet centreline (a) axial velocity and (b) SMD profiles at the axial location of y = 50 mm under the same fuel mass flow rate condition.

The droplet velocity profiles along the centreline of the spray at the downstream location y = 50 mm from spray outlet are shown in Fig. 5.14a. Comparison of the fuel droplet velocity profiles under the same ALR and fuel mass flow rate show almost identical profiles for the fuels considered. The velocity of the droplet gradually decreases with the increasing downstream distance due to the spread and loss of momentum. The corresponding droplet SMD profile at the spray centreline is shown in Fig. 5.14b. At downstream positions between y = 12 and 68 mm, the droplet SMD values for all the fuels are rather similar. The difference in SMD values becomes obvious at axial position 70 mm and beyond where PME and RME show 3-5 μm larger than Jet-A1.

5.1.2.5 Droplet distribution and size-velocity correlations
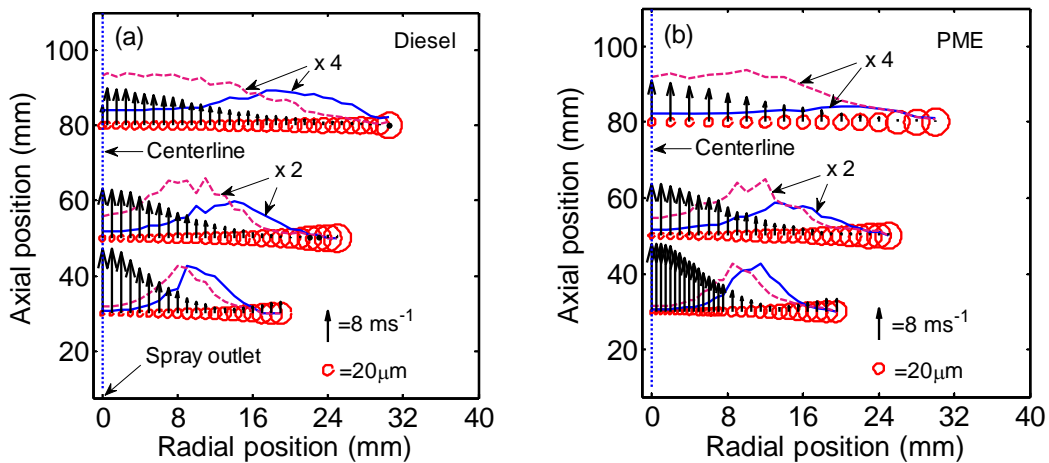
Figure 5.15: Radial distribution of droplet velocity ($\uparrow$), SMD (o), concentrations (—) [#/cm³/s] and volumetric flux (---) [cm³/cm²/s] for (a) diesel and (b) PME under the same fuel mass flow rate condition of 0.14 g/s.

The overall spray structures generated from diesel and PME are presented in Fig. 5.15a and 5.15b respectively. The droplet SMD and velocity distribution are superimposed with the droplet concentration and volume flux profiles. Overall, the small droplets at the center of the spray attain high axial velocity, but the concentration of the droplets and volume flux are relatively low. Most droplets

concentrate at a distance away from the centreline where the droplet velocities are relatively lower with medium droplet size. The figures also show that the droplet number density distribution within the spray does not correspond spatially with the profile of volume flux distribution. Despite the higher concentration of droplets near the spray edge, the volume flux is biased towards the direction of the spray centreline. Comparison of the diesel and PME droplet distributions in Fig. 5.15 shows the relatively similar spray structure. The relatively similar physical properties between diesel and PME results in the almost identical droplet size distribution. Variation of the droplet SMD depends on the physical properties of the fuels while the droplet velocity depends on the relative velocity between the gas and liquid.
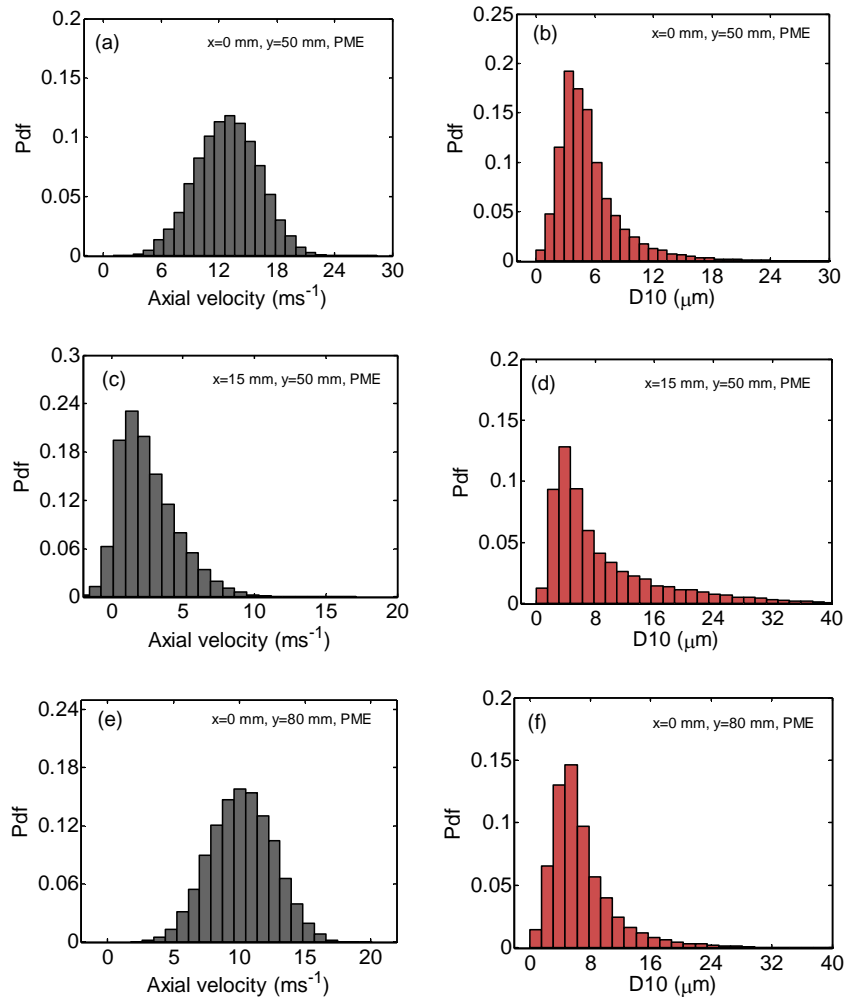
Figure 5.16: Distribution of droplet axial velocity (a,c,d) and mean diameter (D10) (b,d,f) at different spatial positions within the PME spray.

The PDF of PME droplet velocity and SMD distribution at three spatial locations within the spray are shown in Fig. 5.16. At the spray centreline (x = 0 mm) of downstream position y = 50 mm, the droplet velocity shows a normal distribution that spans between 0 and 24 m/s, as shown in Fig. 5.16a. This demonstrates that the small droplet size at the centreline region attain a wide range of velocity that enhances the collision rates between drops. Figure 5.16b shows the droplet size distribution that skews towards smaller droplets diameter with limited presence of large droplets. At the radius of x = 15 mm at the downstream position of y = 50 mm, the droplet velocity shows a skewed distribution biased towards the lower velocity. The droplet concentration is relatively high at this particular position compared to the centreline region, as shown in the Fig. 5.13a. As the relative velocity between the gas and liquid phases is low, the droplet exists in a range of size between 0-40 μm (Fig. 5.16d). The significant presence of larger droplets contributes to the volume flux. At the centreline position with a downstream location y = 80 mm, the droplet velocity and size distributions are rather similar to the centreline location of y = 50 mm, albeit with a different magnitude. The increase of droplet size at the centreline region of the spray at y=80 mm compared to y = 50 mm indicates the possible effect of preferential droplet vaporisation of smaller droplets, local drop dispersion, redistribution of droplets due to the effect of swirling atomizing air or droplet coalescence. The spatial PDF of the droplets are similar between the fuels tested.

147

5.1.3 Effect of blends on droplet SMD
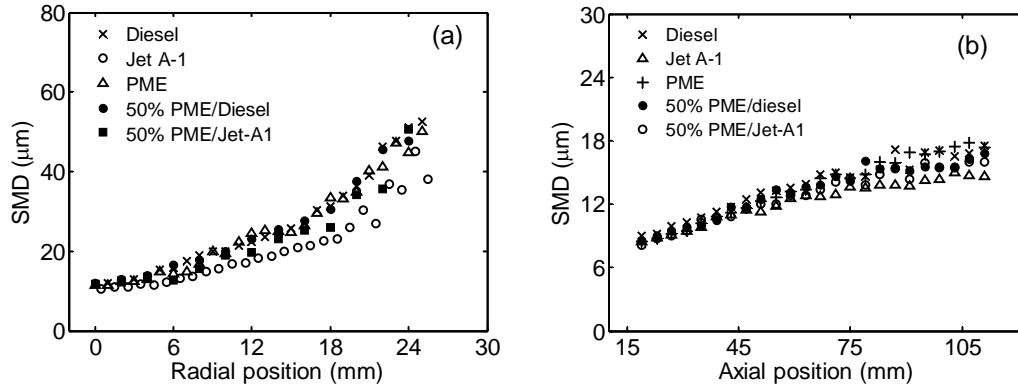
Figure 5.17: (a) Radial distribution of droplet SMD profiles at y = 50 mm and (b) centreline axial distribution of the droplet SMD. Measurement was performed under the condition of same fuel mass flow rate of 0.14 g/s and ALR = 2.

The effect of biodiesel blend with conventional fuels on spray characteristics is investigated for constant fuel mass flow rate of 0.14 g/s. The radial distributions of the droplet SMD profiles of 50 % PME/diesel and 50 % PME/Jet-A1 are compared to unblended fuels in Fig. 5.17a. The profile of the 50 % PME/diesel is similar to diesel and PME, whereas the 50 % PME /Jet-A1 droplet SMD shows slightly higher value than Jet-A1. This shows the dependence of the droplet atomization characteristics on the fuel physical properties. The result shows that the droplet size of the biodiesel blends can be estimated to fall between the parent fuels. This is also shown in the SMD profiles at the axial centreline of spray in Fig. 5.17b. Similar to the trend shown in Fig. 5.14, the droplet SMD values of the blends are similar to those of the parent fuels at the positions between the nozzle outlet and the downstream location y=70 mm. Beyond 70 mm downstream, the droplet SMD of the blends falls in between the parent fuels.

5.1.4 Variation of fuel mass flow rate

5.1.4.1 Droplet mean velocity and SMD distribution

Biodiesel contains lower calorific values than conventional fuels per unit mass. To obtain the same power output when applying biodiesel in an existing combustion

unit, the fuel mass flow rate of biodiesel needs to be increased by 17 % by mass compared to conventional fuels to offset the power difference. For example, diesel and Jet A-1 produce 6 kW at the mass flow rate of 0.14 g/s while biodiesel requires 0.16 g/s to generate the same power output. To investigate the effect of higher fuel mass flow rate on the spray atomization, a constant power output condition is assumed. The fuels tested are metered to produce the same power output of 6 kW while maintaining an ALR ratio of 2.
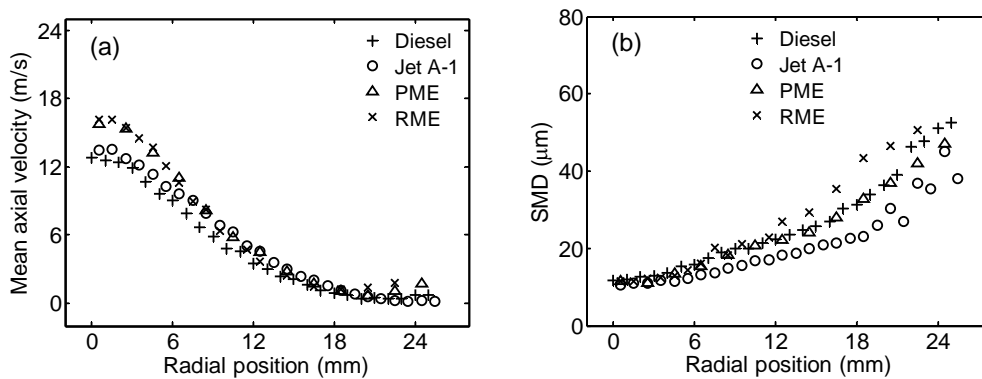
Figure 5.18: Radial distribution of (a) droplet velocity and (b) SMD profiles at axial location y = 50 mm downstream of the atomizer outlet under the same power output condition. The ALR is maintained at 2.

The radial distributions of the droplet velocity and SMD profiles at the downstream axial location of y = 50 mm are shown in Fig. 5.18a and 5.18b respectively. Biodiesels exhibit higher droplet velocity at the centreline region due to the increased air mass flow that corresponds to the increased fuel mass flow rate based on ALR = 2. The higher droplet velocity is limited to the centreline region. Beyond the radial position of x = 6.5 mm, the velocity profiles are similar for all fuels. The increased momentum of biodiesel droplets at the centreline results in longer penetration length of spray, affecting mostly the smaller droplet at the centreline region. The droplet size distribution is shown in Fig. 5.18b exhibits a rather similar trend as the profiles derived from the same fuel mass flow rate as shown in Fig. 5.10. RME droplets exhibit higher SMD values while Jet-A1 shows lowest SMD values. Despite the increase of fuel mass flow rate of biodiesels, the corresponding increase of atomizing air to match the

ALR = 2 prohibits the formation of larger droplet SMD. This shows that ALR can be used as the effective parameter to control the spray droplet size.
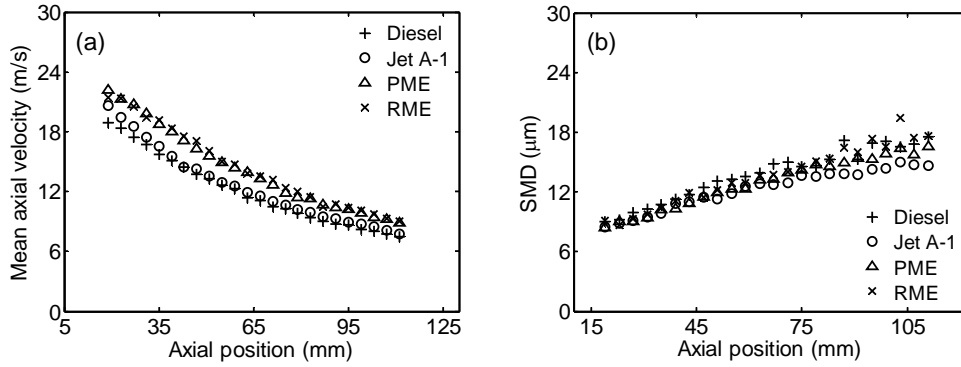
Figure 5.19: Centreline axial distribution of droplet (a) mean axial velocity and (b) SMD under the same power output condition.

The centreline axial mean droplet velocity and SMD profiles under the same power output condition and ALR = 2 are shown in Fig. 5.19a and 5.19b respectively. The increase of atomizing air for PME and RME spray result in higher droplet velocity compared to diesel and Jet-A1. The droplets of PME and RME exhibit high droplet velocity despite the similar droplet size at the centreline region as indicated in Fig. 5.19b. The independence of the droplet SMD size to the velocity is due to the fixed ALR of 2 for all conditions. At downstream condition beyond 70 mm, Jet-A1 shows lower droplet SMD values than diesel and biodiesel due to the nature of higher volatility. The effect of thermal expansion at the atomizer outlet increases the mass convection and evaporation rate for Jet-A1.

5.1.5 Mie scattering of spray

A laser sheet is used to induce the light scattering from the spray droplets. The instantaneous Mie scattered images of PME spray at different ALR are shown in Fig. 5.20. Overall, it is observed that the penetration length of the spray is increased with higher ALR. This is because the increased atomizing air results in higher droplet

momentum. At ALR = 2 as shown in Fig. 5.20a, the presence of individual droplets outside the spray periphery is more distinct compared to the ALR = 4 and 6. This could be due to the expansion of the spray through the air orifice, with higher radial component of the droplets that results in the radial dispersion of droplets. Another reason is that the higher resistance to droplet breakup at low ALR results in the relatively larger droplets that follow different trajectory routes. The distinct Mie scatter signals produced near the spray boundary region at low ALR is consistent with the Mie scattering theory, where the signal intensity scales with the square of droplet diameter. It is observed that the spray is restrained from spreading radially as the ALR increases. The higher axial velocity component forces the droplets to travel further downstream, and hence the spray cone angle is smaller for higher ALR. Determination of the spray cone angle from the Mie scattered images is shown in section 5.1.6.
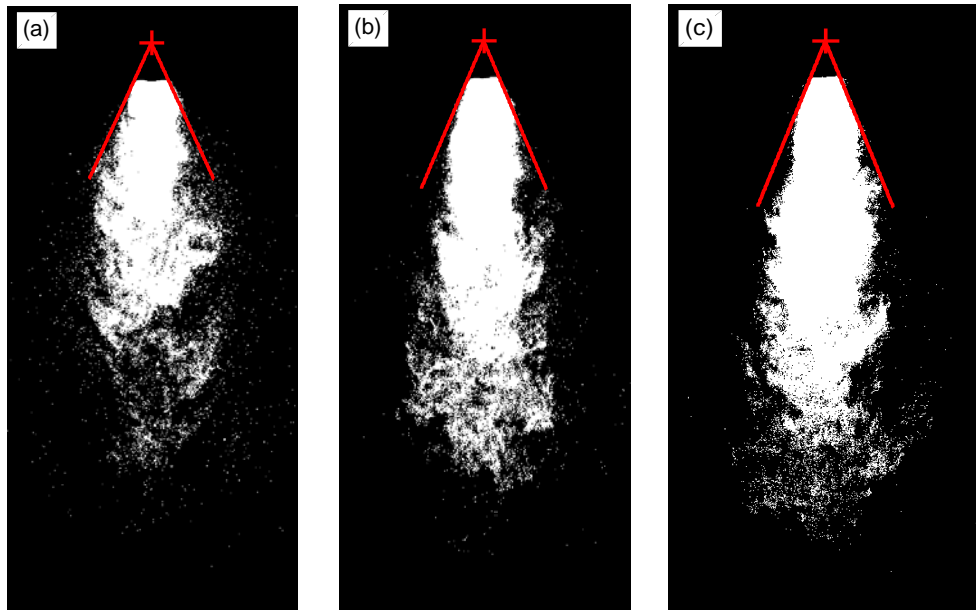
Figure 5.20: Mie scattering of sprays for PME at ALR = (a) 2, (b) 4 and (c) 6. The fuel mass flow rate is maintained at 0.14 g/s for all cases.

5.1.6 Spray cone angle determination

Determination of the spray cone angle is performed by detecting the spray edges of the Mie scattered spray images (averaged of 500 instantaneous shots). Figure 5.21a presents the result of the determined cone angles for Jet A-1, diesel, PME, RME and 50 % PME/diesel blend (D50) sprays using this method. All fuels tested exhibit similar spray cone angle to within ± 5 °. The cone spray angle is found to decrease with ALR. At ALR = 2, the spray cone angle for diesel spray is approximately 55° while the cone angle at ALR = 6 is 45°. The current result is found to be contradictory with the trend shown by Pancharasara *et al.*[9]. They used a similar plain-jet airblast atomizer but reported an increasing trend of spray cone angle with the increase atomizing air. In this study, the increase of atomizing air results in the increase of penetration length of the spray but with a narrower spray cone angle. Nakamura *et al.* [10] shows the decreasing linear trend of spray cone angle with the increase of ALR, which is similar to the present result.
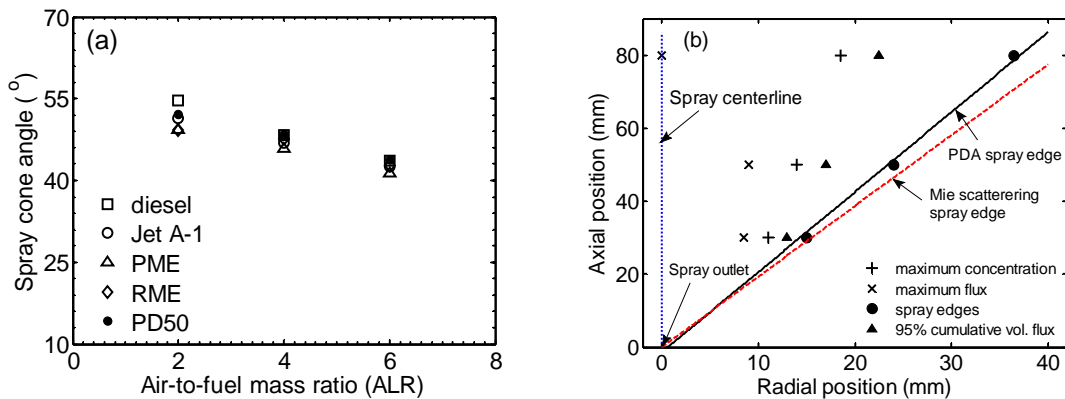
Figure 5.21: (a) Spray cone angles derived from Mie scattered images and (b) relative positions of determined spray edges within the spray. The PDA spray edge is determined based on the last detectable volume flux value by the PDA software at the radial profiles.

The spray cone angle determined from Mie scattering images is compared to the cone angle determined by PDA. The latter method is derived from the droplet volume flux profiles, in which the last detectable position by the PDA software at the radial

profiles is defined as the spray edge. The uncertainty of the determined location is $\pm$ 1 mm, which corresponds to the smallest step in the radial measurements. The spatial locations of the diesel spray edges derived from fuel and air mass flow rates of 0.14 g/s and 0.28 g/s respectively are indicated in Fig 5.21b. The PDA-determined spray cone angle is ~ 50°, which is close to the Mie-scattering determined spray cone angle of 55° to within 10% accuracy. The good agreement shows the feasibility of using these two methods to measure the spray cone angle. Another method attempted is by defining the spray edges as the 95 % of the cumulative volume flux from the centreline. Locations of the 95 % volume flux are indicated in Fig. 5.21b to show the spatial locations relative to the PDA- and Mie scattered-derived spray edges. It is noted that the indicated positions do not form a straight line that intersects with the atomizer outlet. But as the determined 95 % cumulative flux location at downstream axial position y = 30 mm is close to the PDA- and Mie scattered-derived sprays edges, this method is consistent with the Mie-scatter spray cone angle for the region between the nozzle outlet and 30 mm downstream. Spatial locations of the maximum flux and droplets concentrations within the radial profiles are indicated in Fig. 5.21b to qualitatively assess the structure of the spray. The maximum number droplet density is found to locate at radial positions closer to the spray edges compared to the location of maximum volume flux. As the spray continues to develop far downstream, it continues to disperse radially. At a spray downstream axial location of 80 mm, the volume flux profile exhibits a more uniform distribution of flux with the peak locating at the centreline of the spray.

5.2 Reacting spray results

5.2.1 Droplet size and mean velocity distribution
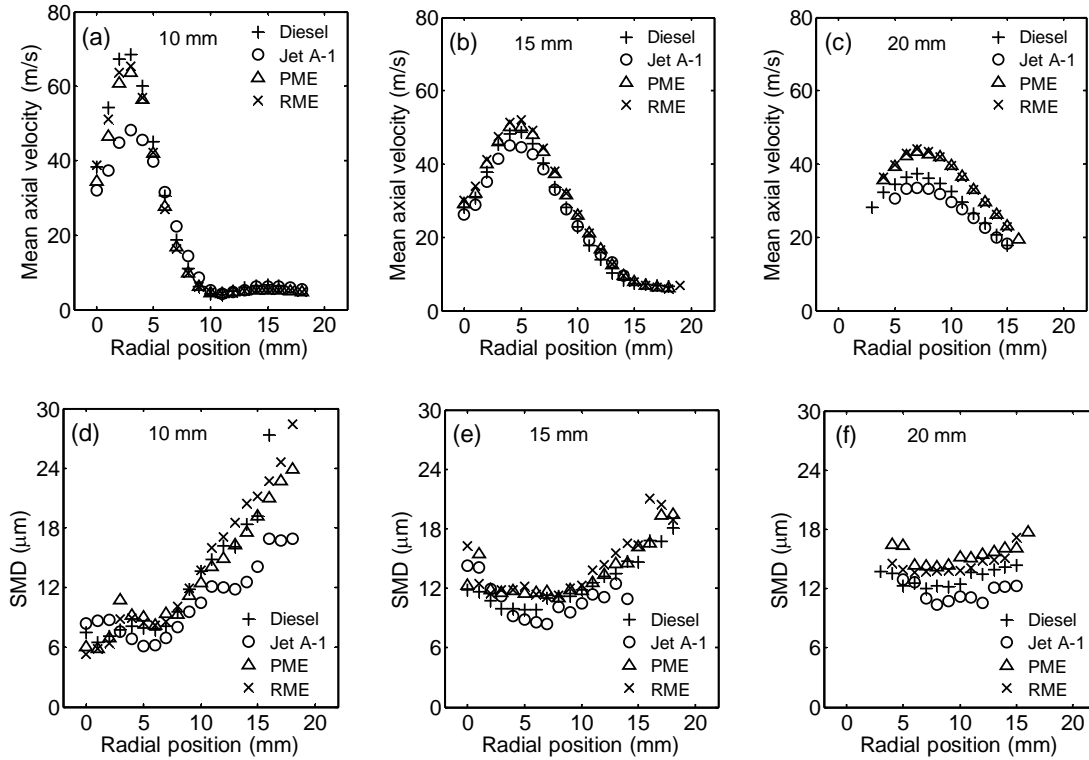
Figure 5.22: Mean droplet axial velocity (a-c) and the SMD (d-f) profiles at different axial positions under the same power output conditions of 6 kW.

The mean droplet velocity and SMD profiles on one side of the centreline are shown in Fig. 5.22 for axial positions 10, 15 and 20 mm from the burner outlet. The x-abscissa indicates the radial profile from the centreline (x = 0 mm) of the burner. At y = 10 mm, the droplet velocity peaks at 3 mm away from the centreline as shown in Fig. 5.22a. The droplet axial velocity profile then decreases as the radial distance increases from the centreline. At further downstream location of 15 mm, the velocity peak appears at a wider radial distance as a result of the interaction of the spray with the main swirling flow as shown in Fig. 5.22b. The strong radial flow from the swirling flow induces a radial pressure gradient, in which the central recirculation zone is formed while the spray spreads radially. The strong reverse flow at the centreline region

interacts with the droplets, which lowers the droplet velocity further downstream. The velocity profiles of all the fuels tested are rather similar at the axial positions at 10 and 15 mm.

Diesel exhibits similar velocity and SMD profiles as PME at y = 10 and 15 mm. RME shows a higher droplet SMD values, especially at radial positions near the spray boundary. In general, a low SMD values is observed at the centreline region but gradually increases with increasing radial positions. Between the radial position at 8 mm and the centreline, the droplets are distributed within the intense heat release region. The heat propagated from the reaction zone assists in vaporising the small droplets within this region. At the radial position of 5 mm, which coincides with the location of maximum volume flux, a slight increase of SMD values for diesel, PME and RME is observed.

The droplet SMD at the centreline is found to be higher at y = 15 mm compared to 10 mm. The increase of droplet SMD is attributed to faster evaporation of where the smaller droplets with higher surface area-to-mass ratio are first consumed while the larger droplets survived the initial vaporisations. The trajectories of the droplets also play a role in the droplet size distribution in the flame. Larger droplets at the spray periphery go into the shear layer and are entrained back into the centre of the flame, thus contributing to the increase of droplet size at the spray centreline as the downstream axial distance increases. Despite the apparent increase of droplet size, the number of droplets at this region is considerably lower, as shown in the droplet concentration profiles in Fig. 5.25. The spray boundary region show lower droplet SMD values at 15 mm compared to 10 mm at the radii between x = 10 and 20 mm. The larger droplets at the spray boundary gradually reduce in size due to evaporation as the droplets travel downstream.

At the downstream location of 20 mm, the difference between droplet velocity and size becomes more obvious, as presented in Fig. 5.22c and 5.22f. PME and RME droplets show higher SMD and velocity values than diesel droplets at the same spatial locations. The larger SMD value for biodiesel droplets is due to the influence of higher viscosity and surface tension values compared to diesel fuel. The small and scarce droplets at the centreline and periphery region have completely vaporised whereas the high droplet density region sustains some larger droplets. The remaining large biodiesel

droplets contain higher momentum and thus enable a longer penetration length with an extended evaporation time.

The Jet-A1 flame shows slightly lower velocity and SMD values compared to diesel and biodiesel at all axial locations. This is because Jet-A1 fuel is more volatile and has a lower boiling point value compared to the heavier hydrocarbons. Hence, droplet vaporisation occurs in a relatively shorter time scale due to the higher dispersion rate and smaller droplet size. The smaller droplets assume lower velocity due to the loss of momentum as the downstream axial distance increases.
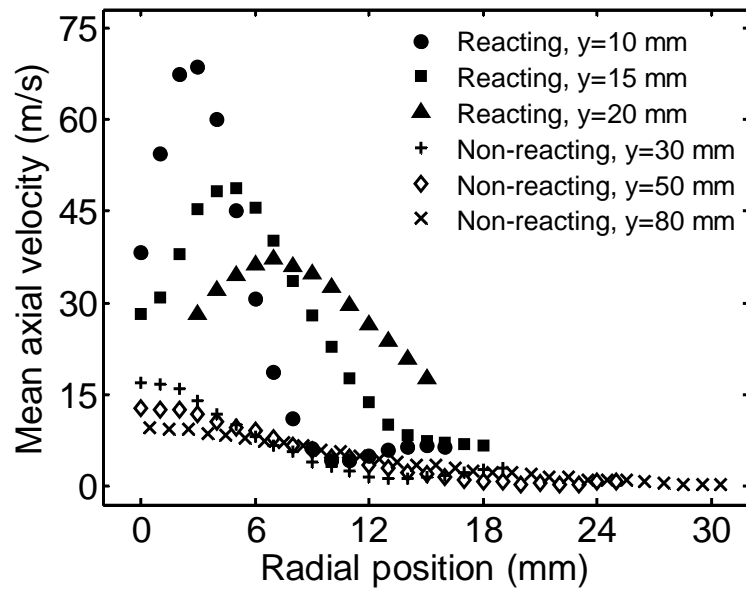
Figure 5.23: Comparison of the mean axial droplet velocity between the reacting and non-reacting spray for diesel.

Comparison of the droplet velocity between the reacting and non-reacting spray is shown in Fig. 5.23. The radial distribution of non-reacting diesel spray data are obtained from the diesel jet spray, as presented in Fig. 5.10. The atomizing air and fuel flow rates of the jet spray are 0.28 g/s and 0.14 g/s respectively for both conditions. Under the reacting flow condition, the jet spray interacts with the main swirling air flow of 4.15 g/s. The reverse flow induced from the centre recirculation zone interacts with the droplets and results in the lower mean droplet velocity at the centreline. The presence of the flame increases the local gas expansion effect and preferential vaporisation of the smaller droplets, which result in an overall larger mean droplet

velocity [11]. Even if the non-reacting spray droplet velocity at the centreline were to be extrapolated to y = 10 mm, the magnitude is still lower than the reacting droplet by a factor of ~ 2. For the non-reacting spray, the absence of reverse flow allows the droplets to attain highest velocity at the centre of the spray.

5.2.2 Droplet RMS velocity distribution

The radial distribution of the droplet rms velocity at the downstream locations 10, 15 and 20 mm from burner outlet are shown in Fig. 5.24a, 5.24b and 5.24c respectively. In general, the velocity rms profiles show the peaks at the radial locations that correspond to the peaks in velocity profiles. The velocity rms values are rather similar for all fuels at all axial downstream positions, including at 20 mm downstream, where biodiesels show similar values as the baseline fuels despite the higher droplet velocity than baseline fuels as shown in Fig. 5.22c. The ratio of the droplet rms velocity to mean axial velocity at the respective spatial locations is shown in Fig. 5.24d, 5.24e and 5.24f. The result indicates the radial positions where the droplet fluctuation is relatively higher. Near the centreline region at all downstream locations, the rms values are observed to be higher due to the presence of a wide range of droplet velocities for the generally small droplets. Another distinct rms peak is near the inflection point of the spray boundary region where the droplet velocity is low. The lowest droplet velocity rms is about 30 % of the droplet velocity for all axial locations y = 10 and 15 mm, while the profiles at y = 20 mm shows the lowest rms values of around 24 %.

157
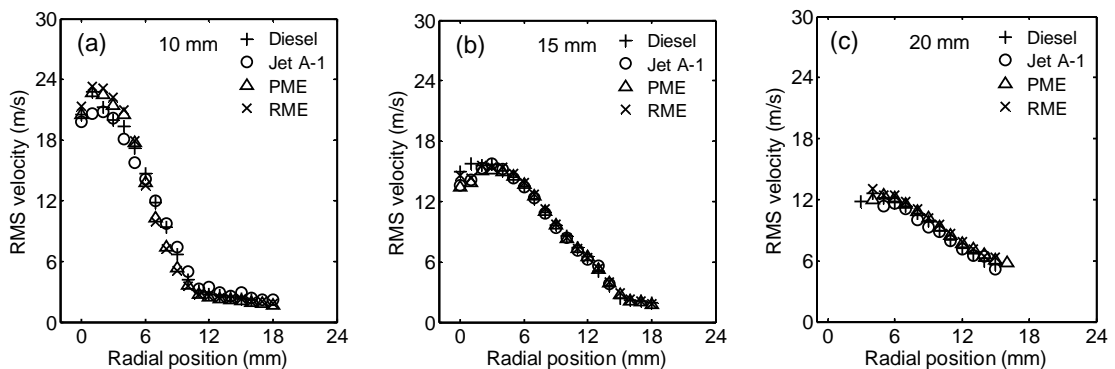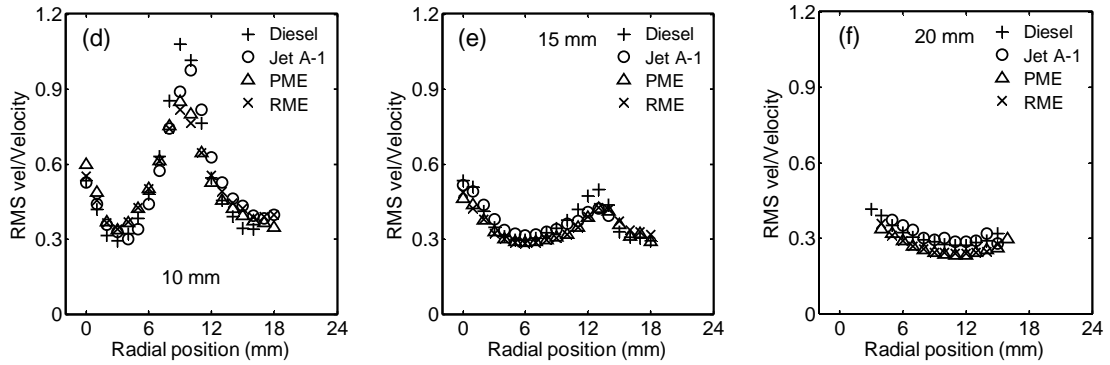
Figure 5.24: The radial distribution of droplet rms velocity (a,b,c) and ratio of rms velocity to velocity (d,e,f) at downstream axial positions of y = 10, 15 and 20 mm from the atomizer outlet under the same power output condition of 6 kW.

5.2.3 Droplet concentration and volume flux

The radial distributions of the droplet number density and volume flux of the spray flames are shown in Fig. 5.25. The distribution at all downstream axial locations indicates that droplet concentration peaks at a distance away from the centreline (x=0 mm). The PME and RME flames present higher peak droplet number densities than diesel and Jet-A1 by a factor of 2 and 4 respectively, at the spatial radial position of x = 7 mm as shown in Fig. 5.25a. The high droplet density of PME and RME is partly in due to the higher mass flow rates by ∼ 17 % compared to the baseline fuels under the constant power condition. The remaining larger PME and RME droplets that are not completely vaporised also contribute to the droplet density count. This could also be the reason that PME and RME show higher droplet concentration values than Jet-A1 and diesel at the centreline region of y=10 mm despite the similar droplet volume flux profiles.
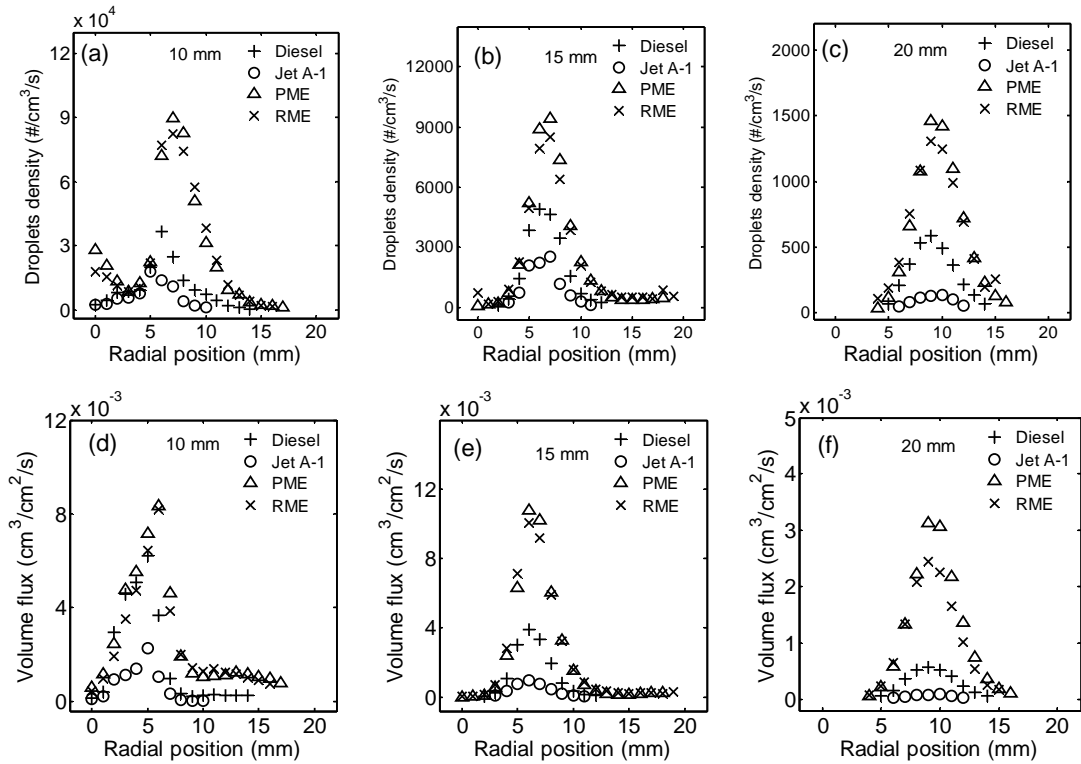
Figure 5.25: Mean radial distribution of droplet number density (a,b,c) and volume flux (d,e,f) at downstream axial locations 10, 15 and 20 mm from the burner exit under the same burner power output condition of 6 kW.

At a downstream location of 15 mm from the burner outlet, the overall droplet number density is reduced by a factor of 10 compared to axial location of 10 mm. The droplet density peaks shifts from radial position 7 mm to 9 mm between downstream axial locations of 15 and 20 mm due to the radial spreading of the spray. In regions where the droplet number density is high, rapid mixing of fuel with air creates a leaner mixture for reactions. The low droplet count at the centreline region is due to the heat propagated from the intense heat reaction zone that further enhances the vaporisation rate of the relatively small droplets. At the axial location 20 mm downstream, PME and RME maintain a higher droplet density than diesel and Jet-A1, but with a reduced magnitude by a factor of 4 compared to the axial location of $y = 15$ mm.

Despite the slight difference of droplet SMD profiles between diesel and biodiesels, the droplet concentration is observed to be lower for diesel at all spatial locations. The higher droplet density shown by biodiesels indicates the relatively longer

penetration length compared to diesel and Jet-A1. Jet-A1 exhibits a significantly lower number of droplets compared to other higher hydrocarbon fuels due to the nature of its higher volatility and larger surface area-to-mass ratio, which facilitates evaporation. Figure 5.25c shows an almost diminished Jet-A1 droplet concentration value compared to other fuels at the downstream location of 20 mm. This shows that Jet-A1 is a light distillate fuel that vaporises and combusts at a relatively shorter time scale.

The corresponding radial distribution of droplet volume flux profiles shows the similar trend as the droplet number density profiles. PME and RME exhibit higher volume flux values than diesel and Jet-A1 at all downstream locations due to the presence of a higher number of surviving droplets. The late vaporisation of biodiesel droplets is attributed to the fuel physical properties such as higher boiling point, viscosity and surface tension. At 20 mm downstream of the burner outlet, the volume flux for PME and RME is reduced by a factor of 3 compared to the profiles at 15 mm, indicating the gradual depletion of droplets in the liquid phase. Jet-A1 shows hardly any value for volume flux due to the almost complete vaporisation at this particular position.

5.2.4 Droplet distribution and size-velocity correlations

The droplet size and velocity distributions for Jet-A1, diesel, PME and RME on one side of the centreline are shown in Fig. 5.26. The droplet concentration and volume flux profiles, normalized with their respective peak magnitudes of their profiles at y = 10 mm, are superimposed on the droplet size-velocity distributions. The general trend for all fuels shows the distribution of smaller droplet SMD at the centreline region of the spray. The droplet velocity at the spray centreline is relatively lower. The droplet velocity peaks located at a radial distance from the centreline before decreasing towards the spray boundary. The lower droplet velocity at the centreline is due to the direct competition between the strong centre reverse flow induced by the centre toroidal recirculation zone and the droplet axial velocity from the atomizer outlet. The adverse pressure gradient between the spray core region and the main swirling flow is induced by the aerodynamic blockage of the bluff body and the radial pressure gradient induced by the swirl, thus forcing the flow to recirculate towards the inner core from

downstream. The stronger reverse flow at the centreline reduces the droplet velocity while causing the spray to spread radially. For profiles at y = 10 and 15 mm downstream, the droplet SMD shows the gradual increase towards the spray boundary. The larger droplets at the spray boundary region attain a low droplet velocity at a low concentration of droplets. The droplets at y = 20 mm downstream however, show a rather evenly distributed droplet size that still attain a significant value of velocity. The scarce droplets at the spray centreline and boundary are completely vaporised.

The superimposed droplet concentration and volume flux profiles shows the spatial distribution of droplets within the spray flame. At y = 10 mm downstream, the droplet concentration peak moves radially outwards. The droplet volume flux profiles show a distribution at different spatial locations due to the weighting effect of droplet sizes. However, the droplet concentration volume flux profiles coincide at the same spatial locations for y = 15 and 20 mm. The overall spray structures and the droplet distribution trends of the fuels considered are almost similar, despite the difference in magnitude. PME and RME show very similar spray structures within the flame. This is expected due to the similar physical characteristics between the two fuels.
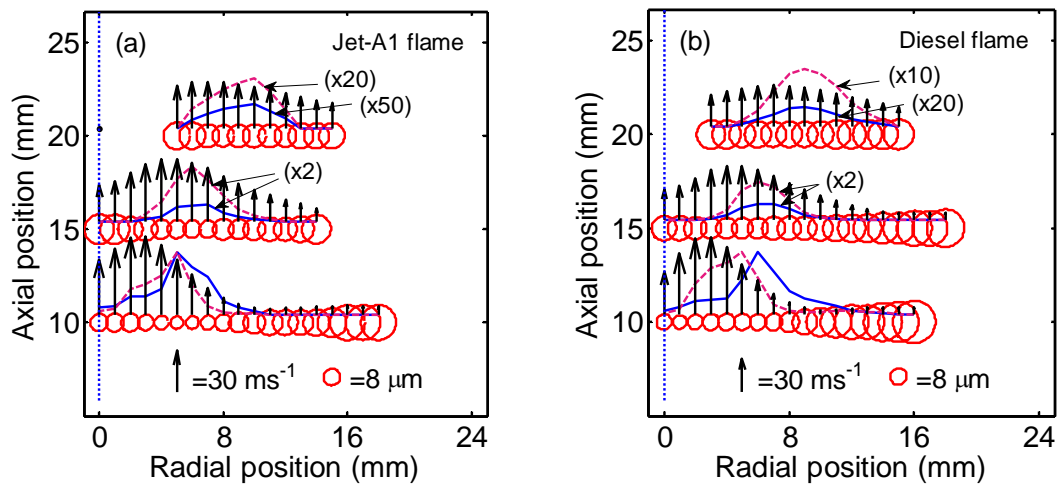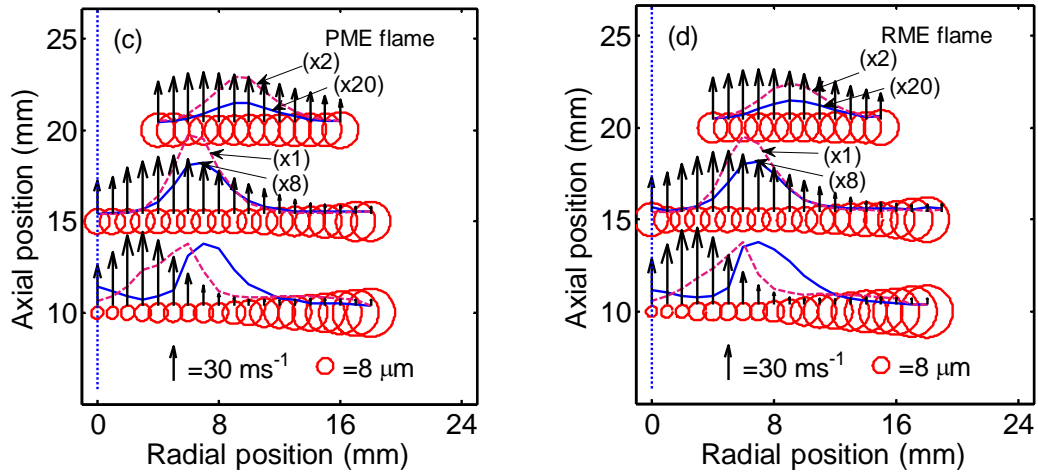
Figure 5.26: Radial distribution of mean ($\uparrow$) droplet velocity, (o) SMD, (—) concentrations ($\#/cm^3$) and (---) volume flux ($cm^3/cm^2/s$) for (a) Jet-A1, (b) diesel, (c) PME and (d) RME at the axial locations of 10, 15 and 20 mm downstream of the atomizer outlet under the same power output condition of 6 kW.

The droplet distribution and trajectories within the swirling spray flame are investigated for the spatial positions indicated in Fig. 5.27. The investigated swirling flame here is established using PME with the fuel mass flow rate of 0.16 g/s at the global equivalence ratio of $\phi = 0.47$. The probability density function (PDF) of the droplet size and velocity distributions is shown in Fig. 5.28. At the centreline of the axial profile y = 10 mm, the droplet velocity shows a normal distribution that spans between -35 and 110 m/s. The droplet density is high at this particular location as shown in Fig. 5.25 and most droplet sizes are distributed within the mean diameter size D10 of 3 μm. The droplet velocity-size correlation shows the wide range of velocities attained by these droplets at this position. The negative velocity exhibited by the droplets indicates the influence of the reverse flow on the spray induced by the central recirculation zone.
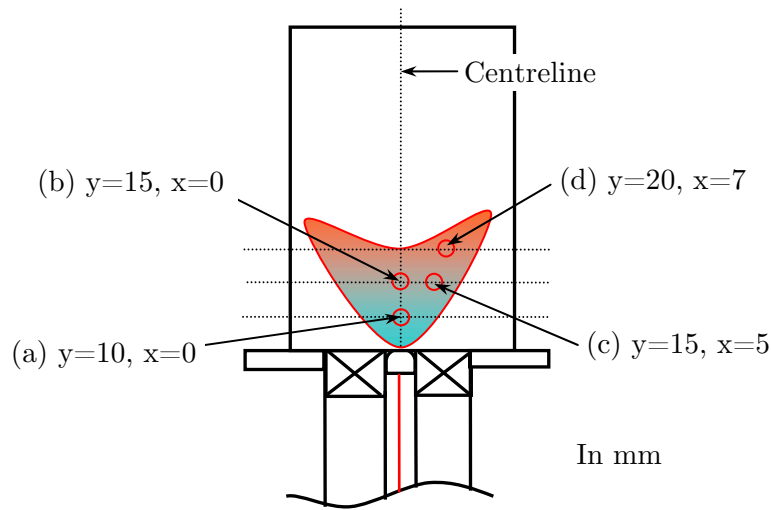
Figure 5.27: Locations where the transport of droplets within the spray flame was investigated.

The droplet count at the centreline position of y = 15 mm is significantly low due to the close proximity to the flame reaction zone. The intense heat propagated from the flame vaporises most of the small droplets within the upstream distance of y = 0 and y = 15 mm. The remaining droplets at this position show the size distribution that is biased towards smaller drop diameters as shown in Fig. 5.28e. Evaporation of the droplets results in the decrease of droplet size and subsequently lowers the droplet momentum and velocity. The droplet size-velocity correlation shows the droplet velocity that spans between 0-80 m/s. At the radial position x = 5 mm from centreline and y = 15 mm, the droplet volume flux is relatively high. This location also corresponds to the peak velocity for the radial profile of y = 15 mm. The PDF of the droplet velocity shown in Fig 5.28g indicates a wide distribution of velocity that ranges between 0-100 m/s, similar to the distribution shown in Fig. 5.28a. The droplet size distribution shows a skewed histogram that is biased to small droplet sizes. The drop size-velocity scatter plots in Figs. 5.28c, 5.28f and 5.28i show that larger droplets attain higher velocities compared to some of the smaller droplets. This indicates the radial spreading of the spray due to the influence of the centreline reverse flow. The change in direction of the droplet trajectories from the centreline axial position is important as the droplet distribution governs the shape of the flame. The

163

dense fuel vapours at the location where the droplet volume flux is high diffuses into the flame zone for local reactions. At the downstream location of y = 20 mm and radii of x = 7 mm, the presence of larger droplets is evident. The droplet velocity shows a narrower distribution (0-80 m/s) due to the reduced presence of smaller droplets. The larger droplets exhibit the droplet velocity that ranges between 30 and 50 m/s as shown in Fig. 5.28l.
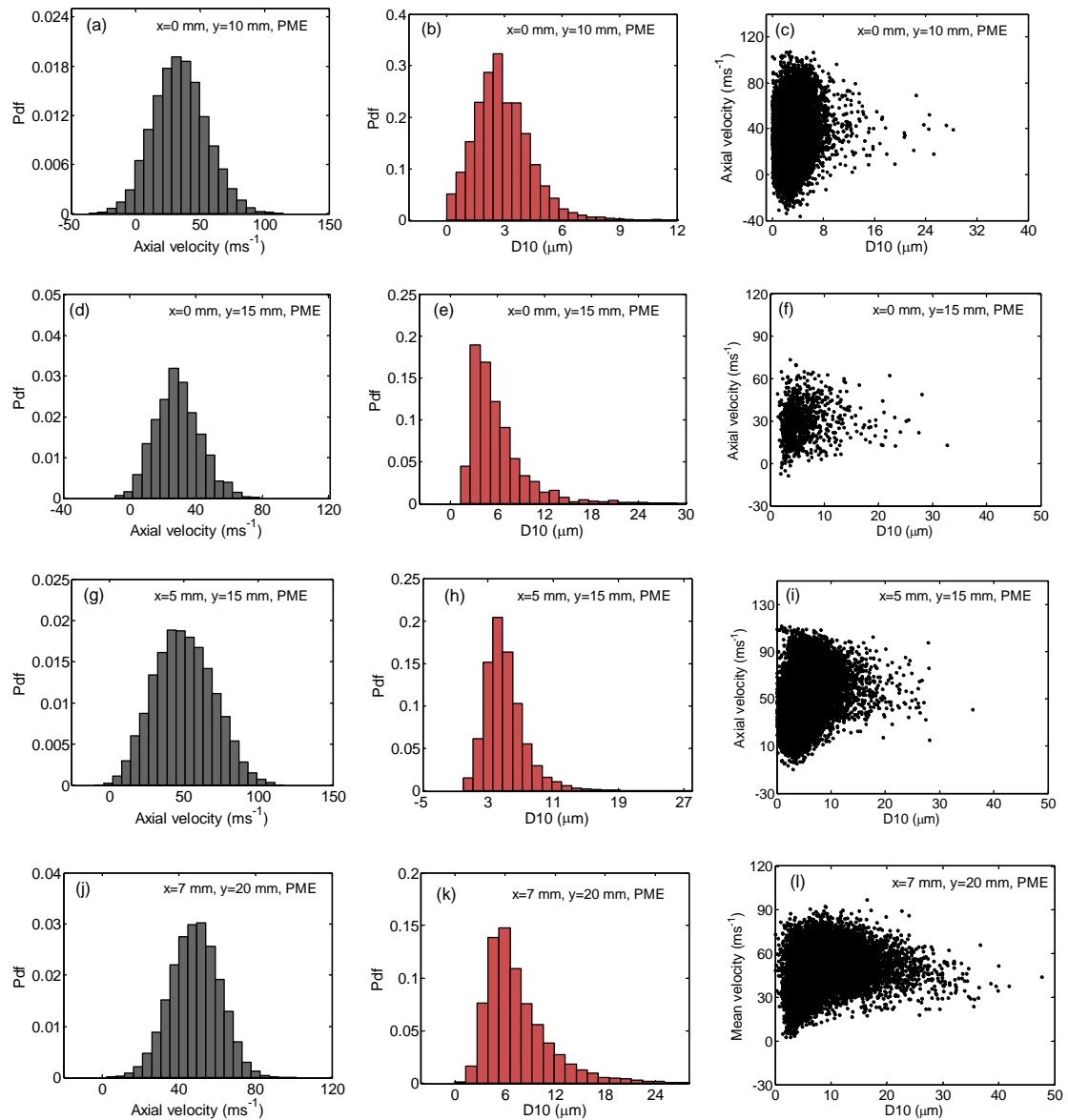
Figure 5.28: The distribution of the droplet (a,d,g,j) axial velocity (b,e,h,k) SMD and (c,f,i,l) droplet size-velocity correlation of the PME swirl flames at locations a, b, c and d as indicated in Fig. 5.27.

5.3 Effect of biodiesel blend on droplets

5.3.1 Blend of 50% PME/Jet-A1
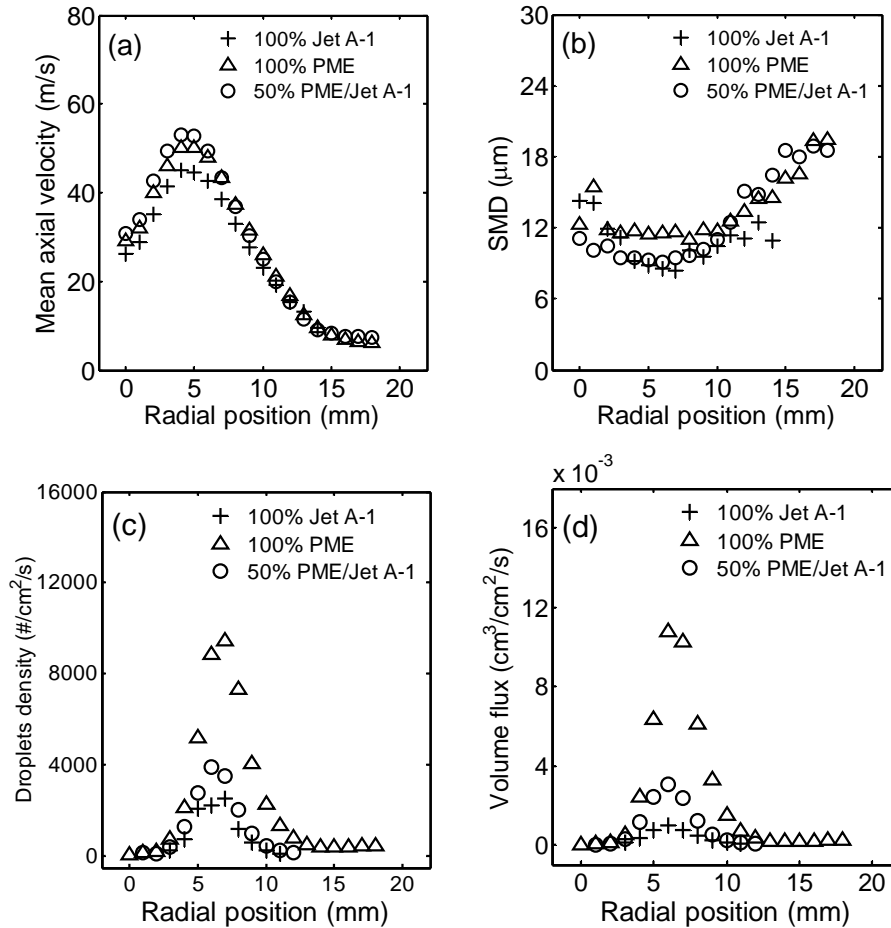
Figure 5.29: Comparison of the droplet (a) velocity, (b) SMD, (c) number density and (d) volume flux profiles between Jet-A1, 50 % PME/Jet-A1 and PME under the same power output condition at the axial location of y = 15 mm from burner exit.

Comparison of the droplet characteristics of spray flames established from Jet-A1, PME and 50 % PME blend with Jet-A1 under the same burner power output of 6 kW is shown in Fig. 5.29. The flame established from the biodiesel blend shows a radial distribution of droplet velocity and SMD profiles similar to Jet-A1 and PME despite the apparent differences in fuel physical properties. This shows the current plain-jet airblast atomizer is effective in atomizing biodiesels and blends with the droplet characteristics comparable to Jet-A1 fuel. The droplet SMD of the biodiesel blend

shows rather similar profiles as Jet-A1 at the radii between x = 0 and x = 10 mm, but slightly lower SMD values than pure PME. The effect of fuel physical properties on spray characteristic is perpetuated in the comparison of droplet concentration and volume flux profiles as shown in Fig. 5.29c and 5.29d respectively. The droplet density profiles show a lower droplet concentration for the biodiesel blend by a factor of 2 compared to PME. Similarly, the volume flux profiles show a lower value for the biodiesel blend by a factor of 3 compared to PME. The spray characteristics of the blended fuels show the expected trend of profiles that fall in between the two parent fuels, although the linearity of the droplet characteristic in relation to the percentage of blend is not evident.
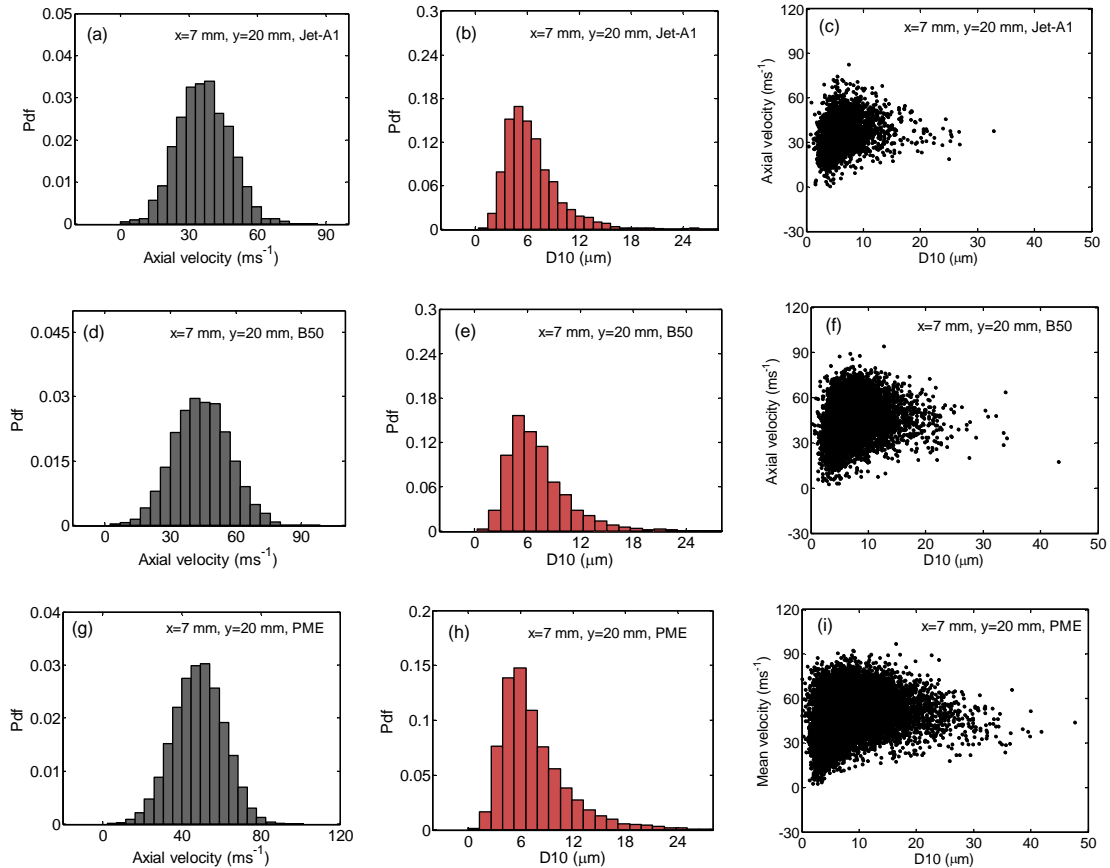
Figure 5.30: Distribution of the droplet (a,d,g) axial velocity (b,e,h) SMD and (c,f,i) droplet size-velocity correlation for Jet-A1, 50 % PME/Jet-A1 and PME swirl flame at spatial location of downstream y = 20 mm and radial position of x = 7 mm under the same power output condition.

The droplet distribution and trajectories at the location of y = 20 mm downstream and radial position of x = 7 mm in the spray flame was investigated. The droplet distributions of velocity, size and the drop velocity-size correlation of PME, Jet-A1 and 50 % PME/Jet-A1 under the same power output of 6 kW are shown in Fig. 5.30. In general, the droplet velocity distributions for all fuels considered are rather similar, with a normal distribution of droplet velocity that spans between 0-80 m/s. The droplet SMD distribution is also similar between the three fuels, although Jet-A1 exhibits a lower PDF peak due to the lower droplet counts. This is evident in the drop velocity-size correlations, where in spite of the relatively similar drop distributions, the number of drops of Jet-A1 is lowest. The presence of large droplets is significantly reduced compared to PME and biodiesel blend. The lower droplet concentration of Jet-A1 compared to other heavier fuels has been shown in Fig. 5.25a. This is because Jet-A1 is relatively more volatile and evaporates faster than PME.

5.3.2 Blend of 50% RME/Diesel

Comparison of the droplet characteristics of 50 % RME blend with the unblended fuels under the same power output condition is shown in Fig. 5.31. The droplet velocity and SMD profiles of the 50 % RME/diesel blend are almost identical to the profiles of diesel and RME as shown in Fig. 5.31a and 5.31b. The indistinguishable droplet size and velocity profiles are not surprising considering the almost identical physical properties between RME and diesel. This concurs with the trend shown in the non-reacting spray investigations where the blend of biodiesel with baseline fuels also exhibits similar profiles as the unblended fuels (section 5.1.3). The droplet concentration and volume flux profiles of the biodiesel blend closely resembles the diesel profiles, indicating the spray droplet characteristic of 50 % RME/diesel blend under the reacting flame is almost similar to diesel fuel. This highlights the compatibility of biodiesel in the burner employing a plain-jet airblast atomizer, in which the nozzle is less dependant on the fuel properties compared to a pressure atomizer.
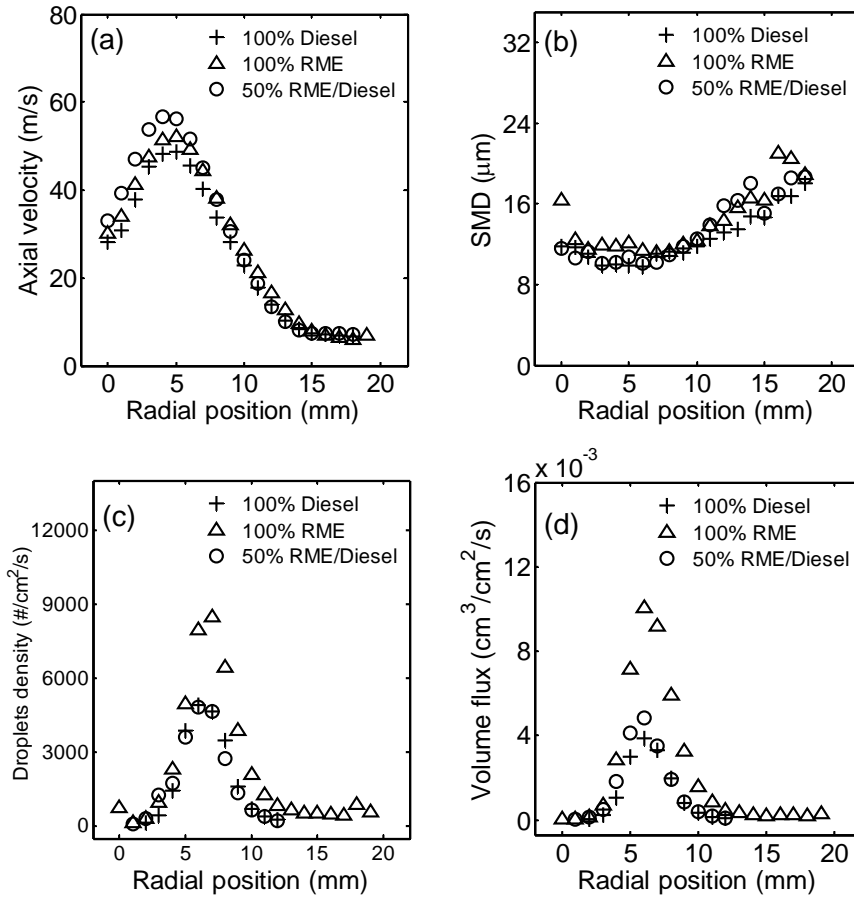
Figure 5.31: Comparison of the droplet (a) velocity, (b) SMD, (c) number density and (d) volume flux profiles between diesel, 50 % RME/diesel and RME under the same power output at the axial location of y = 15 mm from burner exit.

The droplet distribution and trajectories at the spatial position of y = 15 mm downstream of burner outlet and radius x = 5 mm for RME, 50% RME/diesel and diesel are shown in Fig. 5.32. This spatial location within the spray flame corresponds to the peak velocity at the radial profile of y = 15 mm. Comparison of the droplet velocity and size shows almost identical drop distributions between the fuels, highlighting the similarity of the droplet transport behaviour between diesel, RME and the 50 % RME/diesel/blend within the spray flame. The result also shows that the minor differences in that physical property between biodiesel and diesel fuel are not reflected in the flame. Hence, for a gas turbine combustor that employs the present

plain-jet airblast atomizer, the spray characteristics of biodiesel closely resembles diesel fuel.
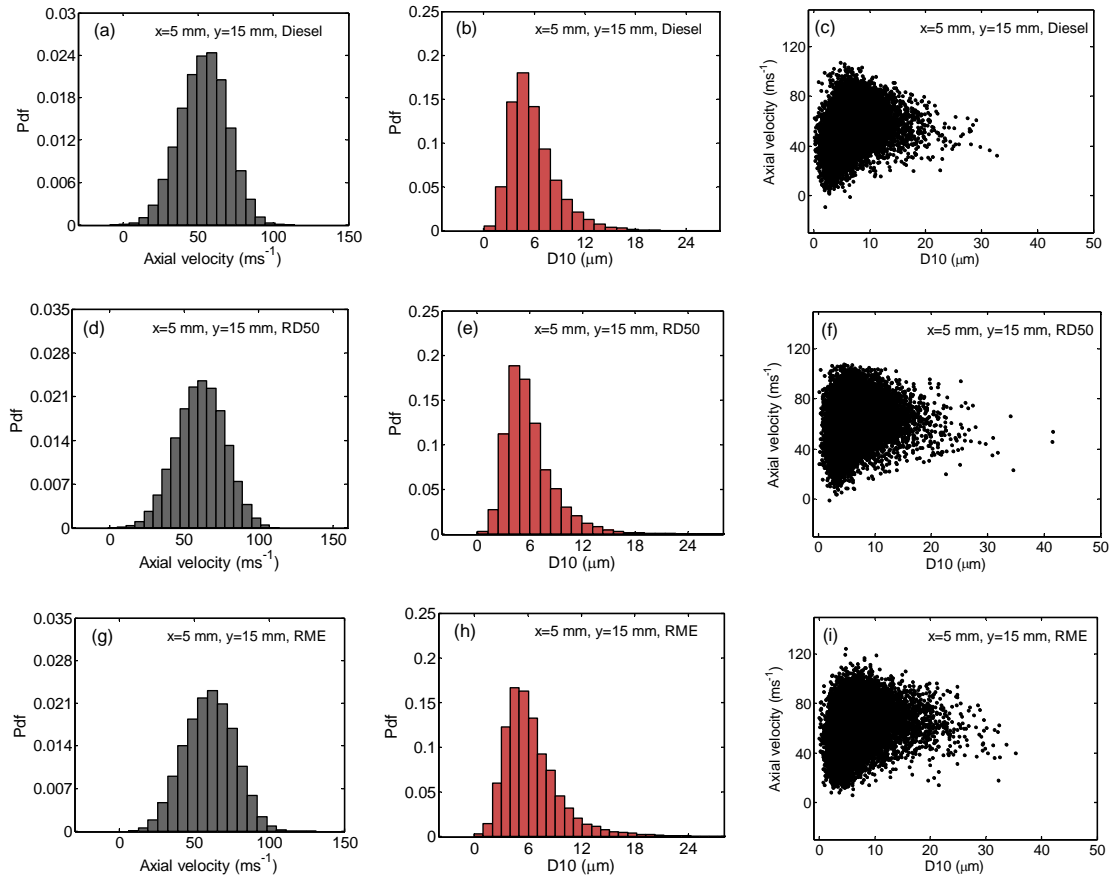
Figure 5.32: Distribution of the droplet (a,d,g) axial velocity (b,e,h) SMD and (c,f,i) droplet size-velocity correlation for (a) diesel, (b) 50% RME/diesel and (c) RME swirl flame at axial position of y = 15 mm and radial position of x = 5 mm under the same power output condition.

5.4 Conclusion

For the non-reacting spray investigation of a plain-jet airblast atomizer, the effect of varying the atomizing air-to-liquid mass ratio on spray is investigated using diesel fuel. The radial profiles of droplets show the distribution of small droplets at the spray centreline region that attain high velocity. As the radial distance from the centreline increases, the droplets become larger with lower velocity. The reduction of SMD with the increase of ALR is effective up to a threshold beyond which further droplet SMD reduction is insignificant. The increase of droplet SMD axially at the centreline region is pronounced for ALR < 4 which could be due to droplet coalescence, redistribution of drops due to the swirling atomizing air or local dispersion of droplets. The effect of fuel physical properties on spray atomization is investigated by comparing the droplet size and dynamics of diesel, Jet-A1, PME and RME at different downstream locations from the nozzle outlet. Biodiesel exhibits larger droplet SMD than diesel and Jet-A1 due to the higher surface tension and viscosity. Droplet velocity appears to be insensitive to the liquid physical properties but primarily to the atomizing air flow rate. Biodiesel blends show relatively similar droplet size and velocity profiles to the unblended fuels. The peaks of the droplet number density and volume flux are found to locate at a distance from centreline. Through the Mie scattering technique, the spray cone angle can be derived by detecting the spray edges of the averaged Mie scattered images. The determined spray cone angle is comparable to the angle determined via the PDA result, where the detection limit of volume flux is identified as the spray edges. This study shows that a plain-jet airblast atomizer is effective to atomize biodiesels and conventional fuels. Despite the difference in droplet ALR, variation of ALR allows the reduction of SMD to match the droplet size of conventional fuels.

The droplet characteristics of the reacting flow under the condition of a swirl burner is investigated. The droplet velocity and SMD profiles are compared under the same burner power output conditions. Under the influence of the co-swirling flow, a reverse flow is induced by the generation of a centre toroidal recirculation zone. The reverse flow interacts with the droplets and lowers the droplet velocity at the spray centreline. PME and RME exhibit the characteristic of larger droplets compared to

diesel and Jet-A1 despite the almost similar velocity profiles. The PME and RME spray flames show higher droplet concentration and volume flux values due to the late vaporisation of the droplets. The Jet-A1 flame presents lower droplet SMD values compared to other hydrocarbons due to its higher volatility, lower surface tension and viscosity. The droplet distribution and trajectories was investigated at several locations within the swirl flame. The spatial distribution of droplets determines the profiles of volume flux and droplet concentration which affects the size and shape of flame reaction zone. The blends of biodiesel/baseline fuels exhibit the expected droplet characteristic behaviour that falls in between the two parent fuels.

5.5 References

[1]   C. D. Bolszo and V. G. McDonell, "Emissions optimization of a biodiesel fired gas turbine," *Proc. Combust. Inst.*, vol. 32, pp. 2949-2956, (2009).

[2]   G. E. Lorenzetto and A. H. Lefebvre, "Measurements of drop size on a plain jet airblast atomization," *AIAA J.*, vol. 15, pp. 1006-1010, (1977).

[3]   N. K. Rizk and A. H. Lefebvre, "Spray characteristics of plain-jet airblast atomization," *J. Eng. Gas Turb. Power*, vol. 106, pp. 634-638, (1984).

[4]   J. Kamrak, B. Kongsombut, G. Grehan, S. Saengkaew, K.-S. Kim, and T. Charinpanitkul, "Mechanistic study on spraying of blended biodiesel using phase Doppler anemometry," *Biomass and Bioenergy*, vol. 33, pp. 1452-1457, (2009).

[5]   H. Eroglu and N. Chigier, "Initial drop size and velocity distributions for airblast coaxial atomizers," *J. Fluids Eng.*, vol. 113, pp. 453-459, (1991).

[6]   C.-P. Mao, G. Wang, and N. Chigier, "An experimental study of air-assist atomizer spray flames," *Symp. (Intl.) Combust.*, vol. 21, pp. 665-673, (1988).

[7]   J. C. Lasheras and E. J. Hopfinger, "Liquid jet instability and atomization in a coaxial gas stream," *Ann. Rev. Fluid Mech.*, vol. 32, pp. 275-308, (2000).

[8]   G. Preaux, J. C. Lasheras, and E. J. Hopfinger, "Atomization of a liquid jet by a high momentum coaxial swirling gas jet," in *Pro. 3rd Int. Conf. Multiphase Flow*, Lyon, France, 1998.

[9]   H. V. Panchasara, B. M. Simmons, A. K. Agrawal, S. K. Spear, and D. T. Daly, "Combustion performance of biodiesel and diesel-vegetable oil blends in a simulated gas turbine burner," *J. Eng. Gas Turb. Power*, vol. 131, pp. 031503.1-031503.11, (2009).

[10]   S. Nakamura, V. McDonell, and S. Samuelsen, "The effect of liquid-fuel preparation on gas turbine emissions," *J. Eng. Gas Turb. Power*, vol. 130, pp. 021506:1-11, (2008).

[11]   C. Presser, A. K. Gupta, and H. G. Semerjian, "Aerodynamic characteristics of swirling spray flames: Pressure-jet atomizer," *Combust. Flame*, vol. 92, pp. 25-30, IN1-IN2, 31-44, (1993).

Chapter 6

PIV, chemiluminescence and emissions results and discussion

In this chapter, the results of the swirl burner flow field under reacting and non-reacting flows obtained from particle imaging velocimetry (PIV) are presented, followed by the results of flame chemiluminescence and emissions measurements using the swirl burner. The descriptions of the experimental setup and operating conditions are shown in Chapter 4.

6.1 PIV results and discussion

6.1.1 Non-reacting flow field in open air

2D PIV was initially performed to characterize the flow fields of the swirl burner under unconfined (open air) condition. An example of the cross-correlated velocity vector map for a non-reacting flow in open air at room temperature is shown in Fig 6.1. The velocity vector map shows a symmetrical swirling flow field at the exit of the burner outlet. The swirling flow consists of axial, radial and tangential velocity components. The 2D PIV vector map derived here displays the axial and radial components. At the burner centreline region, a reverse flow is generated by two toroidal recirculation zones near the burner outlet. The surrounding air is entrained into the main flow at region between $\pm$ 40 and $\pm$ 20 mm as a result of the adverse

pressure gradient induced by the recirculation zones. The flow is seen to diverge outwards from the burner centreline at position 30 mm downstream of the burner. The axial and radial velocity profiles at 10, 20, 30 and 40 mm downstream of the burners for the air flow of 4.36 g/s are demonstrated in Fig 6.2a and 6.2b.

In general, the axial velocity profiles of the swirling flows exhibit the bimodal shape as demonstrated in Fig. 6.2a. At regions near the centreline between the radial position $\pm$ 10 mm, the reverse flow shows the negative velocity values as the centre recirculation zone drives the flow upstream towards the burner outlet. The flow spreads wider further downstream of the burner, with reduced peak velocity magnitudes. Radial velocity profiles at 10 mm from burner outlet exhibit the highest radial velocity peak as shown in Fig 6.2b. The magnitude of the radial velocity component is highest near the exit of the burner but recedes at downstream locations of the burner. At 40 mm from burner exit, the radial component becomes insignificant but the counterpart axial velocity component shows the peak magnitude of ~ 3.0 m/s, indicating the straightening of the flow.
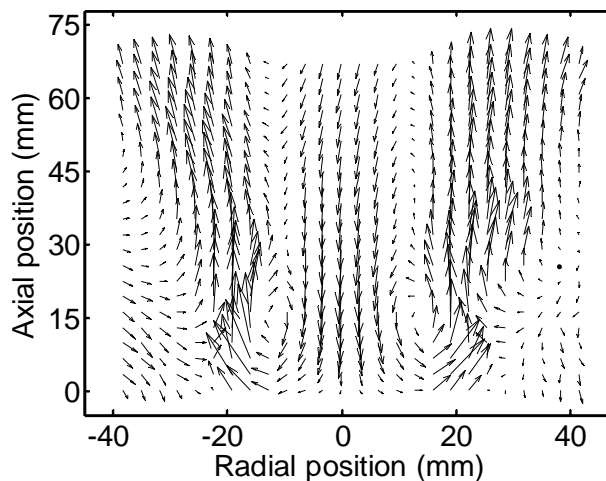
Figure 6.1: Mean 2D velocity vector map for the non-reacting swirling air flow of 4.36 g/s at T = 20 ºC without the spray injection.
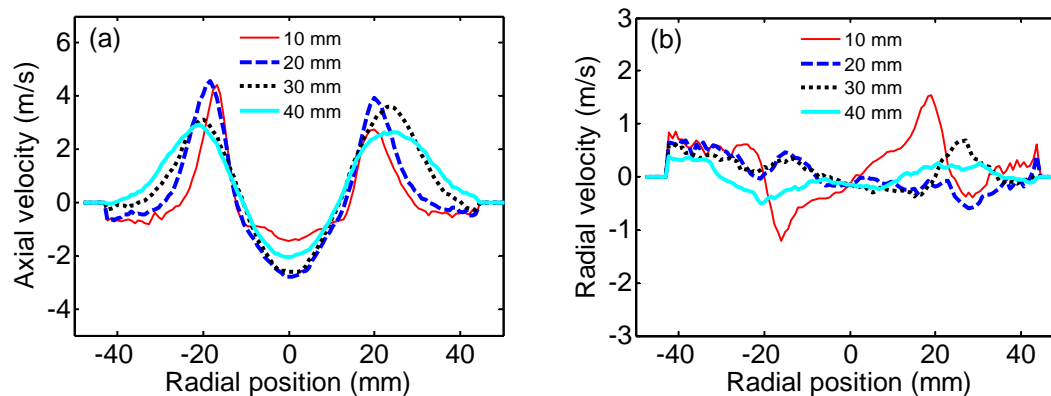
Figure 6.2: Mean (a) axial and (b) radial velocity profiles for the swirling flow with 4.36 g/s at T = 20 ℃.

6.1.2 Effect of temperature on flow field

The swirling air flow is preheated to temperatures of 150 ℃ and 250 ℃. The axial velocity profiles at 20 and 30 mm from burner outlet is shown in Fig 6.3a and 6.3b respectively. Comparison of the profiles shows that preheating the air flow gives the same characteristic flow profile albeit with different peak velocity magnitudes. At the axial position of 20 mm from burner outlet, the peak velocity at room temperature is located at the radial position 19 mm from burner centreline with the magnitude of ∼ 4.6 m/s. The peak velocities of the preheated cases of 150 ℃ and 250 ℃ fall at the same radial locations as the non-heated case with the peak magnitudes of 7.5 m/s and 9.3 m/s respectively. The intensity of the recirculation zone is increased as the main air is preheated. This is evident as the peak magnitude of the reverse flow towards the burner outlet at the centreline increases from 2.8 m/s at T = 20 ℃ to 4.3 m/s at T = 250 ℃. Figure 6.3b shows the velocity profiles at 30 mm downstream of the burner exit. The trend is similar to the profile at 20 mm where the preheating effect increases the air flow velocity. As the distance from the burner outlet increases, the axial velocity profiles become wider with reduced peak velocities due to the spread of the flow.

The radial velocity profiles of the swirling flows at the position 10 mm and 20 mm from burner exit are shown in Fig. 6.3c and 6.3d respectively. The magnitude of the radial velocity increases correspondingly with the increase in temperature due to the expansion of flow and the reduction of air density. The influence of the preheating air is significant for radial profiles at 10 mm. Beyond 10 mm downstream, the radial velocity components recedes as the flow is straightened.
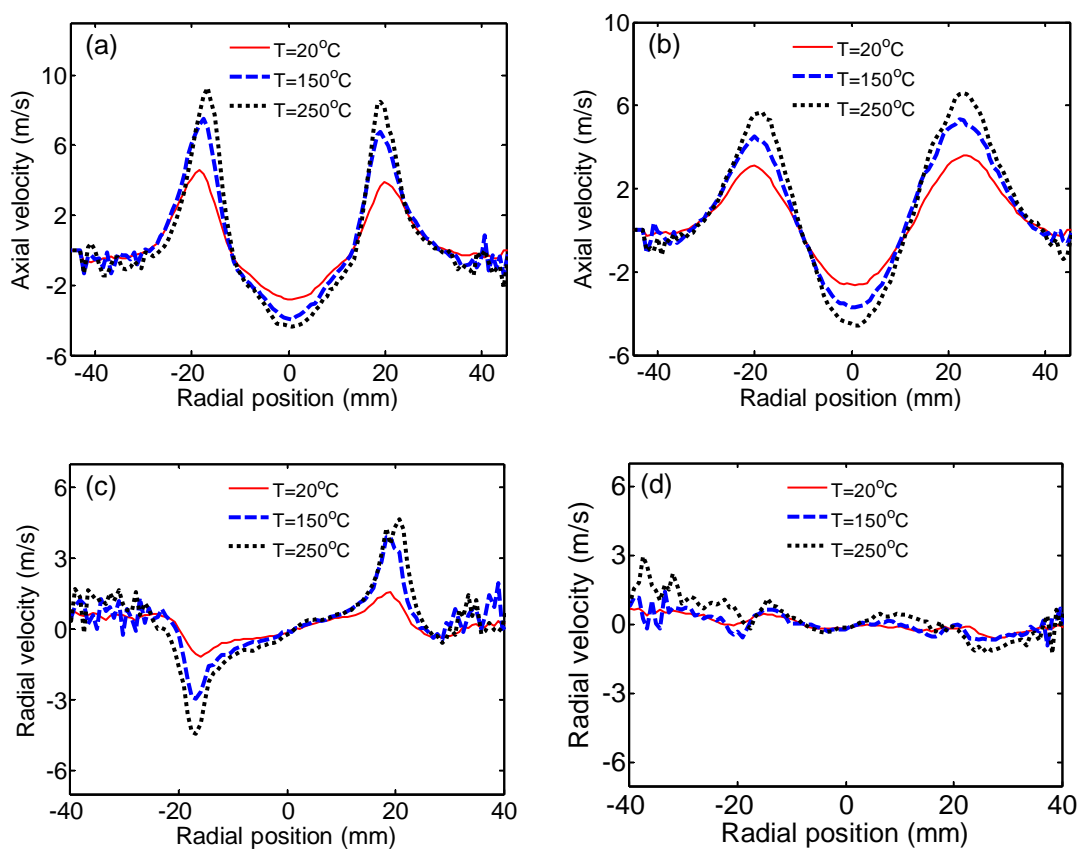
Figure 6.3: Mean axial velocity profile at positions (a) 20 mm, (b) 30 mm and radial velocity profiles at positions (c) 10 mm, (d) 20 mm from the burner outlet at different temperatures for the flow of 4.36 g/s.

6.1.3 Effect of air flow rate on flow field
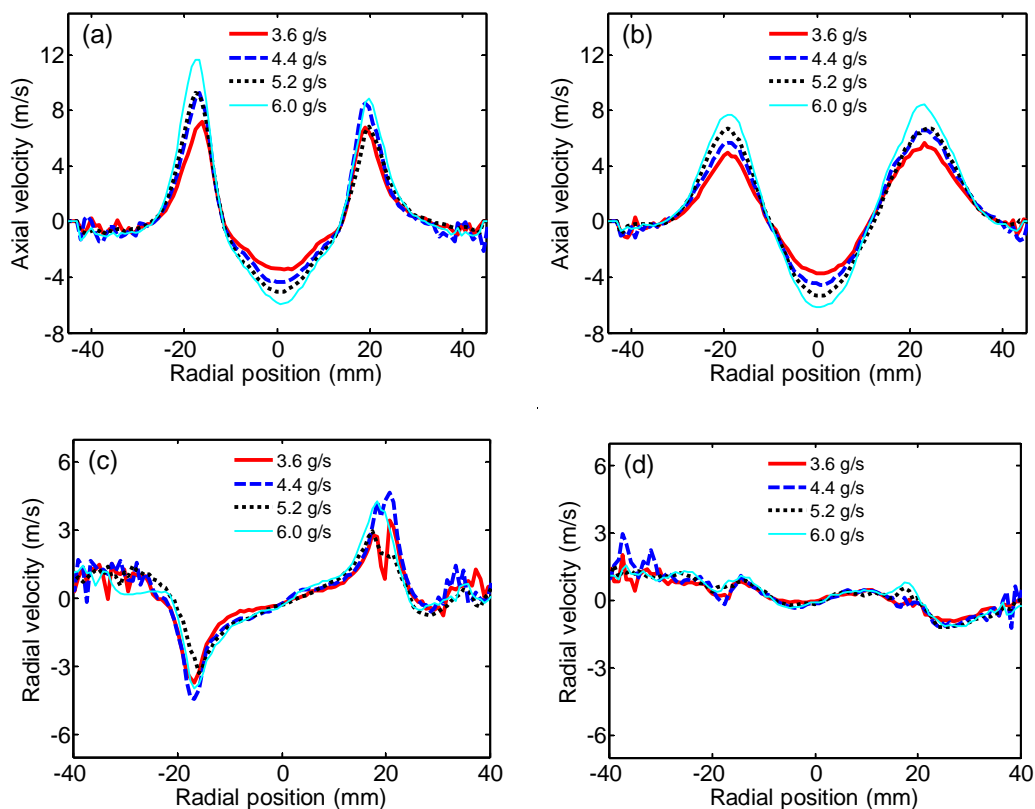
Figure 6.4: Mean axial velocity profile at positions (a) 20 mm, (b) 30 mm and radial velocity profile at positions (c) 10, (d) 20 mm from the burner outlet for different air mass flow rates at an elevated temperature of T = 250 ℃.

The effect of air flow rate variation on the velocity profiles is investigated within the range that will be operated under the reacting flow conditions. The bulk air flows of 3.57, 4.36, 5.15 and 5.95 g/s are preheated to T = 250 ℃. The axial velocity profiles at 20 and 30 mm downstream of the burner outlet are shown in Fig. 6.4a and 6.4b respectively. The profiles show that the peak velocity magnitudes increase correspondingly to the increase of main air flow rates. At the axial location of 20 mm, the peak velocity of 5.95 m/s locates at the radial position of 19 mm with the peak magnitude of 11.7 m/s. The corresponding peak magnitude of the reverse flow is 6 m/s. The peak axial velocity reduces to 8.4 m/s at axial location 30 mm burner downstream. The peak location shifts radially outwards to 22 mm from burner centreline. The radial

velocity profiles are less influenced by the variation of flow rates. At 10 mm from burner outlet, the velocity peaks at the radial location of 17 mm with similar magnitudes as shown in Fig. 6.4c. The similarity of the radial velocity profiles is again shown at 20 mm from burner outlet in Fig. 6.4d.

6.1.4 Effect of liquid spray on flow field

The influence of liquid spray on the velocity flow field is investigated via 2D PIV. The velocity vector maps, superimposed on the spray images generated from Jet-A1 and diesel fuels at T = 20 °C and T = 200 °C are presented in Fig. 6.5a-d. The swirling sprays shown here were conducted at open atmospheric pressure without enclosure. The sprays are produced with the fuel and atomizing air mass flow rates of 0.14 g/s and 0.28 g/s respectively. The main swirling air flow imposes a centrifugal force that pulls the spray apart to form a wide angle spray flow. The formation of a central toroidal recirculation zone is clearly noticeable in all spray flows. The reverse flow conveys droplets from the air/spray shear layers upstream towards the burner outlet. The flow field with the swirling spray is significantly different from the flow field without the liquid spray. The interaction of the swirling air with spray causes the flow field to be widened. The size and intensity of the central recirculation zone is also enhanced compared to the flow without a spray. The air flow temperature also plays an important role. Figure 6.5b shows that Mie scattered Jet-A1 fuel spray region at T = 200 °C is significantly smaller compared to the liquid fuel spray at T = 20 °C (Fig. 6.5a). This is because most droplets are evaporated due to the high volatility and high surface area-to-volume droplets of Jet-A1 fuel. For diesel fuel spray, the elevated temperature of T = 200 °C is not sufficiently high to completely vaporise the droplets and hence the liquid fuel spray region is largely visible in Fig. 6.5d. The diesel spray images in Fig. 6.5c and 6.5d clearly show the droplets sheared by the air flows are entrained by the centre recirculation zone back to the centreline region. This phenomenon is known to contribute to flame stabilization in reacting flow. Mie scattering of the liquid jet spray without the main swirling flow was shown in Fig. 5.20 in Chapter 5. The liquid jet spray, swirling air flow and the flow field as a result of interaction between the liquid jet spray and main swirling flow are shown in Fig. 6.6.
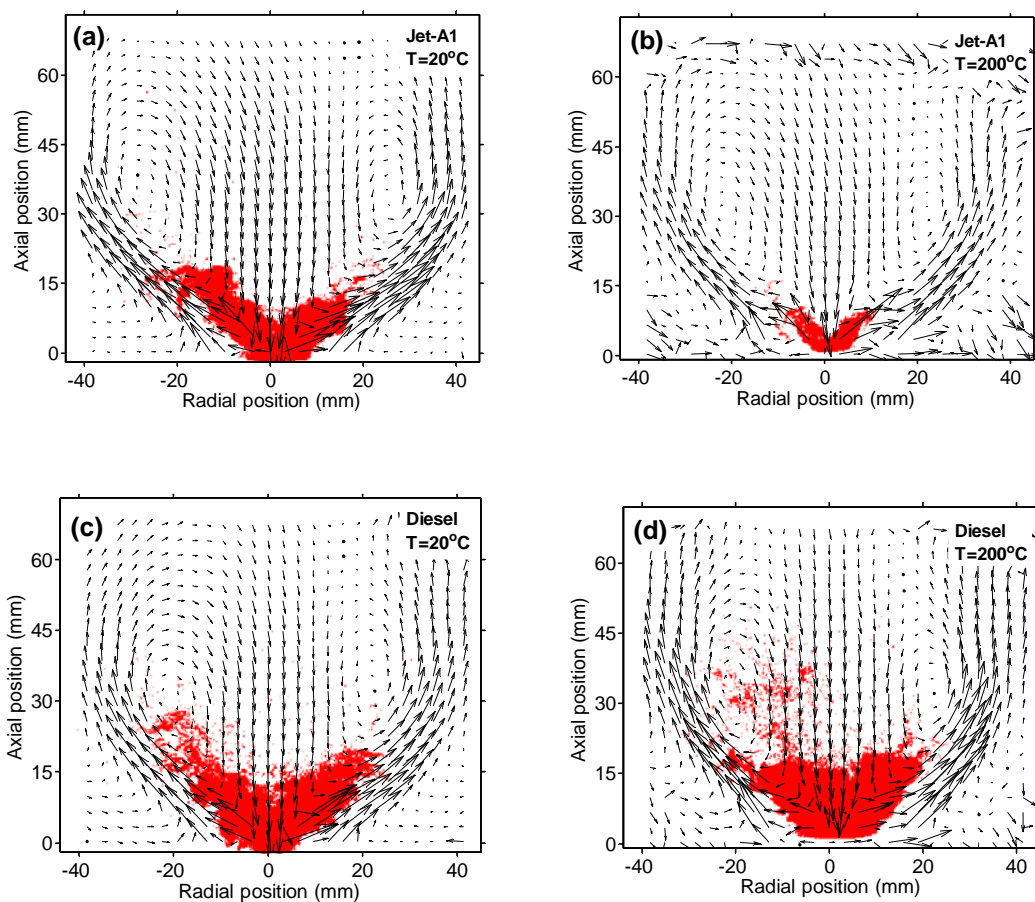
Figure 6.5: Mean 2D vector maps (averaged 300) superimposed on the instantaneous Mie scatter images of spray for (a,b) Jet-A1 and (c,d) diesel obtained at T = 20 ºC and T = 200ºC. The main air and fuel mass flow rates are maintained constant at 4.36 g/s and 0.14 g/s respectively.
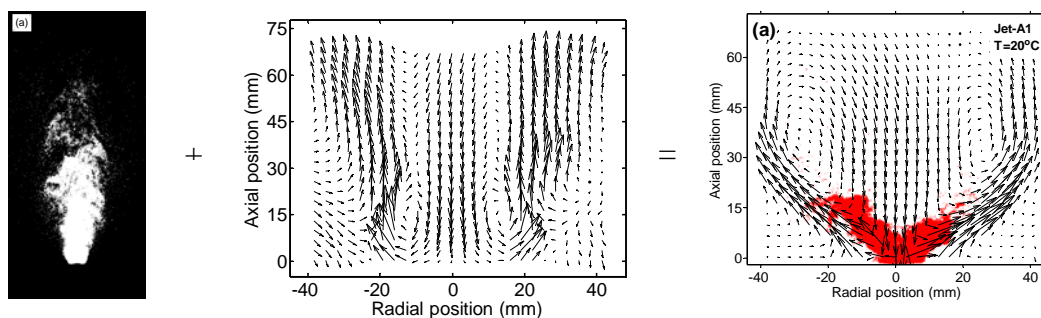
Figure 6.6: (a) Instantaneous Mie-scattered liquid jet spray (b) flow field of main swirling flow and (c) the swirling spray flow field with the instantaneous Mie scattered jet spray.

An example of the 2D velocity map obtained from the non-reacting swirling spray flow is shown in Fig. 6.7. The swirl spray is established with the main air flow rate of 4.36 g/s. The liquid fuel spray is established with 0.14 g/s and 0.28 g/s of diesel fuel and atomizing air respectively. The corner recirculation zone is not present as the flow is unconfined. The axial and radial velocity profiles of the burner downstream are shown in Fig. 6.8a and 6.8b respectively. The axial velocity profile at the location of 10 mm from the burner outlet in Fig. 6.8a indicates a strong centre recirculation zone with the magnitude velocity of ∼ 6 m/s. The peaks of the reverse flow at 20, 30 and 40 mm burner downstream show the magnitude velocity of ∼ 2.5 m/s. Figure 6.8b shows a strong radial velocity with the peak magnitude of ∼ 5 m/s and ∼ 3 m/s at burner downstream locations of 10 and 20 mm respectively. The radial velocity is weakened at 30 mm from burner exit due to the transition of flow induced by the centre recirculation zone. The formation of a centre recirculation zone results from the lower inner core pressure and the aerodynamic blockage imposed by the bluff body near the exit of the burner. The swirling flow creates a strong shear layer with the liquid spray due to the velocity differences that assists in the breakup of droplets.
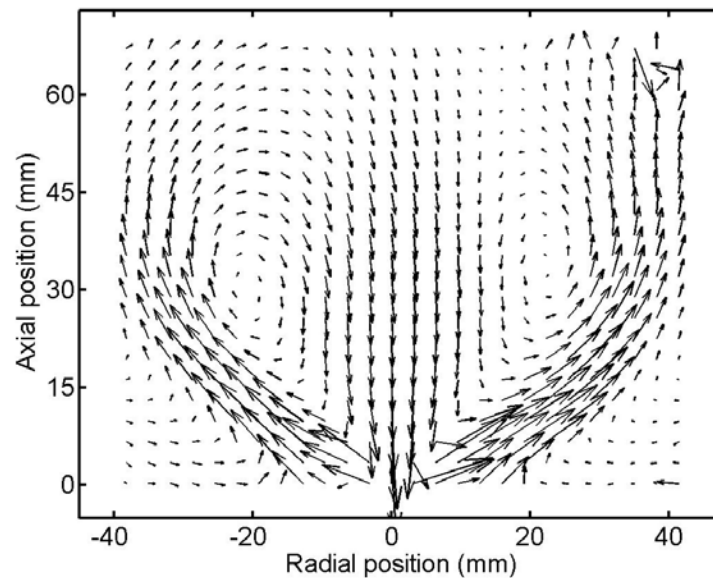
Figure 6.7: 2D Velocity vector map for the non-reacting swirling flow established with 4.36 g/s of air and 0.14 g/s of diesel fuel spray at T = 20 ℃.
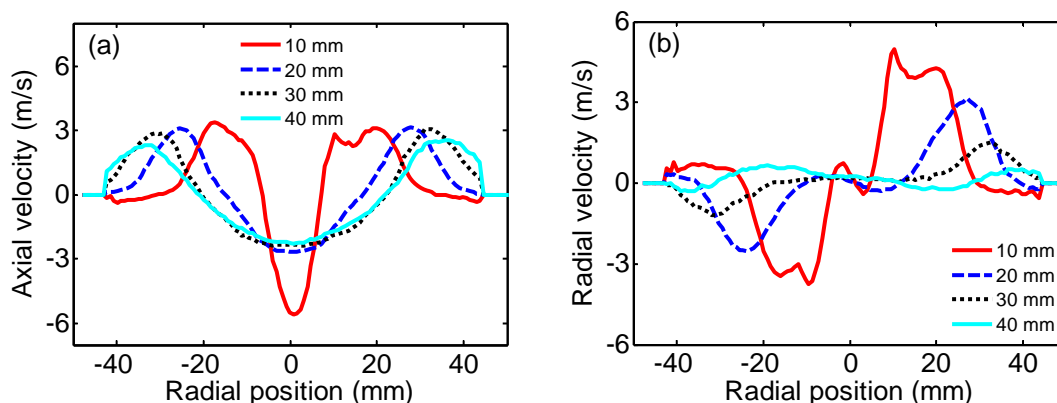
Figure 6.8: Mean (a) axial and (b) radial velocity profiles for the swirling flow of 4.36 g/s with diesel spray at room temperature. The spray is produced from diesel fuel and atomizing air mass flow rates of 0.14 g/s and 0.28 g/s respectively.

6.1.5 Comparison of flow field with and without spray

Comparison of the velocity profiles between the swirling flow with and without spray is shown in Fig. 6.9. The axial velocity profiles at axial locations y = 10 and 30 mm from burner exit are shown in Fig. 6.9a. At 10 mm from burner exit, the reverse flow for the swirling spray flow is distinctively stronger. The swirling spray flow exhibits wider axial velocity profiles but with lower peak velocities than without the spray. At y = 30 mm, the peak of the spray flow locates at a radial position x = 30 mm whereas the non-spray flow peak locates at x = 22 mm from burner centre. The maximum magnitudes of the reverse flow for both flows are ~ 2.5 m/s at this axial location. The axial velocity profiles for locations of y = 20 and 40 mm from burner exit are shown in Fig. 6.9b. The spray flow shows broader profiles with lower peak velocities compared to the non-spray swirl flow. This means the spray flow spreads out radially when the swirling air interacts with the centre jet spray. The reverse flow shows a similar peak velocity magnitude of ~ 2.6 m/s for both flows at the downstream location of y = 20 mm.
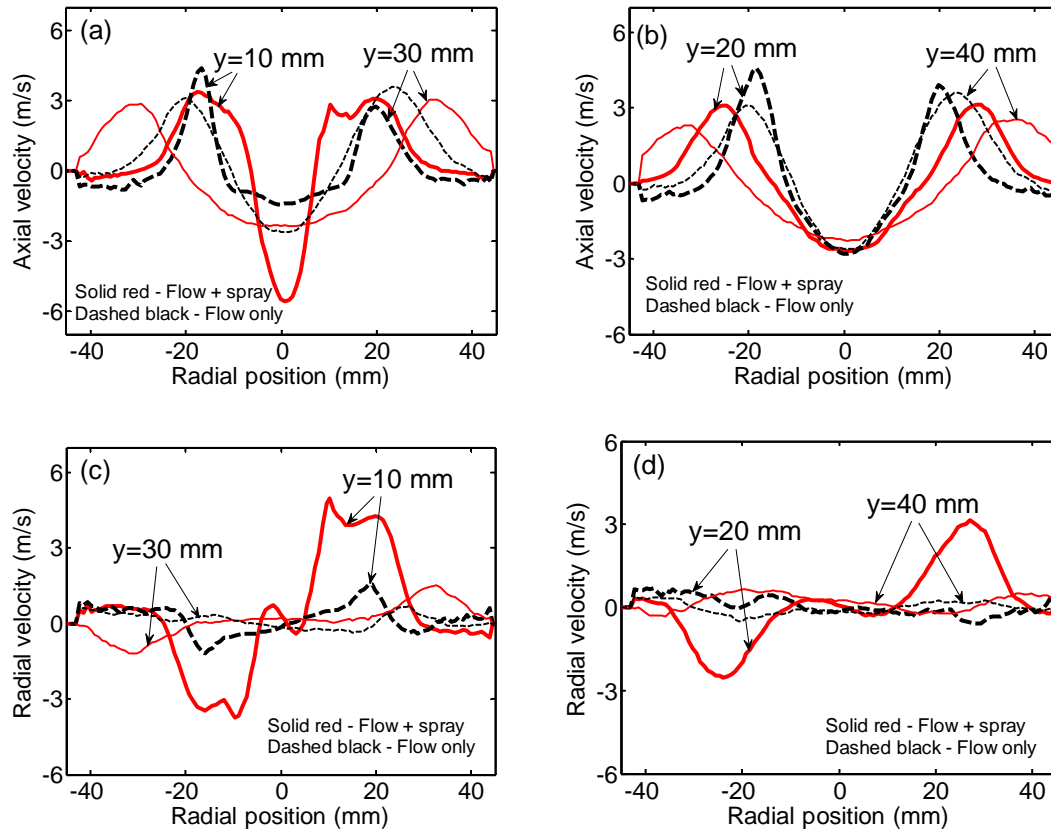
Figure 6.9: Comparison of mean (a, b) axial and (c, d) radial velocity profiles between swirling flow with no spray and swirling flow with diesel spray established at room temperature.

The spray flow shows higher radial velocity magnitude than the non-spray flow by a factor of 3 at 10 mm from burner exit as shown in Fig. 6.9c. At y = 30 mm downstream, both the flows show peak radial magnitude of 1.5 m/s but at different radial positions from the burner. The strong radial component is again shown at the axial location of y = 20 mm in Fig. 6.9d where the peak locates at x = 25 mm from centreline with the magnitude of ~ 2.8m/s. The radial component is not evident for both flows at 40 mm burner downstream as the recirculation zone starts changing the direction of the radial flow.

6.1.6 Non-reacting flow in an enclosed environment

A quartz tube is placed concentrically with the swirl burner outlet to form a generic dump combustor. An example of a vector map derived from the air flow rate of 4.36 g/s without spray within the combustor is shown in Fig. 6.10. The PIV sheet is focused on a half plane of the combustor to enhance the spatial resolution of the vector map. The enclosure induces the formation of corner recirculation zone at the burner outlet and near the wall. The radial position of x = 0 mm indicates the centreline of the burner. The reverse flow formed through the center recirculation zone flows upstream towards the burner outlet. At an axial distance of 25 mm, the flow splits and creates either the corner recirculation zone or centre recirculation zone. The formation of the centre recirculation zone is initiated at location 30 mm from the burner outlet. The absence of vectors at radial position x = -28 mm is due to the reflection from the quartz tube. The axial and radial velocity profiles are shown in Fig. 6.11a and 6.11b respectively.

At the radial position between x = -18 and -40 mm from centreline and at y = 10 mm, the flow moves downstream, as indicated in Fig. 6.11a. The corner recirculation zone causes the flow to reverse direction when approaching the side wall. At the 30 mm downstream location, the flow impinging on the wall splits and forms the centre recirculation zone as indicated by the negative values of axial velocity. The dashed line marks the region where the reflection from the wall that prevents the derivation of accurate velocity vectors.

The radial velocity profiles at an axial location of 10 mm indicates the maximum radial component occurring at the radial position of x = -22 mm. The positive velocity values at radial position of x = -33 mm onwards marks the boundary of the corner recirculation zone. At y = 20 mm downstream, the peak radial velocity locates at the radial position of x = -32 mm from the centreline as the flow approaches the wall. The radial profile at 30 mm downstream shows the presence of central recirculation flow at the region between x = 0 and -25 mm where the magnitude is near zero. Downstream at 40 mm, the radial velocity is near zero as the flow is dominated by the axial recirculation flow heading towards the burner outlet.
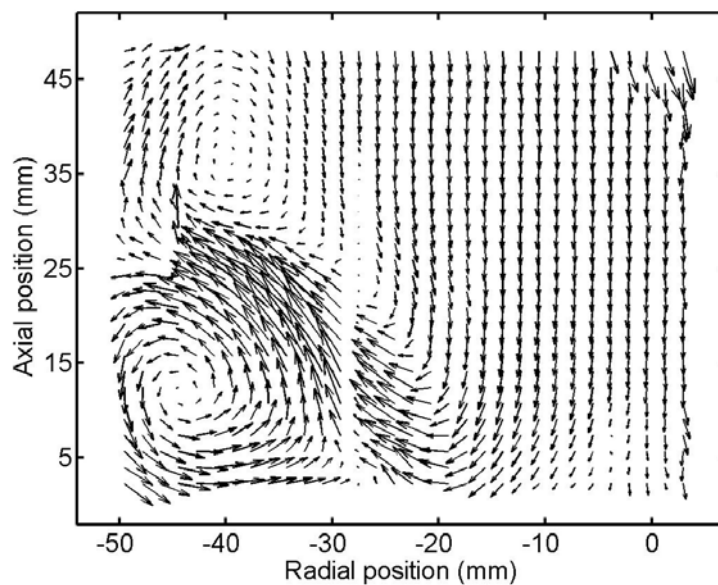
Figure 6.10: 2D velocity vector map for the non-reacting swirling flow established with 4.36 g/s of air at T = 20 ºC.
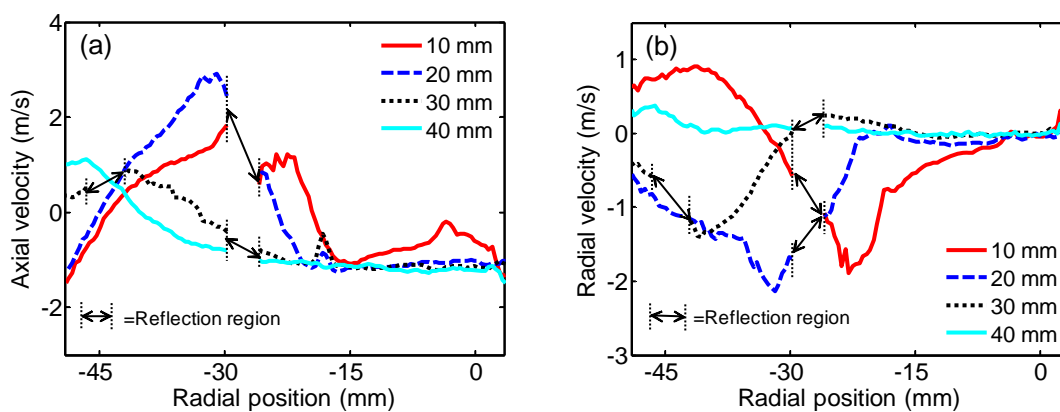
Figure 6.11: (a) Mean axial and (b) radial velocity for the swirling flow of 4.36 g/s within the enclosure at room temperature.

183

6.1.7 Comparison of flow field with and without enclosure

The effect of the enclosure on the flow field is shown through the comparison of axial and radial velocity profiles in Fig. 6.12. With the presence of the enclosure, the flow is pulled towards the wall due to the difference in pressure to form a corner recirculation zone. This causes the peaks of the axial velocity profiles for the enclosed flow to shift radially as seen in the downstream position of y = 10 and 20 mm. The peak axial velocities are lower but the magnitude of the radial velocities increase. The reverse flow region is wider for the enclosed flow compared to the open flow as shown in the axial velocity profiles at the location of y = 30 and 40 mm from burner outlet.
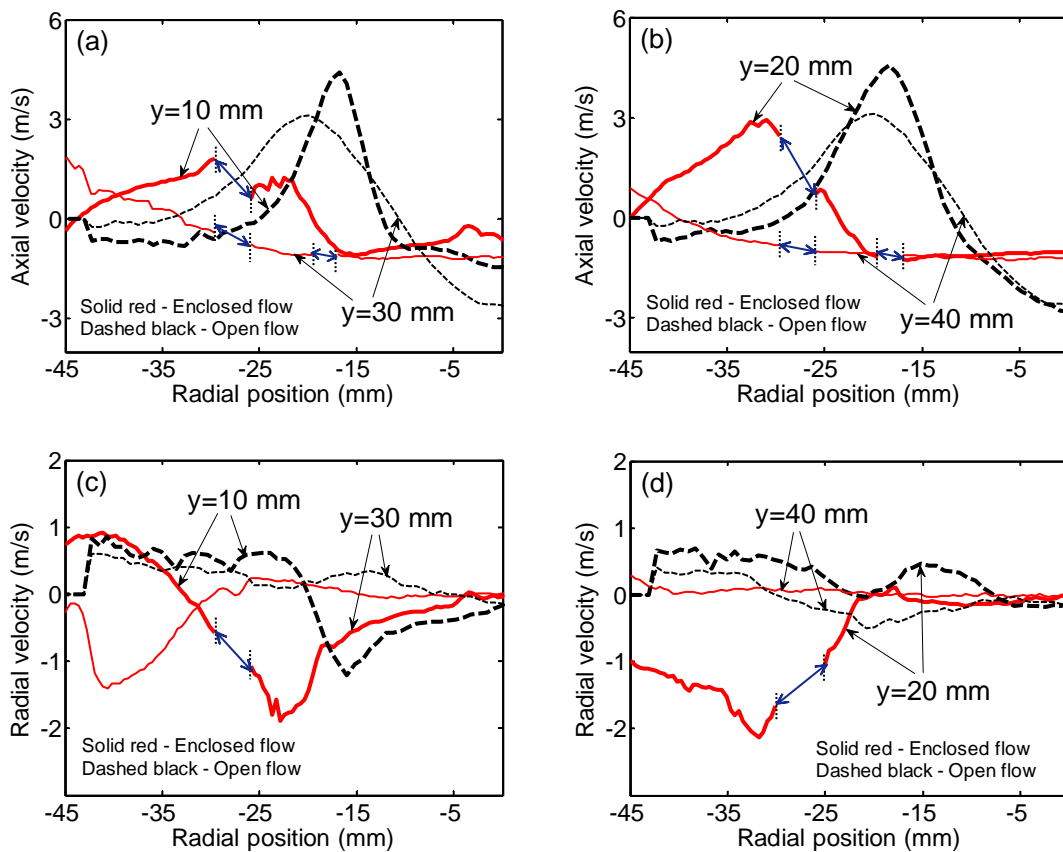
Figure 6.12: Comparison of the (a, b) axial and (c, d) radial velocity profiles between the enclosed swirling flow and the open swirling flow established at T = 20 ℃. Both flows are established with 4.36 g/s of air.

The radial velocity increases for flows within the enclosure. At 10, 20 and 30 mm from burner exit, the radial profile shows an increased velocity magnitude compared to the non-enclosed flow. The radial velocity component subsides at 40 mm downstream for the enclosed flow, indicating the dominance of the axial reverse flow. The positive radial velocity values shown by the open flow at radial positions between x = -22 mm and -45 mm for profiles at y = 10 and 20 mm burner downstream is due to the effect of flow entrainment.

6.1.8 Non-reacting spray flow in an enclosed environment

The velocity vector of the PME spray with a swirling air flow in the combustor is shown in Fig. 6.13. The corner recirculation zone is observed to have elongated radially compared to the non-spray flow shown in Fig. 6.10. This is due to the influence of the relative velocity difference between the air flow and the spray. The spray with a higher velocity induces the air flow towards its direction.
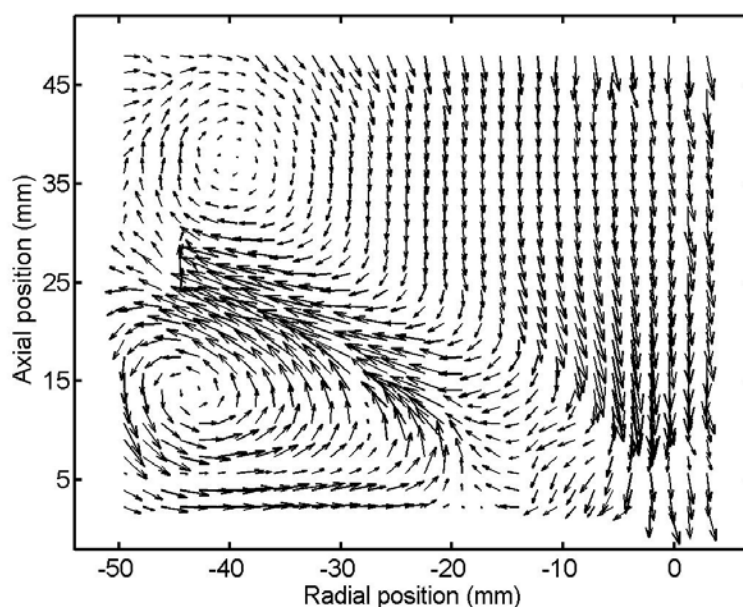
Figure 6.13: Mean 2D velocity vector map for the swirling flow with PME spray established with 4.36 g/s of air at T = 350 ºC. The atomizing air and PME mass flow rates are 0.28 g/s and 0.14 g/s respectively.

To investigate the effect of fuel type on the flow field within the enclosure, PME and diesel fuels were used to generate the swirling spray flow. Both cases are established at the same flow conditions. The main air flow is preheated to T = 350 ℃ at the air mass flow rate of 4.36 g/s. The atomizing air and fuel mass flow rates are 0.28 and 0.14 g/s respectively. Overall, comparison of the axial and radial velocities of both spray flow shows almost identical profiles. This indicates that the effect of fuel type on the swirling flow is negligible.
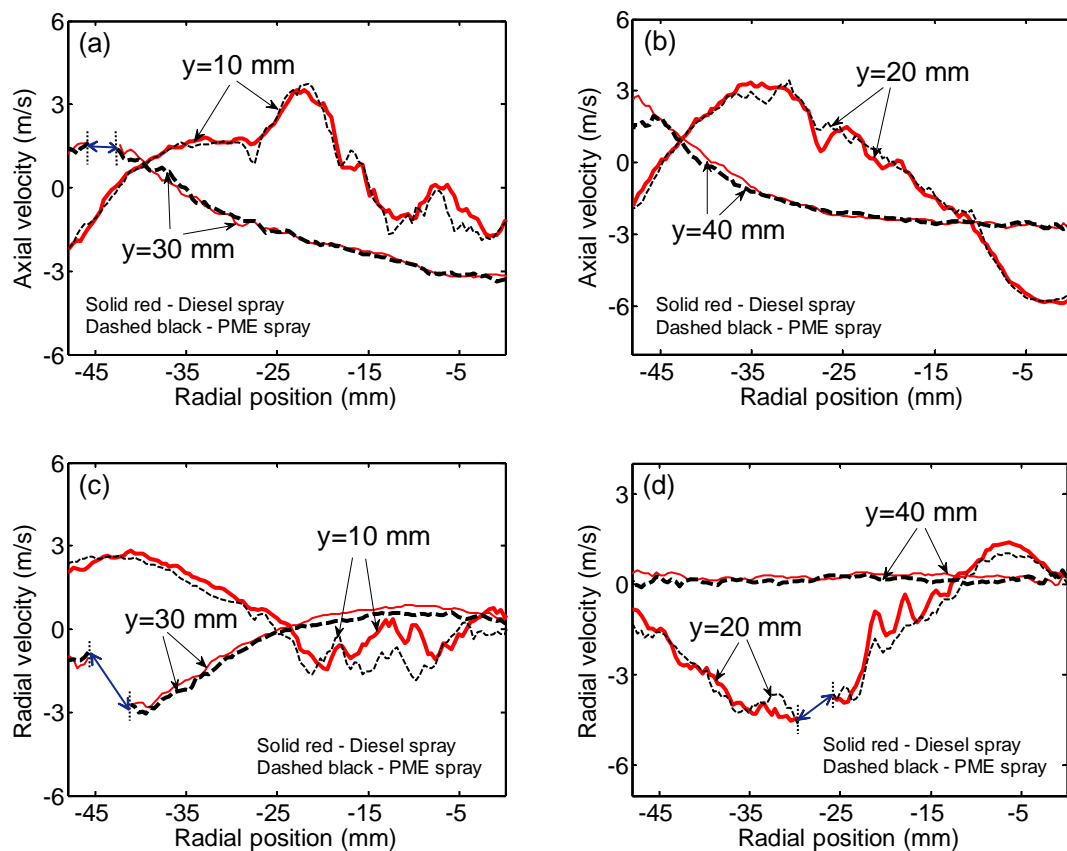
Figure 6.14: Comparison of the mean (a, b) axial and (c, d) radial velocity profiles between the enclosed swirling flow for diesel and PME spray established at T = 350 ℃. The atomizing air and liquid fuel mass flow rates are 0.28 g/s and 0.14 g/s respectively.

The axial velocity profiles in Fig. 6.14a and 6.14b show that the recirculation zone dominates at the downstream axial location of y = 30 and 40 mm with the reverse axial flow. The reverse flow decelerates when approaching the burner as indicated by

186

the lower peak centreline axial velocity of -2.3 m/s at axial location 10 mm compared to the -6 m/s at 20 mm downstream. The corner recirculation zone region exhibits a low axial velocity magnitude of <1 m/s as shown by the profile at y = 10 mm between the radial location of x = -25 mm and the wall.

The corresponding radial velocity profiles are shown in Fig. 6.14c and 6.14d. The radial profile of 10 mm from burner exit exhibits a distinctive positive region representing the corner recirculation zone with the peak of ~ 2.8 m/s. The radial velocity magnitude of the shear layer region is around ~ 3m/s at y = 20 and 30 mm from burner outlet. The region between radial position x = 0 and -20 mm shows the reverse flow region with indistinctive radial velocity. The radial component subsides as the corner recirculation zone is no longer present.

6.1.9 Reacting flow within an enclosure

The 2D velocity map of the reacting flow established with the PME spray in an enclosed environment is shown in Fig. 6.15. The corner recirculation zone of the spray flame is straightened compared to the elongated non-reacting spray case as shown in Fig. 6.13. When the main bulk flow of spray flame approaches the wall, the flow is seen to split at a radial distance of x ~ 10 mm from the wall to form recirculation zones. The flow directed downstream forms the central toroidal recirculation zone while the upstream flow forms the corner recirculation zone. The axial and radial velocity profiles are shown in Fig. 6.16a and 6.16b respectively.

The peaks of the axial velocity profiles shown in Fig. 6.16a correspond to the shear layer region where the axial velocity magnitude is the highest. The peak velocities are approximately ~ 4-4.3 m/s for the axial locations of 10, 20 and 30 mm from burner exit. The reverse flow at the centreline region shows the peak magnitude of ~ 7 m/s at the axial location 20 mm. The flow decelerates to 2.3 m/s at a 10 mm axial distance. The corner recirculation zone region exhibits low axial velocity magnitudes of <1 m/s as indicated by the radial position between -25 mm and the wall. The corresponding radial velocity profiles are shown in Fig. 6.16b. The radial profiles at 10 mm from burner exit shows a distinctive positive curve with the peak magnitude of ~ 2.8 m/s for the corner recirculation zone. The radial velocity magnitude of the shear regions at

downstream locations 20 and 30 mm from burner outlet are ~ 3 m/s. The peak radial velocity component weakens to ~ 2.3 m/s at the radial position of x = -35 mm from centreline.
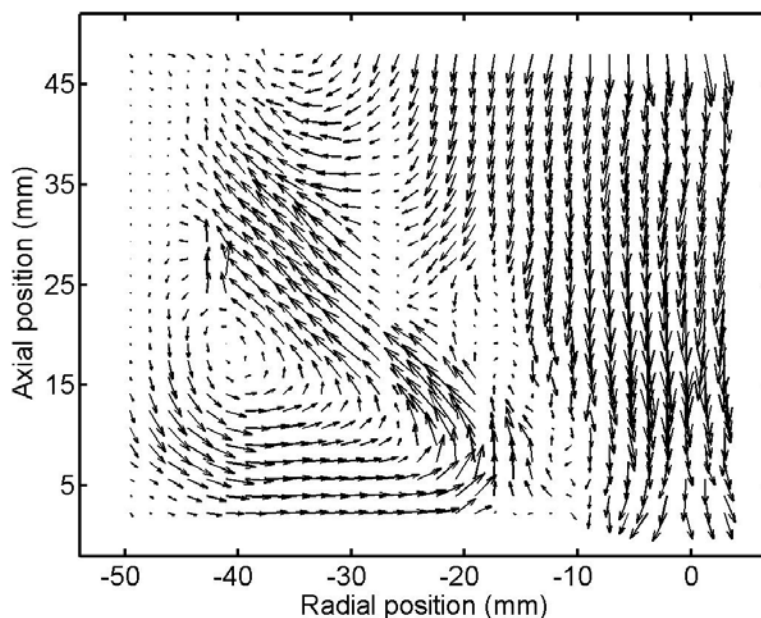
Figure 6.15: Mean 2D velocity vector map for the reacting flow with PME spray established with 4 g/s of air at T = 350 ºC. The atomizing air and PME mass flow rates are 0.32 g/s and 0.16 g/s respectively. The overall equivalence ratio is $\phi = 0.47$ and the power output is 6 kW.
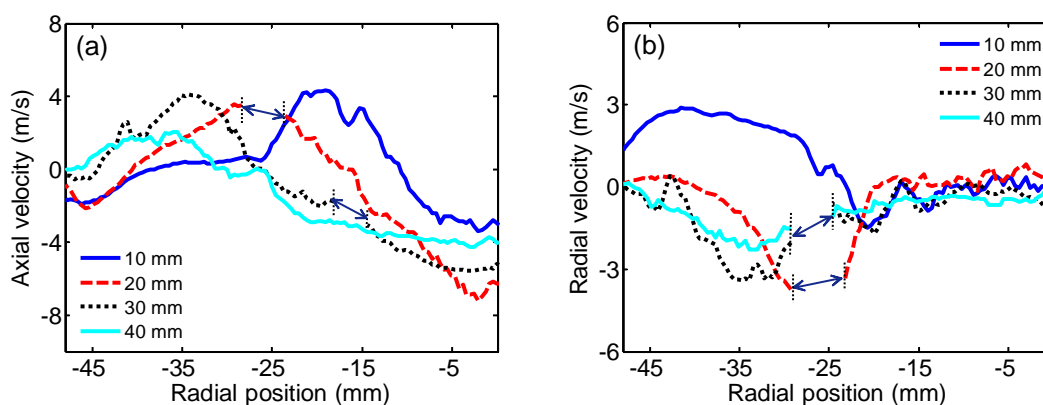
Figure 6.16: Mean (a) axial and (b) radial velocity profile for the swirling flame with PME spray. The equivalence ratio of the mixture is $\phi = 0.47$ and the power output is 6 kW.

6.1.10 Comparison of flow fields of spray flames

The velocity profiles of the swirling flames established with different fuel spray are compared under the same power output condition, i.e., 6 kW and at the global equivalence ratio of $\phi = 0.47$. The flow rates for the fuels considered are shown in Table 4.4 in Chapter 4. The axial velocity profiles at axial locations 20 and 30 mm from burner exit are shown in Fig. 6.17a and 6.17b respectively. The profiles exhibited by the four flames show similar profile shapes, albeit with a slight variation of magnitude due to the fluctuating and unstable flow conditions induced by the flames. The peak velocity at y = 20 mm is ~ 3.5 m/s which corresponds to the shear layer region at x = -30 mm from centreline. The reverse flow induced by the recirculation zone shows the peak velocity of ~ 7.5 m/s but the diesel flame shows a slightly lower peak magnitude of ~ 5.4 m/s. The similarity of the axial velocity profiles is again demonstrated at downstream location 30 mm. The average peak reverse flow magnitude at this location is around 4.5 m/s.

The radial velocity profiles at location 10 and 20 mm from burner outlet are shown in Fig. 6.17c and 6.17d respectively. The profiles of 10 mm from burner outlet show almost identical magnitudes of radial velocity profiles in the corner recirculation zone at the radial position between -25 mm and -45 mm from centreline. However, there seems to be some fluctuation in magnitudes in the region near the centreline where the reverse flow is dominant. The radial velocity profile shown at y = 20 mm shows that the radial velocity magnitude at the shear region between the radial position of -25 mm and -30 mm is highest, while the reverse flow at region between x = 0 and -20 mm from centreline shows almost no radial velocity component.
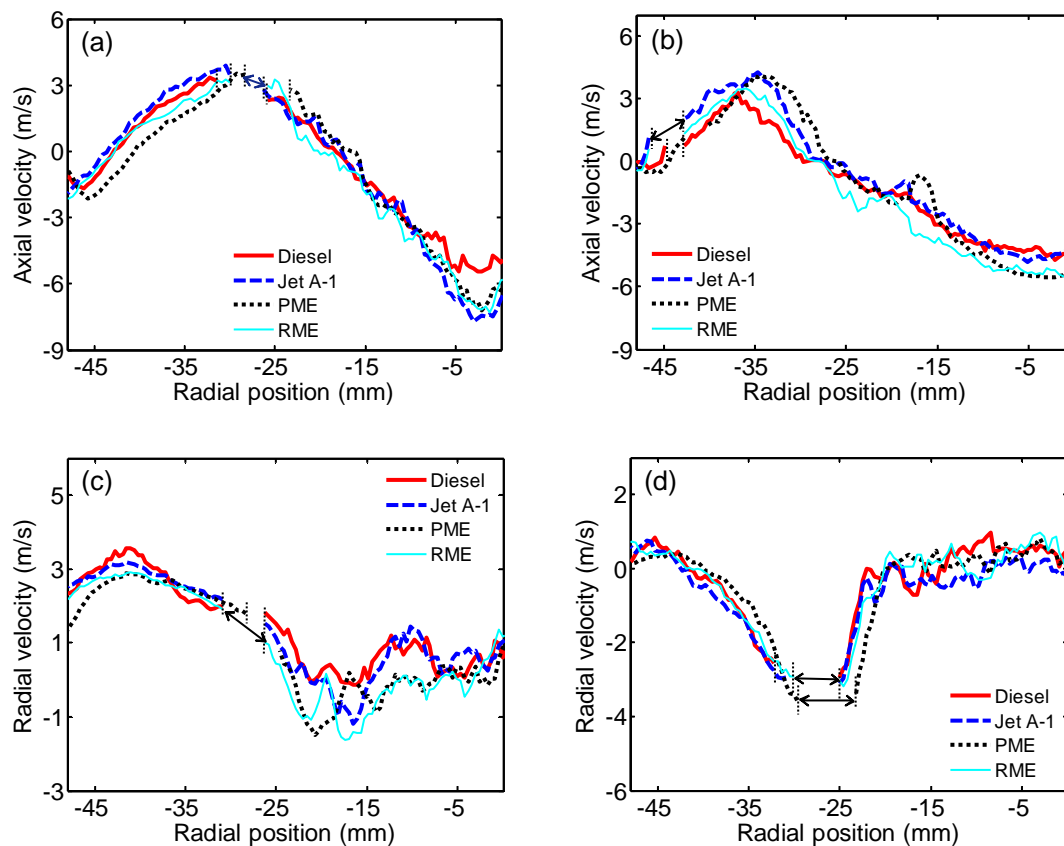
Figure 6.17: Mean axial velocity profile at position (a) 20 mm, (b) 30 mm and radial velocity profile at position (c) 10, (d) 20 mm from the burner outlet for swirl flames established with diesel, Jet-A1, PME and RME at $\phi = 0.47$ and the same power output of 6 kW.

6.1.11 Comparison of non-reacting and reacting flow fields

The effect of the flame on the flow field within the combustor is shown through the comparison of velocity profiles with flows without flame. The non-reacting air flow rate is 4.06 g/s and preheated to T = 350 ℃. The spray flame is established using Jet-A1 fuel with the main air flow rate of 4.06 g/s and fuel mass flow rate of 0.14 g/s. The ALR ratio for the spray is maintained at 2. Figure 6.18a shows the axial velocity profiles at burner downstream locations of 10 and 30 mm. The profiles show that the spray flame flow field exhibits a higher peak velocity 10 mm compared to the non-burning flow due to the flow expansion induced by flame. The increased intensity of the

centre recirculation zone is evident for the spray flame as shown by the high velocity magnitudes at the burner downstream locations of 10, 20 and 30 mm due to the adverse pressure gradient enhanced by the presence of the flame. At 20 mm, the peak reverse flow velocity of the spray flame is 7.5 m/s compared to 1.8 m/s for the non-reacting flow. At the downstream location of 40 mm, the spray flame shows slightly higher axial velocity than the non-reacting flow at the radial positions between x = -24 mm and -44 mm from centreline.

The radial velocity profiles at y = 10 mm show that the intensity of the recirculation zone for both flows is similar at radial positions between x = -35 mm and -45 mm as shown in Fig. 6.18c. This shows that the effect of flame on the corner recirculation zone is less dominant. Downstream of the burner outlet at 30 mm, the radial velocity profile peaks at the radial position of -35 mm due to the high velocity shear flow. The peak radial velocity magnitude for the spray flame is 5.1 m/s compared to 3.6 m/s for the non-reacting flame. In the region between the centreline and x = 15 mm, the spray flame shows an increase radial velocity compared to near zero velocity for the non-reacting flow.

The radial velocity profiles for axial locations 20 and 40 mm from burner outlet are shown in Fig. 6.18d. The flame shifts the peak location of the shear layers towards the direction of the wall at y = 20 mm. The peak radial velocity magnitude is about 3 m/s for the spray flame compared to ~ 2.4 m/s for the non-reacting flow. The effect of flame on radial velocity extends to the downstream location of 40 mm from burner outlet. The spray flame exhibits a gradual increase of magnitude from near zero velocity at the centreline to the peak of ~ 2.5 m/s at the radial position of x = -38 mm. In contrast, the non-reacting flow shows a relatively unperturbed velocity magnitude across the profile, indicating that the flow has been straightened.
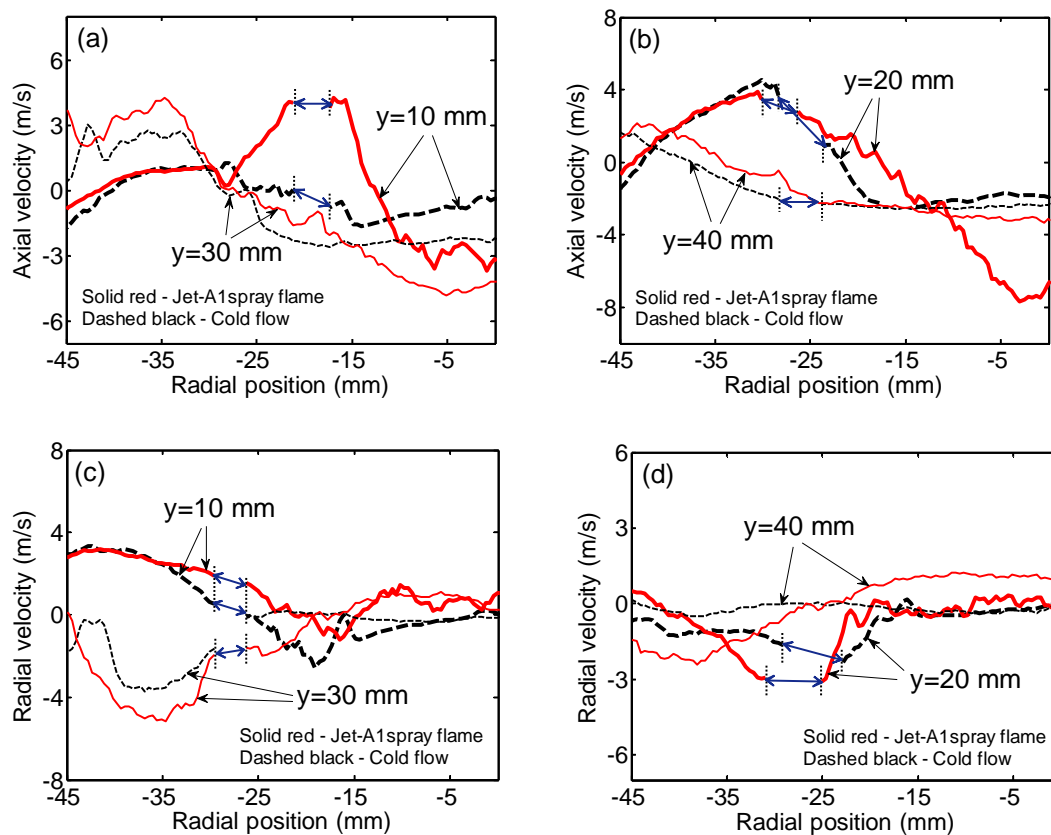
Figure 6.18: Comparison of the mean (a, b) axial and (c, d) radial velocity profiles between the enclosed swirling flow with and without flame. The main air flows are preheated to T = 350 ºC. The non-reacting air flow mass flow rate is 4.06 g/s. The Jet-A1 spray flame is established with the main air and fuel mass flow rate of 4.06 g/s and 0.14 g/s respectively.

6.2 Chemiluminescence and spectroscopy results

From visual observation, the biodiesel flame show different flame emission spectroscopy compared to diesel and Jet-A1 fuels as shown in the flame images taken using a digital camera (Panasonic: Lumix DMC-FS15) in Fig. 6.19. The diesel and Jet-A1 flames show a blusih flame near the flame root which is analogous to a premixed flame, while a yellowish diffusion flame brush is observed at downstream. The PME flame burns "cleanly" as if it was a thoroughly mixed flame. The RME flame shows a

distinct orange-yellow flame brush. In the following section, the OH* and CH* chemiluminescence imaging of the flame reaction zones are investigated, followed by the broadband filtered imaging (> 500 nm). The flame spectroscopy of the flames is spectrally resolved using a spectrometer.

Diesel

Jet-A1

PME

RME

Figure 6.19: Spray flames established from (a) Diesel, (b) Jet-A1, (c) PME and (d) RME under the condition of same burner power output of 6 kW.

6.2.1 Comparison under same power output

OH* Chemiluminescence

The structure of the flames was investigated using an intensified CCD camera to capture the OH* chemiluminescence emitted from the flames. Abel transformation was performed on the line-of-sight global OH* chemiluminescence images to obtain the planar flames structure of the flame. Figure 6.20 shows the comparison of the spray flame OH* chemiluminescence images performed under the same burner power output conditions. Due to the differences in calorific values between the fuel tested, the fuel mass flow rates are adjusted to match the total power output of 6 kW while maintaining the global equivalence ratio of $\phi = 0.47$. The operating conditions are shown in Table 4.4, Chapter 4. The flame structure of Jet-A1 is observed to be quite similar to diesel. The diesel flame exhibits a higher intensity of OH* near the root of the flame, as indicated by the higher intensity peak at an axial location of 4 mm from burner outlet. The length of the reaction zone is almost identical for all flames, which is about 22 mm from the burner exit. PME and RME show different flame reaction zones compared to diesel and Jet-A1. Instead of two distinguishable separate flame fronts, the biodiesel flames show a joined heart-shape flame reaction zone. This is due to the extended droplet vaporisation time of biodiesel droplets compared to conventional fuels.

The corresponding OH* chemiluminescence intensity profiles at 4, 8, 13 and 17 mm from the burner outlet are shown in Fig. 6.20. The profiles show the half plane of the flames where the radial position of x = 0 mm indicates the burner centreline. Jet-A1 shows intense OH* emissions at 4 and 8 mm downstream but lower intensity counts at y = 13 and 17 mm from the burner exit. The diesel flame exhibits a similar flame shape and OH* intensity profiles to Jet-A1. The intensity profile of the diesel flame at a downstream location of 4 mm is slightly higher than Jet-A1. Both PME and RME profiles are almost identical, indicating the similarity in heat release rate. Biodiesels show similar OH* intensity profiles as Jet-A1 and diesel at 4 and 8 mm, but the profile shape is distinctively different at 13 and 17 mm downstream.

CH* Chemiluminescence

The CH* chemiluminescence images obtained under the same power output condition are shown in Fig. 6.21. Similar to the OH* chemiluminescence images as shown in Fig. 6.20, the Jet-A1 and diesel flames show two distinct flame reaction zones, while the biodiesel flames exhibit a heart-shape reaction zone. The length for all the flame reaction zones is approximately 22 mm downstream from burner outlet. The CH* intensity profiles at 4, 8, 13 and 17 mm from the burner outlet are presented in Fig. 6.21. The diesel flame shows the intensity peak that locates at an axial position of 4 mm from burner outlet, indicating high heat release rate concentrating near the flame root. Jet-A1 and diesel flames show the intensity profiles at the axial locations of y = 13 and 17 mm are lower compared to y = 4 and 8 mm. Both PME and RME show that the flame reaction zones locate at a slightly more downstream position. This is indicated by the lower intensity profile at location 4 mm compared the downstream profiles of y = 8, 13 and 17 mm. The higher intensity of heat release rate at the flame root of Jet-A1 and diesel flames could assist flame stability. The CH* profiles exhibit similar trends as OH* intensity profiles that are presented in Fig 6.20, indicating that the emissions of OH* and CH* are closely related.

Broadband spectrum spectroscopy

High energy intensity is obtained in the continuous spectra typically observed in the sooty region of a hydrocarbon flame. To image the continuous spectra as a mean to identify the soot formation tendency of different fuels, a broadband longpass filter (> 550 nm) is used to image the flames. Here, the flame imaging is performed using a CCD camera without an intensifier. The longpass filtered flame images of Jet-A1, diesel, PME and RME flames are presented in Fig. 6.22. The diesel flame image shows high intensity counts in the post flame region, indicating the presence of soot at the continuous spectra of > 550 nm. From visual observation, the flame appears to be yellowish downstream of the reaction zones. The dominant soot formation region is at an axial distance between 20 and 40 mm from burner outlet where the soot intensity is the highest. Jet-A1 flame is also prone to soot formation but at a much lower intensity compared to the diesel flame. It has been shown that the sooting tendency is related to the aromatic content in the fuel [1]. Diesel and Jet-A1 contain about 40 % and 20 % by

volume of aromatics respectively, which explains the higher signal of soot intensity for the former. Contrary to conventional fuels, PME shows the "cleanest" flame among all. The flame appears to be bluish, with the flame intensity concentrated near the flame roots where the reaction zone occurs. Soot is almost non-existent at downstream locations of the reaction zone, and hence the yellowish flame brush at the post reaction zone region is not present. The low luminosity of the PME flame has also been observed by Hashimoto *et al.* [2] in a swirl flame investigation.

As biodiesels contain no aromatic rings, PME and RME show no sign of soot formation or irregular soot structure in the post reaction zone region. Song *et al.* [3] reported that soot formed from biodiesel can be oxidised rapidly due to the high reactivity of the oxygenated molecule. The RME flame shows a different flame spectra compared to the PME flame. From visual observation, the RME shows a yellow-orange flame brush at the locations downstream of the flame reaction zone. The filtered broadband image shows the structure of the flame brush at the post-reaction zone but the intensity is low compared to the upstream reaction zone. The post combustion region shows a uniform flame structure that is significantly different from the irregular structure of soot as shown by the diesel and Jet-A1 flames at the post flame region. This shows that RME is not prone to soot production, similar to PME.

The intensity profiles at 12, 22, 30 and 40 mm from burner outlet are shown in Fig 6.22. Diesel shows a higher luminosity signal than Jet-A1 by a factor of 3 due to the high volume of soot formation. It is noted that the highest intensity of signals occur at an axial location of 30 mm from burner outlet, indicating the high probability of soot formation at this location. In contrast, PME shows almost no soot formation with near zero counts at profiles of 30 and 40 mm downstream. The only intense region is located at 12 mm from the burner outlet where the reaction occurs. For the RME flame, the presence of the yellow-orange flame brush is captured at the downstream axial positions of 22, 30 and 40 mm from the burner outlet. The long flame brush extended from the reaction zone may be attributed to the presence of sodium, an inorganic compound that exhibits the wavelength of 588 nm when ionised.
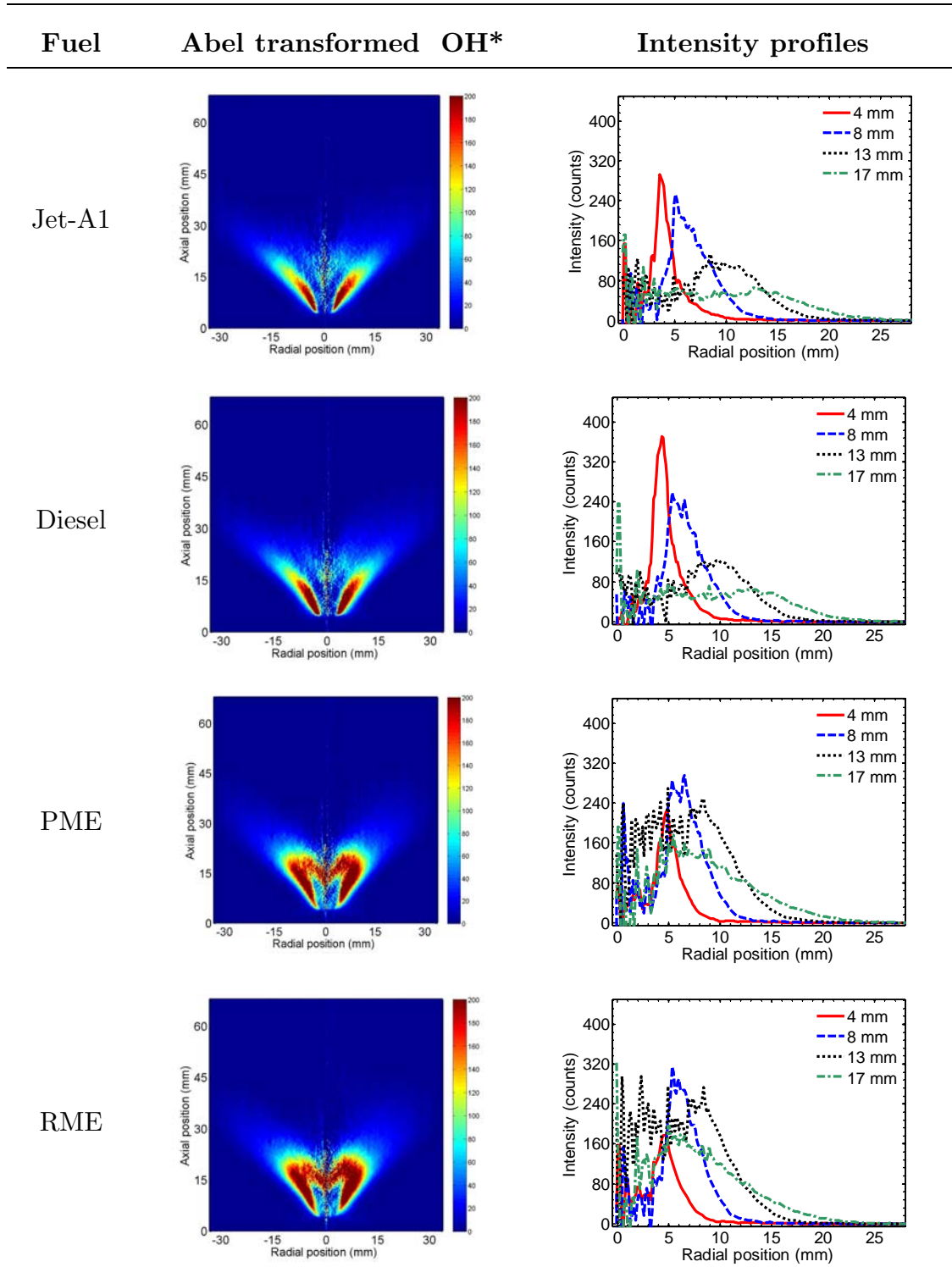
Figure 6.20: Abel transformed OH* chemiluminescence images and the corresponding OH* intensity profiles at $\phi = 0.47$ under the condition of same power output.

Fuel	Abel transformed CH*	Intensity profiles
Jet-A1		
Diesel		
PME		
RME		
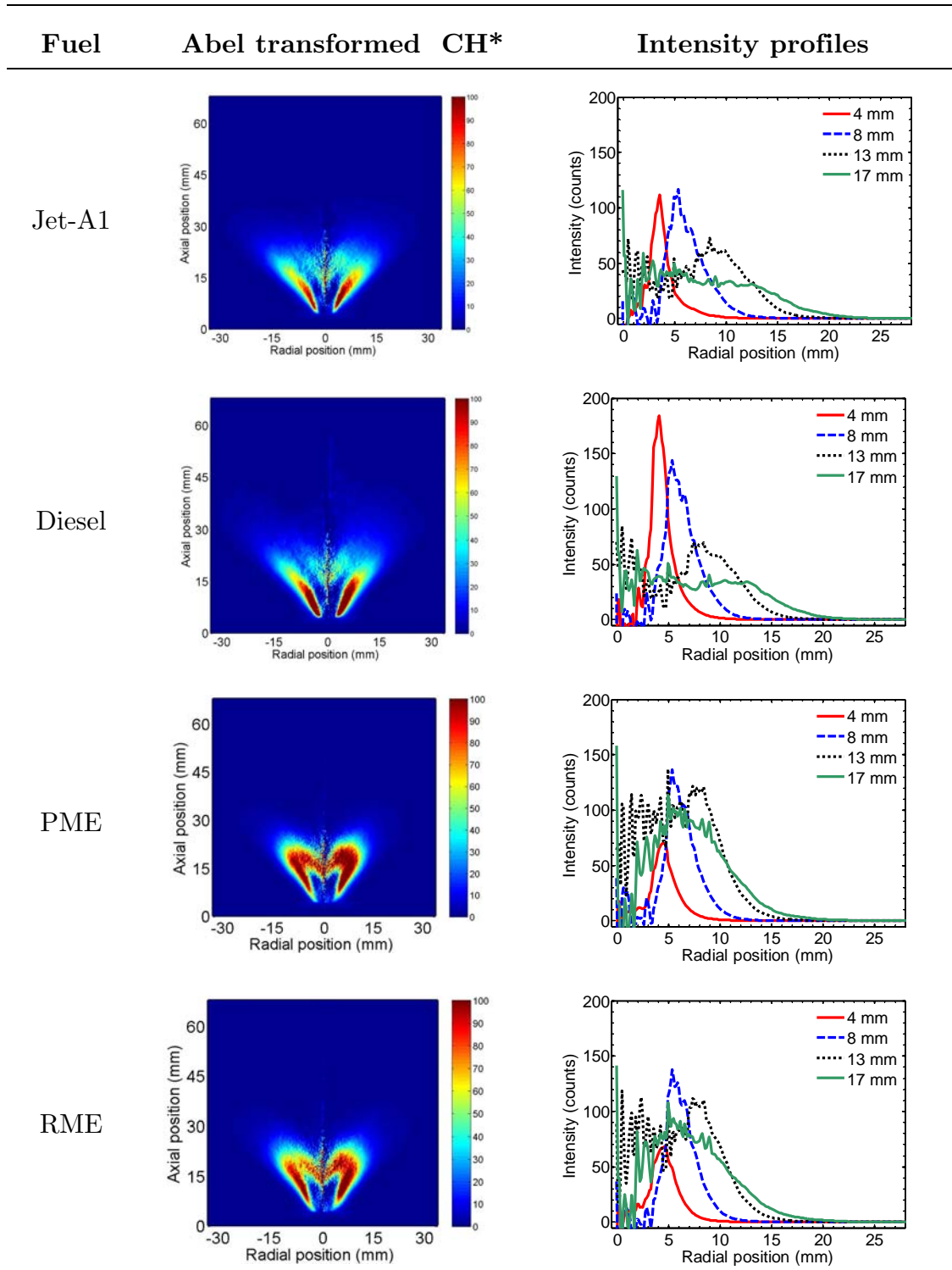
Figure 6.21: Abel transformed CH* chemiluminescence images and the corresponding CH* intensity profiles at $\phi = 0.47$ under the condition of same power output.

Fuel	Abel transformed	Intensity profiles
Jet-A1		
Diesel		
PME		
RME		
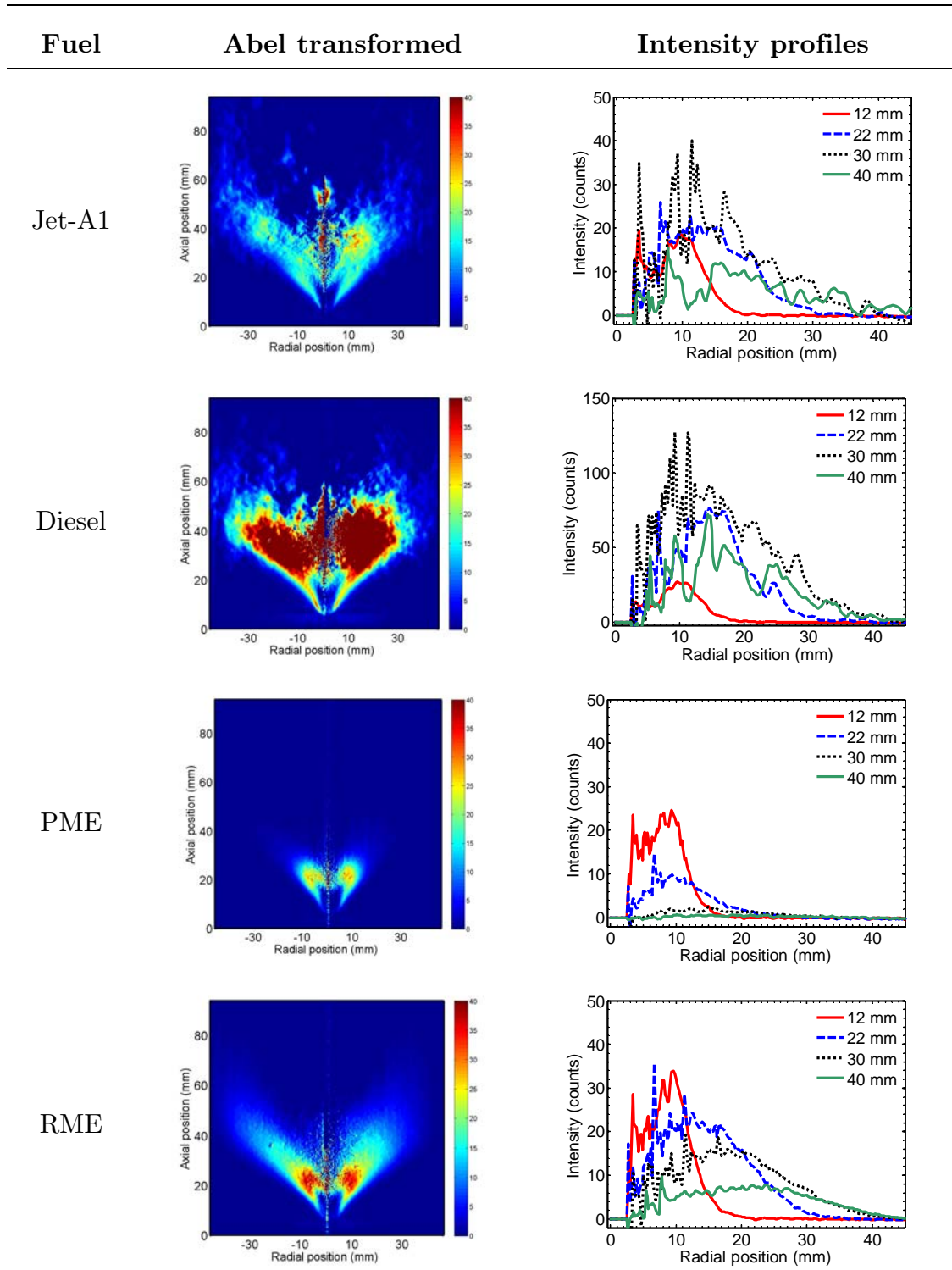
Figure 6.22: Abel transformed flame images obtained from longpass filter (> 550 nm) and the corresponding intensity profiles at $\phi = 0.47$ under the condition of same power output.

6.2.2 Effect of biodiesel blend on flame chemiluminescence

The flame structures of the biodiesel blend of 50 % PME with diesel are presented through OH*, CH* and longpass filtered images. Figure 6.23 compares the OH* chemiluminescence images of biodiesel blend with 100 % diesel and 100 % PME under the condition of same fuel mass flow rate. The operating conditions of the same fuel mass flow rates are shown in Table 4.6. The OH* chemiluminescence shows that 50 % PME blend exhibits two distinct flame brushes similar to the pure diesel flame. The OH* intensity profiles of the biodiesel blend is quite similar to diesel, albeit with a slight difference in the intensity peak value.

The corresponding CH* chemiluminescence images are shown in Fig. 6.24. The biodiesel blend exhibits two distinct flame fronts similar to OH* chemiluminescence. The CH* intensity profiles in Fig. 6.24 shows slightly lower intensity values for the profile at y = 4 and 8 mm compared to pure diesel flames, but a slight increase of intensity at y = 13 and 17 mm. This shows that the biodiesel blend flame exhibits the influence of both diesel and PME.

Figure 6.25 shows the longpass filtered images (> 550 nm) for diesel, 50 % PME blend with diesel and PME flames. Diesel shows the highest intensity of signals due to the high presence of soot. In contrast, the PME flame shows a low intensity with almost zero soot formation. The blending of 50 % PME with diesel shows some soot formed at the post reaction zone between 30 and 50 mm burner downstream but at a significantly reduced amount compared to the pure diesel flame. This shows that blending biodiesel with conventional fuels can potentially reduce soot production.

Fuel	Abel transformed OH*	Intensity profiles
Diesel		
50% PME + 50% diesel		
PME		
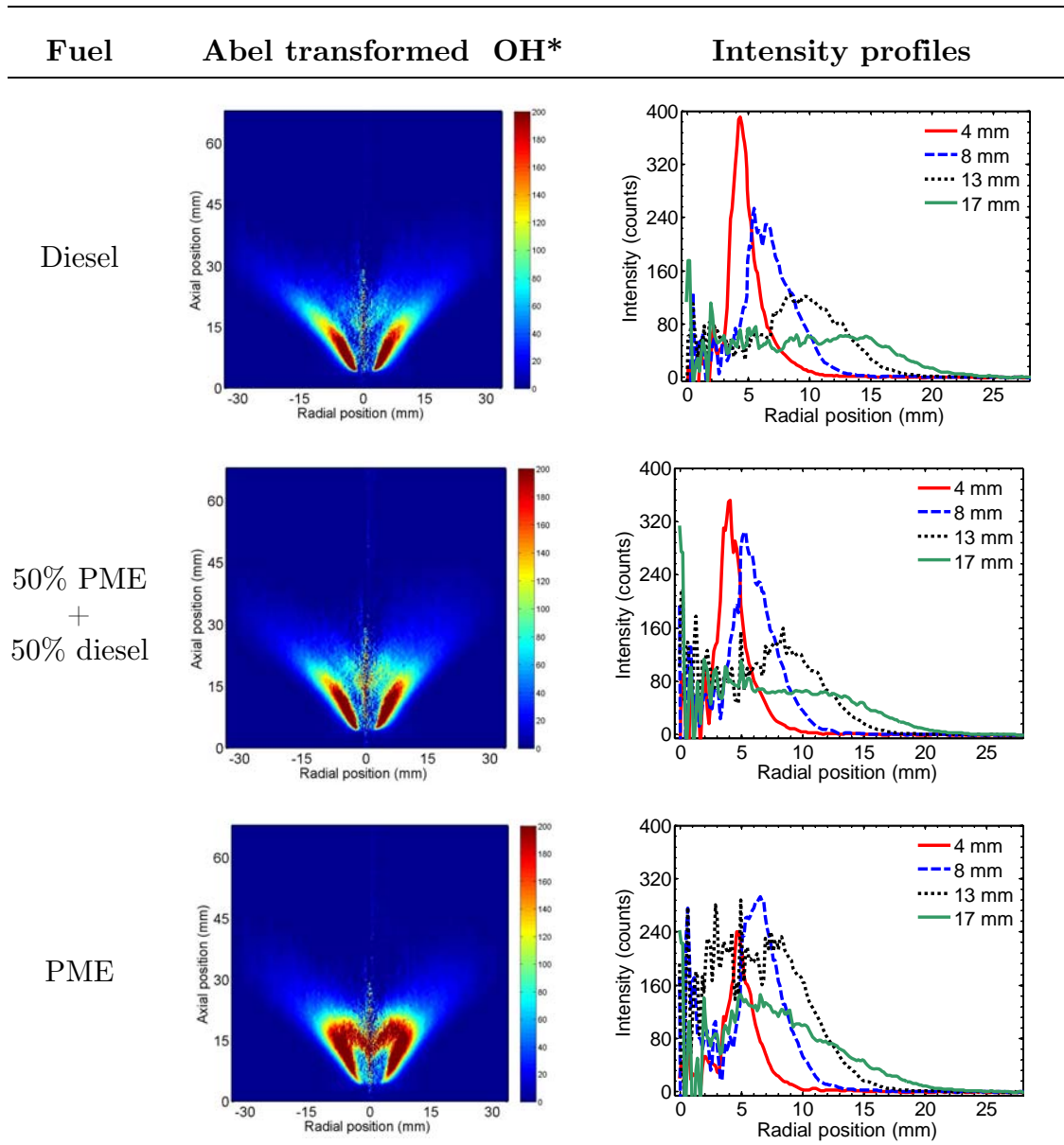
Figure 6.23: Abel transformed OH* chemiluminescence images and the corresponding OH*intensity profiles at $\phi = 0.47$ under the same fuel mass flow rate condition.

Fuel	Abel transformed CH*	Intensity profiles
Diesel		
50% PME + 50% diesel		
PME		
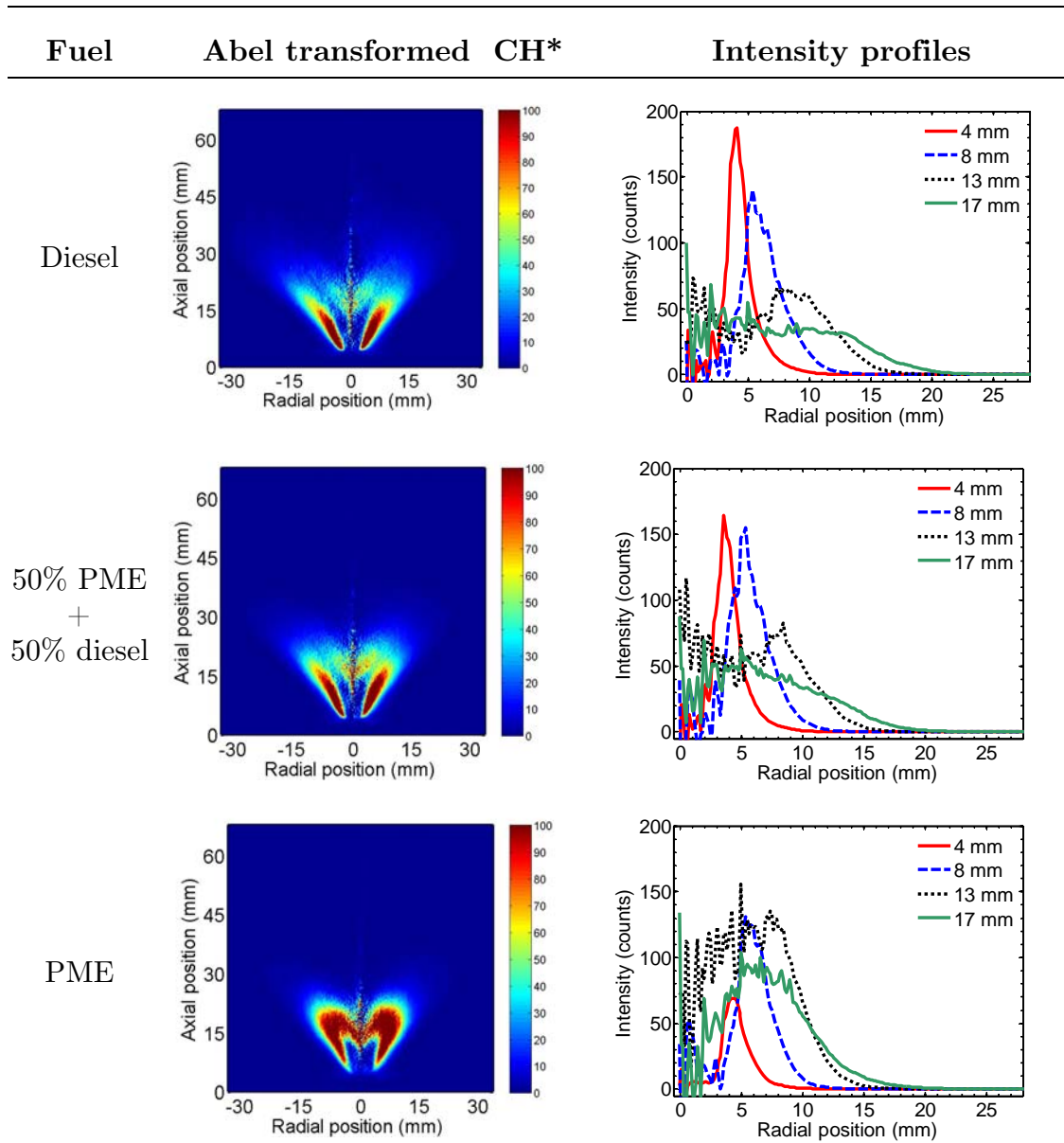
Figure 6.24: Abel transformed CH* chemiluminescence images and the corresponding CH* intensity profiles at $\phi = 0.47$ under the same fuel mass flow rate condition.

Fuel	Abel transformed	Intensity profiles
Diesel		
50% PME + 50% diesel		
PME		
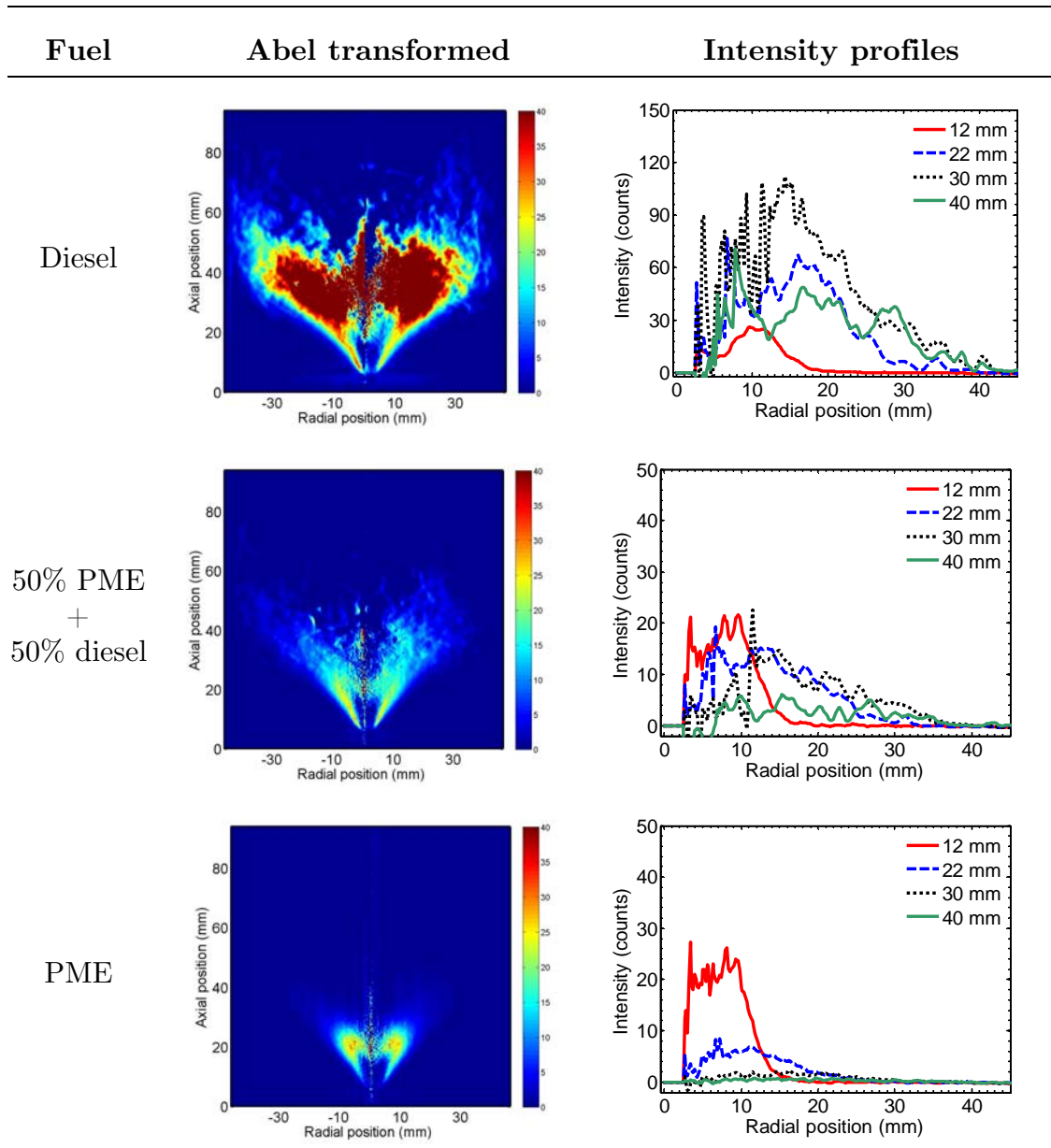
Figure 6.25: Abel transformed of flame images obtained from longpass filter (> 550 nm) and the corresponding intensity profiles at $\phi = 0.47$ under the same fuel mass flow rate condition.

6.3 Flame emission spectroscopy
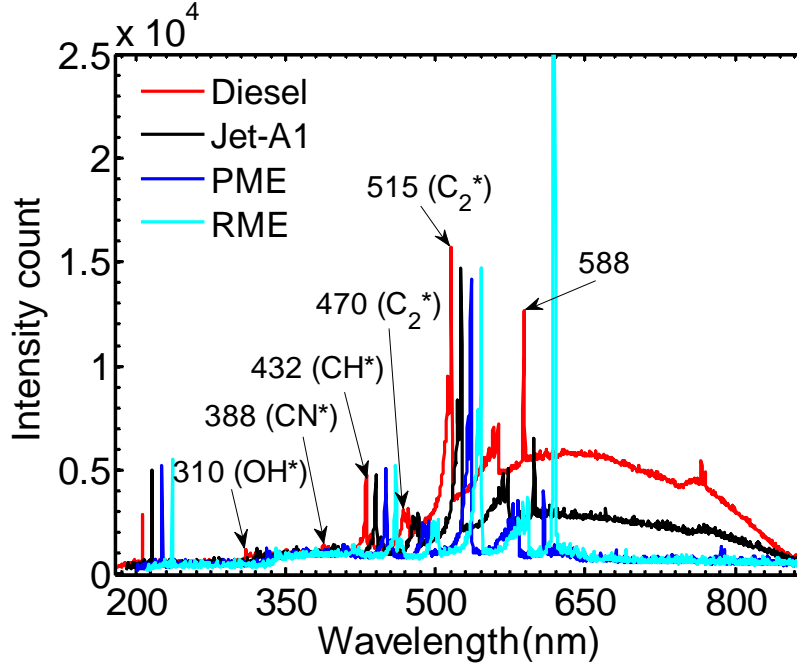
Figure 6.26: Flame emission spectroscopy measurements under the same power output condition. The spectra of Jet-A1, PME and RME are displaced along the wavelength axis with + 10, + 20 and + 30 nm respectively for clarity.

The flame emission spectroscopy was performed using a spectrometer (USB2000+; Ocean Optics) capable of capturing the spectra between the UV and near infrared range (~ 200 nm – 900 nm). The global flame spectrum signal was focused onto the slit of the spectrometer via a focusing lens. Figure 6.26 shows the flame spectra for diesel, Jet-A1, PME and RME flames obtained under the same power output condition. The spectra of Jet-A1, PME and RME are displaced along the wavelength axis with + 10, + 20 and + 30 nm to enable clearer presentation of the peaks. Diesel flame shows a prominent bandwidth curve between 550 to 850 nm. The emission of continuous spectra in the near-infrared region is due to the radiation of soot, which explains the high luminosity of the yellow-orange flame formed in the post-reaction zone region. The spatial distribution of the soot in the flame is shown through the long bandpass (> 550 nm) filtered image in Fig. 6.22.

Contrary to diesel, PME exhibits the characteristic of soot-free spectra as evident in the flat profile between 580 and 900 nm. RME displays an intense peak at the wavelength of 588 nm but the profile at 600 nm and above is almost zero. The absence of the continuous spectra (600 - 850 nm) indicates that RME is not prone to form soot. Instead, the distinct peak at the wavelength of 588 - 589 nm shows the emission from inorganic material such as sodium when combusted. The intense peak of 588 nm explains the visible orange-reddish flame brush in RME. PME however, does not exhibit the emission characteristic of 588 nm but a low luminous bluish flame. Jet-A1 shows the presence of soot as indicated by the continuous spectra at the near infra-red region. The intensity of the soot of Jet-A1 is lower compared to diesel flame, concurring with the trend shown in the spatially resolved longpass filtered images in Fig. 6.22. Comparison of the flame spectra highlights the difference of flame spectrometry between the conventional fuels and biodiesels.

6.3.1 Effect of biodiesel blend on flame spectrum

Comparison of the flame spectra of 20% and 50% PME/diesel blend with diesel and PME under the condition of $\phi = 0.47$ and same fuel mass flow rate is shown in Fig. 6.27. Diesel exhibits the continuous wavelength profile between 550 nm to 850 nm due to the radiation from soot while PME displays the absence of the soot spectra. The 20 % PME blend shows the soot continuous spectrum that locates in between the PME and diesel, while the 50 % PME blend shows an almost soot-free profile similar to the PME. This indicates that biodiesel is more dominant in influencing the spectrometry of the flames. The production of soot is also reduced as indicated by the non-linear reduction of soot spectra relative to the percentage of PME blended with diesel. This result is supported by Fig. 6.25, where the 50 % blend of PME with diesel also exhibits a lower intensity count by a factor of 6 compared to the pure diesel flame at an axial location of y = 30 mm.
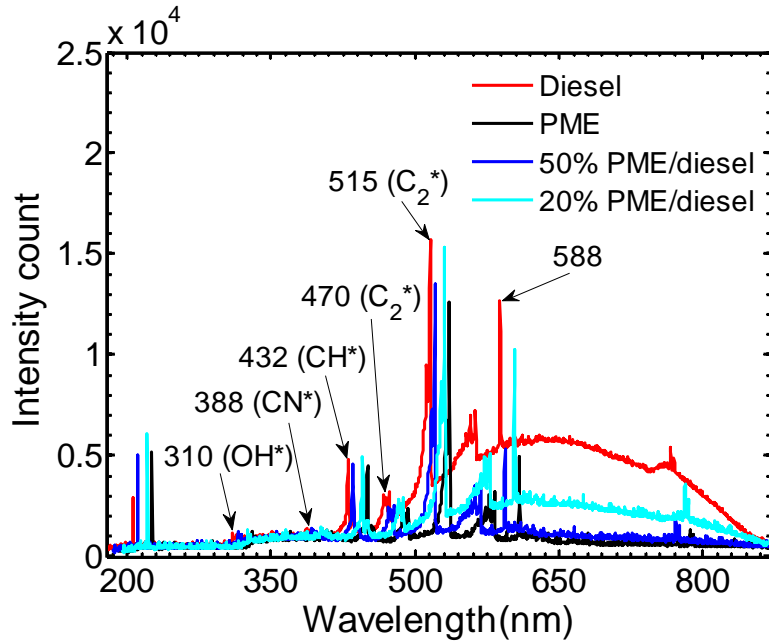
Figure 6.27: Flame emission spectroscopy measurements of diesel, PME, blends of 20 % and 50 % PME with diesel under the condition of same fuel mass flow rate and $\phi = 0.47$. The spectra of PME, 50 % PME/diesel, and 20 % PME/diesel are displaced along the wavelength axis with $+ 10$, $+ 20$ and $+ 30$ nm respectively for clarity.

The spectrometry of the 20 % and 50 % blend of RME with diesel is compared to the unblended fuels in Fig. 6.28 under the same burner power output condition and $\phi = 0.47$. Similar to Fig. 6.27, the presence of biodiesel has a pronounced influence on the flame spectrometry. The 20 % of RME blend reduces the soot luminosity by half while the 50 % RME blend shows almost no emissions of soot spectra. The distinctive peak of 588 nm which is present in RME flame shows up in both the 20 % and 50 % RME blend, indicating the flame spectra of the biodiesel blends is more biased towards the characteristics of RME.
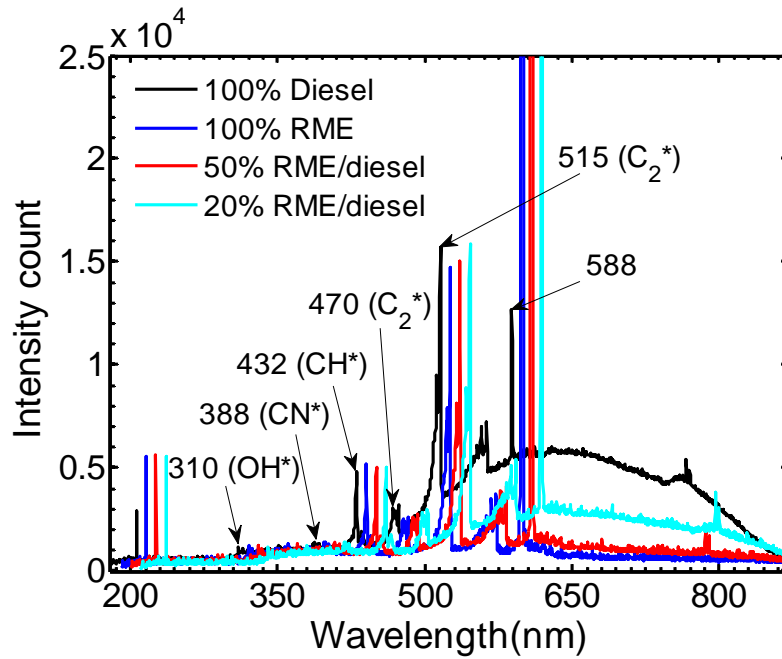
Figure 6.28: Flame emission spectroscopy measurements of diesel, RME, blends of 20 % and 50 % RME with diesel under the condition of $\phi = 0.47$ and same power output of 6 kW. The spectra of RME, 50 % RME/diesel, and 20 % RME/diesel are displaced along the wavelength axis with $+ 10$, $+ 20$ and $+ 30$ nm respectively for clarity.

6.4 Droplet distribution within flame and flow field

The droplets size and velocity distribution is superimposed on the flame reaction zones as shown in Fig. 6.29a and 6.29b for Jet-A1 and PME flames respectively. The flame reaction zones are derived from the Abel transformed mean CH* chemiluminescence signals. Despite the differences in flame reaction zone, the overall spray structure in the reacting flows is rather similar. Most droplets are mainly distributed at a region close to the flame reaction zone. Small droplets are distributed at the centreline region with high velocities. Larger droplets that attain low velocities are located at positions outside the flame reaction zone. The high intensity CH* signals coincide with the droplet distribution with small diameter, indicating the rapid evaporation at locations where the local temperature is considerably high. The intense heat generated from the flame front propagates to the spray core and facilitates droplet evaporation. At the downstream location of $y = 20$ mm, droplets at the centre region are completely vaporised. This explains the absence of CH* signal due to insufficient fuel vapour to sustain local combustion. Beyond $y = 20$ mm downstream, most of the droplets are almost evaporated. The influence of the reverse flow at the spray centreline region causes the bimodal shape of the radial distribution of the droplet axial velocity.

The spatial distribution of the droplets in the PME flame reaction zone and combustor flow field on one side of the centreline is shown in Fig. 6.30. The radial position of $x = 0$ mm indicates the centreline of the burner while $x = 50$ mm represents the wall of the combustor. The swirl flame is established at the global equivalence ratio of $\phi = 0.47$ and the burner power output of 6 kW. The spatial distribution of droplets within the combustor elucidates the interaction of droplets with flame and flow field. The larger droplets are distributed outside the flame reaction zone but at a low concentration. The larger droplets are relatively less influenced by the direct heat generated from the heat reaction zone and hence attain longer evaporation time scale. The unvaporised droplets at the spray periphery interact with the high velocity swirl flow at the shear layer. As a result, the droplets are transported back into the centre of the flame through the centre toroidal recirculation zone. The centre recirculation zone directs the flow back to the burner inner core through the reverse flow. In this process, hot post-combustion products are convected back to the flame reaction zone to

continuously supply heat for reactant preheating. This mechanism has been known to assist in flame stabilization. Another possibility is that the droplets will be carried into the corner recirculation zone and entrained back to the flame root.
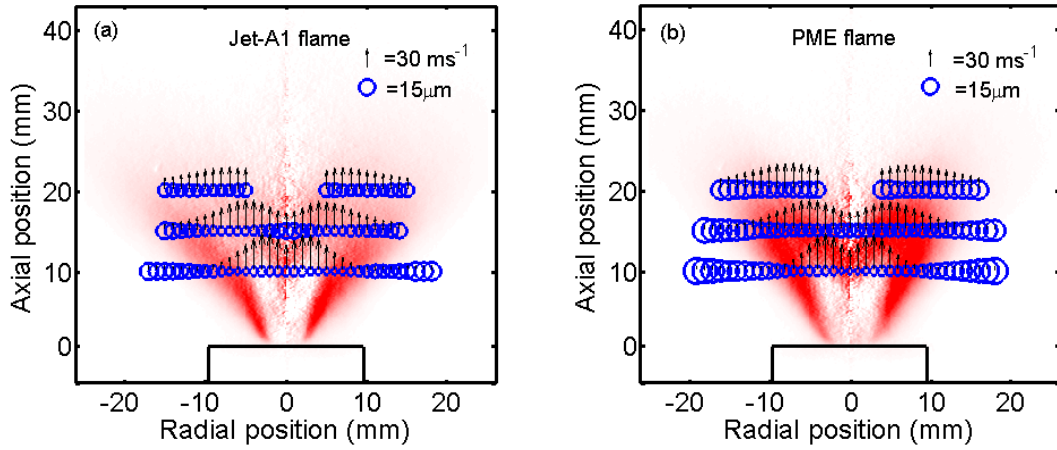
Figure 6.29: Droplet velocity and size distribution within the (a) Jet-A1 and (b) PME swirl flames
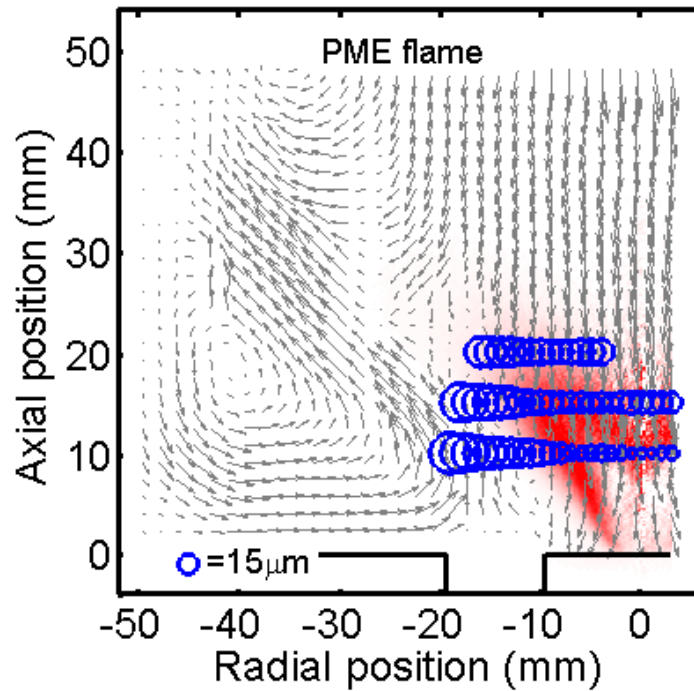
Figure 6.30: Droplet size distribution superimposed on the flame reaction zone and the flow field within the combustor. The PME flame is established from 0.16 g/s of fuel, 0.32 g/s of atomizing air, and the main swirling air flow of 4 g/s.

6.5 Emission results and discussion

6.5.1 Emission profiles at the combustor outlet

Figure 6.31 shows the emission profiles obtained radially across the combustor outlet for diesel, Jet-A1, PME and RME under the same power output condition. The global equivalence ratio for all fuel/air mixture was maintained at $\phi = 0.47$. The measurements were taken under steady state conditions at the burner outlet. The x-abscissa denotes the radial position across the burner outlet in r/D, where r is the radial position from centreline and D is the diameter of the combustor outlet (100 mm). In general, the NO, CO_2 and O_2 profiles are relatively flat at the combustor outlet. For CO and NO_2, the profiles show a dip at the centreline, indicating the inhomogeneous distribution of the species at the combustor outlet. This could be due to the influence of the flow field within the combustor.

Comparison of the profiles shows that PME and RME exhibit lower NO and NO_2 compared to diesel and Jet-A1 at all spatial locations. The overall CO emission is around 5 ppm or below with a slight overlap of profiles. The CO_2 and O_2 profiles for all flames are indistinguishable, indicating the equivalence ratios of for all fuel/air mixtures are almost similar. The measurements were repeated and good repeatability was achieved.
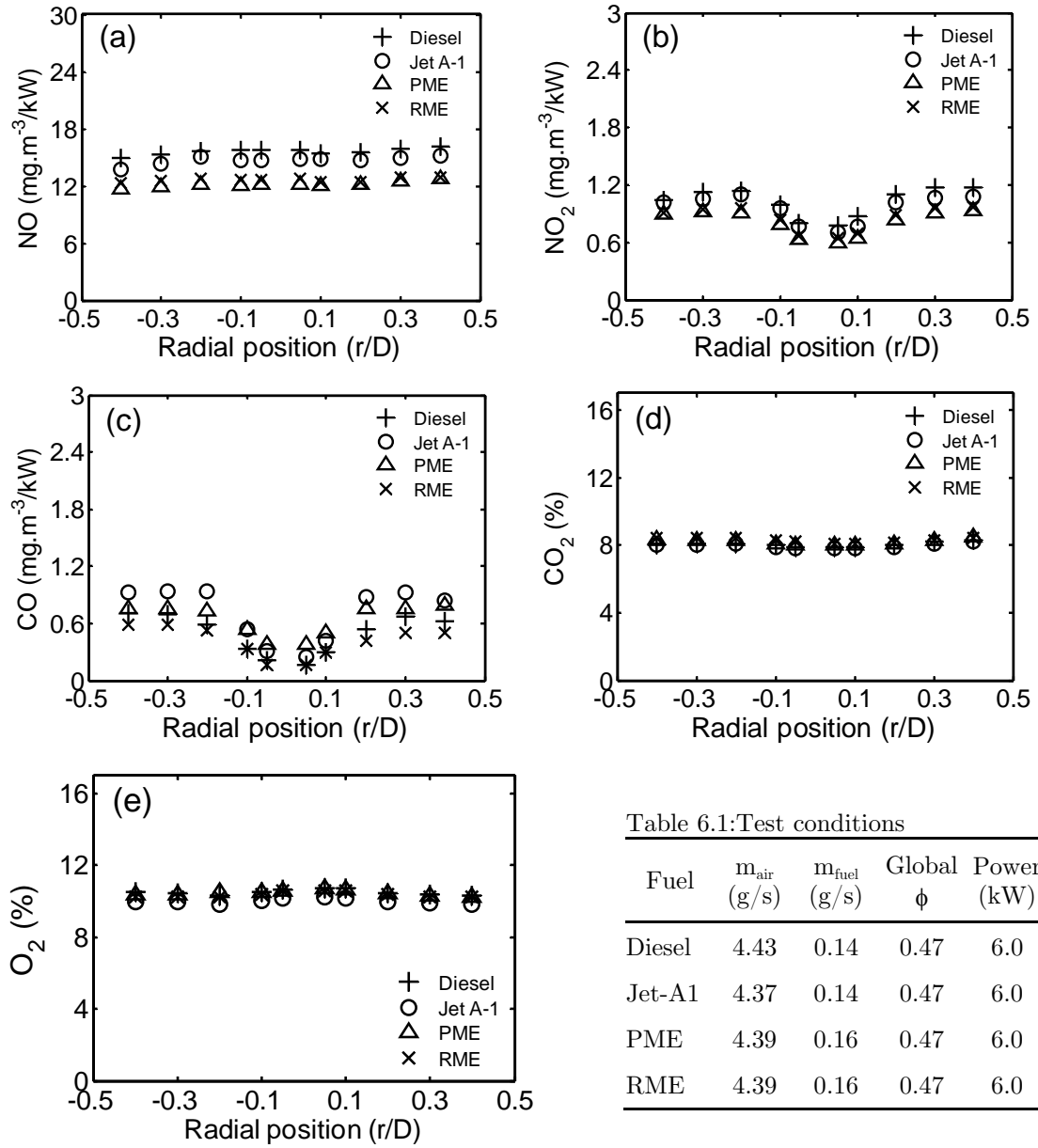
Figure 6.31: Emission profile of (a) NO, (b) NO_2, (c) CO, (d) CO_2 and (e) O2 at the combustor outlet under the same power output condition.

Table 6.1:Test conditions

Fuel	m_{air} (g/s)	m_{fuel} (g/s)	Global ϕ	Power (kW)
Diesel	4.43	0.14	0.47	6.0
Jet-A1	4.37	0.14	0.47	6.0
PME	4.39	0.16	0.47	6.0
RME	4.39	0.16	0.47	6.0

The emission values across the profile are averaged to obtain a single value for comparison. Figure 6.32 show the comparison of NO, NO_2 and CO of the four fuels under the same power output condition. The total power output is maintained at 6 kW with the global equivalence ratio of $\phi = 0.47$. The result shows that NO_x are produced mainly in the form of NO, while the NO_2 produced is about 1/10 of the NO. Diesel and Jet-A1 exhibit higher NO and NO_2 compared to biodiesels due to the presence fuel-bound nitrogen component such as aromatic rings. CO is produced at a very low quantity for all the flames, indicating the almost complete combustion of the mixtures. The production of NO and NO_2 are higher for diesel and Jet-A1 fuels compared to biodiesels. The CO emission is lower than that of NO_2 by a factor of 2 and the values are comparable between the four fuels tested.
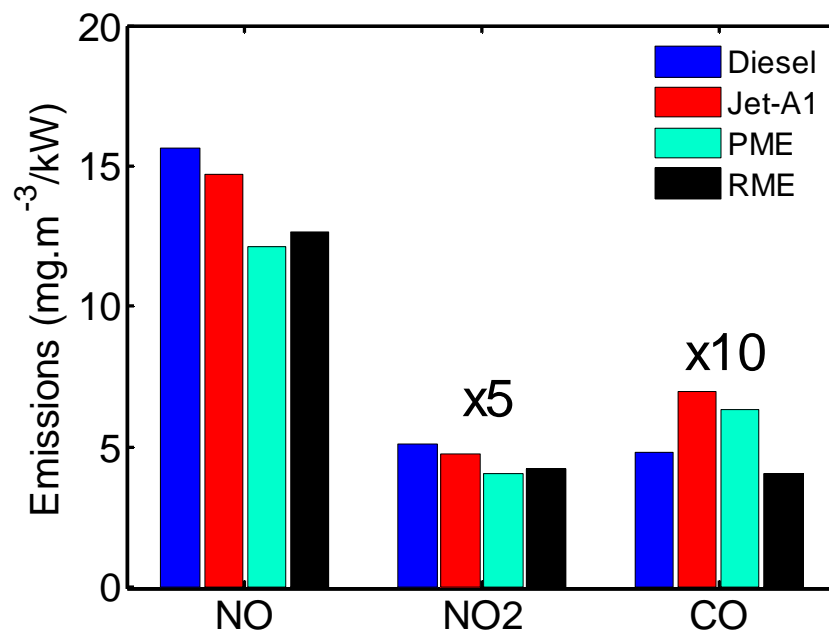
Figure 6.32: Emissions of NO, NO_2, CO for diesel, Jet-A1, PME and RME flames established under the same power output condition.

6.5.2 Emissions under the same power output

The emissions from the burner were measured at 5 spatial locations across the burner outlet as indicated in section 4.6.4, Chapter 4. At each spatial location, the exhaust gas was sampled for two minutes to ensure the reading was stabilized. The emissions values across the profiles are velocity weighted and the mean value is presented as a function of equivalence ratio under the same power output of 6 kW. A comparison of emissions for diesel, Jet-A1, PME and RME is shown in Fig. 6.33.

At conditions where $\phi < 0.4$, the NO and NO_2 emissions are rather similar between the four fuels considered. As the equivalence ratio increases, the discrepancy becomes larger where diesel and Jet-A1 produce higher NO_x. At an equivalence ratio of $\phi = 0.7$, the NO_x produced by diesel and Jet-A1 fuels is observed to be higher by a factor of 2 compared to biodiesels. The NO emissions of diesel and Jet-A1 fuel increase linearly with the equivalence ratio until $\phi \sim 0.6$, beyond which a non-linear trend is shown. The NO_2 profile however, shows a rather linear trend with the equivalence ratio.

Figure 6.33a shows that RME and PME exhibit lower NO emissions than diesel and Jet-A1. The lower NO_x emission is unexpected given that the droplets generated by biodiesels are somewhat larger than diesel and Jet-A1 under the reacting flow condition as shown in section 5.2.1, Chapter 5. The emissions profiles of RME and PME are rather similar despite the differences in methyl ester compositions. The NO emissions of biodiesels increases linearly with the increase of equivalence ratio until $\phi \sim 0.55$ before a decreasing trend is shown. Figure 6.33b shows the overall NO_2 emissions are lower by an order of magnitude compared to NO. Diesel and Jet-A1 exhibit similar NO_2 emissions as biodiesels at equivalence ratio $\phi < 0.4$, but the difference becomes more obvious as the equivalence ratio is increased.

Similar to NO, the initially linear NO_2 profiles start showing a reverse trend at $\phi \sim 0.6$. The decreasing trend of NO and NO_2 is surprising given that the increased of equivalence ratio results in higher temperature that would facilitate the formation of thermal NO. The reason for the reduced NO_x could be due to the incomplete mixing of the spray droplets and swirling air. The relatively lower swirling air flow rate at $\phi = 0.6$ and 0.75 could result in the insufficient centrifugal force to "pull" the spray apart to form a strong shear layer for complete mixing. Subsequently, combustion occurs mainly

due to the mixing between the atomizing air and liquid spray while the main swirling flow has degenerated into a coaxial flow. The swirling air is induced by the recirculation zone to cool the post combustion products and hence lowering the NO values. The increase of CO shows incomplete combustion under such partially premixed conditions.

The CO emission profiles show a non-linear relationship with equivalence ratio. The trend shows a decrease of CO between $\phi = 0.3$ and 0.5, but an exponential increase of CO is observed between $\phi = 0.55$ and 0.75. The increase of CO corresponds to the decrease of NO due to the incomplete combustion under the partially premixed mode in between $0.55 < \phi < 0.75$. Overall, diesel and Jet-A1 emit higher CO than biodiesels. The CO_2 and O_2 profiles show linear relations with the stoichiometries investigated. CO_2 increases with equivalence ratio while the corresponding O_2 profiles show the inverse linear trend. The biodiesels are observed to exhibit slightly higher O_2 and lower CO_2 concentration which could be attributed to the presence of oxygen in the molecules.
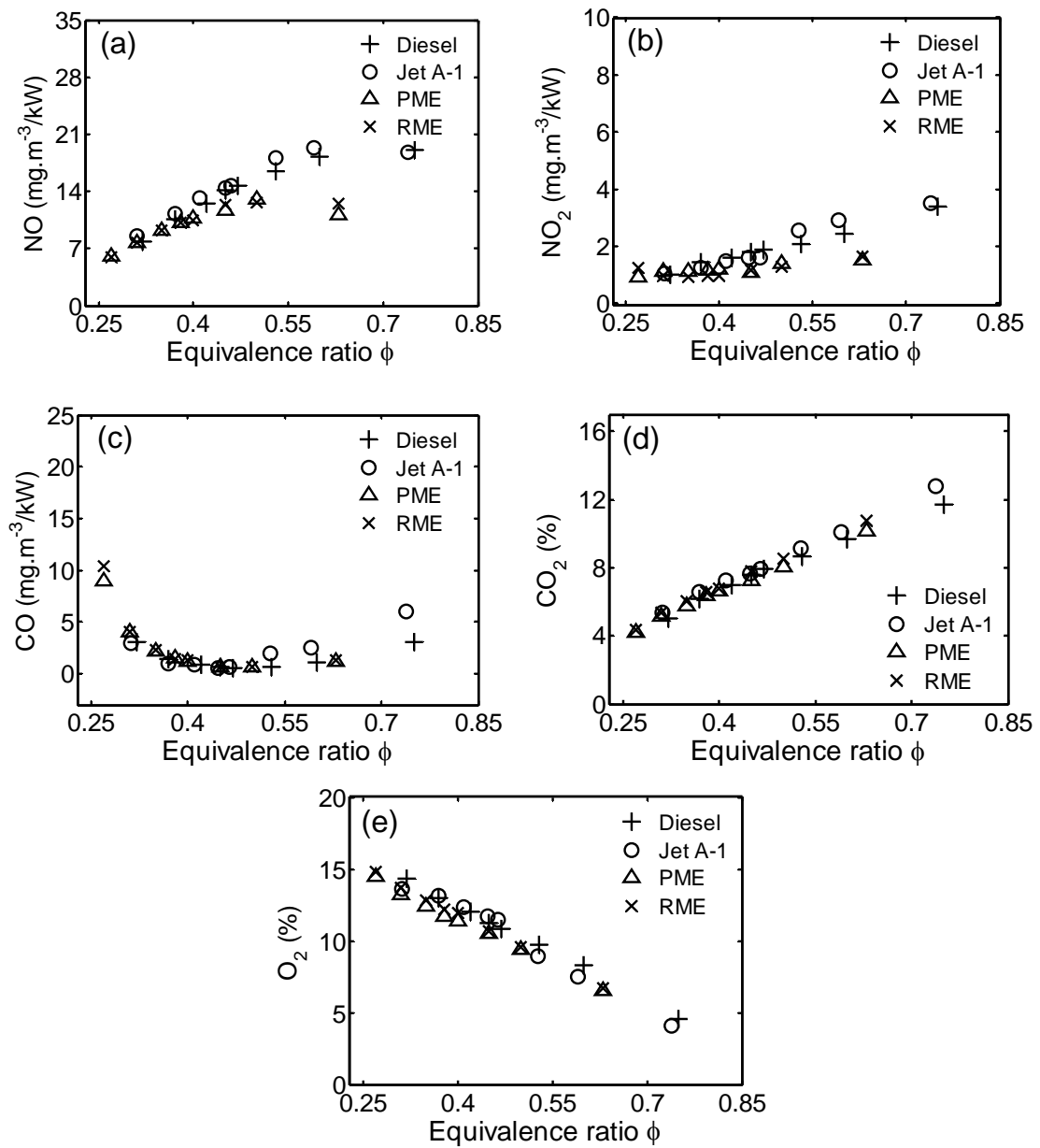
Figure 6.33: Emissions of (a) NO, (b) NO_2, (c) CO, (d) CO_2 and (e) O_2 as a function of equivalence ratio under the same power output condition.

6.5.3 Effect of blends on emissions

The emission of biodiesel blends relative to unblended fuels under the condition of same power output of 6 kW is shown Fig. 6.34. The emissions from the blends of 50 % PME/Jet-A1 and 50 % RME/Jet-A1 are compared against the unblended parent fuels as a function of excess air ratio. The emission index is expressed as a function of excess air ratio, which is defined as $(AFR\text{-}AFR_{stoic})/AFR_{stoic}$. At excess air ratio $= 0$, the fuel/air mixture is at stoichiometric. Higher values of the excess air ratio denote lean mixtures.

The NO and NO_2 emissions for biodiesel blends are located in between the unblended parent fuels, as shown at low excess air ratio in Fig. 6.34a and 6.34b. This also shows that biodiesel blends exhibit lower NO_x emissions than pure diesel and Jet-A1 fuels. As the excess air ratio is increased, the difference in NO emission between the blends and pure biodiesel decreases. This shows that NO reduction is not apparent for biodiesel or blends at ultra-lean conditions. A similar trend is observed for the NO_2 emissions although the value is relatively low. It is noted that diesel and Jet-A1 fuels produce higher NO_x than biodiesels. The measured O_2 and CO_2 values are rather close between the fuels considered including the biodiesel blends. The CO emission trend of the blends is similar to other fuels, where CO is seen to increase at excess air ratios of < 0.5 and > 1.2.
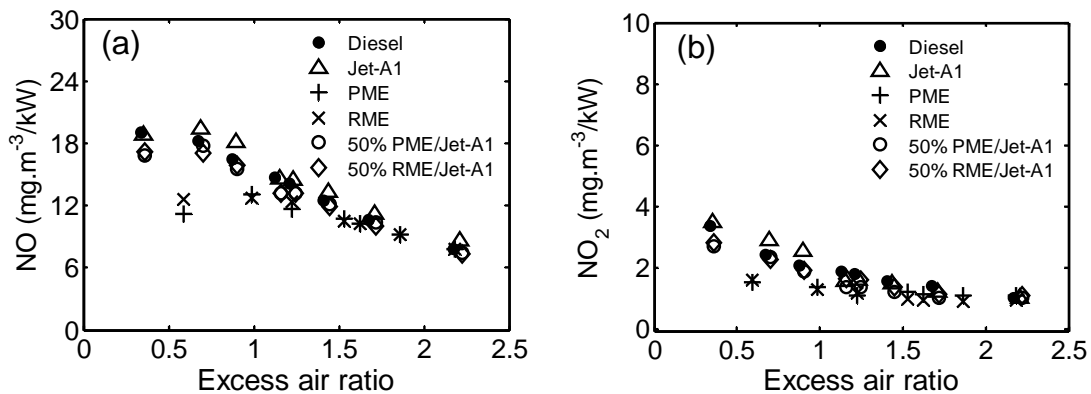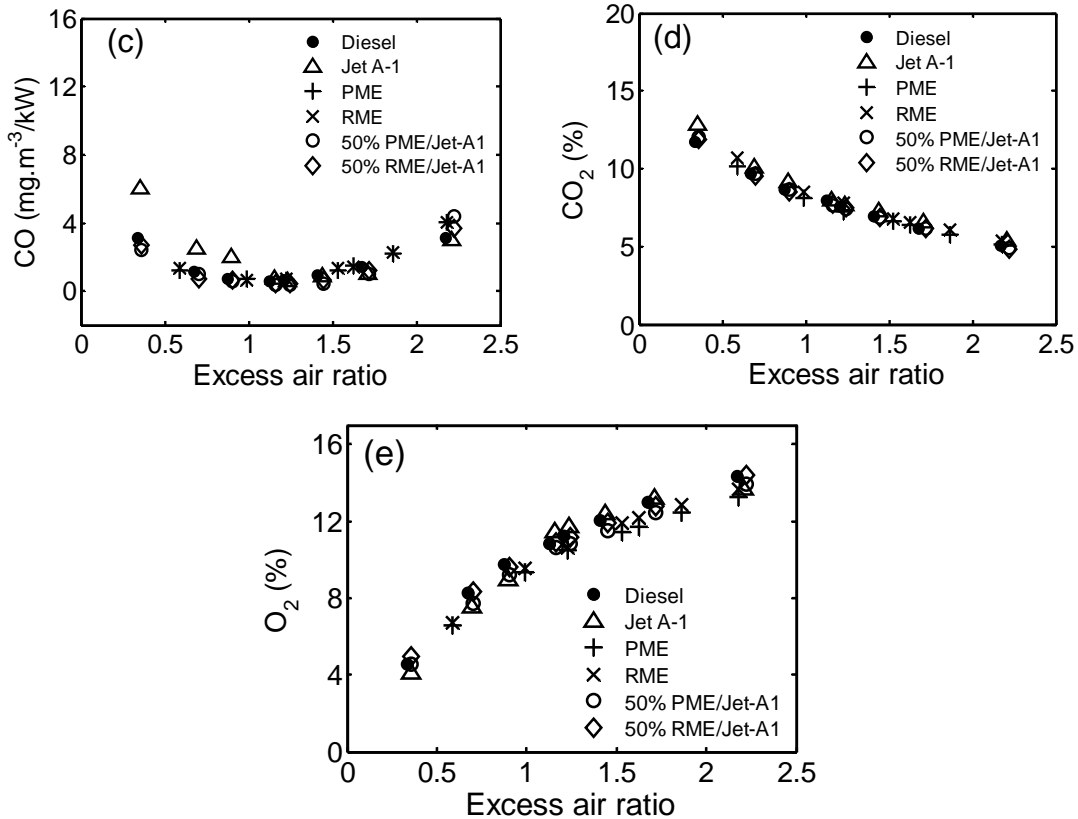
Figure 6.34: The effect of biodiesel blended fuels on the emissions of (a) NO, (b) NO_2, (c) CO, (d) CO_2 and (e) O_2 as a function of excess air ratio under the same power output condition.

6.5.4 Effect of power variation

The emission results for Jet-A1, diesel, PME and RME obtained under different burner power outputs are shown in Fig. 6.35. The flames are established under the same air/fuel mass ratio of 32. The overall trend shows that NO decreases as the power output increases. The reduction of NO at higher power outputs could be due to the influence of the flow field, where the increased strength of the recirculation zone under the higher air flow rates quenches the formation of NO. Diesel and Jet-A1 fuels generally produce higher NO emissions than biodiesels and blends, consistent with the trend shown in the previous sections. The NO emissions of the 50 % PME/diesel and 50 % RME/diesel blends are located in between the values of the baseline fuels and

biodiesels. This shows that blending conventional fuel with biodiesel could reduce NO_x emissions as the overall nitrogen-bound component in the blends is reduced.

On the contrary, NO_2 shows a slight increasing trend as the power output increases. The baseline fuels show slightly higher NO_2 emission than the biodiesel and blends. The CO emissions also show an increase with the power output and the quantity is of the same order of magnitude as NO_2. The reverse trend of the NO_2 and CO emissions compared to NO indicates that the flow fields within the combustor could have an influence on the emissions. At the higher power output condition, the higher swirling air flow increases the intensity of recirculation zone. This could result in the quenching of thermal NO_x due to the increase of turbulence intensity and faster mixing time scale.

The CO_2 and O_2 emissions profiles are relatively flat at all power output. This demonstrates that the air/ fuel ratios are the same. The oxygenated fuels of biodiesels show slightly higher O_2 and lower CO_2 formation than diesel and Jet-A1 fuels. This is because the equivalence ratio for biodiesels ($\phi = 0.4$) is lower than diesel and Jet-A1 ($\phi = 0.47$) under the same air/fuel mass ratio.
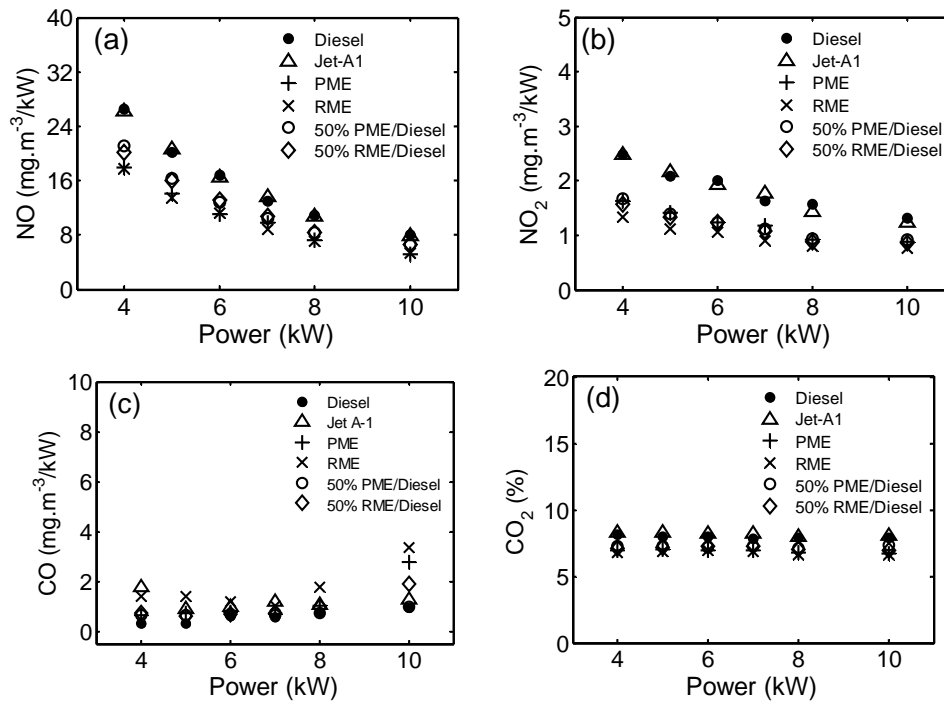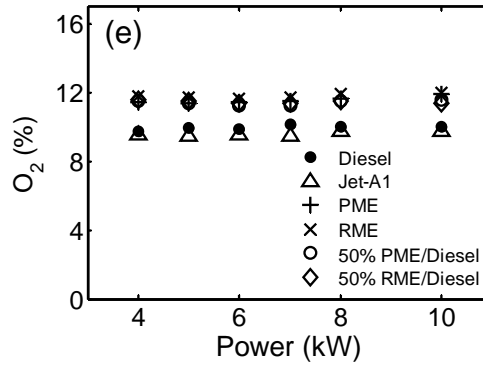
Figure 6.35: Emissions of (a) NO, (b) NO_2, (c) CO, (d) CO_2 and (e) O_2 as a function of burner power output under the same air/fuel mass ratio.

6.5.5 Effect of atomizing air-to-liquid mass ratio

In a plain-jet airblast atomizer, the atomizing air breaks up the liquid fuel jet into multiple fine droplets and forms a partially premixed mixture. The enhanced fuel/air mixing results in the distinctive characteristic of a bluish flame near the root of the flame. The supply of atomizing air affects the flame temperature and subsequently the NO_x formation. This shows that the atomizing air-to-liquid mass ratio (ALR) can be used an effective method to control the emissions. In this section, the effect of the ALR on the emissions is investigated under the same power output condition. The power output of the burner is maintained at 6 kW while the fuel/air mass ratio is maintained at 32 for all flames.
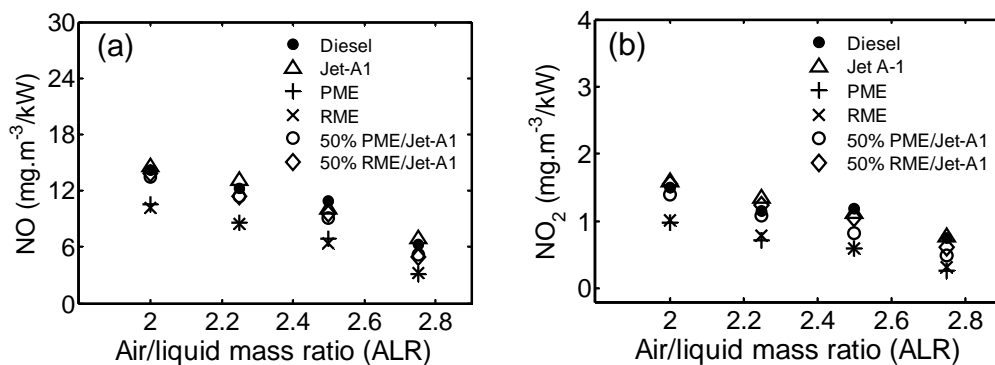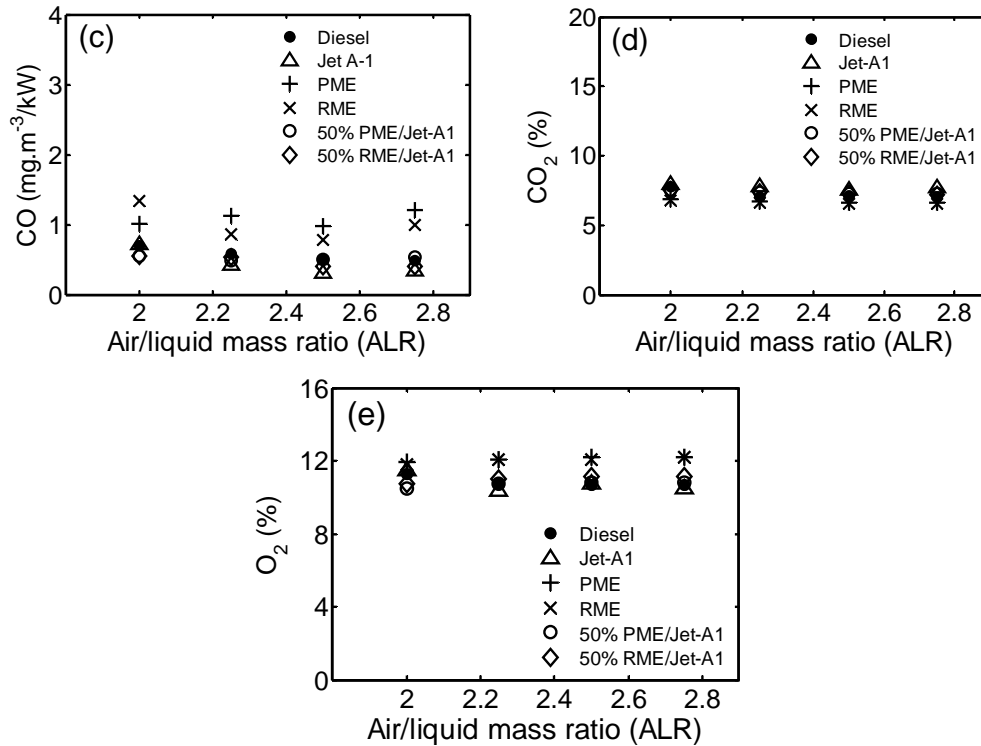
Figure 6.36: Emissions of (a) NO, (b) NO$_2$, (c) CO, (d) CO$_2$ and (e) O$_2$ as a function of atomizing air-to-liquid mass ratio under the same power output condition.

The emission results of NO, NO$_2$, CO, CO$_2$ and O$_2$ are shown in Fig. 6.36 as a function of the atomizing air-to-liquid ratio (ALR) under the condition of same power output. An increase of the ALR ratio shows a reduction of NO$_x$ as an almost linear trend. This shows the effectiveness in using the atomizing air to reduce NO$_x$ emissions using airblast atomizer. The utilisation of the ALR as a control for NOx emissions has been demonstrated by Bolszo and McDonell [4]. At ALR = 2.75, the emissions of NO$_x$ are reduced by a factor of ~1.5-2 compared to ALR = 2. The high air momentum of air results in the breaking up of the liquid jet into fine droplets, as shown quantitatively in section 5.1.1, Chapter 5. The vaporisation time scale for the smaller droplets becomes shorter due to the increased droplet surface area-to-mass ratio. The increase of atomizing air also enhances the mixing with fuels. This reduces the potential for localized droplets burning in the diffusion mode which tends to produce high level of NO$_x$ due to the increase of the local temperature. The atomizing air significantly affects

the flame structure and temperature field. The penetration length of the spray is increased and the high temperature region is pushed downstream. Although NOx reduction is achieved with the increase of ALR, the CO production shows insignificant changes. The O_2 and CO_2 remain constant at all ALRs, indicating the consistency of the overall fuel/air mixture ratio.

6.6 Conclusion

PIV measurements have been performed on the swirl burner under non-reacting and reacting conditions. Characterization of the flow field at the burner outlet was performed at an open air condition. The effect of main air flow preheating and flow rate variation on burner flow field was investigated. The introduction of the liquid fuel spray changes the flow field at the burner outlet where the radial velocity components are enhanced. The flow field at the open air condition is compared to the flow field within an enclosed tube. The enclosure generates the corner recirculation zone that intensifies the strength of the radial components. Comparison of the flow field under the spray flame condition shows almost similar velocity profiles for different fuels.

The OH* and CH* chemiluminescence imaging technique has been employed to obtain the spatially-resolved heat release region in the flame. Comparison of the chemiluminescence images was performed under both the same fuel mass flow rate and the same power output. The results show that diesel and Jet-A1 exhibit similar flame shape and structure as indicated by the OH* and CH* chemiluminescence images. The biodiesel flames show different flame shapes compared to diesel and Jet-A1 even though the flame reaction zone length is almost the same. Imaging of the soot region in the flame was performed using a longpass broadband filter (> 550 nm). Comparison of the longpass filtered images shows significant variation in the flame structure due to the presence of soot. The diesel flame shows the highest soot intensity in the post flame zone. The Jet-A1 flame shows less sooting tendency compared to the diesel flame. The PME and RME show no sign of soot formation due to the absence of aromatic rings. The 50 % biodiesel blend shows the chemiluminescence intensity signals that fall in between the two parent fuels.

Flame emission spectrometry shows the distinct soot thermal spectra of the diesel flame radiation established at the wavelengths between 550 and 850 nm. Jet-A1 shows a similar soot spectra but at a lower intensity than diesel flame. PME and RME show no sign of soot spectra but the latter exhibits a distinct peak of 588 nm which indicates the presence of inorganic material, i.e., sodium. The luminosity of the flames is significantly reduced when biodiesel is blended with diesel or Jet-A1 as reflected in the spectra of the biodiesel blended flames. The intensity of the soot

spectra is reduced by half for 20% biodiesel blend compared to the diesel flame, while 50% biodiesel blend shows no sign of a soot spectra.

The emissions of NO, NO_2, CO, CO_2 and O_2 have been measured with flames established from diesel, Jet-A1, RME, PME and their blends under the same power output conditions. The results show that the emissions of NO and NO_2 for biodiesels are consistently lower than diesel and Jet-A1 fuels despite the larger droplet size. This is because biodiesel fuel contains no nitrogen-bound components. The presence of oxygen in biodiesel also assists in the more complete combustion and reduces the tendency of local droplet combustion in diffusion mode. The emission of CO is not pronounced given that the measurements were conducted under fuel-lean conditions. As the power of the burner increases, the emission of NO decreases while NO_2 shows an increasing trend due to the effect of the flow field. Biodiesel blends show reduced emissions of NO_x compared to diesel and Jet-A1 fuel. Another parameter tested is the effect of atomizing air-to-fuel ratio (ALR) on emissions. By increasing the ALR, the NO and NO_2 is reduced but the effect on CO is small. The reduction of NO_x is attributed to smaller droplets, faster evaporation and enhanced mixing at higher ALR.

6.7 References

[1]   R. Wang and P. Cadman, "Soot and PAH production from spray combustion of different hydrocarbons behind reflected shock waves," *Combust. Flame*, vol. 112, pp. 359-370, (1998).

[2]   N. Hashimoto, Y. Ozawa, N. Mori, I. Yuri, and T. Hisamatsu, "Fundamental combustion characteristics of palm methyl ester (PME) as alternative fuel for gas turbines," *Fuel*, vol. 87, pp. 3373-3378, (2008).

[3]   T. H. Song and R. Viskanta, "Interaction of radiation with turbulence-Application to a combustion system," *J. Termophysics Heat Trans.*, vol. 1, pp. 56-62, (1987).

[4]   C. D. Bolszo and V. G. McDonell, "Emissions optimization of a biodiesel fired gas turbine," *Proc. Combust. Inst.*, vol. 32, pp. 2949-2956, (2009).

Chapter 7

Summary and conclusion

7.1 Summary of research

The current work focuses on the research of combustion properties of practical liquid fuels (i.e. diesel, Jet-A1 and biodiesels). Emphasis is placed on the measurements of laminar flame speed, fuel spray characterisation under non-reacting conditions, and the characterisation of a swirling spray flame in a generic gas turbine combustor. The laminar flame speed of mixtures of air with methane, acetone, acetone/methane, n-heptane, Jet-A1, diesel, PME, PME/diesel and PME/Jet-A1 were measured using the jet-wall stagnation flame technique. The measured flame speeds can be used as validation data for chemical kinetic mechanisms or as direct input for turbulent flame modelling. For the non-reacting spray investigation, a plain-jet airblast atomizer was utilised to atomize liquid fuels. The spray characteristics of the atomizer and the effect of fuel properties on spray atomization were examined using a PDA. The spray combustion characteristics of liquid fuels in a generic gas turbine combustor were investigated. The flow field within the burner was measured using PIV, while the droplet velocity and SMD in the flames was measured using a PDA. Flame imaging was performed to visualize the global flame reaction zone and the sooting region in the post-combustion region. The emission performance of different fuels was investigated using a gas analyzer at the combustor outlet under steady state conditions. The techniques and methodology employed can be utilised to investigate new candidate alternative fuels.

7.2 Conclusion

Laminar flame speed measurements (Chapter 2 and 3)

The jet-stagnation flame technique coupled with PIV has been utilised to measure the laminar flame speed of gaseous and liquid fuels. The technique was applied to measure the effect of acetone seeding to methane/air mixtures at 298 K and 1 atm over a range of equivalence ratios. The results show that the effect of a small quantity of acetone seeding, between 0-20% by mol, on methane/air mixtures is more significant in the fuel-rich region. The laminar flame speed is increased by 3-6 cm/s for rich mixtures while the lean mixtures exhibit a difference of less than 2 cm/s. Simulation of the flame speed using the GRI-Mech 3.0 chemical mechanism coupled with an acetone submechanism shows good agreement with the measurement.

Measurement of the flame speed was performed on acetone/air over range of stoichiometry at 1 atm. The results show that acetone/air flame speed propagates faster than methane/air flame across the whole range of equivalence ratios. Simulation results obtained from the modified GRI-Mech 3.0 agrees well with the experimental data. This shows that the methane-based mechanism coupled with an acetone sub mechanism can potentially be used to describe acetone flame.

The jet-stagnation flame configuration technique was extended to measure the laminar flame speeds of higher hydrocarbon liquid fuels. The system was upgraded with a heating facility to vaporise liquid fuel at elevated temperatures. N-heptane/air flame speeds were measured at 293 K, 400 K and 470 K and 1 atm. The results show good agreement with the literature data. The laminar flame speed of practical liquid fuels including Jet-A1, diesel, palm methyl esters and blends have been measured at an elevated temperature of 470 K and 1 atm over a range of equivalence ratios. Comparison to n-decane and n-dodecane shows that large n-alkanes can be used as surrogates for Jet-A1 fuel due to their similar reactivity. Both PME/air and diesel/air mixtures exhibit lower flame speeds at fuel-lean and stoichiometric compared to n-decane and n-dodecane.

Laminar flame speed measurements of PME blends with Jet-A1 and diesel at 10%, 20% and 50% by volume at 1 atm and 470 K were performed. The results show a

decrease of flame speed on the lean side and an increase on the rich side. The peak temperatures of the PME/hydrocarbon blends shift slightly to the fuel-rich side. The Jet-A1 flame speed and reactivity is influenced more by the blending of PME than diesel fuel. The oxygen content and lower heat of combustion of PME are factors that led to the discrepancy of laminar flame speed and reactivity compared to pure Jet-A1 and diesel flame.

Non-reacting spray characteristics (Chapter 4,5)

The spray and atomization characteristics of a plain-jet airblast atomizer were examined using a PDA. The effect of the ALR on the droplet characteristics was investigated. The droplet SMD values increase with increasing ALR until a threshold where further reduction of SMD values is not significant. This trend agrees well with the empirical correlations developed by previous researchers using similar atomizer configuration. Through the Mie scattering technique, the sprays were imaged to determine the spray cone angles. An increase of ALR extends the penetration length of the spray but reduces the spray cone angle. The variation of ALR can be used as a control parameter in optimizing droplet SMD values in the combustor which leads to more efficient combustion.

The droplet velocity profiles show the peak velocity at the centreline of the spray and appear to be insensitive to liquid fuel physical properties. The droplet SMD profiles show a dependence on the properties of liquid fuels, in which biodiesel droplets generate higher SMD values compared to Jet-A1 and diesel. The droplet SMD values are lowest at the spray centreline but increase radially towards the boundary of the spray. Physical properties that influence droplet SMD are viscosity and surface tension. The droplet number density and volume flux profiles exhibit a peak value that locates at a radial distance away from the centreline. The droplet size is prone to increase at the spray centreline for ALR$<$4.

Spray combustion characteristics (Chapter 4, 5 and 6)

A single swirl gas turbine type burner was developed and utilised to investigate the spray combustion characteristics of biodiesels and conventional fuels. The main swirling air was preheated to an elevated temperature of 623 K. The main air co-axially enveloped the liquid fuel spray that was generated using a plain-jet airblast atomizer at the centre of the burner outlet. Characterization of the burner flow field was performed using PIV. The combination of the swirling flow field with the liquid fuel spray results in the enhanced radial velocity components and the broadening of the axial velocity profiles. The velocity profiles of the flow field in the open condition are compared to the flow field in an enclosed tube. The enclosure leads to a corner recirculation zone and intensifies the centre recirculation zone. The combined liquid fuel spray with preheated main air flow shows a different flow field compared to the flow field without spray. Comparison of the flow fields between diesel, Jet-A1, PME and PME spray flames show almost similar axial and radial velocity profiles in the combustor.

The liquid fuel droplet characteristics in sprays flames were investigated using a PDA. Comparison of the droplet velocity and SMD profiles between different fuels was performed. The results show that droplet velocity profiles exhibit a lower droplet velocity peak at the burner centreline due to the interaction with the reverse flow induced by the centre recirculation zone. Palm and rapeseed biodiesels exhibit the characteristics of larger droplets compared to diesel and Jet-A1 fuel due to the higher boiling point. Jet-A1 shows the lowest droplet SMD values due to the high volatility that promotes droplet vaporisation. The late vaporisation of biodiesels increases the presence of droplets within the flame as indicated by the higher droplet concentration and volume flux. Biodiesel blend spray flames exhibit droplet characteristics similar to biodiesel but the droplet concentration and volume flux vary depending on the volatility of the blended fuels.

The spray flame structures were investigated via OH* and CH* chemiluminescence imaging. The result shows that diesel and Jet-A1 flames structures are different from PME and RME flames. The biodiesel flames show an increased reaction zone due to the late vaporisation of the biodiesel droplets. Imaging of the flames using a CCD camera coupled with a longpass filter (>550 nm) was performed to

examine the sooting tendency of different fuels. The result shows that diesel exhibits the highest amount of soot in the post-reaction zone region, followed by Jet-A1 while biodiesel spray flames show insignificant presence of soot formation. The 50% biodiesel blend shows chemiluminescence intensity that falls in between the parent fuels. The presence of soot is indicated by the flame emission spectroscopy at wavelengths between 550 and 850 nm. The Jet-A1 flame shows a lesser intensity soot spectra than the diesel flame. The biodiesel flames show no sign of soot but the RME flame exhibits a distinct peak of 588 nm which indicates the presence of sodium. The intensity of the soot spectra is reduced by half for 20% biodiesel blends while 50% biodiesel blends show almost no soot formation.

Emissions measurement (Chapter 6)

The emission measurement shows that PME and RME swirl flames emit lower NO and NO_2 than Jet-A1 and diesel fuel when compared under the condition of same fuel mass flow rate and same power output. The lower NO_x emission of biodiesels is attributed to the absence of nitrogen-bound components. The increase of power output of the burner from 4 kW to 10 kW shows a decrease of NO but an increase of NO_2 and CO. Another parameter tested is the effect of atomizing air-to-fuel ratio (ALR) on emissions. An increase of ALR lowers the emissions of NO and NO_2, but the effect on CO is small. The increased atomizing air lowers the local temperature and provides high momentum for droplet atomizing. Smaller droplets are generated at high ALR and this allows faster droplet vaporisation and enhanced fuel/air mixing. Biodiesel blends show reduced NOx emissions compared to pure diesel or Jet-A1.

From the above investigations, it has been shown that PME and RME can be used as a substitute fuel for gas turbine power generation. The reactivity of PME is shown to be comparable to diesel fuel. Despite the slight difference in droplet size, biodiesel flames show an overall similar flame shape and length compared to diesel and Jet-A1 flames. The NOx emissions of biodiesels are also shown to be lower.

7.3 Suggestion for future research

- The present study suggests that knowledge of the fundamental combustion properties of biodiesels is still lacking. Apart from the laminar flame speed, combustion data such as the extinction stretch rate and ignition delay time are desirable from the point of view of combustor design and chemical mechanism modelling.

- The laminar flame speed of higher liquid hydrocarbon such as n-decane, n-dodecane, n-hexadecane can be measured and compared to practical liquid fuels.

- The laminar flame speed of biodiesels of different feedstock can be measured. Understanding of the reactivity between saturated methyl esters and unsaturated methyl esters is desirable. Hence, flame speed investigations can be extended to pure methyl esters such as methyl palmitate or methyl linoleanate.

- Investigation of the fuel droplet characteristics with biodiesels can be performed using a pressure swirl atomizer and compared to the present plain-jet airblast type atomizer.

- For swirling spray flames in a generic gas turbine combustor, characterisation of the flow field can be investigated using a 3D PIV that includes the measurement of tangential velocity components. Characterisation of the droplet under reacting flow conditions can be performed using 2D/3D PDA to better understand the droplet distributions in the radial directions and to provide a more extensive modelling target.

- A spark ignitor can be installed at the base of the combustor to investigate the ignition phenomenon of flames. The ignition of alternative fuels relative to baseline fuels can be compared from various parameters including the location and the energy of the spark energy supplied.

- A solid metal combustor with a dedicated sampling port instead of a quartz tube can be used for emission measurements.

- The methodology used in this dissertation can be extended to other alternative fuels such as bioethanol, Fisher-Tropsch fuel or bio-oil.

Appendix A1
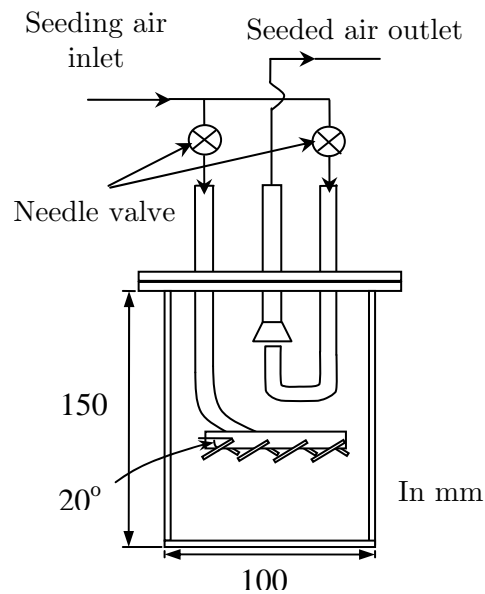
Figure A4: Schematic of the solid particle seeder

The solid particle seeder used in the PIV experiment is made from brass. The seeding air is fed into a disk which directs the air flow at an angle to fluidize the seeding particles. The strength of the seeding flow rate is regulated by two needle valves. The particles near the outlet (funnel) will exit the seeder with the other stream of air. The heavier particles fall back into the container due to drag while the lighter particles follow the exit flow. The seeding rate used is approximately 0.2 g/min. The design of the solid particle seeder is adapted from Mendes-Lopez (1984).

J. M. C. Mendes-Lopes, *Influence of Strain Fields on Flame Propagation.* PhD: University of Cambridge, 1984.

Appendix A2
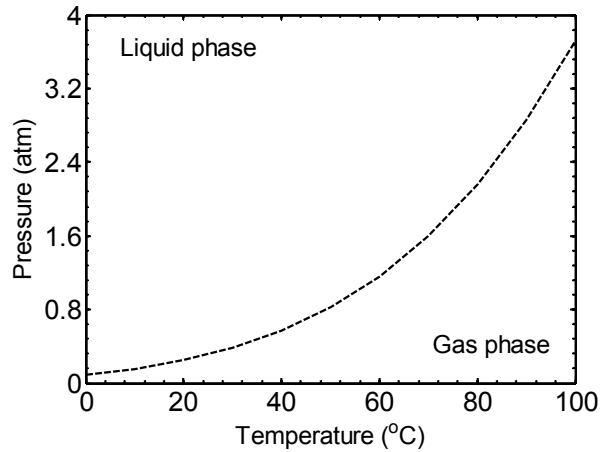
Figure A2: Vapour-pressure line of acetone

      The vapour-pressure line of acetone is shown in Fig. A2. The acetone vapour pressure is maintained below the saturation line to avoid condensation of acetone in the system. (Data from: www.fluidat.com)
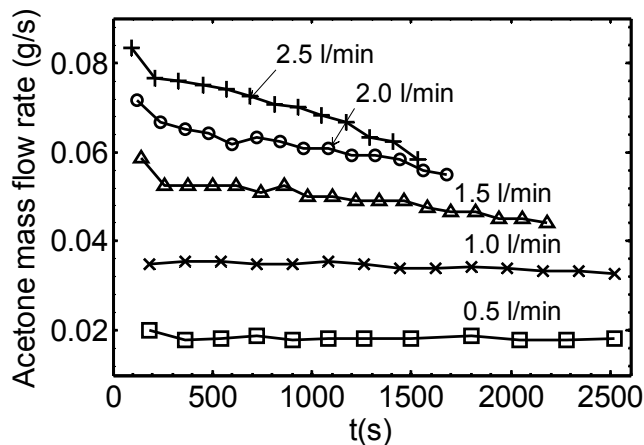
Figure A3: Acetone bubbling method

Figure A3 shows the acetone mass flow rate as a function of time at a different bubbling air flow rates at T=25 °C. The acetone vaporisation rate becomes inconsistent at high bubbling rate due to the decreasing volume of acetone that results the disequilibrium of temperature between the liquid and air chamber, which subsequently changes the acetone partial pressure. Hence, only low flow rates of air (< 1 l/min) are used as bubbling air for acetone seeding.

Appendix B1

Table B1: Biodiesel specifications

Test parameter	European standard (EN 14214:2003)	*PME (FAME-W10)	**RME
Methyl ester, %	96.5	97.7	99.1
Density@15ºC, kg/m3	860-900	879.3	0.8835
Viscosity@40ºC, mm2/s	3.5-5.0	4.423	4.5
Flash point, ºC	120 min	172	>120
Sulfur content, mg/kg	10 max	2.0	<10
Carbon residue (10% distillation residue), %m/m	0.3 max	0.03	<0.3
Cetane number	51 min	55.7	>51
Sulfated ash content,%m/m	0.02 max	<0.01	<0.02
Water content, mg/kg	500 max	590	237
Total contamination, mg/kg	24 max	15	10
Copper strip corrosion, 3h@50oC	Class 1	1a	1
Oxidation stability @110oC, hrs	6.0 min	10.5	10.4
Acid value, mg KOH/g	0.5 max	0.436	0.18
Iodine value, g Iodine/100g	120 max	96.38	113.7
Linolenic Acid methyl ester, %m/m	12.0 max	<0.1	9.7
Polyunsaturated (≥4 double bonds)	1 max	<0.1	<1
Methanol content, %m/m	0.2 max	<0.1	0.04
Monoglyceride content, %m/m	0.8 max	0.054	0.65
Diglyceride content,%m/m	0.2 max	0.056	0.14
Triglyceride content, %m/m	0.2 max	0.02	0.05
Free glycerol, %m/m	0.02 max	< 0.02	0.00
Total glycerol, %m/m	0.25 max	0.024	0.19
Na+K, mg/kg	5.0 max	0.8	1.52
Ca+Mg, mg/kg	5.0 max	0.1	0.03
Phosphorous content, mg/kg	10.0 max	0.6	1.0
Cold filter plugging point, ºC	-6 max	-12	-27

* Winter grade palm methyl esters supplied by Carotino Sdn. Bhd., Malaysia
** Rapeseed methyl esters supplied by ADM International Sarl, Switzerland

Appendix B2

Table B2: ASTM D7467 Standard for biodiesel blends with diesel between 6% to 20% v/v.

Properties	B6 to B20
Acid Number, mg KOH/g, max.	0.3
Viscosity, mm2/s at 40°C	1.9–4.1
Flash Point, ^{o}C, min	52
Cloud Point, ^{o}C, max	-
Sulfur Content, (μg/g)d	15
mass %, max.	0.05 (S500)
mass %, max.	0.5 (S5000)
Distillation Temperature, ^{o}C, 90% evaporated, max.	343
Ramsbottom carbon residue on 10% bottoms, mass %, max.	0.35
Cetane Number, min.	40
One of the following must be met:	
(1) Cetane index, min.	40
(2) Aromaticity, vol %, max.	35
Ash Content, mass %, max.	0.01
Water and Sediment, vol %, max.	0.05
Copper Corrosion, 3 h @ 50°C, max.	No. 3
Biodiesel Content, % (V/V)	6–20
Oxidation Stability, hours, min.	6
Lubricity, HFRR @ 60°C, micron, max.	520

Appendix C1

$\Delta P=3.6m-0.41$
for $0.13<m<1$ g/s of Air
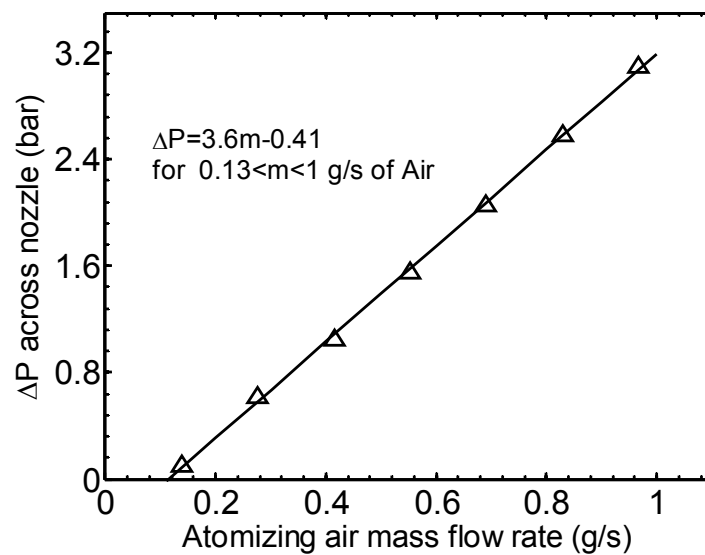
Figure C1: Pressure drop across the plain-jet airblast atomizer used in the non-reacting spray experiment (Chapter 4) as a function of air mass flow rate

The injection of air through the nozzle air orifice would incur a pressure drop. The pressure drop across the air orifice is linearly related to the atomizing air mass flow rate as shown in Fig. C1.